# Robotic Micromanipulation of the Nematode Worm *Caenorhabditis Elegans*

by

**Xianke Dong**

**Department of Mechanical Engineering**
**McGill University**

**Montreal, Quebec, Canada**

Feb 2019

A thesis submitted to McGill University in partial fulfillment of the requirements for a doctoral degree

# Dedication

*To my dear parents for their love, care and support*

# Table of Contents

# List of Figures

# Abstract

The nematode worm *Caenorhabditis elegans* (*C. elegans*) is a tiny biological model organism with a ~1000 $\mu m$ long ~80 $\mu m$ wide transparent body composed of ~1000 somatic cells (exact 959 in male; exact 1031 in hermaphrodite). Because of its many advantages of short life cycle, well characterized nervous system, well known neuronal wiring connections, and plenty of genetic tools facilitate its study, *C. elegans* is particularly amenable to neuronal, developmental, and genetics studies. In worm biology laboratories, however, the basic operations of *C. elegans* screening by developmental stages and *C. elegans* microinjection of DNA plasmid for transgenic worm generation are still manually conducted by skilled operators, which is especially time-consuming and labor-intensive. In this thesis, automated robotic micromanipulation techniques and systems for *C. elegans* screening and microinjection experiments are developed, which provide superior throughput, accuracy and success rate compared over manual operations. In addition, an automated patterned-light projection system under an inverted microscope is designed to enable automated optogenetic excitation on the worm body for worm locomotion control. By initiating the contraction of muscular cells with the optogenetic method, the modelling and vision feedback close-loop control techniques are successfully designed to automatically regulates the locomotion of the worm.

This thesis research is composed of three projects that facilitate the automated operation of *C. elegans*: automated worm sorting, robotic worm microinjection and optogenetic worm locomotion control. For the worm sorting, unlike the existing microfluidic worm sorting devices that purely rely on passive sorting mechanisms, the proposed system can accurately measure the worm body size parameters and actively sort individual worms based on their body lengths. This function was realized by automatic control of a double-layer microfluidic device with computer-controlled microvalves. Real-time image processing algorithms were developed to measure the worm length and width parameters, visually monitor the on-chip events, and provide feedback signals to the system to regulate the microvalve states for sequential loading, trapping, and sorting of single worms. Based on sorting experiments of 319 worms, the sorting speed and success rates of the system were tested to be 10.4 worms/min and 90.3%, respectively.

The worm microinjection system was developed based on a double-layer microfluidic device with computer-controlled pneumatic valves to load individual worms, and a three-degree-of-freedom

(3-DOF) micromanipulator to conduct automated microinjection. Robust image processing algorithms were developed to identify the injection needle tip position, detect the contact between the needle tip and the substrate, and constantly monitor the loading/unloading of single worm in the microfluidic channel. From the experiments on 240 worms, the robotic system demonstrated automated, continuous worm injection at a speed of 6 worms per minute (10 s/worm) with an operation success rate of 78.8% , which are 23 times faster and >1.5 times higher than the injection speed (~4 min/worm) and success rate (~30%) of a proficient human operator.

Besides the automated worm sorting and worm injection, an automated patterned-light projection system was developed to automatically track the worm and spatial selectively deliver patterned laser beam to target muscle cells of a single paralyzed worm. This capability enables artificial perturbation of the contraction and inhabitation of the muscles on the worm body. the crawling dynamics of the worm on agar plate is studied and muscular excitation patterns that drives the worm with stable movement are identified. By applying the light patterns to the paralyzed worm body muscles through the proposed miniature projection system, the normal behaviors on worms of straight forward moving, shallow turns, gradual turns and omega turns were artificially reproduced on a paralyzed worm. Moreover, by characterizing the worm crawling behavior with a kinematic model, the worm moving direction and destination can be controlled. This study shows the potential of turning a live worm into a computer vision-feedback soft microrobot, and may also provide an effective tool for the worm behavioral studies.

# Résumé

Le nématode *Caenorhabditis* elegans (*C. elegans*) est un organisme modèle mesurant approximativement 1000 um long 80 um large avec un corps transparent composé de près d'un miller cellule somatiques. (exactement 959 chez le mâle; 1031 chez l'hermaphrodite). A cause de plusieurs avantages tels qu'un cycle de vie très courte, un système nerveux bien caractérisé, connexions neuronale bien connue ainsi que plusieurs outils génétiques facilitant l'étude, *C. elegans* est particulièrement convenable aux études neuronales, développementaux et génétiques. Cependant, dans les laboratoires de biologie, les opérations de basique de criblage du *C. elegans* par stades de développement et de la micro-injection de *C.elegants* du plasmide d'ADN pour la génération mutants sont toujours effectuées manuellement pars des opérateurs qualifié, demandant beaucoup de temps et de travails. Dans cette thèse, nous allons automatiser les criblages et les micro-injections via des techniques de micromanipulation robotisées avec un débit, une précision et un taux de réussite supérieurs à ceux des opérations manuelles. De plus, un système de projection miniature a haute précision a été développé sous microscope inversé afin de permettre une excitation optogénétique automatisée sur le corps du ver avec une résolution unicellulaire. En initiant artificiellement les contractions des cellules musculaires avec les méthodes optogenetiques, nous avons développé avec succès les techniques de modélisation et de contrôle en boucle fermée pour réguler automatiquement la locomotion du ver.

Cette thèse est composée de trois sous-projets qui facilitent l'opération automatisée de *C. elegans*, ainsi que celle du microrobot souple de *C. elegans*: tri automatisé des vers, microinjection de vers robot et contrôle optogénétique de la locomotion des vers. Pour le triage des vers, contrairement aux dispositifs de tri microfluidiques existants qui reposent uniquement sur des mécanismes de triage passifs, le système proposé peut mesurer avec précision les paramètres de taille du corps du ver et trier activement les vers individuels en fonction de la longueur de leur corps. Cette fonction est réalisée par le contrôle automatique d'un dispositif microfluidique à double couche doté de microvalves commandées par ordinateur. Des algorithmes de traitement d'image en temps réel ont été développés pour mesurer les paramètres de longueur et de largeur du ver, surveiller visuellement les événements sur-puce et de fournir des signaux de rétroaction au système afin de réguler les états de la microvalve pour le chargement, le piégeage et le triage séquentiels des vers

individuels. Basant sur des expériences de triage de 319 vers, la vitesse du triage et les taux de réussite du système ont été testés à 10,4 vers / min et 90,3%, respectivement.

Le système de microinjection a également été développé basant sur un dispositif microfluidique à double couche avec des vannes pneumatiques commandées par ordinateur pour charger les vers et d'un micromanipulateur XYZ 3-DOF pour effectuer des microinjections automatisées. Des algorithmes de traitement d'image robustes ont été développés pour identifier la position de la pointe de l'aiguille d'injection, détecter le contact entre la pointe de l'aiguille et le substrat et surveiller en permanence le chargement / déchargement d'un seul ver dans le canal microfluidique. D'après les expériences menées sur 240 vers, le système robotique a démontré une injection automatique et continue de vers à une vitesse de 6 vers par minute (10 s / ver) avec un taux de réussite de l'opération de 78,8%, soit 23 fois plus rapide avec une vitesse d'injection 1.5 fois plus élevé qu'un opérateur humain (~4 min/vers et taux de réussite de ~30%).

Outre que le triage et l'injection automatisés des vers, un système de projection miniature est développé pour taquer automatiquement le ver et de délivrer spécialement de façons sélectives le faisceau laser aux cellules cibles. Cette capacité permet une perturbation artificielle de la contraction et de l'inhibition des muscles du corps du ver avec une résolution monocellulaire. Nous avons étudié la dynamique de rampage du ver sur une plaque de gélose et identifié les schémas d'excitation musculaire qui entraînent le ver avec un mouvement 2D stable. En appliquant les patterns aux muscles du corps du ver paralysés par le biais du système de projection miniature proposé, nous avons constaté, grâce à des expériences, que les comportements normaux des vers, des virages droits, des virages peu profonds, des virages graduels et des virages oméga peuvent être reproduits artificiellement sur un ver paralysé. De plus, en caractérisant le comportement de rampage du ver avec un modèle cinématique, la direction et la destination de déplacement du ver peuvent être contrôlées. Cette étude transforme le ver vivant en microrobot mou et constitue un outil efficace pour les enquêtes comportementales sur le ver.

# Acknowledgement

My sincere gratitude and amiable thanks belong to a group of people including the professors at McGill and UofT, my family and my friends. Without their help, support and encouragement, my thesis would never be completed. First of all, I would like to express my greatest appreciation to my Ph.D. supervisor, Prof. Xinyu Liu for his help, guidance, and training on the starting phase of my academic journey. He was a great mentor during the past several years and his persistent passion for science and engineering will be a great source of inspiration in my future professional career. I owe my profound thanks to Prof. Zhen Mei at the Lunenfeld-Tanenbaum Research Institute for her scientific advices and instructions during my visiting to University of Toronto. I also would like to expose my deep gratitude to Prof. Michael Hendricks at the biological department of McGill University for his suggestions and supports in the first year of my research. In addition, I convey my special thanks here to Prof. Meyer Nahon at the mechanical department of McGill University for his support during the transitional phase for the relocation of our group. I want to extend this gratitude to other members of my PhD advisory committee: Prof. Luc Mongeau and Prof. Yaoyao Fiona Zhao for their useful insights and suggestions.

I appreciate the Faculty of Engineering at McGill University, the Faculty of Mechanical and Industrial Engineering at University of Toronto, the Natural Sciences and Engineering Research Council of Canada, and the Chinese Scholarship Council for their collaborative financial support of my Ph.D. research.

I would like to express my greatest appreciation to the former and current members of our group: Dr. Xiao Li, Dr. Chen Zhao, Dr. Weize Zhang, Dr. Pengfei Song, Dr. Ran Peng, Juntian Qu, Qiyang Wu, Binbin Ying, Hao Fu, Peng Pan, Sina Kheiri, Zhen Qin, Yueyue Pan, and Linghao Du. They were my true friends. We shared the happiness and tears in the past several years.

Last but not least, I would like to say my deepest thanks to my father and mother, who devoted their lives to raise me up from a baby to a man through the hard days. All that I am, or hope to be, I owe to my angel mother.

# Contributions of the Author

This is a manuscript-based thesis consisting of three journal articles, one review paper and one book chapter. The title of manuscripts, name of the authors, and their contributions are listed below:

**1) Robotic Micromanipulation of Cells and Small Organisms**

Xianke Dong[1], Wes Johnson[2], Yu Sun[2], Xinyu Liu[1]

[1]Department of Mechanical Engineering, McGill University, 817 Sherbrooke Street West, Montreal, Quebec, Canada H3A 2K6

[2]Department of Mechanical and Industrial Engineering, University of Toronto, 5 King's College Road, Toronto, Ontario, Canada, M5S 3G8

Published as a book chapter in: *Micro-and Nanomanipulation Tools*, eds. Yu Sun and Xinyu Liu. Wiley-VCH, 2015.

***Author contributions**:*

XD: Performed the literature review, identified the key ideas in the development of robotic micromanipulation of bio-samples, and wrote the manuscript.

WJ and YS: Helped edit the text.

XL: Supervised the research and wrote the manuscript.

**2) Bio-Agent Microrobots: A Review**

Xianke Dong and Xinyu Liu

[1]Department of Mechanical Engineering, McGill University, 817 Sherbrooke Street West, Montreal, Quebec, Canada H3A 2K6

[2]Department of Mechanical and Industrial Engineering, University of Toronto, 5 King's College Road, Toronto, Ontario, Canada, M5S 3G8

To be submitted.

***Author contributions**:*

XD: Performed the literature review, identified the major topics in the field of bio-agent robot, and wrote the manuscript.
XL: Supervised the research and wrote the manuscript.

**3) An Automated Microfluidic System for Morphological Measurement and Size-Based Sorting of *C. elegans***

Xianke Dong[1,2], Pengfei Song[1], Xinyu Liu[1,2]

[1]Department of Mechanical Engineering, McGill University, 817 Sherbrooke Street West, Montreal, Quebec, Canada H3A 2K6
[2]Department of Mechanical and Industrial Engineering, University of Toronto, 5 King's College Road, Toronto, Ontario, Canada, M5S 3G8
In press: *IEEE Transactions on NanoBioScience,* DOI: 10.1109/TNB.2019.2904009, 2019.
***Author contributions**:*
XD: Designed the microfluidic device, constructed the hardware and software setup for worm sorting, performed the sorting experiments, analyzed the data, and wrote the manuscript.
PS: Co-designed the microfluidic device, helped with experiments, prepared the worms for experiments.
XL: Proposed the idea, designed the experiments, analyzed the data, and wrote the manuscript.

**4) Automated Robotic Microinjection of the Nematode Worm *Caenorhabditis* Elegans**

Xianke Dong[1,2]*, Pengfei Song[1]*, Xinyu Liu[1,2]

[1]Department of Mechanical Engineering, McGill University, 817 Sherbrooke Street West, Montreal, Quebec, Canada H3A 2K6
[2]Department of Mechanical and Industrial Engineering, University of Toronto, 5 King's College Road, Toronto, Ontario, Canada, M5S 3G8
Submitted to: *IEEE Transactions on Automation Science and Engineering,* under review.
***Author contributions**:*
XD and PS contributed equally to this work.

XD: Constructed the system hardware system for automatic microinjection, composed the software manipulation GUI for experiments, designed and performed the experiments, analyzed the data, and wrote the manuscript.

PS: Designed the microfluidic device, cultured the worms for experiments, performed the experiments, analyzed the data, and helped figure preparation.

XL: Proposed the idea, designed the experiments, analyzed the data, and wrote the manuscript.

**5) Towards A Soft Microrobotic Animal: Light-Driven Locomotion Control of *Caenorhabditis Elegans***

Xianke Dong[1,2], Sina Kheiri[2], Yangning Lu[3,4], Zhen Mei[3,4], Xinyu Liu[1,2]

[1]Department of Mechanical Engineering, McGill University, 817 Sherbrooke Street West, Montreal, Quebec, Canada H3A 2K6

[2]Department of Mechanical and Industrial Engineering, University of Toronto, 5 King's College Road, Toronto, Ontario, Canada, MS 3G8

[3]Lunenfeld-Tanenbaum Research Institute, 600 University Avenue, Room 870

Toronto, Ontario, Canada, M5G 1X5

[4]Department of Physiology, University of Toronto, 1 King's College Circle, Toronto, Ontario, Canada, M5S 1A8

To be submitted.

***Author contributions**:*

XD: Designed the experiments, developed the patterned illumination system, composed the software GUI to regulate each component, developed the dynamic model for worm crawling locomotion, conducted close-loop locomotion control of *C. elegans*, collected and analyzed experimental data, prepared the figures, and wrote the manuscript.

SK: Helped with the experiments, analyzed the data, and prepared the 3D figures.

YL and MZ: Provided worm mutants, and assisted in the worm culture, preparation and chemical treatment.

XL: Proposed the idea, designed the experiments, analyzed the data, and wrote the manuscript.

# Chapter 1

# Introduction

# Chapter 1: Introduction

In worm biology laboratories, a variety of basic biological experiments are still conducted manually, which are usually time-consuming and labor-intensive. The generation of a stable transgenic worm, for instance, starts with the accurate delivery of a small amount of deoxyribonucleic acid (DNA) plasmid into the gonad of adult hermaphrodite individuals by microinjection, where the DNA plasmid will have a chance to be integrated into the fertilized eggs during their development [1]. To guarantee that the F1 generation of the injected worms contains the desired gene, a redundant batch of 20~30 individuals are manually injected. The microinjection process conducted by a human operator usually have a relatively low success rate of ~30%; nevertheless, several hours of continuous work are still required even for an experienced operator. In the following few days, in addition, thousand individuals of the F1 and F2 generation will be screened with the fluorescent phenotype expressed by the bio-marker attached on the DNA plasmid to find the stably integrated transgenic worms. The operations in the entire process, including the worm microinjection and worm screening, are highly repetitive and especially tedious for human operators, but amenable to automated operations conducted by machines [2]. Thus, there is a high demand for automated, high-throughput micromanipulation of *C. elegans* in biology laboratories.

In the past two decades, the microfluidic devices have been widely used for micromanipulation of *C. elegans*, benefiting from its many advantages such as the ability to cope with small sized objects, automated operations, high throughput, excellent bio-safety and reliability, to name just a few [3]. The material commonly used to construct the microfluidic devices for *C. elegans* micromanipulation is polydimethylsiloxane (PDMS), a transparent polymer that is gas permeable, flexible and highly biocompatible. Fabricated via soft lithography, the PDMS-based microfluidic device can create sophisticated on-chip microchannels capable of manipulating micrometer-sized objects.

PDMS-based microfluidics has enabled various studies in the field of automated *C. elegans* screening and manipulation [2, 4-10]. Among these microfluidic systems, several novel architectures such as the ‘smart maze’ [8], engineered pillar arrays [10], and size-tunable microfluidic channels [9] have been proposed for age-dependent *C. elegans* screening at different stages. These sorting methods were usually designed based on the passive fluidic mechanism, that

is smaller worms have better mobility in narrow or dense microfluidic structures, to separate a batch of worms based on their sizes. Similar microfluidic systems designed based on the electrotactic [5] and electrotaxis responses [7] of the worms have been also proposed. However, these designs cannot accurately measure the worm sizes, and thus they are unsuitable for use in experiments that directly employ worm size regulation as phenotypic trait and require size quantification and size-based sorting of many worms. On the other hand, for *C. elegans* microinjection, a few microfluidic systems are constructed to facilitate the microinjection process [2, 4, 6]. An open channel microfluidic device was developed [4], which immobilizes single worms using a vacuum-channel array in an open fluid micro-pool. This design is relatively complex and incapable of conducting continuous loading and immobilization of many worms with high reliability. Another nanomanipulation system was reported to deliver nano-beads into the worm body within an environmental scanning electron microscope (E-SEM) [6]. However, E-SEM still cannot provide a completely biocompatible environment for fluid injection of live *C. elegans* due to its radiation and vacuum environment.

In this thesis research, fully automated systems to facilitate the process of *C. elegans* screening and microinjection are developed, leveraging robotic micromanipulation and image processing techniques. An automated patterned-light illumination system was also developed with spatial selectivity of single cells on an inverted microscope, for optogenetic stimulation of *C. elegans*. Based on optogenetic experiments on worm muscles, the phase difference between the muscular torque and body shape is identified to generates the thrust force for serpentine locomotion of the worm body. By artificially reproducing the phase difference on the worm body with optogenetic method, the normal nematode crawling behaviors of straight forward moving, shallow I turn, shallow II turn, gradual turn, and omega turn are reproduced on a paralyzed worm. Further, an image feedback close-loop control was designed to regulate the worm moving direction and destination, which turned a live worm into the first-of-its-kind controllable microrobotic animal.

### 1.1 Thesis objectives

The overall objective of this thesis is to leverage the robotic micromanipulation, microfluidics, and image processing techniques to develop automated systems for automated operations of *C. elegans* sorting, microinjection and optogenetic locomotion control. Specific objectives of this thesis include:

- To develop a computer-controlled microfluidic system with real-time vision feedback to measure the morphologic features (i.e. centerline length, body diameter, and volume) of free-swimming worms, and to automatically screen and collect the target individuals based on their sizes with high accuracy.
- To develop a microfluid-assisted robotic system which can perform high-throughput loading of individual worms, and in the meanwhile, control a micropipette for automated robotic worm microinjection.
- To create a vision-feedback close-loop system to track the freely-moving *C. elegans* within the microscope field of view (FOV) by a XY 2-DOF motorized stage with high dynamic performance.
- To develop an automated system with the capability of manipulating light beam patterns on a 2D plane for selectively stimulating the target muscle cells on a worm body.

## 1.2 Thesis organization

This is a manuscript-based thesis composed of six chapters. The current chapter briefly describes the general concept and development in the field of robotic micromanipulation of *C. elegans*, and outlines the research objective and structure of this thesis.

Chapter 2 presents a survey of the state-of-the-art advances in micromanipulation of *C. elegans*, single cells, and other small organisms, and describes the roles of microfluidic devices in the *C. elegans* research. The previous work on the fluorescent imaging, automatic sorting and the microinjection of *C. elegans* is summarized.

Chapter 3 reviews the current development in the field of bio-agent microrobots and discusses important theoretical and technical references for the *C. elegans* microrobot-animal. Unlike Chapter 2 that introduces the research topics that employ external automation components to facilitate the micromanipulation of bio-samples, this chapter review the previous works in literature that directly develop the biological organism as a controllable microrobot. Three major types of bio-agent microrobot and the related techniques are introduced in detail, including the magnetotactic bacteria microrobot, the sperm-based micro-swimmer, and the insect-machine hybrid microrobot.

Chapter 4 introduces the development of an automated system for high-throughput size-based sorting of *C. elegans*. To perform high-throughput worm sorting, a double-layer microfluidic device, designed with 6 on-chip microvalves, is developed to sequentially separate individual worm from a swarm pre-sorted worm batch for downstream image processing and automatic sorting. The detailed structure of the microfluidic device designed for the worm loading, trapping and screening is introduced, followed by the overall operation flows for the entire sorting process. Based on the OpenCV image processing class, an algorithm designed for the on-the-fly analysis of worm length and diameter are thoroughly discussed. Furthermore, a software integrated with the proposed image processing algorithm is composed in c++ to coordinate the functions of each hardware for the automated sorting process. In the experiment section, the performance of the system is tested by sorting 5 batches of 319 worms, and the success rate, evaluated by post-sorting measurement of the sorted worms with a golden standard commercial software, is tested to be 90.3%.

In Chapter 5, a robotic system for the automatic microinjection of *C. elegans* is introduced. Similar worm separation mechanism to the worm sorting system is employed for the one-by-one loading of individual *C. elegans*. However, unlike the worm sorting system that contains a large observation chamber for the free swimming of the loaded worms, the microinjection device is designed with an array of micro-pillars to quickly immobilize the loaded worm in the microchannel. The micro-pillar array, with the pitch of 115 μm, is placed at the end of the injection channel which connects the microfluidics to the macro world. Thus, the injection needle can be controlled to insert through the injection channel and perform microinjection to the immobilized worm with a XYZ 3-DOF micromanipulator. The development of a customized pressure regulation system is descried for the control of the microfluidic within the channel and the regulation of on-chip microvalves, followed by the general description of the overall procedures for the automated microinjection. After that, the techniques for contact detection and coordinates mapping for the fully automated microinjection are discussed. To test the performance of the system, the automatic microinjection of 240 worms were performed with the speed of 9.97 sec per worm with a pre-sorting success rate of 78.8%.

Chapter 6 reports a pattern-light projection system on an inverted microscope to create patterned laser beams for optogenetic stimulation of *C. elegans* with single-cell resolution. The projection

system is constructed with a computer-controlled digital micro mirror device (DMD) to create artificial patterns and reflect the patterned laser beams into the microscope for projection. The dichroic on the major light path within the microscope has been replaced to make the reflected laser pattern pass through the objective and form on the sample plane. A worm tracking system is developed to keep the *C. elegans* in the center of the microscope FOV for stable laser illumination. The performance of the developed pattern-light illumination system is calibrated and the pattern resolution under 4× and 20× is 17 μm and 3 μm, respectively, which provides the system with the ability to target single cells on the worm body. Then, from the perspective of both dynamic model simulation and the more general view for the release of muscular energy, the phase difference between the worm body shape and the muscular torque is demonstrated to be the reason for the stable crawling locomotion. By applying stable phase difference to the worm body through the optogenetic stimulation on muscular cells, the crawling locomotion of the worm is successfully triggered and the normal movement patterns of straight forward movement, shallow turn, gradual turn, and omega turn are reproduced on live paralyzed worm. A vision feedback close-loop control technique is proposed based on a kinematic movement model for the direction and destination control of worm crawling locomotion.

Finally, Chapter 7 concludes the main achievements and contributions of this thesis research, and provides perspectives for future work that can be pursued to further develop the proposed systems and techniques.

## 1.3 References


[1] L. A. Berkowitz, A. L. Knight, G. A. Caldwell, and K. A. Caldwell, "Generation of stable transgenic C. elegans using microinjection," *Journal of visualized experiments: JoVE,* no. 18, 2008.

[2] P. Song, X. Dong, and X. Liu, "A microfluidic device for automated, high-speed microinjection of Caenorhabditis elegans," *Biomicrofluidics,* vol. 10, no. 1, p. 011912, 2016.

[3] J. R. Anderson *et al.*, "Fabrication of topologically complex three-dimensional microfluidic systems in PDMS by rapid prototyping," *Analytical chemistry,* vol. 72, no. 14, pp. 3158-3164, 2000.

[4] X. Zhao, F. Xu, L. Tang, W. Du, X. Feng, and B.-F. Liu, "Microfluidic chip-based C. elegans microinjection system for investigating cell–cell communication in vivo," *Biosensors and Bioelectronics,* vol. 50, pp. 28-34, 2013.

[5] P. Rezai, S. Salam, P. R. Selvaganapathy, and B. P. Gupta, "Electrical sorting of Caenorhabditis elegans," *Lab on a Chip,* vol. 12, no. 10, pp. 1831-1840, 2012.

[6] M. Nakajima *et al.*, "Local Nano-injection of Fluorescent Nano-beads inside C. elegans based on Nanomanipulation," in *2012 IEEE/RSJ International Conference on Intelligent Robots and Systems*, 2012, pp. 3241-3246: IEEE.

[7] B. Han, D. Kim, U. H. Ko, and J. H. Shin, "A sorting strategy for C. elegans based on size-dependent motility and electrotaxis in a micro-structured channel," *Lab on a Chip,* vol. 12, no. 20, pp. 4128-4134, 2012.

[8] F. Geier, A. Leroi, J. Bundy, J. Edel, and A. DeMello, "High-throughput age synchronisation of Caenorhabditis elegans," *Chemical communications (Cambridge, England),* vol. 47, no. 35, pp. 9801-9803, 2011.

[9] L. Dong, M. Cornaglia, T. Lehnert, and M. A. Gijs, "Versatile size-dependent sorting of C. elegans nematodes and embryos using a tunable microfluidic filter structure," *Lab on a Chip,* vol. 16, no. 3, pp. 574-585, 2016.

[10] X. Ai, W. Zhuo, Q. Liang, P. T. McGrath, and H. Lu, "A high-throughput device for size based separation of C. elegans developmental stages," *Lab on a Chip,* vol. 14, no. 10, pp. 1746-1752, 2014.

# Chapter 2

# Robotic Micromanipulation of Cells and Small Organisms

# Chapter 2: Robotic Micromanipulation of Cells and Small Organisms

**Xianke Dong[1], Wes Johnson[2], Yu Sun[2], Xinyu Liu[1]**

*[1]Department of Mechanical Engineering, McGill University, 817 Sherbrooke Street West, Montreal, Quebec, Canada H3A 2K6*

*[2]Department of Mechanical and Industrial Engineering, University of Toronto, 5 King's College Road, Toronto, Ontario, Canada, M5S 3G8*

Published as a book chapter in: *Micro-and Nanomanipulation Tools*, eds. Yu Sun and Xinyu Liu. Wiley-VCH, 2015.

## 2.1 Abstract

In cell biological laboratories and hospitals, the basic tasks of single cell injection were commonly conduct manually, which is especially repetitive, tedious, time-consuming and skill-dependent for human operators, but amenable to standard operations automated by machines. Thus, in the past two decades, automated single cell injection has been arising as an important topic in both academic studies and commercial applications. Leveraging the techniques in robotic micromanipulation, micro-electro-mechanical systems (MEMS), and computer vision, automatic single cell injection is increasingly automated, reliable, accurate, efficient, intelligent, and plays a critical role in a series of applications in the fields of artificial fertilization of human test-tube baby, genetic manipulation of biological organisms, and mechanical investigation of cells and subcellular organelles, to name just a few. In this book chapter, we provide a brief review of the current techniques proposed in the automatic cell injection process, and discuss the facilities, hardware and novel devices designs proposed as well. The robotic modelling and control for microinjection system, image processing algorithms under microscope field of view, the related MEMS and microfluidic devices designs are detailly presented in separate sections. Finally, we discuss practical applications of the single cell injection and conclude the future perspectives of this field.

## 2.2 Introduction

In the past two decades, a number of novel and effective robotic systems have been developed to target various micromanipulation tasks, with motivations to automate the micromanipulation processes and provide much enhanced manipulation accuracy, efficiency, and consistency. This

review discusses the systems, techniques, and methodologies for robotic manipulation of cells and small organisms.

Of the topics to be discussed, cell injection is well established in both the engineering and medicine communities owing to its important applications such as intracytoplasmic sperm injection (ICSI) which greatly improves in vitro fertilization results. Although it is one of the oldest forms of cell manipulation, the use of robotic techniques in cell injection has allowed for many recent technical innovations and performance improvements, as will be discussed in Section 2.3.

*C. elegans* micromanipulation is another topic that is attracting intensive research attentions in the past two decades. Contributed by the development of microfluidic systems and the micromanipulation techniques, the basic operations of *C. elegans* screening and *C. elegans* microinjection have been transferred from a tedious time-consuming manual work to standard operations automated by machines, as will be discussed in Section 2.4.

This review then moves on to discuss robotic biosample transfer, which includes the transportation of cells or small organisms to a desirable target location. Examples of biosample transfer include the relocation of a nucleus or other organelles inside a cell, or the relocation of cells within the culture medium. Conventionally, this type of experiment is conducted by a highly skilled operator through a manually controlled micropipette. New advancements in robotic micromanipulation have opened up many new options for biosample transfer, as will be discussed in Section 2.5.

The final section introduces robotic techniques for mechanical characterization of biosamples, which has attracted significant research interests from the fields of both engineering and biological/medical sciences. Mechanical characterization of single cells is of great importance from an engineering point of view as it provides useful information for a robotic system on how to interact with delicate cells. In biology and medicine, the mechanical property of certain types of cells can be used as an additional clue for identifying pathological conditions because some diseases (e.g., cancer and leukemia) are known to alter cellular physical characteristics.

### 2.3 Robotic cell microinjection

Several experimental methods have been developed to introduce foreign materials into single cells, including virus vectors [1, 2], lipofection [3], electroporation [4-6], and microinjection [7]. Among these methods, virus vectors and lipofection rely on engineered molecules (modified viruses and

liposomes) to introduce foreign molecules into cells and are performed in batches of cells. Electroporation and microinjection both belong to the same category of physical methods, which use mechanical and electrical forces respectively to make the foreign material cross over the cell membrane [4]. Cell injection is performed by puncturing the cell membrane with a glass needle and subsequently delivering the material by applying a well-controlled pressure pulse to the pipette capillary. Although electroporation could cause less cell damage than microinjection, microinjection has the advantage that the quantity of the delivered material can be well controlled by adjusting the duration and amplitude of the applied pressure pulse. In addition to this, microinjection allows for the selection of the intracellular target location (e.g., cytoplasm or nucleus) to which the material is deposited. Compared with other methods mentioned above, microinjection is a more universal approach since it is applicable to many types of cells and materials. Meanwhile, the whole injection process is controllable and feasible to be standardized. With all these advantages, microinjection is widely used in transgenic animal production [8], in vitro fertilization [9-11], stem cell study [12], and developmental biology [13].

In biological laboratories, cell injection is conventionally performed by well-trained human operators. According to the cell types, cell injection can be divided into two types, suspended cell injection (e.g., zebrafish and mouse oocytes/embryos) [13, 14] and adhesive cell injection (e.g., Hela cells, fibroblasts, endothelial) [15, 16]. Conventional suspended cell injection employs a holding pipette for immobilizing a cell and an injection pipette for penetrating the cell and delivering foreign materials. The manipulation tasks of controlling the holding pipette, searching, immobilizing, and injecting a cell are highly skill-dependent, tedious, and time-consuming. For instance, several months are needed for training an operator for microinjection of mouse oocytes/embryos, and the risk of operation inconsistency and sample contamination due to human involvement could reduce the success and survival rates of cell injection.

Teleoperated robotic cell injection systems have been developed to provide solutions to these technical obstacles and improve the injection process [17-21]. These systems typically employ bilateral master/slave architecture with multi-modality feedback (position, vision, and force) which allows an operator to control the position of a micromanipulator and feel/regulate the interaction forces during cell injection. Compared with traditional cell injection systems, the

teleoperated robotic systems improve operation accuracy, consistency, and reliability by providing the operator with visual and tactile feedback.

Although teleoperated robotic systems provide useful assistance for manual cell injection, fully automated cell injection systems are desired to further improve operation accuracy and efficiency and eliminate possible inconsistency due to human involvement. Multidisciplinary expertise from robotics, automation, and MEMS has been utilized to realize fully automated injection of both suspended and adherent cells. Since the early work of Sun and Nelson (Figure 2-1A) [8], a number of automated robotic injection systems have been developed in the past decade for injecting different types of cells [11, 13-16, 22-28]. For suspended cell injection, the automated cell injection system reported in [13] immobilizes a large number of zebrafish embryos into an regular pattern using a cell holding device, and coordinately controls multiple robotic devices for high-speed cell injection. The tasks of system calibration, cellular structure recognition, multi-robot coordinate position control, and cell injection have all been automated, and high success and survival rates (both close to 100%) have been achieved thanks to the highly consistent robotic operation [13].

Figure 2-1B shows the automated robotic system for zebrafish embryo injection [13]. The system includes a vacuum-based cell holding device for immobilizing an array of cells, an optical microscope with a digital camera for supervising the operation process and providing visual feedback, a three-degree-of-freedom (3-DOF) micromanipulator (microrobot-A) for positioning the cells immobilized on the cell holding device, a 3-DOF micromanipulator (microrobot-B) for control motions of the injection needle, a pressure-driven microinjector for regulating the amount of deposited material, and a host computer for running image processing and motion control algorithms. The cell holding device immobilizes 25 zebrafish embryos within 12 seconds. An image processing algorithm identifies the structure of the target cell and the position of the pipette tip in the field of view of the microscope, and the visual feedback information is used by the robotic system for coordinate motion control of the two micromanipulators.

For adherent cell injection, the cells are directly injected on their culture petri dishes, and no cell immobilization process is needed. The tasks of system calibration and position control can be realized using similar techniques to the ones used in suspended cell injection; however, there are two unique challenges for injecting adhesion cells. First, the irregular shapes of adherent cells

make visual recognition of the cellular structures more difficult [29]. Ghanbari et al. proposed a pattern recognition algorithm to identify the nucleus boundary of adherent cells and thus the centroid of the nucleus as the injection target [30]. Becattini et al. developed a diffusion-tensor-based algorithm for anisotropic cell contour completion and identification of injection target points on adherent cells [1]. There are also other advanced image processing and computer algorithms that have been developed for adherent cell recognitions but have not yet been applied to robotic cell injection [31, 32]. Second, the height of an adherent cell attaching to the culture substrate typically ranges in 3-6 μm, with large variations from cell to cell. The vertical position control of the injection pipette tip during cell injection requires accurate knowledge of the relative position of the pipette tip and the cell. Lukkari et al. [33] proposed the use of electrical impedance between the pipette tip and the target cell for contact detection. Wang et al. developed a vision-based technique for detecting the contact between the pipette tip and the culture substrate (accuracy: 0.2 μm), and an average distance of 3 μm was used as the height of the cell nuclei relative to the culture substrate [15]. In addition, another image-based contact detection algorithm for needle tip and cell membrane is proposed by Liu et al., which is based on visual recognition of the movement of the cell surface upon touching by a pipette and can detect the contact of the pipette tip and any surface.

In the following sub-sections, the major techniques that have been utilized for robotic cell injection will be reviewed in detail, including suspended cell immobilization methods, image processing and computer vision techniques, control system design, force sensing and control, and parallel cell injection.

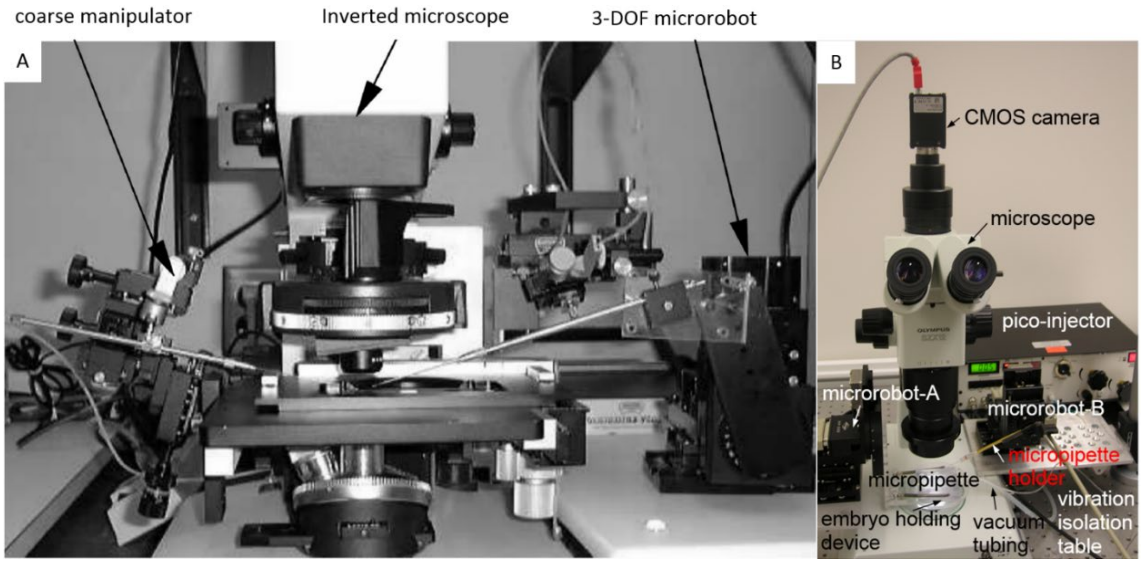


Figure 2-1 Typical system setups of automated cell injection systems (from[8, 13]).

### 2.3.1 Cell immobilization

Cell immobilization is an important procedure of automated suspended cell injection, which can greatly simplify the cell search/positioning tasks and improve operation efficiency. Four types of cell immobilization methods have been reported. As shown in Figure 2-2A, the conventional method, which is most widely used in manual injection, is to immobilize a cell using a holding pipette. The holding pipette, made from a glass capillary, has an inner diameter at a fraction of the target cell diameter and an outer diameter much larger than the inner one, forming a flat side wall at the tip for supporting the cell when it is injected laterally by an injection pipette (Figure 2-2A). The holding pipette is connected with a negative pressure source and immobilizes the cell [8]. The second method, illustrated in Figure 2-2B, is to immobilize multiple cells into a regular pattern via vacuum suction [11, 13, 14]. An advantage of this method is that, upon suction, the cells are automatically positioned and immobilized at locations of through-holes underneath, and the remaining un-immobilized cells are flushed away for next injection batches. Cell holding devices with an array of through-holes connected to a vacuum source have been demonstrated to immobilize zebrafish, mouse and human embryos/oocytes. To immobilize cells of different sizes, the size of the through-holes ranges from tens of micrometers to over one millimeter. Either conventional machining or microfabrication was used to construct the cell holding devices. A similar suction-based method has also been used to immobilize and inject *Xenopus laevis* and zebrafish oocytes [34, 35]. The third method utilized half-circular grooves combined with cavities

in the grooves for immobilizing a number of zebrafish embryos, and the device was fabricated via micro-molding of agarose gel [26]. The inner walls of the groove/cavity provide mechanical support for cells during injection. The last method, illustrated by Figure 2-2D, is to attach single cells on a substrate surface by gluing [22, 36, 37]. Note that, for all the four methods, the immobilization process always requires certain level of manual operation (e.g., depositing cells onto the cell holding device and positioning cells to the locations of grooves/cavities or glue points).

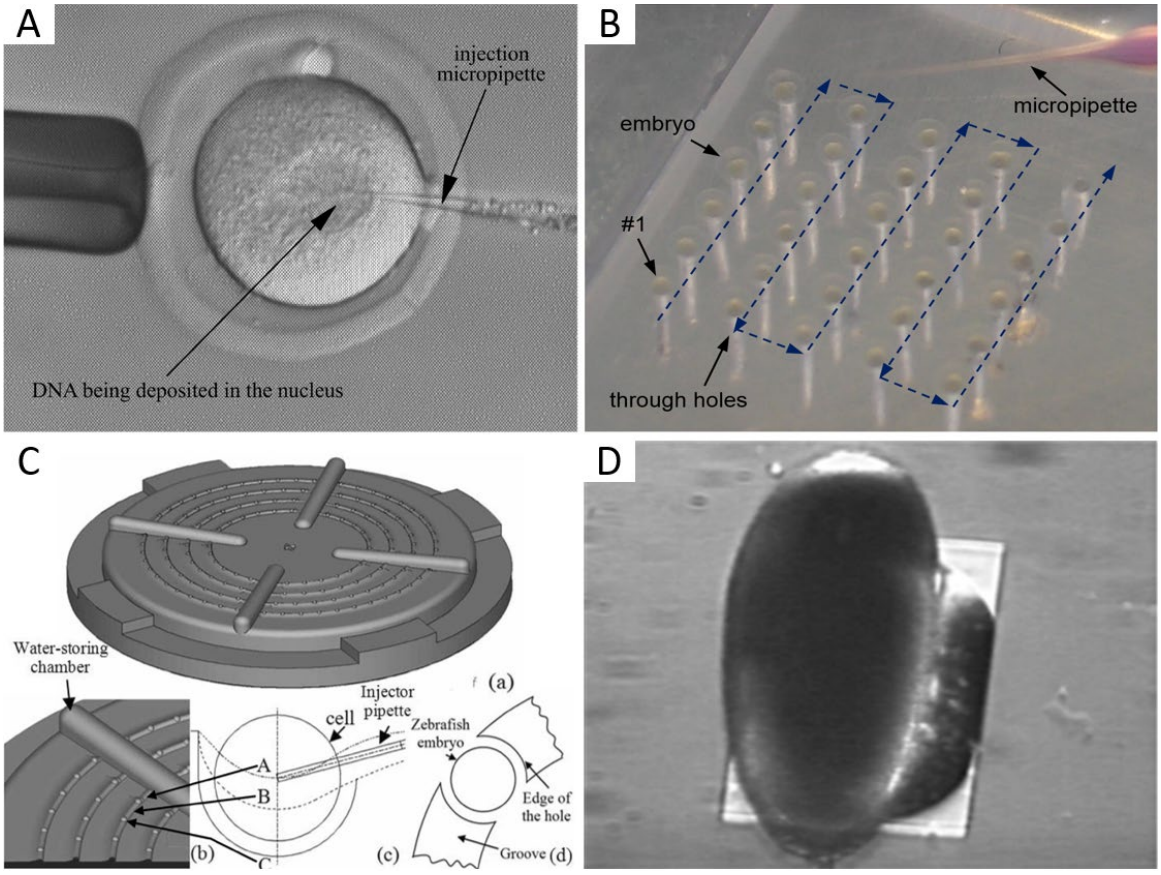


Figure 2-2 Example cell immobilization methods (from [8, 13, 26, 37]).

### 2.3.2 Image processing techniques and control system design

Image processing and computer vision algorithms has been widely used for recognizing the structure of the target cell and the position of the injection needle tip [38], providing visual feedback for robotic control [9, 10] and analyzing cellular forces from cell contour deformations [39-41]. Edge detection algorithms are usually employed as the first step for obtaining edge and corner information of the cellular structure. The *Canny edge detector* is the most commonly used edge detection algorithm, which minimizes the distance between the detected and real edge pixels.

For the tracking of low-contrast objects, the *Canny edge detector* may be less feasible since the edges in low-contrast images are often blurry or even lost. Based on the Mumford-Shah functional for segmentation and level sets, Chan et al. developed an active-contour-based algorithm that is capable of detecting objects whose boundaries are not necessarily defined by a gradient [42]. The detected edges containing geometry and position information of the target cell are further analyzed by feature extraction/recognition algorithms. The *Hough transform* algorithm is effective for detecting regular shapes that can be characterized by a line, rectangle, or ellipse. However, the *Hough transform* is ineffective for recognising samples with complex geometric features. In this regard, mathematical morphology based imagine processing algorithms are used to recognize the complex shapes of cell contours and find target locations for injection. For instance, an imaging processing algorithm utilized convex hulls formed on cytoplasmic contours of zebrafish embryos to identify the orientation of embryo's yolk and cells [13]. Based on a motion history image and an active contour model, Liu et al. proposed a technique that can search for out-of-focus, low-contrast end effectors with complex contours and applied it to robotic micromanipulation including cell injection [38].

Since microscopic vision is the major feedback modality available in cell injection systems, visual servo control is one of the most often adopted control schemes, and image-based visual servo control is employed frequently. Robotic micropositioning devices are driven by direct-current (DC) or stepper motors, which can be treated as linear components in large motion ranges. Thus, conventional proportional-integral-derivative (PID) controllers can be effective as the visual servo control law. Figure 2-3 shows typical image-based visual servo control architecture of a robotic cell injection system. Compared to regular visual servo systems [43, 44], the visual servo controller used in robotic cell injection is simplified due to two factors. (1) The camera is fixed on the microscope, and the system operation is observed from a top-down view, yielding a simple two-dimensional (2D) visual servo problem. (2) The cell injection process usually requires only translational motions of the cell samples and the injection needle tip. Thus, robots involved in cell injection (e.g., microrobot-A and microrobot-B in Figure 2-1B) are typically three-axis Cartesian (*x*-*y*-*z*) micropositioning devices, and their coordinate frames can be pre-aligned to avoid rotational coordinate transformations [25].

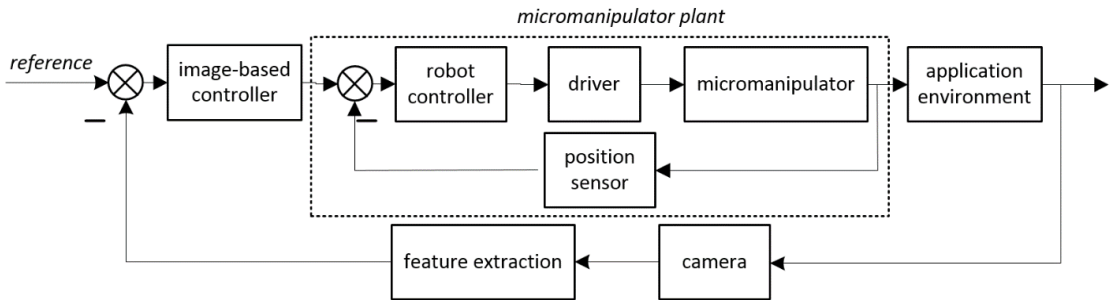


Figure 2-3 Image-based visual servo control architecture for robotic micromanipulation.

In some cell injection systems, only closed-loop position control of the micropositioning devices was employed, and no closed-loop visual servo control was involved to avoid potential visual tracking failure [13, 14]. In these systems, either image processing algorithms or human input (through computer mouse clicking on the screen) was used to identify a target cell and the injection pipette tip and feed the information into the position controller, forming a "looking-then-moving" architecture [43]. For force-controlled cell injection, a hybrid position/vision/force control scheme is needed to coordinate the three feedback loops and complete different steps of the injection task via different control loops and control laws [26].

### 2.3.3 Force sensing and control

From the robotics perspective, it is a straightforward option to integrate force sensing and control capabilities into the cell injection system, which could potentially improve manipulation dexterity and reliability. It has been demonstrated that measurement and control of interaction forces between the target cell and the injection pipette tip provide three useful functionalities. (1) Monitoring the axial injection force could accurately predict the penetration of the cell membrane during injection, which is a useful indicator for the injection system to deposit the foreign material after penetration [45, 46]. As shown in Figure 2-4, the cell injection force of a zebrafish embryo gradually increases when the pipette tip comes in contact with the cell membrane and drops to zero when the membrane is penetrated [47]. The time point of cell penetration can be accurately detected from the injection force data. (2) Measuring the injection force and corresponding cell deformation data could allow the injection system to perform *in-situ* cell mechanical characterization during injection, and the measured mechanical property of the target cell could provide useful information about the quality of the cell [46]. (3) Measuring the lateral contact force (along the tangential direction of the injection pipette motion) between the pipette tip and the target

cell could assist the alignment of the tip and the center of the target cell once the tip is in contact with the cell, because the lateral contact force becomes minimal once the tip and the cell center is well aligned [48]. Another possible benefit of controlling the injection force to follow a desired profile is the potential reduction of injection-induced damage to the cell and the resultant enhancement of the post-injection survival rate [26, 49]. This speculated benefit has not been experimentally confirmed through comparing the survival rate of cells injected with and without the use of a force controller.

The injection forces for different cell types are in the range of (sub)nanonewtons to micronewtons [28, 47], the measurement of which requires micro force sensors with high resolutions. Although silicon-based MEMS piezoresistive and capacitive force sensors have been used to measure injection forces of zebrafish and mouse embryos [45, 48], it is relatively difficult to efficiently integrate these fragile silicon-based force sensors into a practical robotic cell injection system, especially considering the fact that the injection pipette, attached to the force sensor, needs to be replaced frequently. Piezoelectric polyvinylidene fluoride (PVDF), as a flexible fluoropolymer material, has also been used to fabricate micro force sensors for measuring injection forces [17, 28], which are more robust mechanically for integration with robotic cell injection systems.

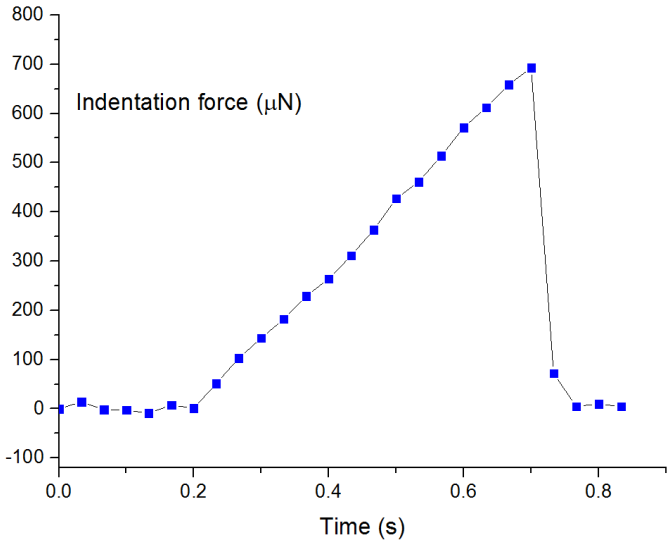


Figure 2-4 Injection force profile during microinjection of a zebrafish embryo (from [46]).

Another force sensing strategy is visual-based force measurement [39-41, 46, 50], which maps the injection force from deformations of a cell membrane or low-stiffness elastomeric structures

(which supports the cell being injected). The relationship of the injection force and the induced cell deformation is a nonlinear mapping determined by a proper cell mechanical model. With major parameters of the cell mechanical model (i.e., cell mechanical property) estimated through off-line calibration, injection forces can be calculated from the cell deformation data [39, 40, 49, 50]. Uncertainties of this technique can be attributed to mechanical property variations across cells, and off-line calibrated data may become significantly off from the real mechanical property of the target cell being injected.

Instead of using cell deformation for injection force calculation, Liu et al. developed a polydimethylsiloxane (PDMS) cell holding device on which flexible micro-posts were used to support the target cell during injection (Figure 2-5A) [46]. The injection force was then transmitted to the supporting micro-posts. Deflections of the micro-posts (Figure 2-5B) were fed into a linear mechanical model to calculate the injection force. As PDMS is a highly elastic material with consistent mechanical property, the calculation of the injection force from the micro-post deflections can be highly accurate with properly characterized mechanical properties of the PDMS micro-posts. Note that, although vision-based force measurement does not add to the hardware complexity of the cell injection system, its sampling rate is limited to the frame rate of microscopic vision (e.g., ≤100 Hz).

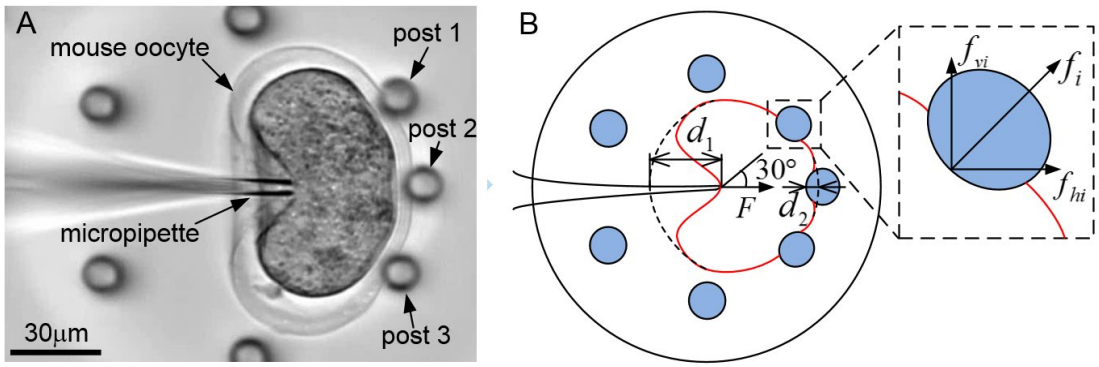


Figure 2-5 PDMS-based mechanical characterization of cells (from [51])

For force-controlled cell injection, a hybrid position/vision/force control scheme is needed to coordinate the three feedback loops and complete different steps of the injection task via different control loops and control laws. Figure 2-6 illustrates the block diagram of a hybrid position/vision/force control system. Huang et al. proposed a hybrid control scheme with decoupled force and position control loops, where an impedance force control loop was applied

along the *z*-axis of the injection pipette to regulate the injection force, and a position control loop along the *x* and *y* axes of the pipette for controlling in-plane motions of the pipette tip [26].

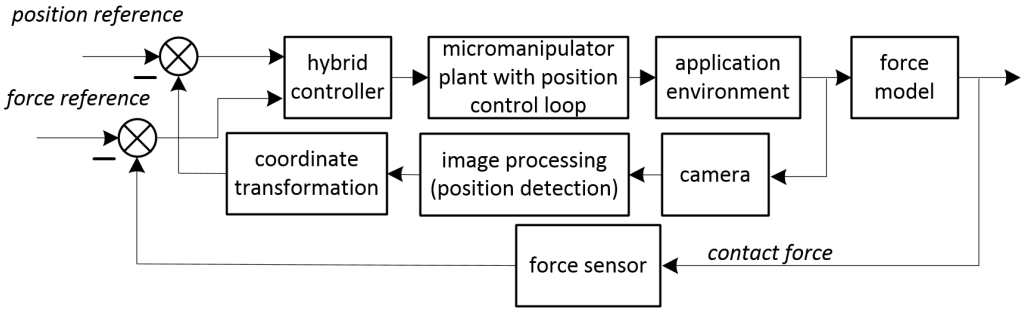


Figure 2-6 Block diagram of a hybrid force/vision feedback control architecture.

## 2.4 Automatic micromanipulation of *C. elegans*

The micromanipulation of *C. elegans* is greatly facilitated by the development of microfluidics, as it not only provides convenient platforms for the handling and manipulation of the micrometer sized animal, but also allows for controlled chemical stimuli delivery. The neuronal sensory analysis under precise chemical order stimulation was investigated in [52] with a microfluidic immobilization and chemical delivery system. The quantitative analysis of worm sensory and behavior is conducted with a patterned microfluidic structure [53]. In addition, the high-throughput fluorescent imaging [54], screening and microinjection [55], laser ablation and nerve regeneration [56] are also successfully investigated under automatic microfluidic platform incorporated with micromanipulation and image processing techniques. Here, we discuss existing techniques for worm immobilization, which is a challenge that needs to be solved in the development of robotic worm sorting and microinjection systems. Existing robotic worm injection and sorting systems reported in the literature will also be briefly discussed.

### 2.4.1 *C. elegans* screening

There is a basic need for sufficient quantities of worm individuals of a certain type (size, age, phenotype, etc.) either creating a new transgenic worm or treating the worm with chemical in biological laboratories, in order to compensate for the uncertainty in biological experiments. The commercial system COPAS was developed as an automated platform for size-based worm sorting twenty years ago. Subsequently, a more advance system BioSorter was released for the sorting of worms and cells based on the size, shape and fluorescent biomarker, which provides abundant features and modulations. These commercial systems provide effective tools for the sorting of

worms with reliable accuracy and fast speed, however, their prices are prohibitive for most of the laboratories, and their operations are sophisticated for common users. Thus, automated microfluidic systems with affordable costs are proposed to facilitate sorting process.

The reported worm sorting system in literature can be separated into 3 categories from the respective of sorting mechanisms: passive microfluidic designs, fluorescent imaging, and worm electrotaxis response. The passive microfluidic worm sorting systems are usually designed based on the fluidic dynamics that the small worms possess higher mobility and consequently faster speed than large worms when passing through narrow channels or crawled pillar arrays. The microfluidic device, termed "smart maze", that contains micro-pillar structures of various dimensions is reported to perform size-based worm screening with the accuracy of 94% [57]. In addition, in Dong et al. proposed a size adjustable microfluidic channel to sort the worms with a certain diameter [58]. A filtration approach is proposed in [59] to collect the worms with certain developmental stages from a size-mixed batch by using microfluidic pillar arrays with calibrated pitch and density. The passive microfluidic sorting systems are with especially fast sorting speed and high throughput, however, the sorting accuracy is usually limited because the worm sizes are not check individually. On the other hand, the fluorescent imaging-based sorting systems are proposed with the automatic operations of the microscopes to measure the fluorescent phenotypes of every single worms individually from the microscope image, and perform worm screening based on the measurement results. A microfluidic system was developed with subcellular accuracy of fluorescent phenotype measurement for automatic worm screening [54]. Optical laser fiber is integrated into a microfluidic device for laser illumination and fluorescence sensing, which constructs a worm screening system with 100% efficiency [60]. Electrotaxis response is the tendency of worms to react inherently to desirable electric signals and move towards the favorable electrode [61]. Since young worms and elder worms have different preferences in electric fields, the electrotaxis methods is also used to screen the worms based on their sizes in microfluidic systems [62, 63].

### 2.4.2 *C. elegans* immobilization and microinjection

Most of the techniques discussed in Section 2.3 are applicable to worm microinjection, however, unlike the microinjection of cells, *C. elegans* need to be reliably immobilized first before injection. The immobilization of *C. elegans* is challenging because the worm is a live organism and is highly

locomotive. The worm immobilization mechanism should be able to capture, immobilize, and release individual worms in a rapid fashion. In conventional manual injection, the worms are attached to the substrate of a petri dish via gluing or anesthetics [64], which is a low-throughput, labour-intensive process. Researchers from the microfluidics community have developed a series of microfluidic techniques for immobilizing *C. elegans* for applications such as high-resolution imaging and laser microsurgery [65-67]. However, these techniques immobilize worms in enclosed microfluidic channels, and therefore do not allow the injection pipette to reach the worms for injection. To solve this issue, Zhao et al. developed an open-channel microfluidic device to load and inject single worms sequentially [68]. The microfluidic device was designed to immobilize the worm by sucking the head and tail in an open microfluidic channel. Using the device, manually controlled worm injection was demonstrated. Other work focused on the development of worm injection systems and still used the conventional gluing method for worm immobilization. For instance, Hirano et al. developed an injection method for *C. elegans* based on a hybrid system combining optical microscopy and environmental scanning electron microscopy (E-SEM) [69]. Although E-SEM provides a low-vacuum environment for the worms to survive, the exposure to electron-beam radiation and negative pressure may still pose adverse effect on the injected worms.

### 2.5 Robotic transfer of biosamples

Biosample transfer is another important application of robotic micromanipulation. By transferring cells or small organisms from one location to another, numerous tasks can be conducted, such as cell sorting and isolation [70], cell interaction [71], cell fusion [72], and other potential applications in biomedical engineering and the drug industry. The most commonly used transfer tools are transfer pipettes, mechanical microgrippers, untethered microrobots, and optical tweezers, which will be reviewed in this section.

#### 2.5.1 Pipette-Based Cell Transfer

Pipette-based transfer is a traditional approach widely used in biological experiments for single cell manipulation [73-75]. This technique employs a glass micropipette, connected with a pressure unit, to aspirate and dispense cells. When the pipette tip approaches a target suspended cell, a negative pressure is applied in the capillary to aspirate the cell into the pipette or at the tip. After the cell is moved to the desired location, a positive pressure is applied to release the cell. For

system setup, the micropipette is attached to a micromanipulator which controls the position of the pipette. Several pipette-based manual manipulation systems are commercially available, such as the Quixell® Cell Transfer and Selection System (Stoelting, Wood Dale, USA) and the Eppendorf TransferMan® NK 2 micromanipulator (Eppendorf, Hamburg, Germany). Both commercial systems allow a user to use a joystick or a computer mouse/keyboard for controlling a pipette and transferring biosamples; however, the user still need to be heavily involved to perform the tasks.

Pipette-based transfer can be divided into two categories, whole cell aspiration [74] and partial cell aspiration [76], as shown in Figure 2-7A. For whole cell aspiration, the inner diameter of the pipette tip should be slightly larger than the size of the target cell so that the whole cell can be aspired into the pipette. The whole cell aspiration technique has been used in robotic ICSI [9, 11], in which an injection pipette aspires a single sperm cell and injects it into a human oocyte (Figure 2-7B). Before injection, the aspirated sperm needs to be brought to the pipette tip and an image-based visual servo controller was developed to automatically move the sperm to the desired location inside the pipette by regulating the sucking pressure generated by a syringe pump connected to the pipette [9]. The whole robotic ICSI process includes the following steps [11]. A motile sperm is first detected and tracked using computer vision. The sperm is then immobilized by using the pipette tip to 'tap' the sperm tail, and then aspirated into the injection pipette. The location of the sperm inside the pipette is accurately controlled to be at the pipette tip by the visual servo controller. Finally, the pipette penetrates the human oocyte and delivers the sperm into the oocyte's cytoplasm.

For partial cell aspiration, the inner diameter of the glass pipette must be smaller than the size of the target cell so that the target cell can be immobilized at the tip of the pipette for transfer, as shown in Figure 2-7C [74]. A small portion of the cell is aspirated into the pipette by a low negative pressure. According to [74], a negative pressure of 180 Pa caused a cell elongation of 1 μm into the pipette for fibroblasts and endothelial cells. Besides cell transfer, partial aspiration can also be used as the immobilization technique for cell injection, as discussed in Section 2.3.1.

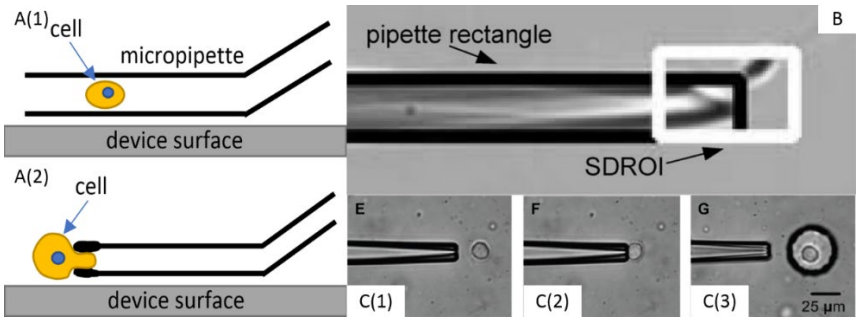


Figure 2-7 Whole cell and partial cell aspiration ((B) from [9], (C) from [74])

### 2.5.2 Microgripper/Microhand-Based Cell Transfer

Besides micropipettes, microgrippers and microhands have also been developed to manipulate cells. These end-effectors are able to conduct manipulation tasks such as grasping, transferring, releasing, and even cell microsurgery [21, 77-80]. In addition, force-controlled microgrippers can also be used to characterize the mechanical property of single cells, which will be discussed in Section 2.6.

To securely manipulate cells, the two grasping arms of a microgripper must have a size matching that of a single cell. In addition, displacements of the grasping arms should be controlled in suitable ranges with high resolutions. MEMS devices can meet these requirements, and some of these devices have evolved into commercial products (e.g., Femtotool® FT-G100). For details of design and fabrication of MEMS devices, one can refer to [81]. For biomanipulation, MEMS microgrippers are usually required to partially operate in liquid media, and the operation of microgrippers in liquid media should not alter the properties (e.g., chemical composition, temperature, and eletrical property) of the media. Meanwhile, the actuation mechanism that converts certain type of energy (typically electrical energy) into mechanical motions should be selected by taking the aqueous environment into account.

Most MEMS actuation mechanisms are not suitable for operation in liquid media [77]. For example, electrostatic actuators can cause electrolysis in electrolytic media [78]. Electrothermal microgrippers are activated based on the deformation of a beam at high temperatures, which is not typically compatible with liquid environment. A widely adopted solution is to design long gripping arms of the microgripper, which can be immerged into liquid media and keep the actuator part of the device out of the liquid during operation [78, 79, 82]. To avoid interference between the on-chip actuator and the aqueous environment, the gripping arm must be electrically insulated. N.

Chronics et al. [77] proposed an SU-8 based microgripper that can operate in both air and liquid environments. The design leverages the large coefficient of thermal expansion of SU-8, which allows for electrothermal actuation in ionic physiological solutions at low voltage and temperature changes.

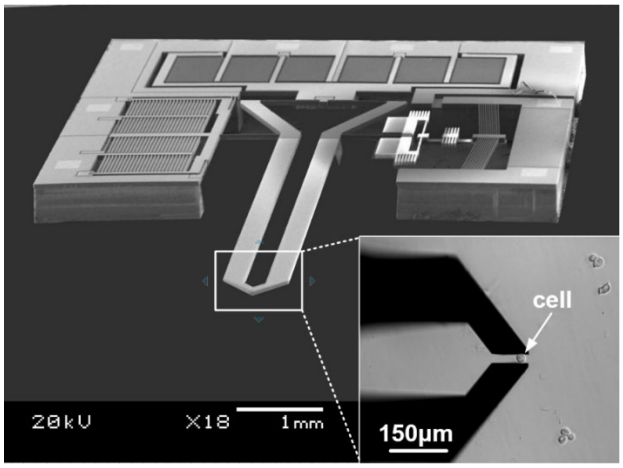


Figure 2-8 MEMS microgripper with an electrothermal actuator and a two-axis capacitive force sensor for force-controlled cell manipulation (from [79]).

Accurate measurement and control of the grasping force during microgripper-based cell transfer is necessary for avoiding cell damage. Several MEMS microgrippers have integrated multi-axis force sensors [78, 79], and closed-loop grasping force control has been performed [79]. Kim et al. developed a MEMS microgripper (Figure 2-8) with electrothermal actuator and two-axis capacitive force sensor for measuring the gripping force and the contact force (between the gripping arm tips and the biosample/substrate along the axis of gripping arms) [79]. Closed-loop control of the grasping force was performed during pick-transport-place of single cells, and nanonewton-level force control resolution was achieved. Another method of performing force measurement on MEMS microgrippers is vision-based force measurement, where deformations of flexure beams on the MEMS device are measured through real-time visual tracking [83, 84].

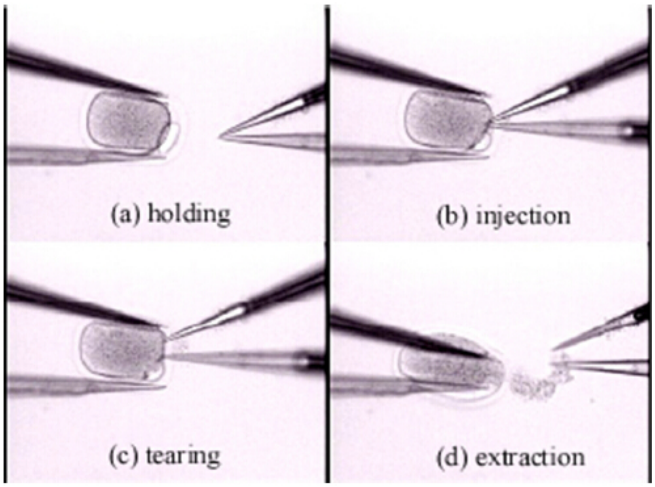


Figure 2-9 Operations of a two-fingered microhand (from [85]).

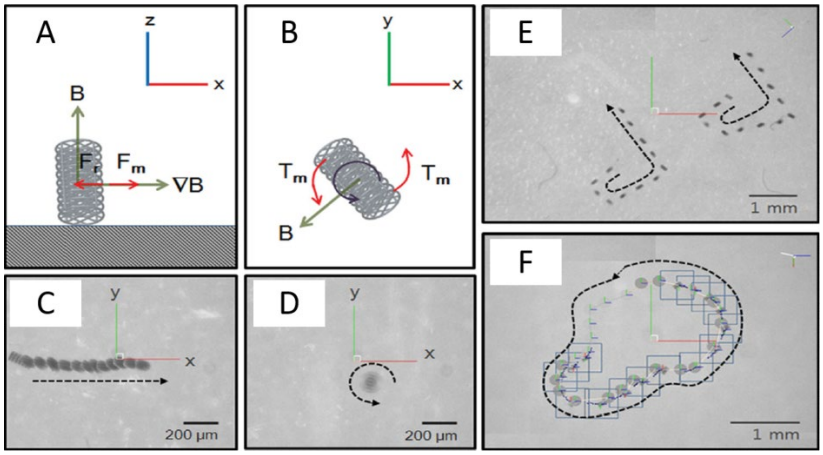


Figure 2-10 Untethered magnetic microrobot for cell manipulation (from [86])

Besides MEMS microgrippers, a two-finger microhand has also been developed for manipulating single cells. The microhand consists of two sticks with sharp micrometer-sized tips [85, 87-89], which are actuated by two 3-DOF parallel mechanisms and mimick the operation strategy of chopsticks for cell manipulation. The user interface for controlling the micro-hand includes custom-made software [87] and a haptic device [89]. With cooperative control implemented, the two fingers of the micro-hand work like the thumb and forefinger of a hand, with high dexterity and flexibility. In addition to common cell manipulation tasks such as pick-transport-place and injection, the two-fingered micro-hand is also capable of rotating and tearing cells and extracting intracellular species (Figure 2-9) [85].

### 2.5.3 Microrobot-Based Cell Transfer

Magnetically actuated microrobots have also been used in cell manipulation [90, 91]. These microrobots are made from ferromagnetic materials and can act as a mobile manipulator in aqueous solutions. With the surrounding magnetic field regulated by currents in coils of external circuitry, forces acting on a megnetic microrobot can be accurately controlled. Since most cells and small organisms are not sensitive to magnetic fields, these biosamples can be manipulated by the microrobot without being displaced by the magnetic field. Magnetic microrobots are effective in pushing the biosample in plane. Furthermore, viscous forces dominate inertial forces on the microscale, and the motion of the microrobot causes little mixing or agitation of the surrounding aqueous environment. Thus, microrobot-based transfer is a less-invasive manipulation method. Figure 2-10 illustrates the process of transferring multiple cells by a three-dimensional (3D) porous magnetic microrobot reported in [86]. The 3D transporter was fabricated from a photocurable polymer and coated with Nickel (Ni) and titanium (Ti), where a number of human embryonic kidney 293 cells were cultured. The microrobot was capable of translational and rotational motions, and accurate following of a pre-defined route for cell transfer.

### 2.5.4 Laser-Trapping-Based Cell Transfer

Laser trapping is able to apply controlled manipulative forces on micro/nano-particles for manipulation. When illuminated by a focused low-power laser beam (also called laser traps) on one side (Figure 2-11A), a particle can overcome the viscous force and move to the center of the laser beam due to the optical trapping force [92]. This technique can manipulate cells and particles with sizes ranging from tens of micrometers down to sub-micrometers, and function as robotic end-effectors [92-94]. For cells that are larger than the laser beam focal volume, the optical trap acts like laser tweezers exerting strong forces near the boundaries of the cell. For small cells or organisms, it exerts maximum force at the point of maximum intensity gradient within the beam focal region [95].

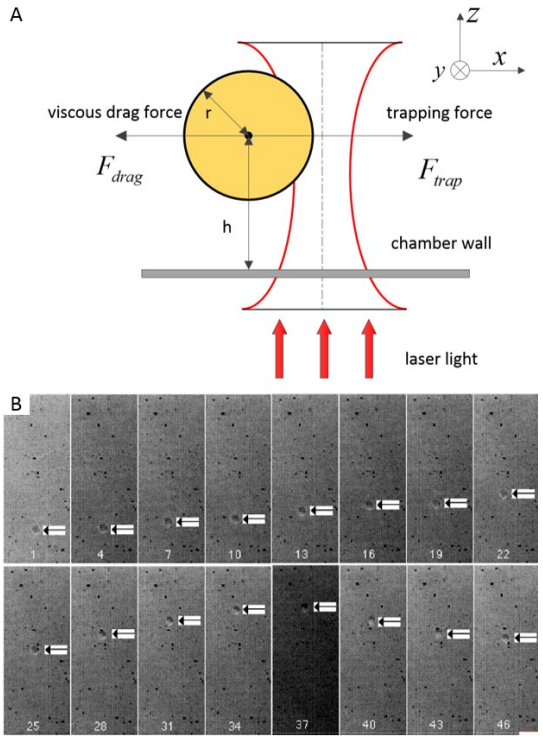


Figure 2-11 Laser-trapping-based Cell Transfer. (A) Schematic diagram of a cell in a laser trap. (B) Cell transfer by laser trapping (from [96]).

Despite the concern of potential laser-induced damage to cells, laser trapping is capable of precise, flexible, and parallel manipulation of cells. Figure 2-11B shows an example of transporting of bovine red blood cell using a laser trapping manipulation system [96]. Based on the dynamic model of cells in laser traps, Hu et al. proposed a trajectory planning and path tracking/control algorithm [92]. Because of its high resolution, laser trapping has also been applied to manipulating intracellular organelles. Ashkin et al. [95] developed a laser trapping system that applies well controlled forces inside a cell while keeping the cell membrane intact. Using infrared laser traps, intracellular microsurgeries were demonstrated for manipulating large organelles such as chloroplasts and nuclei and studying biological problems such as cytoplasmic streaming, intracellular membranes, and organelle attachments. In addition, laser trapping has also been applied to mechanical characterization of cells, which will be discussed in Section 2.6.

## 2.6 Robot-assisted mechanical characterization of cells

Cell mechanics reflects developmental and physiological states of cells, such as locomotion, differentiation, electromotility, and cell pathology [97]. The onset and progression of certain

diseases are known to be associated with changes in cellular mechanical property. In addition, cell mechanical characterization techniques are also used for experimental validation of cell mechanical models, which could facilitate biomanipulation tasks such as cell injection and grasping. Consequently, much effort has been made on developing micromanipulation systems for cell mechanical characterization [40, 47, 48, 51, 98-107]. This section discusses four major strategies of cell mechanical characterization, including MEMS-based characterization, micropipette aspiration, laser-trapping-based characterization, and atomic force microscopy (AFM) based characterization.

### 2.6.1 MEMS-Based Cell Characterization

A number of MEMS-based micromanipulation systems have been developed for mechanical characterization of biosamples [47, 48, 51, 93, 98, 102]. Sun et al. [48] developed a two-axis capacitive MEMS force sensor for characterizing the mechanical property of mouse embryo membranes (zona pellucida), and established a point-load mechanical model of the membrane for extracting the mechanical property from force-deformation data. Using force feedback from a MEMS microgripper, Kim et al. [93] quantified elastic and viscoelastic parameters of alginate microcapsules. The developed technique can be readily extended to characterizing single cells.

Unlike silicon-based MEMS devices with dedicated force sensors, polymer-based MEMS devices often make use of vision-based force measurement to measure forces applied to a cell. The PDMS cell holding device developed by Liu et al. [46] was used for characterizing the elastic and viscoelastic properties of mouse oocytes [51]. The characterization process was conducted during cell injection, and the injection force was measured in real time by tracking micro-post deflections and inputting the deflection data into a force-analysis model. A two-step, large-deformation mechanical model was used to quantify mouse oocytes' elastic and viscoelastic properties.

### 2.6.2 Laser Trapping Based Cell Characterization

As discussed in Section 2.5, laser trapping is an effective biomanipulation method for performing cell transfer tasks. It has also been applied to cell mechanical characterization [108, 109]. Laser traps are used to apply a known force to a cell and induce a measurable deformation, and the force-deformation information is used to calculate the mechanical properties of the cell. To deform a cell, micro-beads are typically attached to the cell membrane and laser traps are applied to the micro-beads to stretch the cell (Figure 2-12). The applied trapping force is a function of a few

experimental parameters, including: (i) the intensity of laser power; (ii) the shape of laser focus; (iii) the size and shape of the trapped micro-beads; and (iv) the refraction index of the micro-beads relative to the surrounding medium. Overall, the trapping force can be expressed as $F = -kx$, where $k$ is the trap stiffness, and $x$ the displacement of the micro-bead away from the center of laser trap. Details for the calibration of the trap stiffness can be found in [110]. For calibrating cells in culture medium, hydrodynamic drag forces on the micro-beads also need to be considered, which are usually in the laminar-flow regime [109]. This method has been used to characterize the mechanical properties of a variety of cell types such as red blood cells [108] and human embryonic stem cells [109].

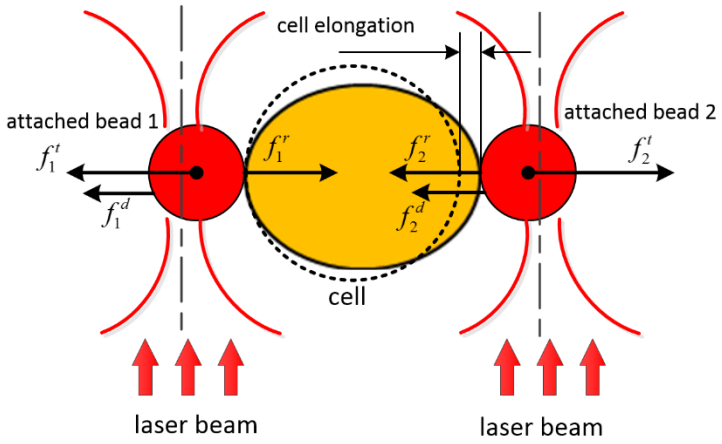


Figure 2-12 Schematic of a cell stretched by two micro-beads driven by laser traps, where $f^t$ is the laser trapping force, $f^r$ is the cell restoration force caused by elongation, and $f^d$ is the viscous drag force exerted on the bead by the fluid (from [97]).

### 2.6.3 Atomic Force Microscopy (AFM) Based Cell Characterization

AFM uses micro-cantilevers with micrometer- to nanometer-sized tips to interact with cell surfaces, and the cantilever deflection is converted to the contact force (between the cantilever tip and the cell) and cell surface topography [111]. Cell mechanical characterization is conducted by indenting a cell using an AFM cantilever to obtain experimental data of indentation force vs. cell deformation (indentation depth). The Young's modulus of the cell in the contact area is calculated by fitting an appropriate contact mechanics model to the force-displacement data. In [112], a haptics-enabled AFM system was developed to mechanically manipulate and characterize embryonic stem cells. Based on force and vision feedback control, contact mechanics of human cervix epithelial HeLa cells was investigated in [113]. The researches on the dynamics and mechanical properties of

intact cells associated with different cell events such as locomotion, differentiation, aging, physiological activation, electromotility and pathology are reviewed in [114]. Many other AFM characterization systems have also been reported for cell mechanical characterization [114-120].

AFM nanoindentation has also been integrated into a scanning electron microscope (SEM) for cell mechanical characterization. Ahmad et al. [93] developed an environmental SEM (E-SEM) based system which uses a customized AFM cantilever with a nanoneedle for indentation of single yeast cells. With the calibrated buckling characteristics of the nanoneedle, local Young's moduli of the yeast cells were measured via visual tracking of the nanoneedle deformations.

### 2.6.4 Micropipette Aspiration

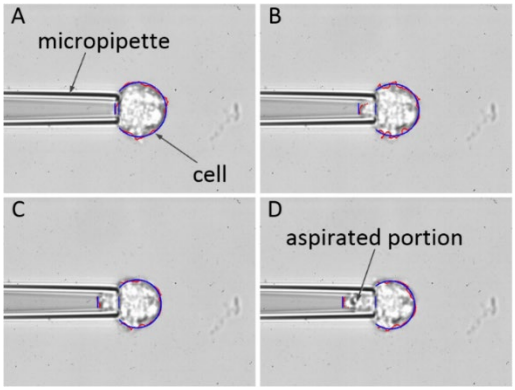


Figure 2-13 Micropipette aspiration of single cells (from [24]).

Micropipette aspiration is a conventional technique developed for cell mechanics studies [121], and its principle is to aspirate a portion of a cell into a glass micropipette using a precisely applied negative pressure. Cell mechanical properties are calculated from the applied pressure and the measured cell deformation using well-established elastic and viscoelastic models [121]. Figure 2-13 shows a sequence of microscopic images showing a cell being characterized via micropipette aspiration. Robotics and automation techniques have been developed to improve the accuracy and efficiency of micropipette aspiration. Liu et al. [24] proposed an automatic cell contour measurement technique and a data synchronization mechanism for real-time, high-accuracy micropipette aspiration of mammalian cells such as interstitial cells and white blood cells. Shojaei-Baghini et al. [122] developed a robotic micromanipulation system for automating the entire process of micropipette aspiration. Using the automated system, malignant urothelial cells were

characterized to have significantly lower Young's modulus values compared to benign urothelial cells in voided urine [123].

## 2.7 Summary and future perspectives

Leveraging emerging techniques in robotics, automation, and MEMS, robotic micromanipulation has found important applications in biological and medical research. Foreign materials can be effectively delivered into single cells and small organisms. Single cells can be transferred to a desired environment. Cellular mechanical properties can be efficiently measured. Even the internal elements of a cell or organism can be manipulated by these micromanipulation systems. This review provided an introduction to existing robotic micromanipulation techniques and systems and their applications to three classical biomanipulation tasks—microinjection, transfer, and mechanical characterization—for handling single cells and small organisms. Significant innovations have been made to create new robotic tools for: (i) assisting in the conventional manual operations; (ii) automating the manipulation processes with unparalleled accuracy, consistency, and throughput; and (iii) enabling new types of manipulation tasks that cannot be achieved with conventional techniques. With new advancements in biology and medicine, the demand for enabling and powerful biomanipulation tools becomes stronger. It is believed that the field of robotic biomanipulation will grow more and more rapidly with focuses on: (i) further technological innovations to meet requirements of newly emerging biomanipulation tasks; and (ii) continuous engineering development of existing prototype systems and platforms to make them more practical and reliable for real use by biological and medical end-users.

## 2.8 References


[1] J. White *et al.*, "Myocardial gene delivery using molecular cardiac surgery with recombinant adeno-associated virus vectors in vivo," *Gene Therapy,* vol. 18, no. 6, pp. 546-552, 2011.

[2] M. Nonnenmacher and T. Weber, "Intracellular transport of recombinant adeno-associated virus vectors," *Gene Therapy,* vol. 19, no. 6, pp. 649-658, 2012.

[3] E. Enlund *et al.*, "Establishment of lipofection for studying miRNA function in human adipocytes," *PloS ONE,* vol. 9, no. 5, p. e98023, 2014.

[4] J. C. Weaver and Y. A. Chizmadzhev, "Theory of electroporation: a review," *Bioelectrochemistry and Bioenergetics,* vol. 41, no. 2, pp. 135-160, 1996.

[5] J. C. Weaver, "Electroporation of cells and tissues," *Plasma Science, IEEE Transactions on,* vol. 28, no. 1, pp. 24-33, 2000.

[6] K. Sakaki, N. Dechev, R. D. Burke, and E. J. Park, "Development of an autonomous biological cell manipulator with single-cell electroporation and visual servoing

capabilities," *Biomedical Engineering, IEEE Transactions on,* vol. 56, no. 8, pp. 2064-2074, 2009.

[7] Y. Zhang and L.-C. Yu, "Microinjection as a tool of mechanical delivery," *Current Opinion in Biotechnology,* vol. 19, no. 5, pp. 506-510, 2008.

[8] Y. Sun and B. J. Nelson, "Biological cell injection using an autonomous microrobotic system," *The International Journal of Robotics Research,* vol. 21, no. 10-11, pp. 861-868, 2002.

[9] X. Zhang, C. Leung, Z. Lu, N. Esfandiari, R. F. Casper, and Y. Sun, "Controlled aspiration and positioning of biological cells in a micropipette," *Biomedical Engineering, IEEE Transactions on,* vol. 59, no. 4, pp. 1032-1040, 2012.

[10] C. Leung, Z. Lu, N. Esfandiari, R. F. Casper, and Y. Sun, "Automated sperm immobilization for intracytoplasmic sperm injection," *Biomedical Engineering, IEEE Transactions on,* vol. 58, no. 4, pp. 935-942, 2011.

[11] Z. Lu, X. Zhang, C. Leung, N. Esfandiari, R. F. Casper, and Y. Sun, "Robotic ICSI (intracytoplasmic sperm injection)," *Biomedical Engineering, IEEE Transactions on,* vol. 58, no. 7, pp. 2102-2108, 2011.

[12] H. Matsuoka, S. Shimoda, Y. Miwa, and M. Saito, "Automatic positioning of a microinjector in mouse ES cells and rice protoplasts," *Bioelectrochemistry,* vol. 69, no. 2, pp. 187-192, 2006.

[13] W. Wang, X. Liu, D. Gelinas, B. Ciruna, and Y. Sun, "A fully automated robotic system for microinjection of zebrafish embryos," *PloS one,* vol. 2, no. 9, p. e862, 2007.

[14] X. Liu *et al.*, "Automated microinjection of recombinant BCL-X into mouse zygotes enhances embryo development," *PloS one,* vol. 6, no. 7, p. e21687, 2011.

[15] W. Wang, Y. Sun, M. Zhang, R. Anderson, L. Langille, and W. Chan, "A system for high-speed microinjection of adherent cells," *Review of Scientific Instruments,* vol. 79, no. 10, 2008.

[16] J. Liu *et al.*, "Robotic Adherent Cell Injection (RACI) for Characterizing Cell-Cell Communication," *Biomedical Engineering, IEEE Transactions on,* vol. 62, no. 99, pp. 119-125, 2014.

[17] A. Pillarisetti, M. Pekarev, A. D. Brooks, and J. P. Desai, "Evaluating the effect of force feedback in cell injection," *Automation Science and Engineering, IEEE Transactions on,* vol. 4, no. 3, pp. 322-331, 2007.

[18] J. Kim, H. Ladjal, D. Folio, A. Ferreira, and J. Kim, "Evaluation of telerobotic shared control strategy for efficient single-cell manipulation," *Automation Science and Engineering, IEEE Transactions on,* vol. 9, no. 2, pp. 402-406, 2012.

[19] L. Mattos and D. Caldwell, "Interface design for microbiomanipulation and teleoperation," in *the 2nd International Conferences on Advances in Computer-Human Interactions (ACHI)*, 2009, pp. 342-347: IEEE.

[20] I. Gaponov, J.-H. Ryu, S.-J. Choi, H.-C. Cho, and Y. Poduraev, "Telerobotic system for cell manipulation," in *IEEE/ASME International Conference on Advanced Intelligent Mechatronics (AIM)*, 2008, pp. 165-169: IEEE.

[21] A. P. Vijayasai, G. Sivakumar, M. Mulsow, S. Lacouture, A. Holness, and T. E. Dallas, "Haptic controlled three-axis MEMS gripper system," *Review of Scientific Instruments,* vol. 81, no. 10, p. 105114, 2010.

[22] S. Zappe, M. Fish, M. P. Scott, and O. Solgaard, "Automated MEMS-based Drosophila embryo injection system for high-throughput RNAi screens," *Lab on a Chip,* vol. 6, no. 8, pp. 1012-1019, 2006.
[23] E. Cornell *et al.*, "Automating fruit fly Drosophila embryo injection for high throughput transgenic studies," *Review of Scientific Instruments,* vol. 79, no. 1, p. 013705, 2008.
[24] X. Liu, Y. Wang, and Y. Sun, "Cell contour tracking and data synchronization for real-time, high-accuracy micropipette aspiration," *Automation Science and Engineering, IEEE Transactions on,* vol. 6, no. 3, pp. 536-543, 2009.
[25] W. H. Wang, X. Y. Liu, and Y. Sun, "High-throughput automated injection of individual biological cells," *Automation Science and Engineering, IEEE Transactions on,* vol. 6, no. 2, pp. 209-219, 2009.
[26] H. B. Huang, D. Sun, J. K. Mills, and S. H. Cheng, "Robotic cell injection system with position and force control: toward automatic batch biomanipulation," *Robotics, IEEE Transactions on,* vol. 25, no. 3, pp. 727-737, 2009.
[27] G. Becattini, L. S. Mattos, and D. G. Caldwell, "A fully automated system for adherent cells microinjection," *Biomedical and Health Informatics, IEEE Journal of,* vol. 18, no. 1, pp. 83-93, 2014.
[28] H. Huang, D. Sun, J. K. Mills, W. J. Li, and S. H. Cheng, "Visual-based impedance control of out-of-plane cell injection systems," *Automation Science and Engineering, IEEE Transactions on,* vol. 6, no. 3, pp. 565-571, 2009.
[29] P. Kallio and J. Kuncová, "Manipulation of living biological cells: Challenges in automation," in *IEEE/RSJ International Conference on Intelligent Robots and Systems (IROS)*, 2003: Citeseer.
[30] A. Ghanbari, W. Wang, C. E. Hann, J. G. Chase, and X. Chen, "Cell image recognition and visual servo control for automated cell injection," in *4th International Conference on Autonomous Robots and Agents (ICARA)*, 2009, pp. 92-96: IEEE.
[31] X. Long, W. L. Cleveland, and Y. L. Yao, "A new preprocessing approach for cell recognition," *Information Technology in Biomedicine, IEEE Transactions on,* vol. 9, no. 3, pp. 407-412, 2005.
[32] A. E. Carpenter *et al.*, "CellProfiler: image analysis software for identifying and quantifying cell phenotypes," *Genome Biology,* vol. 7, no. 10, p. R100, 2006.
[33] M. Lukkari, M. Karjalainen, R. Sarkanen, M. Linne, T. Jalonen, and P. Kallio, "Electrical detection of the contact between a microinjection pipette and cells," in *26th Annual International Conference of the IEEE Engineering in Medicine and Biology Society (EMBS)*, 2004.
[34] S. F. Graf, T. Madigou, R. Li, C. Chesné, A. Stemmer, and H. F. Knapp, "Fully automated microinjection system for Xenopus laevis oocytes with integrated sorting and collection," *Journal of the Association for Laboratory Automation,* vol. 16, no. 3, pp. 186-196, 2011.
[35] R. C. Hogg, F. Bandelier, A. Benoit, R. Dosch, and D. Bertrand, "An automated system for intracellular and intranuclear injection," *Journal of neuroscience methods,* vol. 169, no. 1, pp. 65-75, 2008.
[36] R. W. Bernstein, M. Scott, and O. Solgaard, "BioMEMS for high-throughput handling and microinjection of embryos," in *Photonics Asia*, 2004, pp. 67-73: International Society for Optics and Photonics.
[37] R. W. Bernstein, X. Zhang, S. Zappe, M. Fish, M. Scott, and O. Solgaard, "Positioning and immobilization of Drosophila embryos in 2-D arrays for drug injection," in *the*

*International Conference on Miniaturized Systems for Chemistry and Life Sciences (MicroTAS)*, 2002, pp. 793-795: Springer.

[38] J. Liu *et al.*, "Locating end-effector tips in robotic micromanipulation," *Robotics, IEEE Transactions on,* vol. 30, no. 1, pp. 125-130, 2014.

[39] M. L. Han, Y. L. Zhang, M. Y. Yu, C. Y. Shee, and W. T. Ang, "Non-contact force sensing for real-time stressing of biological cells," *Micro & Nano Letters,* vol. 6, no. 5, pp. 306-310, 2011.

[40] Y. Zhang, M. Han, J. Vidyalakshmi, C. Shee, and W. Ang, "Automatic control of mechanical forces acting on cell biomembranes using a vision-guided microrobotic system in computer microscopy," *Journal of Microscopy,* vol. 236, no. 1, pp. 70-78, 2009.

[41] M. A. Greminger and B. J. Nelson, "Vision-based force measurement," *Pattern Analysis and Machine Intelligence, IEEE Transactions on,* vol. 26, no. 3, pp. 290-298, 2004.

[42] T. F. Chan and L. A. Vese, "Active contours without edges," *Image Processing, IEEE transactions on,* vol. 10, no. 2, pp. 266-277, 2001.

[43] S. Hutchinson, G. D. Hager, and P. I. Corke, "A tutorial on visual servo control," *Robotics and Automation, IEEE Transactions on,* vol. 12, no. 5, pp. 651-670, 1996.

[44] F. Chaumette and S. Hutchinson, "Visual servo control. I. basic approaches," *IEEE Robotics & Automation Magazine,* vol. 13, no. 4, pp. 82-90, 2006.

[45] L. Zhe, C. Y. C. Peter, N. Joohoo, G. Ruowen, and L. Wei, "A micromanipulation system with dynamic force-feedback for automatic batch microinjection," *Journal of Micromechanics and Microengineering,* vol. 17, no. 2, p. 314, 2007.

[46] X. Liu, Y. Sun, W. Wang, and B. M. Lansdorp, "Vision-based cellular force measurement using an elastic microfabricated device," *Journal of Micromechanics and Microengineering,* vol. 17, no. 7, p. 1281, 2007.

[47] X. Liu, R. Fernandes, A. Jurisicova, R. F. Casper, and Y. Sun, "In situ mechanical characterization of mouse oocytes using a cell holding device," *Lab on a Chip,* 10.1039/C004706F vol. 10, no. 16, pp. 2154-2161, 2010.

[48] Y. Sun, K.-T. Wan, K. P. Roberts, J. C. Bischof, and B. J. Nelson, "Mechanical property characterization of mouse zona pellucida," *NanoBioscience, IEEE Transactions on,* vol. 2, no. 4, pp. 279-286, 2003.

[49] Y. Xie, D. Sun, C. Liu, H. Y. Tse, and S. H. Cheng, "A force control approach to a robot-assisted cell microinjection system," *The International Journal of Robotics Research,* vol. 29, no. 9, pp. 1222-1232, 2010.

[50] M. A. Greminger and B. J. Nelson, "A deformable object tracking algorithm based on the boundary element method that is robust to occlusions and spurious edges," *International Journal of Computer Vision,* vol. 78, no. 1, pp. 29-45, 2008.

[51] X. Liu, J. Shi, Z. Zong, K.-T. Wan, and Y. Sun, "Elastic and viscoelastic characterization of mouse oocytes using micropipette indentation," (in English), *Annals of Biomedical Engineering,* vol. 40, no. 10, pp. 2122-2130, 2012/10/01 2012.

[52] N. Chronis, M. Zimmer, and C. I. Bargmann, "Microfluidics for in vivo imaging of neuronal and behavioral activity in Caenorhabditis elegans," *Nature methods,* vol. 4, no. 9, p. 727, 2007.

[53] S. R. Lockery *et al.*, "Artificial dirt: microfluidic substrates for nematode neurobiology and behavior," *Journal of neurophysiology,* 2008.

[54] K. Chung, M. M. Crane, and H. Lu, "Automated on-chip rapid microscopy, phenotyping and sorting of C. elegans," *Nature methods,* vol. 5, no. 7, p. 637, 2008.

[55] C. B. Rohde, F. Zeng, R. Gonzalez-Rubio, M. Angel, and M. F. Yanik, "Microfluidic system for on-chip high-throughput whole-animal sorting and screening at subcellular resolution," *Proceedings of the National Academy of Sciences,* vol. 104, no. 35, pp. 13891-13895, 2007.
[56] S. X. Guo *et al.*, "Femtosecond laser nanoaxotomy lab-on-a-chip for in vivo nerve regeneration studies," *Nature methods,* vol. 5, no. 6, p. 531, 2008.
[57] F. Geier, A. Leroi, J. Bundy, J. Edel, and A. DeMello, "High-throughput age synchronisation of Caenorhabditis elegans," *Chemical communications (Cambridge, England),* vol. 47, no. 35, pp. 9801-9803, 2011.
[58] L. Dong, M. Cornaglia, T. Lehnert, and M. A. Gijs, "Versatile size-dependent sorting of C. elegans nematodes and embryos using a tunable microfluidic filter structure," *Lab on a Chip,* vol. 16, no. 3, pp. 574-585, 2016.
[59] X. Ai, W. Zhuo, Q. Liang, P. T. McGrath, and H. Lu, "A high-throughput device for size based separation of C. elegans developmental stages," *Lab on a Chip,* vol. 14, no. 10, pp. 1746-1752, 2014.
[60] Y. Yan *et al.*, "A continuous-flow C. elegans sorting system with integrated optical fiber detection and laminar flow switching," *Lab on a Chip,* vol. 14, no. 20, pp. 4000-4006, 2014.
[61] B. Gupta and P. Rezai, "Microfluidic approaches for manipulating, imaging, and screening C. elegans," *Micromachines,* vol. 7, no. 7, p. 123, 2016.
[62] P. Rezai, A. Siddiqui, P. R. Selvaganapathy, and B. P. Gupta, "Electrotaxis of Caenorhabditis elegans in a microfluidic environment," *Lab on a Chip,* vol. 10, no. 2, pp. 220-226, 2010.
[63] B. Han, D. Kim, U. H. Ko, and J. H. Shin, "A sorting strategy for C. elegans based on size-dependent motility and electrotaxis in a micro-structured channel," *Lab on a Chip,* vol. 12, no. 20, pp. 4128-4134, 2012.
[64] N. Chronis, "Worm chips: Microtools for C. elegans biology," *Lab on a Chip,* vol. 10, no. 4, pp. 432-437, 2010.
[65] C. L. Gilleland, C. B. Rohde, F. Zeng, and M. F. Yanik, "Microfluidic immobilization of physiologically active Caenorhabditis elegans," *Nature Protocols,* 10.1038/nprot.2010.143 vol. 5, no. 12, pp. 1888-1902, 11//print 2010.
[66] T. V. Chokshi, A. Ben-Yakar, and N. Chronis, "CO 2 and compressive immobilization of C. elegans on-chip," *Lab on a Chip,* vol. 9, no. 1, pp. 151-157, 2009.
[67] S. E. Hulme, S. S. Shevkoplyas, J. Apfeld, W. Fontana, and G. M. Whitesides, "A microfabricated array of clamps for immobilizing and imaging C. elegans," *Lab on a Chip,* vol. 7, no. 11, pp. 1515-1523, 2007.
[68] X. Zhao, F. Xu, L. Tang, W. Du, X. Feng, and B.-F. Liu, "Microfluidic chip-based C. elegans microinjection system for investigating cell–cell communication in vivo," *Biosensors and Bioelectronics,* vol. 50, pp. 28-34, 2013.
[69] T. Hirano, M. Nakajima, M. Kojima, N. Hisamoto, M. Homma, and T. Fukuda, "Selective nano-injection using nano-probe based on nanomanipulation under hybrid microscope," in *2011 International Symposium on Micro-Nano Mechatronics and Human Science (MHS)*, 2011, pp. 216-221: IEEE.
[70] X. Wang *et al.*, "Enhanced cell sorting and manipulation with combined optical tweezer and microfluidic chip technologies," *Lab on a Chip,* vol. 11, no. 21, pp. 3656-3662, 2011.

[71] P. J. Lee, P. J. Hung, R. Shaw, L. Jan, and L. P. Lee, "Microfluidic application-specific integrated device for monitoring direct cell-cell communication via gap junctions between individual cell pairs," *Applied Physics Letters,* vol. 86, no. 22, pp. -, 2005.
[72] R. W. Steubing, S. Cheng, W. H. Wright, Y. Numajiri, and M. W. Berns, "Laser induced cell fusion in combination with optical tweezers: the laser cell fusion trap," *Cytometry,* vol. 12, no. 6, pp. 505-510, 1991.
[73] M. Takeuchi, M. Nakajima, M. Kojima, and T. Fukuda, "Probe device for soft handling of single cells using thermoresponsive polymer," in *2011 IEEE International Conference on Robotics and Automation (ICRA)*, 2011, pp. 3163-3168: IEEE.
[74] Z. Lu, C. Moraes, G. Ye, C. A. Simmons, and Y. Sun, "Single cell deposition and patterning with a robotic system," *PloS ONE,* vol. 5, no. 10, p. e13542, 2010.
[75] K. Zhang *et al.*, "Hand-held and integrated single-cell pipettes," *Journal of the American Chemical Society,* vol. 136, no. 31, pp. 10858-10861, 2014.
[76] Y. H. Anis, M. R. Holl, and D. R. Meldrum, "Automated selection and placement of single cells using vision-based feedback control," *Automation Science and Engineering, IEEE Transactions on,* vol. 7, no. 3, pp. 598-606, 2010.
[77] N. Chronis and L. P. Lee, "Electrothermally activated SU-8 microgripper for single cell manipulation in solution," *Microelectromechanical Systems, Journal of,* vol. 14, no. 4, pp. 857-863, 2005.
[78] F. Beyeler *et al.*, "Monolithically fabricated microgripper with integrated force sensor for manipulating microobjects and biological cells aligned in an ultrasonic field," *Microelectromechanical Systems, Journal of,* vol. 16, no. 1, pp. 7-15, 2007.
[79] K. Kim, X. Liu, Y. Zhang, and Y. Sun, "Nanonewton force-controlled manipulation of biological cells using a monolithic MEMS microgripper with two-axis force feedback," *Micromechanics and Microengineering, Journal of* vol. 18, no. 5, p. 055013, 2008.
[80] T. G. Leong, C. L. Randall, B. R. Benson, N. Bassik, G. M. Stern, and D. H. Gracias, "Tetherless thermobiochemically actuated microgrippers," in *the National Academy of Sciences of the United States of America*, 2009, vol. 106, no. 3, pp. 703-708.
[81] C. Liu, *Foundations of MEMS*. Pearson Education India, 2006.
[82] B. A. Wester, S. Rajaraman, J. D. Ross, M. C. LaPlaca, and M. G. Allen, "Development and characterization of a packaged mechanically actuated microtweezer system," *Sensors and Actuators A: Physical,* vol. 167, no. 2, pp. 502-511, 2011.
[83] Z. Ni, A. Bolopion, J. Agnus, R. Benosman, and S. Régnier, "Asynchronous event-based visual shape tracking for stable haptic feedback in microrobotics," *Robotics, IEEE Transactions on,* vol. 28, no. 5, pp. 1081-1089, 2012.
[84] M. A. Greminger, A. S. Sezen, and B. J. Nelson, "A four degree of freedom MEMS microgripper with novel bi-directional thermal actuators," in *IEEE/RSJ International Conference on Intelligent Robots and Systems (IROS)*, 2005, pp. 2814-2819.
[85] K. Inoue, T. Tanikawa, and T. Arai, "Micro-manipulation system with a two-fingered micro-hand and its potential application in bioscience," *Journal of biotechnology,* vol. 133, no. 2, pp. 219-224, 2008.
[86] S. Kim *et al.*, "Fabrication and Characterization of Magnetic Microrobots for Three-Dimensional Cell Culture and Targeted Transportation," *Advanced Materials,* vol. 25, no. 41, pp. 5863-5868, 2013.
[87] C.-N. Nguyen, K. Ohara, E. Avci, T. Takubo, Y. Mae, and T. Arai, "Automated micromanipulation for a microhand with All-In-Focus imaging system," in *2011 IEEE/RSJ*

*International Conference on Intelligent Robots and Systems (IROS)*, 2011, pp. 427-432: IEEE.

[88] D. Kawakami *et al.*, "Cell hardness measurement by using two-fingered microhand with micro force sensor," in *2011 IEEE/RSJ International Conference on Intelligent Robots and Systems (IROS)*, 2011, pp. 25-30: IEEE.

[89] T. Tanikawa and T. Arai, "Development of a micro-manipulation system having a two-fingered micro-hand," *Robotics and Automation, IEEE Transactions on,* vol. 15, no. 1, pp. 152-162, 1999.

[90] E. B. Steager, M. Selman Sakar, C. Magee, M. Kennedy, A. Cowley, and V. Kumar, "Automated biomanipulation of single cells using magnetic microrobots," *The International Journal of Robotics Research,* vol. 32, no. 3, pp. 346-359, March 1, 2013 2013.

[91] Z. Ye and M. Sitti, "Dynamic trapping and two-dimensional transport of swimming microorganisms using a rotating magnetic microrobot," *Lab on a Chip,* 10.1039/C4LC00004H vol. 14, no. 13, pp. 2177-2182, 2014.

[92] S. Hu and D. Sun, "Automated transportation of single cells using robot-tweezer manipulation system," *Journal of Laboratory Automation,* vol. 16, no. 4, pp. 263-270, 2011.

[93] M. R. Ahmad, M. Nakajima, S. Kojima, M. Homma, and T. Fukuda, "In situ single cell mechanics characterization of yeast cells using nanoneedles inside environmental SEM," *Nanotechnology, IEEE Transactions on,* vol. 7, no. 5, pp. 607-616, 2008.

[94] F. Arai, H. Maruyama, T. Sakami, A. Ichikawa, and T. Fukuda, "Pinpoint injection of microtools for minimally invasive micromanipulation of microbe by laser trap," *Mechatronics, IEEE/ASME Transactions on,* vol. 8, no. 1, pp. 3-9, 2003.

[95] A. Ashkin and J. Dziedzic, "Internal cell manipulation using infrared laser traps," in *the National Academy of Sciences of the United States of America*, 1989, vol. 86, no. 20, pp. 7914-7918.

[96] R. Applegate Jr, J. Squier, T. Vestad, J. Oakey, and D. Marr, "Optical trapping, manipulation, and sorting of cells and colloids in microfluidic systems with diode laser bars," *Optics Express,* vol. 12, no. 19, pp. 4390-4398, 2004.

[97] Y. Tan, D. Sun, S. H. Cheng, and R. A. Li, "Robotic cell manipulation with optical tweezers for biomechanical characterization," in *IEEE International Conference onRobotics and Automation (ICRA)*, 2011, pp. 4104-4109: IEEE.

[98] D. B. Serrell, J. Law, A. J. Slifka, R. L. Mahajan, and D. S. Finch, "A uniaxial bioMEMS device for imaging single cell response during quantitative force-displacement measurements," *Biomedical Microdevices,* vol. 10, no. 6, pp. 883-889, 2008.

[99] D.-H. Kim, C. N. Hwang, Y. Sun, S. H. Lee, B. Kim, and B. J. Nelson, "Mechanical analysis of chorion softening in prehatching stages of zebrafish embryos," *NanoBioscience, IEEE Transactions on,* vol. 5, no. 2, pp. 89-94, 2006.

[100] Y. Tan, D. Sun, W. Huang, and S. H. Cheng, "Mechanical modeling of biological cells in microinjection," *NanoBioscience, IEEE Transactions on,* vol. 7, no. 4, pp. 257-266, 2008.

[101] H. Ladjal, J.-L. Hanus, and A. Ferreira, "Micro-to-nano biomechanical modeling for assisted biological cell injection," *Biomedical Engineering, IEEE Transactions on,* vol. 60, no. 9, pp. 2461-2471, 2013.

[102] S. Yang and T. Saif, "Reversible and repeatable linear local cell force response under large stretches," *Experimental Cell Research,* vol. 305, no. 1, pp. 42-50, 2005.

[103] J. L. Tan, J. Tien, D. M. Pirone, D. S. Gray, K. Bhadriraju, and C. S. Chen, "Cells lying on a bed of microneedles: an approach to isolate mechanical force," in *the National Academy of Sciences of the United States of America*, 2003, vol. 100, no. 4, pp. 1484-1489.
[104] B. Li, L. Xie, Z. C. Starr, Z. Yang, J. S. Lin, and J. H. C. Wang, "Development of micropost force sensor array with culture experiments for determination of cell traction forces," *Cell Motility and the Cytoskeleton,* vol. 64, no. 7, pp. 509-518, 2007.
[105] O. Du Roure *et al.*, "Force mapping in epithelial cell migration," in *the National Academy of Sciences of the United States of America*, 2005, vol. 102, no. 7, pp. 2390-2395.
[106] M. T. Yang, N. J. Sniadecki, and C. S. Chen, "Geometric considerations of micro-to-nanoscale elastomeric post arrays to study cellular traction forces," *Advanced Materials,* vol. 19, no. 20, pp. 3119-3123, 2007.
[107] M. Dembo and Y.-L. Wang, "Stresses at the cell-to-substrate interface during locomotion of fibroblasts," *Biophysical Journal,* vol. 76, no. 4, pp. 2307-2316, 1999.
[108] C. T. Lim, M. Dao, S. Suresh, C. H. Sow, and K. T. Chew, "Large deformation of living cells using laser traps," *Acta Materialia,* vol. 52, no. 7, pp. 1837-1845, 4/19/ 2004.
[109] Y. Tan, C.-w. Kong, S. Chen, S. H. Cheng, R. A. Li, and D. Sun, "Probing the mechanobiological properties of human embryonic stem cells in cardiac differentiation by optical tweezers," *Journal of Biomechanics,* vol. 45, no. 1, pp. 123-128, 1/3/ 2012.
[110] H. Zhang and K.-K. Liu, "Optical tweezers for single cells," *Journal of The Royal Society Interface,* vol. 5, no. 24, pp. 671-690, 2008.
[111] V. J. Morris, A. R. Kirby, and A. P. Gunning, *Atomic force microscopy for biologists*. World Scientific, 1999.
[112] A. Pillarisetti, C. Keefer, and J. P. Desai, "Mechanical Response of embryonic stem cells using haptics-enabled atomic force microscopy," in *International Symposium on Experimental Robotics*, 2009, pp. 261-269: Springer.
[113] M. Girot, M. Boukallel, and S. Régnier, "Modeling soft contact mechanism of biological cells using an atomic force bio-microscope," in *IEEE/RSJ International Conference on Intelligent Robots and Systems*, 2006, pp. 1831-1836: IEEE.
[114] T. G. Kuznetsova, M. N. Starodubtseva, N. I. Yegorenkov, S. A. Chizhik, and R. I. Zhdanov, "Atomic force microscopy probing of cell elasticity," *Micron,* vol. 38, no. 8, pp. 824-833, 2007.
[115] A. Meister *et al.*, "FluidFM: combining atomic force microscopy and nanofluidics in a universal liquid delivery system for single cell applications and beyond," *Nano Letters,* vol. 9, no. 6, pp. 2501-2507, 2009.
[116] I. Obataya, C. Nakamura, S. Han, N. Nakamura, and J. Miyake, "Nanoscale operation of a living cell using an atomic force microscope with a nanoneedle," *Nano Letters,* vol. 5, no. 1, pp. 27-30, 2005.
[117] E. Takai, K. D. Costa, A. Shaheen, C. T. Hung, and X. E. Guo, "Osteoblast elastic modulus measured by atomic force microscopy is substrate dependent," *Annals of Biomedical Engineering,* vol. 33, no. 7, pp. 963-971, 2005.
[118] X. Tian, L. Liu, N. Jiao, Y. Wang, Z. Dong, and N. Xi, "3D nano forces sensing for an AFM based nanomanipulator," in *International Conference on Information Acquisition*, 2004, pp. 208-212: IEEE.
[119] C. K. M. Fung *et al.*, "Investigation of human keratinocyte cell adhesion using atomic force microscopy," *Nanomedicine: Nanotechnology, Biology and Medicine,* vol. 6, no. 1, pp. 191-200, 2010.

[120] M. Li *et al.*, "Investigating the morphology and mechanical properties of blastomeres with atomic force microscopy," *Surface and Interface Analysis,* vol. 45, no. 8, pp. 1193-1196, 2013.
[121] R. M. Hochmuth, "Micropipette aspiration of living cells," *Journal of Biomechanics,* vol. 33, no. 1, pp. 15-22, 1// 2000.
[122] E. Shojaei-Baghini, Y. Zheng, and Y. Sun, "Automated micropipette aspiration of single cells," (in English), *Annals of Biomedical Engineering,* vol. 41, no. 6, pp. 1208-1216, 2013/06/01 2013.
[123] E. Shojaei-Baghini, Y. Zheng, M. A. S. Jewett, W. B. Geddie, and Y. Sun, "Mechanical characterization of benign and malignant urothelial cells from voided urine," *Applied Physics Letters,* vol. 102, no. 12, 2013.

# Link between chapter 2 and chapter 3

In the previous chapter, the basic methodologies and engineering techniques for the recent development in the field of micromanipulation of bio-samples is reviewed, including the microinjection of cells and *C. elegans*, robotic transfer of cells and small organisms, and the robotic mechanical characterization of cells. For the discussed micromanipulation topics, the fundamental objective is to replace the conventional time-consuming and labor-intensive manual tasks with standard operations automated by machines. In addition, the automated micromanipulation has brought unprecedented advances that is far beyond the capability of manual operations, such as the micro-Newton force measurement and control, mechanical calibration of the intercellular organelles, and the automated single sperm injection for artificial fertilization, to name just a few. These research topics are employing the external automation hardware components to fulfill predesigned tasks based on the bio-sample platform, however, they are not developing the bio-sample itself as an untethered microrobot.

To fully investigate the current development in the field of bio-agent microrobots, and provide theoretical and technical references to the *C. elegans* micro robo-worm in Chapter 6, another literature review in the field of bio-agent microrobots is performed. Three major types of bio-agent microrobots, including the magnetotactic bacteria microrobot, sperm-based micro-swimmer, and the insect-machine hybrid microrobot. The detailed concept and techniques are introduced in the next chapter

# Chapter 3

# Bio-Agent Microrobots: Review

# Chapter 3: Bio-Agent Microrobots: Review

**X. Dong[1,2] and X. Liu[1,2]***

*[1]Department of Mechanical Engineering, McGill University, 817 Sherbrooke Street West, Montreal, Quebec, Canada H3A 2K6*

*[2]Department of Mechanical and Industrial Engineering, University of Toronto, 5 King's College Road, Toronto, Ontario, Canada M5S 3G8*

*corresponding author: (xyliu@mie.utoronto.ca)

To be submitted.

## 3.1 Abstract

For the small-scale robot swimming in the fluid or crawling on the ground, the viscosity and friction emerge as the most important forces dominating the robot behaviors, which greatly differs to the actuation of macro-scale robots. Inspired by the locomotion patterns of small-scale natural organisms, numerous attempts have been made to develop artificial robots to mimic the movements of sperms, bacteria, and nematode, to name just a few. Nevertheless, the untethered power supplies for small scale robot, the sensing method, and control synthesis are the critical technical problems that greatly limit our steps. A hybrid route is to harness the movement of biological organisms directly as robotic movement actuator and turn the living creature into controllable robot, for which we name it as the bio-agent robot. In this review, three kinds of bio-agent robots, including the magnetotactic bacteria (MTB) nanorobot, the sperm microrobot, and the insect-machine hybrid robot, are discussed to provide the basic techniques and perspectives for the current development in the field.

## 3.2 Introduction

Robotics emerges as the mimic of the locomotion patterns of biological creatures. It has been nowadays developed into a fundamental support of the modern world, appearing in every aspect of the human life. When robotics evolves into small sizescales of millimeter or micrometer, extreme technical requirements of structure design and fabrication, energy storage and supply, and system modelling and control appear and slow down the development of robotics. In the microscale fluidic environment, it has long been a worldwide target to develop microrobot to conduct microsurgery on the lesions tissues [1]. Several attempts of artificial microrobots have

been made to step towards this objective during the past two decades [2-6]. A novel helical-shape micro-swimmer, powered and controlled by the external rotating magnetic field to mimic the movement pattern of bacterial flagella in low Reynolds number environment, is designed by B. J. Belson et. al. [3] for microsurgery. Schmidt et. al. [6] proposed a microtube robot in the hydrogen peroxide solution to generate $O_2$ bubbles on the inner surface of the tube and propel the microrobot to move forward in liquid environment. These artificial microrobots have greatly broadened the field of robotic research, however, their practical applications are still limited as for the strict requirement of functioning environment, limited controllability and lack of feedback approaches.

Biological organisms, with the size scale from the whale to the bacteria, and the living environment from the sky to the sea, have developed a wide range of locomotion patterns through evolution. Therefore, an alternative approach for small scale robot development is to design the biology-machine hybrid robots and harness the movement of biological organisms directly. The concept of developing robot directly from biological organisms is defined as bio-agent robot in this review.

Several novel bio-agent robots have been proposed and rapidly surpass their counter parts of artificial rigid-body robots [7, 8] [9] [10] [11]. For instance, in 2007, the MTB is designed as a controllable self-propelled nanorobot and manipulated for the micro-assembly of microparticles [8]. Later in 2016, S. Martel et. al. [7] has used the MTB as a robotic carrier for drug delivery in a mouse. A sperm microrobot, able to swim and steer under magnetic field, is proposed by capturing a single sperm within the cavity of microtube [9]. In addition, with a novel thermal controlled self-rolling microtube to release the sperm, this robot is used for artificial fertilization [10]. In the field of flapping-wing MAVs, the insect-machine hybrid robot is proposed to control the flight of the beetles in the untethered way [11], which avoids the long standing problem of high nonlinearity dynamics of MAVs. Thus, the field of bio-agent robot is continuously attracting more and more attention recently.

In this review, we will discuss the concepts, technical details and applications of three kinds of bio-agent robots, including the MTB nanorobot, the sperm microrobot, and the insect-machine hybrid robot. The pros and cons for the bio-agent robot will be concluded.

## 3.3 Magnetotactic bacteria as controlled micro-swimmers

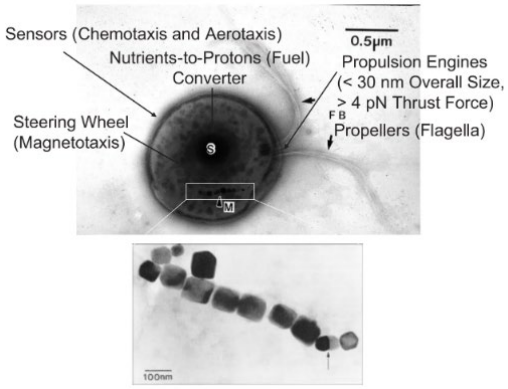


Figure 3-1 The microscope image for the intracellular structure of the MC-1 MTB. Magnetosomes is shown at bottom. (from [12])

Magnetotactic bacteria (MTB) is a group of micro-scale procaryotic organisms with the ability to align themselves according to the geomagnetic field lines. This unique magnetotaxis character is achieved based on an intracellular organelle, magnetosomes, which are membrane-bounded mineral crystals as shown in the bottom of Figure 3-1 [13, 14]. Because of the mineral crystals, rotating torques will be generated to orient the cell when it is placed in a magnetic field. The magnetic torque passively works like a compass during the migration of the organism, and it is still in function even in some of the dead MTBs.

All strains of MTB are using flagella as the locomotion organellem, which has been previously proved to be the most effective propulsion mechanism in the low Reynolds number fluidic environment [1]. The flagella are helical-shaped hollow tubes with the length of 1-2 μm and the width of 20-30 nm [12]. The base of the flagella on the cell body is an ATP-powered rotor that operates at 200-1000 rpm. When flagella rotate counter clockwise along the rotor, fluids will be pushed away to achieve the moving thrust force for swimming forward.

### 3.3.1 Select the MTB strains for robotics applications

From the composition of the mineral crystals, the MTB are subdivided into two categories, magnetite (Fe3O4) based MTB and greigite (Fe3S4) based MTB. The greigite-producing MTBs live in strict anaerobic environments, while the magnetite-producing MTBs can survive in aerobic environment. This is the major reason that magnetite-producing MTBs are usually considered to be developed as a robot. In addition, according to the magneto-aerotatic-mechanism, MTB can be

subdivided as polar and axial. The axial MTB have flagella in two ends of organism, which enable them with the ability of swimming in either direction along the magnetic field lines of spontaneous direction reversals without turning around. When axial MTBs are exposed to magnetic field lines, however, the bacteria are observed swimming in both directions along the magnetic line, rendering it difficult for control applications. Thus, unlike the axial MTB, the locomotion of polar magneto-aerotatic MTB is more predictable. It is able to swim persistently in one direction along the magnetic field lines, and it will swerve as a group and change swimming direction when exposed to a more powerful local magnetic field. Because of these advantages, the interested MTB is usually chosen from the magnetite polar MTB strains for the development of controlled microrobot [15] and the carrier of medicines [16].

Another consideration for the choosing of the MTB strain for microrobot development is the moving speed of the bacteria. Most flagella bacteria swim with the speed of about 30 μm/s. As the ATP powering the flagella gradually consumed, the MTB robots slow down and become inefficient and out of control. Therefore, the MTB with high swimming speed is of highly interest. A successful development of controlled MTB is reported in [8] with the MC-1 MTB strain. This bacteria strain is reported to have controlled swimming speed of 200 μm/s which is 150 times its body length. For more information on the chose of MTB strains for microrobots, one can refer to [16, 17].

### 3.3.2 Motion control of the MTB microrobot

In natural status, the swimming of MTB is regulated by both magnetotaxis and chemotaxis to find the suitable living environment [13, 16]. In [18], Metin et al. calibrated the swimming speed of *Serratia marcescens* bacteria with regards to the L-serine gradient, and used the bacteria to push a 3.1 μm polystyrene bead move in a predesigned direction. Since copper ions is able to stop the motion of the rotators of the flagella, chemotaxis method is also used to achieve the on/off motion control of the bacteria by adjusting the concentration of copper ions in the solution [19]. Nevertheless, the unique property of MTB is that when subjected to a local magnetic field slightly stronger than the geomagnetic field, the directional motion of MTB is mainly regulated by magnetotaxis and therefore fully controllable. Consequently, the magnetotaxis method is usually adopted for the control of MTB microrobot.

Unlike the traditional well-established methods of Lagrangian equations for the development of rigid body robotic dynamics, it is difficulty to derive an accurate theoretical model for the migration response of BTM with response to environmental stimulation. This is because that the biological process are usually nonlinear and uncertain [20]. Even if we quantitatively identified the theoretical principle, the parameters within the model can also vary in each biological individual. The speed of the MC-1 MTB, for instance, distributed within a range from 30 μm/s to 300 μm/s when the bacteria is exposed to the magnetic environment [12]. Therefore, the speed regulation and steering control of MTB microrobots are highly experiment-dependent. In addition, to facilitate the controllability of the BTM microrobot, the bacteria individuals with similar swimming speed are usually pre-screened before experiments.

**a) Speed regulation of MTB microrobots with magnetotaxis method**

In the experiments of magnetotaxis-based motion control of MTB microrobots, the speed of a pre-screened BTM strain is jointly influenced by the fluid viscosity, temperature, magnetic field, and the biological fatigability. To facilitate the controllability of the swimming speed, the environmental influence factors are usually normalized by fixing the environmental parameters. The moving speed of the BTM is mainly subject to the power of the magnetic field.

For a swarm of pre-screened MTB, the initial swimming speed of the MTB increase as the power of magnetic field increase from 0 to geomagnetic field of 0.5 Gauss. The speed will decrease when the magnetic fields is sufficiently large (>10 Guass). The detailed speed variance with respect to magnetic field is calibrated in [12]. The MTB will stop moving when exposing to a magnetic field stronger than 1.5T. Compared with the chemotaxis method of adding chemicals into the solution to stop the movement of bacteria, the magnetotaxis method is much more convenient. After continuous working for a long period of time, the swimming speed of MTB will decrease dur to the biological fatigability. The variance of velocity with respect to experiment duration is calibrated in [12]. This disadvantage is avoided by choosing the fast-moving strains of MTB to reduce the experimental time span.

**b) Aggregation of a swarm of MTB microrobots: Time-average magnetic monopole**

Without a magnetic field, the MTB usually even distributed at the bottom of a culture media. To develop them as microrobot for micro-assembly or drug delivery, it is necessary to firstly gather

them as a swarm. As the MTB always moves along the magnetic lines in magnetic field, the only method to gather thousands of these micro-organisms distributed in the solution is to create a "magnetic monopole"[21]. Since the magnetic monopole is still a theoretical hypothesis, the practical method is to create a time-average magnetic monopole at a specific position in the MTB solution.

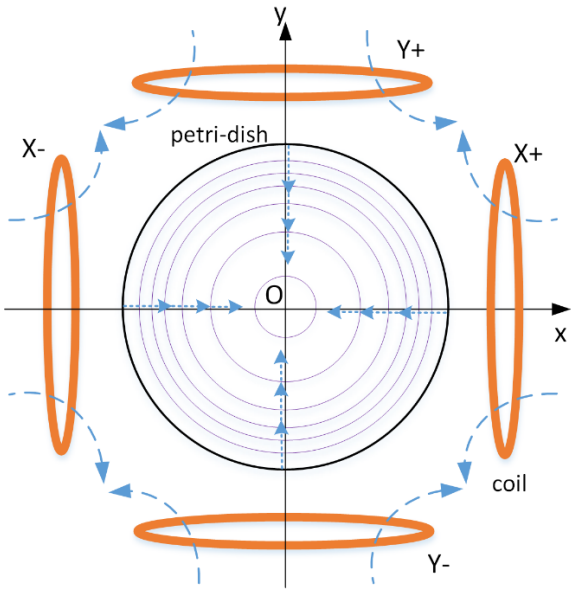


Figure 3-2 The schematic for time-average magnetic monopole in 2D space.

To illustrate the generating of time-average magnetic monopole, we take the 2D situation of controlling the aggregation of MTB in a flat petri-dish for example. As shown in Figure 3-2, the petri-dish is placed in the center of XY two-dimension coil sets with one coil placed on each of the direction. The dash lines indicate DC magnetic field lines when the coil is charged with DC current. We denote the electrical current in each coil that generates magnetic field line pointing to the center of the petri-dish by +, otherwise it is denoted by -. Once the same amount of current $I$ is charged in all the coils, the center point $O$ of the petri-dish will be the universal neutral magnetic state and a stable equilibrium in the whole XY plane. On the other hand, if we discharge one of the 4 coils, the magnetic direction of point $O$ will be pointing to the uncharged coil. By evenly distributing the discharging time span of the coils, a repeating time sequence for the charging of each coils are designed as *Table 3.3-1* to create a time-average magnetic monopole at $O$. The 3D

aggregation of a swarm of MTB microrobots under the time-average magnetic monopole is investigated in [21].

Table 3.3-1 Time sequence for the charging of coils

| period | X+ | X- | Y+ | Y- | Duration |
|---|---|---|---|---|---|
| 1 | 0 | I | I | I | T |
| 2 | I | 0 | I | I | T |
| 3 | I | I | 0 | I | T |
| 4 | I | I | I | 0 | T |

**c) Motion control**

Once the MTBs are gathered in the center of the petri-dish, the swimming direction of the MTB swarm can be controlled by generating a converged magnetic field line along the predesigned direction. For example, we can make the MTB move along the positive direction of X axis by discharging the current in the coils of X+.

Since the moving speed of the individual bacteria in the MTB swarm varies to each other, displacement error will accumulate in the experiments. To re-gather the MTB microrobot, a new stable overall equilibrium should be generated. This can be achieved by modifying the current values in Tab. 1 to get a biased equilibrium point other than $O$. The simulation of the stable equilibrium points in 3D space are discussed in [22].

### 3.3.3 Track the MTB microrobot

Since a swarm of MTB can be obviously seen in a clear solution, the real-time position and speed of the MTB microrobots can be easily measured by a camera [8]. For the targeted drug delivery, however, the MTB will be used as a medicine carrier and swims within the blood capillaries, rendering the camera-based measurement unpracticable. In this case, the magnetic resonance imaging (MRI) is adopted to track the MTB in the animal body, as the magnetosomes in the bacteria will cause a local distortion of the magnetic field inside the MRI system and act as MRI contrast agent [15]. Benefitting from the MRI, we can not only track the displacement of the MRI swarm but also measure the concentration distribution of the bacteria individuals in the animal

body. This method can be used to evaluate the effectiveness of the drug delivery by measuring the MTB concentration around the targeted tumour.

### 3.3.4 MTB microrobot as a controlled micro-carrier

A significant application of the MTB microrobots is to develop the bacteria as a controlled micro-carrier and deliver the cargo to interested environment that is difficult to reach using other methods [23]. There are mainly 4 types of cargo loading/delivering strategies developed up to now, as shown in Figure 3-3. For the targeted drug delivery in cancer therapy, the MTB microrobot carrying the medicines will swim through the capillaries in the animal body, and therefore the more reliable delivery strategies of Figure 3-3(A) and Figure 3-3(C) are of highly interest. Figure 3-3 (A) shows that a group of 170 nm liposomes nanoparticles containing the therapeutic agent is attached to the surface of MC-1 MTB by carbodiimide chemistry method for targeted drug delivery [7] [24]. The cargos bring little drag force for the MTB and therefore induce no significantly degrade of the speed for controlled swimming, because of their small sizes. The antibody coating approach is also used to attach these small nanoparticles to the surface of MTB [25, 26]. A more secured loading mechanism is to attach it directly into the cell body, as shown in Figure 3-3 (C), in which the DNA functionalized goad nanoparticles (AuNPs) are loaded into the MTB through endocytosis [27]. The MTB loaded with AuNPs is directly engulfed through the phagocytic activity of the targeted cell, and the cargo is release by applying the magnetic hyperthermia to heat up the magnetosomes and dissociate the entire bacteria body. In [28], a single drug-loaded polyelectrolyte multilayer microparticle is attached to the surface of the *Escherichia coli* bacterium with embedded magnetic nanoparticles, as shown in Figure 3-3 (B). A large amount of cargo can be loaded by this method, however, the cargo will greatly decrease the swimming speed of the MTB microrobot, and the size of the microrobot is too large to be carried within capillaries. In addition, the fluid resist will be greatly changed with a large cargo, which in turn disturbs the motion control of the MTB microrobot. The last strategy is to push a large cargo moving forward with a swarm of BTM. For instance, Figure 3-3(D) illustrates a swarm of MTB microrobots that are controlled to assemble a pyramid with several PDMS micro-bricks [8] [29]. To apply this method, the BTM microrobots need to be first gathered at one point in the solution, which has been discussed in the previous section.

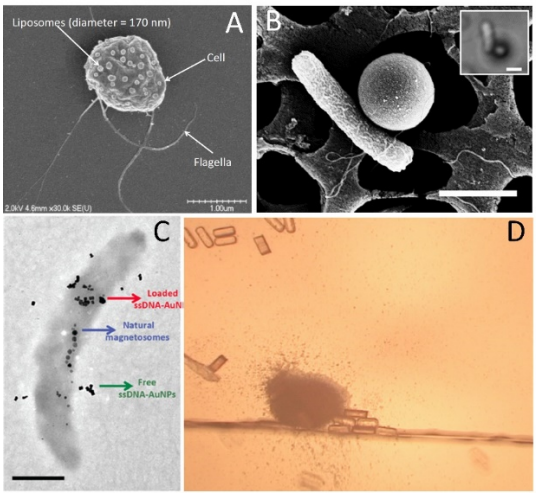


Figure 3-3 Loading strategies of the BTM microrobot. A. Several small nanoparticles attached to membrane of a bacteria (from [30]). B. One microparticle is attached to the membrane of a bacteria (from [28]). C. ssDNA-Au nanoparticles loaded into the bacteria (from [27]). D. A swarm of bacteria assembling a millimeter sized particle (from [8]).

### 3.4 Sperm-based micro-bio-robot

Sperm is the male haploid reproductive cell with a limited life span. The whole-life objective of a sperm is to reach the ovum and deliver two intracellular organelles, the male nucleus and the centrioles, into the ovum. For this delivery task, they have developed powerful locomotion mechanism, and developed most efficient movement strategy in low Reynolds number viscous fluids [1].

The anatomy structure of a sperm consists of head, neck, midpiece and tail, from the tip to the end sequentially. The sperm head is coated with acrosomal in the anterior part, the enzymes used to penetrate the ovum. The midpiece consists a filamentous core with mitochondria around it. For a healthy sperm, the sperm midpiece continuously transfer the stored nutrients into ATP to power the lashing movement of the tail, and finally propel the sperm cell.

#### 3.4.1 Sperm-driven microtube swimmer

Most mammal sperms have the length of 50-100 μm and the thickness of 5-10 μm, which provides the perfect micro-motor for the movement propulsion in low Reynolds number fluidic environment. Several attempts are designed to harness the movement pattern of the sperms as artificial microrobot [31]. For instance, magnetic nanoparticles have been applied to sperms for drug

delivery [32]. Since the nanoparticles can penetrate the membrane of cells and intracellular organelles and disrupt the functionalities of the organism, this method was further proofed to be toxic. A laser-printed microstructure coated with a nanometric layer of iron is used to trap the sperm to delivery the drug in the predesigned destination [33]. The cargo will be released when the microrobot pushes against the tissue surface and bend the drug holding arms. The idea of integrating mechanical microrobots for microsurgery in human body is still in concept, as the system biocompatibility and the powering durability will continue to be huge challenge based on current techniques.

Among these attempts, the most significant system proposed in literature is the controlled micro-swimmer designed by O. G. Schmidt et al. [9, 34, 35], as shown in Figure 3-4. The sperm has powerful swimming performance and it interacts with rolled-up magnetic microtubes by mechanically trapping within the tube cavity to push it forward. This hybrid sperm-machine structure is designed as a controlled sperm microtube swimmer. Once the sperm is successfully trapped, an X-Y tow dimension external magnetic coil is used to regulate the magnetic field at the sperm solution, and control the steer direction of the microrobot [35]. The sperm microtube swimmer is reported to display controlled movement with the speed of 25±10 μm /s towards a reference position.

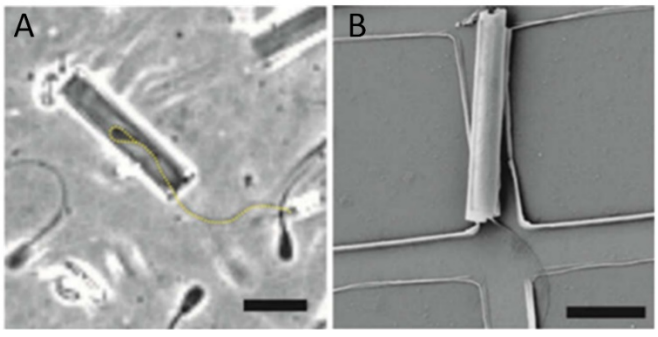


Figure 3-4 Sperm-driven microtube swimmer. (A) microscope image of a bovine sperm trapped within a 50 μm length Ti/Fe microtube. (B) SEM image of a sperm-driven microtube swimmer. Scale bars 20 μm. (from [35])

**a) Fabrication of the microtubes swimmer**

Since the microtube swimmer consists by trapping a bovine sperm within the cavity of a microtube, the critical procedure to build up the swimmer is to fabricate the polarized metal microtube that can be steered by external magnetic field. The bovine sperm's head usually has the length of 10 μm, diameter of 5 μm and thickness of 1 μm. To firmly trap the sperm head within the microtube cavity without limiting the movement of the sperm tail, the microtube with the diameter of 5-8 μm and width of 50 μm is designed, as shown by the fabrication process of Figure 3-5.

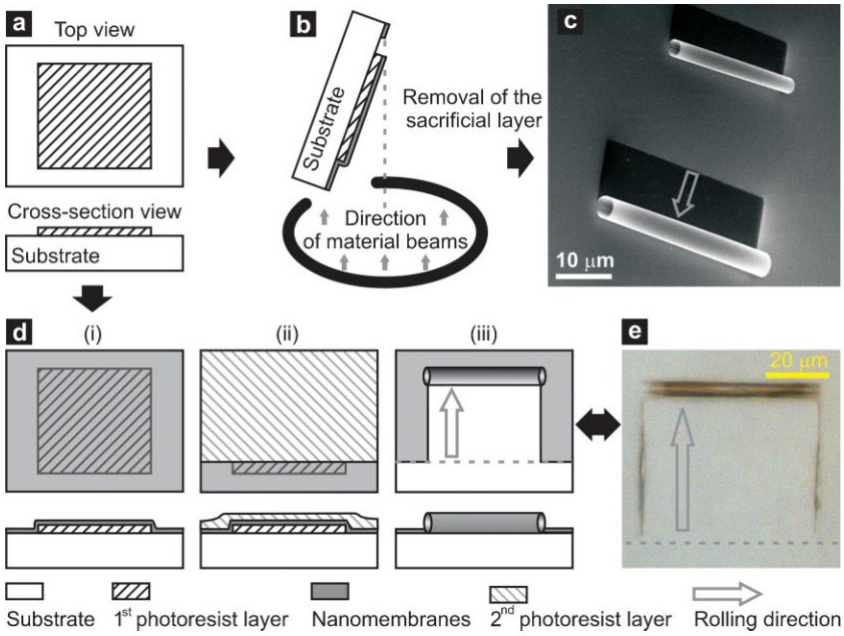


Figure 3-5 Process for rolled-up nanomembrane. (from [36]) a. Patterned photoresist layer on the substrate. b. Tilted position for the metal coating. c. Rolled- up the Ti/Au nanomembrane. d. Flow control for dolling up deposited films with high conformity. e. $Al_2O_3$ nanomembrane fabricated by procedure.

The microtubes are made through cleanroom microfabrication. A stressed metal nanomembrane is deposited onto a polymer sacrificial layer pre-patterned on a substrate. The stress is implemented by the difference in deposition rate and deposition temperature between the top and bottom layers. Once gradually remove the sacrificial layer from the exposed side to the covered side with a solvent, the nanomembrane will roll up to a microtube because of the unbalanced stress between the exposed surface and the inner surface. The length and rotation numbers are determined by the initial size and shape of the patterned sacrificial layer. The diameter of the microtube can be tuned by regulating the built-in strain and the thickness of the deposited nanomembrane. The

performance of various materials and material combinations for the microtube fabrication are detailly calibrated in [36]. As shown in Figure 3-5, to accurately integrate microtubes on a single chip, two completely different deposition techniques have been proposed. For the materials that is suitable to be deposited by e-beam, thermal evaporation or sputtering deposition, a narrow deposition gap will form at the far end of the patterned sacrificial layer with glancing angle deposition, as shown in Figure 3-5b. This gap allows the enter of the solvent to etch the sacrificial layer and roll up the nanomembrane. For the material is deposited onto the substrate with chemical vapor deposition or atomic layer deposition, the gap disappears due to the perfect deposition conformity. In these cases, the standard lithography techniques are adopted instead. As shown in Figure 3-5d, a second sacrificial layer is deposited on the surface after deposition of the nanomembrane to open a window at one side of the membrane. Then, the exposed nanomembrane can be selectively removed to expose the bottom sacrificial layer for etching.

When the microtube has been fabricated they are emerged into the sperm solution, so that the sperm will have a chance to swim into the cavity and trapped inside the microtube to form the sperm microrobot. It is reported that 14 out of 21 microtubes are coupled by immersing the tube in the sperm solution with the density of $10^8$ cells/ml. An improved coupling rate can be achieved by depositing an additional bio-functional binding layer of Fn or hyaluronic acid on top of the nanomembrane to enhance the binding between the sperm and the microtube [34]. To separate the fabricated sperm microrobot with normal microtubes, a straight channel microfluidic device is designed in [9]. With external magnetic field applied along the direction of the microchannel, the coupled microtube robot will swim through the channel, living the uncoupled ones left behind.

**b) Motion control**

Similar to the structure of MTB discussed in the previous section, the polarized microtube functions as the magnetosome in the MTB cell body. Thus, the motion control of sperm microrobot is also achieved by regulating the direction of the external magnetic field. It is reported that 22mT magnetic field is strong enough to regulate the direction of the microtube, and it can be further reduced by increasing the thickness of the microtube [35]. With an image processing algorithm feeding back the XY position and the direction of the tube in real time to form a close control loop, a point-to-point motion position control of the sperm microtube robot is achieved in [35].

The difference between the MTB and sperm micro-swimmer is that the speed of the sperm micro-swimmer displays no response to the strength change of the magnetic field, while the magnetic strength is used as an active regulation method to control the MTB microrobot speed. To find out the effective means to regulate the speed of the sperm robot, several significant influence factors for the sperm speed are investigated.

**Penetration ratio** [9]: The confinement of the sperm within the microtube reduces the amplitude of the undulation of the sperm tail down to the tube diameter. The longer penetration of the sperm within the microtube cavity, the more confinement will induce to the sperm movement, which reduce the speed of the microrobot consequently. It is reported that the penetration ratio can be actively reduced by shrinking the inner diameter of the microtube.

**Temperature** [9]: Temperature increase induces higher metabolism of the sperm cell and improve the speed of the microrobot. When the temperature of the media increases from 5 C to 40 C, the robot swimming speed will increase from 10 μm/s to 90 μm/s correspondingly. Thus, temperature is adopted as a stop/move mechanism for the speed regulation of the sperm microrobot.

**Length of the microtube** [34]: Short tube results in small system mass and fluid resists, and therefore improves the speed of the sperm microrobot. When the tube length is reduced from 50 μm to 30 μm, the average speed is reported to increase from 33.3 μm/s to 10.4 μm/s.

**Chemical** [34]: Caffeine increases the calcium level in the sperm by opening calcium channels in the membrane of the sperm tail which hyperacute the cell. Adding caffeine into the solution will significantly improve the speed of the microrobot.

**c) Sperm microtube swimmer for artificial fertilization**

The most important application for the sperm microrobot is artificial fertilization. The point-to-point position control of the sperm microtube robot can easily guide the sperm to the vicinity of the egg cell, however, special techniques are required to release the sperm and complete the fertilization. A Fe-Ti-PNIPAM 3-layer material is developed in [10] to fabricate the microtube for the development of the sperm robot. This metal layer will response to the external magnetic field and the polymer layer will unfold the coiling of the nanomembrane and release the sperm if the temperature increases to 33-35 C.

### 3.4.2 Magnetic helix swimmer for the delivery of sperms.

Besides the sperm microrobot developed based on the coupling with microtube, another type of the sperm-based microrobot is the helix swimmer coupler [37, 38]. The magnetic microhelices is a simplified artificial mimic for the natural undulation movement of a flagella or cilia of living microorganisms, which can rotate along its central axis and move forward under a rotating magnetic field. The microhelices are fabricated by direct laser writing and coated with a Ni-Ti soft-magnetic bilayer to make it responsible to magnetic field. The detailed fabrication procedure of the microhelices are developed by B. Nelson et al.[39]. The image-based position feedback and movement control of the microhelices are investigated in [40, 41].

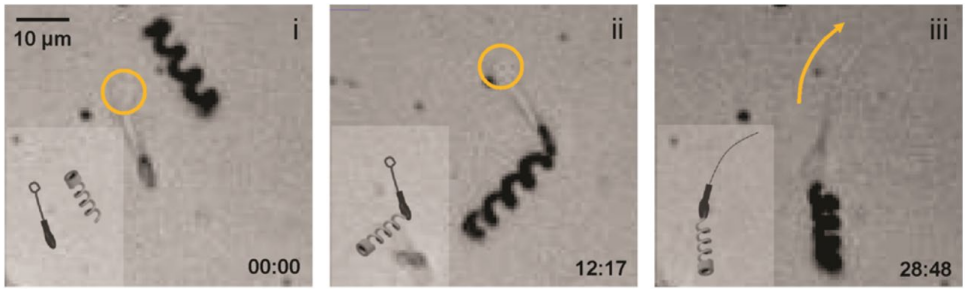


Figure 3-6 Coupling of the sperm cell with a magnetic helix (from [37])

Unlike the sperm micro-swimmer which harnesses the sperm motion to propel a microtube, the microhelices provides active movement powered by rotating magnetic field. With this capability, the microhelices can transfer both immotile and healthy sperm. It is demonstrated that the acrosome integrity is essential to achieve successful fertilization, and immotile sperms are not necessarily infertile. A discrimination method between the immotile sperm and defective sperm is proposed in [37]. The coupling procedure of the microhelices and the sperm is shown in Figure 3-6.

## 3.5 Beetle insect-machine hybrid robot

During the past two decades, the field of micro and nano air vehicles are attracting intensive research attentions [42]. However, because of the huge obstacles existing in the flight control, energy storage and structure design of the vehicles, significant trade-offs have to be made between payload mass, flight range, and navigating speed based on current techniques. An alternative idea is to develop the insect-machine hybrid robot by artificially regulating the movement of insects [11, 43-55]. The beetles have powerful locomotion organs of flapping wings and legs that are well

developed through millions of years of evolution. In addition, their flight control and sensing systems of neurons perfectly accommodate to the aerodynamics nonlinearities in this size scale. As a micro or nano fly/crawl creature, the beetles are far more delicate than any of the artificial microrobot humans have ever developed. Therefore, attempts have been made to transfer the beetles into controllable micro flapping wings platform.

To control the fly/crawl locomotion behavior of the beetles, microsurgery is performed to insert electrical probe into the brain or muscles of the insects, and deliver artificial signals for muscular contraction control. High ethical standards need to be taken special care of during the treatment of the insects so as to minimally disturb its viability [56]. Besides the insect platform, the untethered insect-machine usually includes a radio transceiver module, a microcontroller, the neural stimulators, the muscle stimulators, and a micro battery integrated in the body. The host computer sends control signals through the radio module and commands the onboard microcontroller to generate electrical pulses on the probes that regulates the locomotion of the beetle. In this section, the two kinds of insect-machine hybrid robot will be discussed.

### 3.5.1 Flying insect-machine hybrid robot

In the natural state, the flying conditions of the beetles are controlled via the modulation of the wing movements with flight muscles. Two major kinds of flight muscle control mechanism exist in beetles [45], depending on the response to artificial stimulations. For some insects, such as the dragonflies and locusts, the oscillation of the flight muscles synchronous to the stimulus episodes of neurons. Other insect species, like the dipera and coleoptera, have asynchronous flight muscle contraction under indirect control of the fire or inhibition of neurons. Instead, the motor neurons fire at much lower frequency than the wing oscillation rates in these species. The neuronal output serves to control the on and off of the muscle oscillation and tune the power. The species with asynchronous muscle regulation are easier to be artificially controlled, since it avoids the direct and continuous triggering of wing muscles in each contraction phase. The insects that have been developed as hybrid robot include *Cotinis texana* [44, 45, 50], *Mecynorrhina torquata* [43, 47, 49, 52], and *Periplaneta Americana* [53]. A typical flying insect-machine hybrid robot build on *Mecynorrhina torquata* is shown in Figure 3-7.

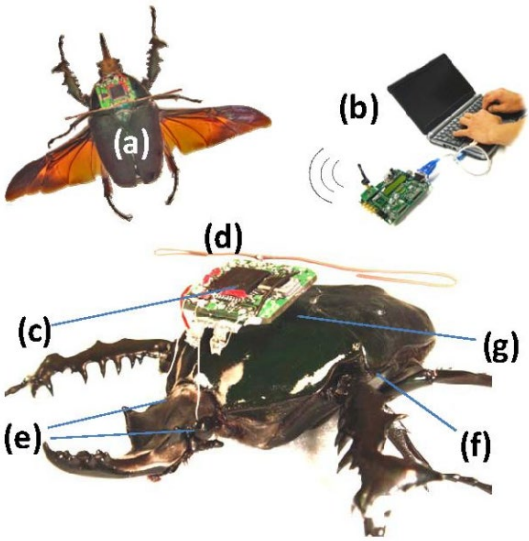


Figure 3-7 Image of a remote controlled flying insect-machine robot. (from [49]) (a) The live beetle platform of Mecynorrhina torquata. (b) The wireless module controlled by a host computer. (c) Radio receiver assembly. (d) Half-wave dipole antenna. (e) stimulating electrode terminals at optic lobes. (f) Basalar flight muscle (left). (g) Micro-battery.

**a) Microsurgery for the development of the flying insect-machine hybrid robot**

Different microsurgeries are required for different beetle species to control its flight. We will take the insect platform of *Mecynorrhina torquata* for instance in this section. The insect platform of *Mecynorrhina torquata* is a beetle with the body length of 6 cm and the weight of 8 g. It is able to flying with the load of 20%-30% of its body weight [45]. Since the flight control of the insect will be directly regulated by electric stimulation of the brain and muscle, microsurgery of the insect is needed to implant the electric probes into the corresponding positions. The Teflon-coated silver wire electrodes were burned to expose the bare silver core at both terminals. Two electrodes are implanted into the flight muscles at both sides with the insertion depth of about 3 mm, as shown in Figure 3-7(f). Another two electrodes are implanted into the left and right optic lobes. The brain and posterior pronotum are also implanted with electric probe. All the other terminals of the silver probe are connected to the outputs of the microcontroller carried on the back of the insect platform, as shown in Figure 3-7(c).

**b) Control of the flying insect-machine hybrid robot**

The flight control of the insect-machine robot is achieved by stimulating the neurons and muscles by the implanted electric probes. The stimulation strategies vary for different insect species. Generally, the flight initiation and cessation are controlled by stimulating the brain, and the flight turning is regulated by stimulating the flight muscles on the left and right side.

**Flight initiation, cessation**: For *Cotinis texana*, stimulation of alternative positive and negative potential pulses between the electrode implanted into the brain and the posterior pronotum generate flight initiation and cessation. Each individual insect has a voltage threshold of the pulses for the flight initiation. The average is 3.2 V for *Cotinis texana* [45].

For *Mecynorhina torquata,* a electric pulse between the electrodes implanted at the left and right optic lobes induce flight initiation and cessation in unthethered free-fly beetle without degrading its ability of steering [49]. Once the flight is initiated, it will persist without additional stimulation until a single pulse between the optic lobes stops it.

**Elevation control:** For both *Cotinis texana* and *Mecynorhina torquata*, the stimulation of the brain at 100 Hz leads to the depression of flight. The insect will repeatedly lower the flight attack angle to horizon and drop the flying altitude [50] under stimulation.

**Turning control**: For all types of beetles, the turning of the hybrid robot is elicited by the stimulus of the left and right flight muscles with positive potential pulse trains with respect to the posterior pronotum. The beetle will turn in the direction opposite to the stimulated side. For *Cotinis texana*, the flight muscles oscillate at the frequency of 76 Hz under the stimulation of motor neuron pulses of 8 Hz. The turning is triggered by 100 Hz probe pulses at one side of the flight muscle with the amplitude of 2 V [50]. The pulses amplitude is 1.3 V for *Mecynorhina torquata*.

**Speed control**: Instead of stimulating the flight muscle directly to induce the turnings, the stimulus of the muscle group beside the flight muscle (subalar muscle) lead to the decrease of flight speed. It is reported in [47] that 3V, 50-70 Hz pulse stimulation on the subalar muscle decelerates the speed by 0.5 m/s. The speed degrade varies with respect to the stimulation time and frequency.

Besides the stimulating mechanism by electric probes, a less invasive strategy is proposed in [44] where the turning control is achieved by an array of onboard LED lights, since the beetle consistently tracks the stripe motions ahead. For most cases, the flight control of the insect-machine hybrid robot exists as open loo, and the parameters are calibrated offline to achieve the

desired performance. The performance measurement is conducted by a camera [50] measuring the position of the robot, or an onboard MEMS accelerometer measuring the attack angle and acceleration [47].

### 3.5.2 Crawling insect-machine hybrid robot

Instead of controlling flight of insects, another type of the insect-machine hybrid robot is the crawling insect robot. The platform for the development of these robot is *Gromphadorhina protentosa* [48, 51, 55] *Zophobas morio* [46], since they have relative large body to carry loads and long lifespan of 3 months. A typical sample of the crawling insect-machine hybrid robot build on *Gromphadorhina protentosa* is shown in Figure 3-8. The structure of this type of hybrid robot is the same to the flying robot discussed in the precious section. However, unlike the open loop control of flight, the 2D locomotion of the crawling hybrid robot can be controlled in closed loop with much higher accuracy.

Figure 3-8 The photograph of a crawling insect-machine hybrid robot. (from [48])

**a) Microsurgery for the development of the crawling insect-machine hybrid robot**

Before the surgery, the insect is anesthetized under 4 C cold-treatment for 45-60 minutes to minimize the injury. High ethical standard should be taken care of during the treatment of the insect [56]. The flagellums of both antennae are removed to the insertion of the electrodes. The Teflon coated stainless steel with the diameter of 200 μm is used as the electrode probe for implantation. The third electrode (ground) is implanted into the ganglia by inserting it into the first segment of the thorax via an incised hole [48]. The insertion areas are sealed by synthetic glue. After the implantation of the electrodes, the insect is left to recuperate for the experiments.

**b) Locomotion control of the robot**

Pulse stimulus on the electrodes of one or both the antennae generates an illusion of obstacles ahead the insect on the stimulated side, and hence trigger the escape mechanism to make the insect turn. For *Zophobas morio*, the stimulation of 2 V, 20-50 Hz induces the turning of the insect with the success rate of 85% [46]. Continuous backward locomotion is induced by stimulating the two antennae electrodes alternatively. The turning curvature on the locomotion trajectory is calibrated in detail with respect to the pulse type, shapes, amplitude, and frequency. Since the crawling motion has much less influence factors than the flight, the locomotion of the hybrid robot can be regulated in close loop with the position feedback of a camera [48]. A smaller control loop was built to control the movement of a single beetle leg with the motion feedback of VICON system [43].

### 3.6 Advantages and limitations of bio-agent robots

The biological organisms have developed the motion systems that are more elaborate than any artificial robot from nanoscale to macroscale through billion years of evolution. From the above review of the MTB micro robot, sperm robot, and the insect-machine hybrid robot, it is not difficult to find that the bio-agent robot is a great enlightenment to explore the motion patterns in micro-scale. They perfectly overcome the current technical obstructs of the untether power supply, motion control, structure design, system integration and assembly in the development of artificial small scale robot. However, we need to clarify that some limitations of the bio-agent robot cannot be ignored.

**a) No universal methods can be developed to harness the motion of all biological organisms.**

The locomotion regulation methods come in neuronal level (flight initiation of the insect hybrid robot), muscular level (turning of the insect hybrid robot), and motion level (MTB nanorobot and sperm microrobot). All these strategies are developed greatly depend on the biological understanding of the organism motion basis, and they also vary greatly for different species. Thus, unlike the well-developed universal methods of modelling and control for the rigid body robot, the motion of biological organisms cannot be harnessed by any common methods based on current technologies.

**b) Controllability of the robotic system is limited.**

The biological individuals usually contain strong nonlinearity and uncertainty. Although some basic principles for the movement are uncovered by biological studies, development of control models of the system is challenging as the biological organism usually displays significant peer-to-peer variance. In addition, the feedback of the motion usually depends on a camera, which limits the applications in practical circumstances. Thus, most of the motion control of bio-agent robots still appear as open loop.

## 3.7 Conclusions

The bio-agent robot is a new type of hybrid biology-machine robot that harness the motion of biological organisms as the robotic movement actuator. It helps overcome the technical obstacles we are facing for the development of artificial robotics in the small size scale. In this paper, we reviewed the three types of bio-agent robot up to now, including MTB nanorobot, the sperm-based microrobot and the insect-machine hybrid robot. The working principle, supporting techniques and the applications for each type of the robot are discussed.

## 3.8 Reference


[1] J. J. Abbott, Z. Nagy, F. Beyeler, and B. J. Nelson, "Robotics in the small, part I: microbotics," *IEEE Robotics & Automation Magazine,* vol. 14, no. 2, pp. 92-103, 2007.

[2] !!! INVALID CITATION !!! [2-4].

[3] L. Zhang, J. J. Abbott, L. Dong, B. E. Kratochvil, D. Bell, and B. J. Nelson, "Artificial bacterial flagella: Fabrication and magnetic control," *Applied Physics Letters,* vol. 94, no. 6, p. 064107, 2009.

[4] L. Zhang *et al.*, "Characterizing the swimming properties of artificial bacterial flagella," *Nano letters,* vol. 9, no. 10, pp. 3663-3667, 2009.

[5] V. Magdanz, G. Stoychev, L. Ionov, S. Sanchez, and O. Schmidt, "Stimuli-Responsive Microjets with Reconfigurable Shape," *Angewandte Chemie International Edition,* vol. 53, no. 10, pp. 2673-2677, 2014.

[6] V. M. Fomin, M. Hippler, V. Magdanz, L. Soler, S. Sanchez, and O. G. Schmidt, "Propulsion mechanism of catalytic microjet engines," *IEEE Transactions on Robotics,* vol. 30, no. 1, pp. 40-48, 2014.

[7] O. Felfoul *et al.*, "Magneto-aerotactic bacteria deliver drug-containing nanoliposomes to tumour hypoxic regions," *Nature nanotechnology,* vol. 11, no. 11, pp. 941-947, 2016.

[8] S. Martel and M. Mohammadi, "Using a swarm of self-propelled natural microrobots in the form of flagellated bacteria to perform complex micro-assembly tasks," in *Robotics and Automation (ICRA), 2010 IEEE International Conference on*, 2010, pp. 500-505: IEEE.

[9] V. Magdanz, S. Sanchez, and O. G. Schmidt, "Development of a Sperm-Flagella Driven Micro-Bio-Robot," *Advanced Materials,* vol. 25, no. 45, pp. 6581-6588, 2013.

[10] V. Magdanz, M. Guix, F. Hebenstreit, and O. G. Schmidt, "Dynamic polymeric microtubes for the remote-controlled capture, guidance, and release of sperm cells," *Advanced materials,* vol. 28, no. 21, pp. 4084-4089, 2016.

[11] H. Sato *et al.*, "Deciphering the role of a coleopteran steering muscle via free flight stimulation," *Current Biology,* vol. 25, no. 6, pp. 798-803, 2015.
[12] S. Martel, M. Mohammadi, O. Felfoul, Z. Lu, and P. Pouponneau, "Flagellated magnetotactic bacteria as controlled MRI-trackable propulsion and steering systems for medical nanorobots operating in the human microvasculature," *The International journal of robotics research,* vol. 28, no. 4, pp. 571-582, 2009.
[13] L. Yan, S. Zhang, P. Chen, H. Liu, H. Yin, and H. Li, "Magnetotactic bacteria, magnetosomes and their application," *Microbiological research,* vol. 167, no. 9, pp. 507-519, 2012.
[14] S. Dasdag and H. Bektas, "Magnetotactic bacteria and their application in medicine," *J. Phys. Chem. Biophys,* vol. 2, no. 4, pp. 2161-0398.1000141, 2014.
[15] S. Martel, "Magnetotactic bacteria for microrobotics," *Microbiorobotics: biologically inspired microscale robotic systems. Elsevier, Oxford,* pp. 201-210, 2012.
[16] A. S. Mathuriya, "Magnetotactic bacteria: nanodrivers of the future," *Critical reviews in biotechnology,* vol. 36, no. 5, pp. 788-802, 2016.
[17] Z. Hosseinidoust, B. Mostaghaci, O. Yasa, B.-W. Park, A. V. Singh, and M. Sitti, "Bioengineered and biohybrid bacteria-based systems for drug delivery," *Advanced drug delivery reviews,* vol. 106, pp. 27-44, 2016.
[18] J. Zhuang and M. Sitti, "Chemotaxis of bio-hybrid multiple bacteria-driven microswimmers," *Scientific reports,* vol. 6, 2016.
[19] B. Behkam and M. Sitti, "Bacterial flagella-based propulsion and on/off motion control of microscale objects," *Applied Physics Letters,* vol. 90, no. 2, p. 023902, 2007.
[20] Y. Ou, P. Kang, M. J. Kim, and A. A. Julius, "Algorithms for simultaneous motion control of multiple T. pyriformis cells: Model predictive control and Particle Swarm Optimization," in *Robotics and Automation (ICRA), 2015 IEEE International Conference on*, 2015, pp. 3507-3512: IEEE.
[21] D. De Lanauze, O. Felfoul, J.-P. Turcot, M. Mohammadi, and S. Martel, "Three-dimensional remote aggregation and steering of magnetotactic bacteria microrobots for drug delivery applications," *The International Journal of Robotics Research,* vol. 33, no. 3, pp. 359-374, 2014.
[22] D. Loghin, C. Tremblay, M. Mohammadi, and S. Martel, "Exploiting the responses of magnetotactic bacteria robotic agents to enhance displacement control and swarm formation for drug delivery platforms," *The International Journal of Robotics Research,* vol. 36, no. 11, pp. 1195-1210, 2017.
[23] Y. Chen, P. Kosmas, and S. Martel, "A feasibility study for microwave breast cancer detection using contrast-agent-loaded bacterial microbots," *International Journal of Antennas and Propagation,* vol. 2013, 2013.
[24] S. Taherkhani, M. Mohammadi, J. Daoud, S. Martel, and M. Tabrizian, "Covalent binding of nanoliposomes to the surface of magnetotactic bacteria for the synthesis of self-propelled therapeutic agents," *ACS nano,* vol. 8, no. 5, pp. 5049-5060, 2014.
[25] Z. Ni, A. Bolopion, J. Agnus, R. Benosman, and S. Régnier, "Asynchronous event-based visual shape tracking for stable haptic feedback in microrobotics," *Robotics, IEEE Transactions on,* vol. 28, no. 5, pp. 1081-1089, 2012.
[26] C. Chen, L. Chen, P. Wang, L.-F. Wu, and T. Song, "Magnetically-induced elimination of Staphylococcus aureus by magnetotactic bacteria under a swing magnetic field," *Nanomedicine: Nanotechnology, Biology and Medicine,* vol. 13, no. 2, pp. 363-370, 2017.

[27] S. K. Alsaiari, A. H. Ezzedine, A. M. Abdallah, R. Sougrat, and N. M. Khashab, "Magnetotactic bacterial cages as safe and smart gene delivery vehicles," *OpenNano,* vol. 1, pp. 36-45, 2016.
[28] B.-W. Park, J. Zhuang, O. Yasa, and M. Sitti, "Multifunctional bacteria-driven microswimmers for targeted active drug delivery," *ACS nano,* vol. 11, no. 9, pp. 8910-8923, 2017.
[29] A. V. Singh and M. Sitti, "Patterned and Specific Attachment of Bacteria on Biohybrid Bacteria-Driven Microswimmers," *Advanced healthcare materials,* vol. 5, no. 18, pp. 2325-2331, 2016.
[30] S. Martel, S. Taherkhani, M. Tabrizian, M. Mohammadi, D. de Lanauze, and O. Felfoul, "Computer 3D controlled bacterial transports and aggregations of microbial adhered nano-components," *Journal of Micro-Bio Robotics,* vol. 9, no. 1-2, pp. 23-28, 2014.
[31] V. Magdanz, M. Medina-Sánchez, L. Schwarz, H. Xu, J. Elgeti, and O. G. Schmidt, "Spermatozoa as Functional Components of Robotic Microswimmers," *Advanced Materials,* 2017.
[32] Y. Pan, X. Du, F. Zhao, and B. Xu, "Magnetic nanoparticles for the manipulation of proteins and cells," *Chemical Society Reviews,* vol. 41, no. 7, pp. 2912-2942, 2012.
[33] H. Xu, M. M. Sanchez, V. Magdanz, L. Schwarz, F. Hebenstreit, and O. G. Schmidt, "Sperm-hybrid micromotor for drug delivery in the female reproductive tract," *arXiv preprint arXiv:1703.08510,* 2017.
[34] V. Magdanz, M. Medina-Sánchez, Y. Chen, M. Guix, and O. G. Schmidt, "How to improve spermbot performance," *Advanced Functional Materials,* vol. 25, no. 18, pp. 2763-2770, 2015.
[35] I. S. Khalil, V. Magdanz, S. Sanchez, O. G. Schmidt, and S. Misra, "Biocompatible, accurate, and fully autonomous: a sperm-driven micro-bio-robot," *Journal of Micro-Bio Robotics,* vol. 9, no. 3-4, pp. 79-86, 2014.
[36] Y. Mei *et al.*, "Versatile approach for integrative and functionalized tubes by strain engineering of nanomembranes on polymers," *Advanced Materials,* vol. 20, no. 21, pp. 4085-4090, 2008.
[37] M. Medina-Sánchez, L. Schwarz, A. K. Meyer, F. Hebenstreit, and O. G. Schmidt, "Cellular cargo delivery: Toward assisted fertilization by sperm-carrying micromotors," *Nano letters,* vol. 16, no. 1, pp. 555-561, 2015.
[38] M. Medina-Sánchez and O. G. Schmidt, "Medical microbots need better imaging and control," *Nature,* vol. 545, no. 7655, pp. 406-408, 2017.
[39] S. Tottori, L. Zhang, F. Qiu, K. K. Krawczyk, A. Franco-Obregón, and B. J. Nelson, "Magnetic helical micromachines: fabrication, controlled swimming, and cargo transport," *Advanced materials,* vol. 24, no. 6, pp. 811-816, 2012.
[40] P. Katsamba and E. Lauga, "Micro-tug-of-war: A selective control mechanism for magnetic swimmers," *Physical Review Applied,* vol. 5, no. 6, p. 064019, 2016.
[41] T. Y. Huang *et al.*, "3D printed microtransporters: Compound micromachines for spatiotemporally controlled delivery of therapeutic agents," *Advanced Materials,* vol. 27, no. 42, pp. 6644-6650, 2015.
[42] P. Chirarattananon, Y. Chen, E. F. Helbling, K. Y. Ma, R. Cheng, and R. J. Wood, "Dynamics and flight control of a flapping-wing robotic insect in the presence of wind gusts," *Interface focus,* vol. 7, no. 1, p. 20160080, 2017.

[43] F. Cao *et al.*, "A biological micro actuator: graded and closed-loop control of insect leg motion by electrical stimulation of muscles," *PloS one,* vol. 9, no. 8, p. e105389, 2014.
[44] H. Sato *et al.*, "A cyborg beetle: insect flight control through an implantable, tetherless microsystem," in *Micro Electro Mechanical Systems, 2008. MEMS 2008. IEEE 21st International Conference on*, 2008, pp. 164-167: IEEE.
[45] M. M. Maharbiz, "A cyborg beetle: wireless neural flight control of a free-flying insect," in *Proceedings of the 22nd Annual Symposium on Integrated Circuits and System Design: Chip on the Dunes*, 2009, p. 3: ACM.
[46] T. T. Vo Doan, M. Y. Tan, X. H. Bui, and H. Sato, "An Ultralightweight and Living Legged Robot," *Soft Robotics,* 2017.
[47] T. V. Doan, Y. Li, F. Cao, and H. Sato, "Cyborg beetle: Thrust control of free flying beetle via a miniature wireless neuromuscular stimulator," in *Micro Electro Mechanical Systems (MEMS), 2015 28th IEEE International Conference on*, 2015, pp. 1048-1050: IEEE.
[48] T. Latif and A. Bozkurt, "Line following terrestrial insect biobots," in *Engineering in Medicine and Biology Society (EMBC), 2012 Annual International Conference of the IEEE*, 2012, pp. 972-975: IEEE.
[49] H. Sato, Y. Peeri, E. Baghoomian, C. Berry, and M. Maharbiz, "Radio-controlled cyborg beetles: a radio-frequency system for insect neural flight control," in *Micro Electro Mechanical Systems, 2009. MEMS 2009. IEEE 22nd International Conference on*, 2009, pp. 216-219: IEEE.
[50] H. Sato *et al.*, "Cyborg beetles: The remote radio control of insect flight," in *Sensors, 2010 IEEE*, 2010, pp. 1-4: IEEE.
[51] J. C. Erickson, M. Herrera, M. Bustamante, A. Shingiro, and T. Bowen, "Effective stimulus parameters for directed locomotion in Madagascar hissing cockroach biobot," *PloS one,* vol. 10, no. 8, p. e0134348, 2015.
[52] T. Vo Doan and H. Sato, "Insect-machine Hybrid System: Remote Radio Control of a Freely Flying Beetle (Mercynorrhina torquata)," *J. Vis. Exp,* vol. 115, p. e54260, 2016.
[53] C. J. Sanchez, C.-W. Chiu, Y. Zhou, J. M. González, S. B. Vinson, and H. Liang, "Locomotion control of hybrid cockroach robots," *Journal of The Royal Society Interface,* vol. 12, no. 105, p. 20141363, 2015.
[54] H. Sato and M. M. Maharbiz, "Recent developments in the remote radio control of insect flight," *Frontiers in neuroscience,* vol. 4, p. 199, 2010.
[55] T. Latif, E. Whitmire, T. Novak, and A. Bozkurt, "Towards fenceless boundaries for solar powered insect biobots," in *Engineering in Medicine and Biology Society (EMBC), 2014 36th Annual International Conference of the IEEE*, 2014, pp. 1670-1673: IEEE.
[56] C. Eisemann *et al.*, "Do insects feel pain?—A biological view," *Experientia,* vol. 40, no. 2, pp. 164-167, 1984.

# Link between chapter 3 and chapter 4

In the previous two chapters, the current development in the field of robotic micromanipulation of bio-samples is reviewed, including the microinjection of cells and *C. elegans*, robotic transfer of cells and small organisms, and the robotic mechanical characterization of cells. The basic concept, fundamental techniques and recent development of bio-agent microrobot, such as the magnetotactic bacteria microrobot, sperm-based micro-swimmer, and the insect-machine hybrid microrobot, are also reviewed. The introduce of robotic micromanipulation techniques, such as the image processing, force measurement and control, microfluidics devices, etc., has brought unprecedented throughput, accuracy and success rate for the manipulation of bio-samples.

Despite these significant advances, the automated micromanipulation of *C. elegans* (automated *C. elegans* screening and automated *C. elegans* microinjection) remains difficult due to its intrinsic problem that the *C. elegans* individuals are always moving either cultured on agar substrate or maintained in M9 solutions. The previous works on the sorting of *C. elegans* are usually proposed based on passive microfluidic mechanisms and lack the capability of accurately measuring the morphologic features of individual worms. The next chapter therefore address the problem of automatic morphologic features measurement for free-moving *C. elegans*. Based on the measurement results, the large number statistics that employ the worm morphologic features as direct readout, and the size-based *C. elegans* screening can be automated by machines.

# Chapter 4

# An automated microfluidic system for morphological measurement and size-based sorting of *C. elegans*

# Chapter 4: An automated microfluidic system for morphological measurement and size-based sorting of *C. elegans*

**X. Dong[1,2], P. Song[1], X. Liu[2]***

*[1]Department of Mechanical Engineering, McGill University, 817 Sherbrooke Street West, Montreal, Quebec, Canada H3A 2K6*

*[2]Department of Mechanical and Industrial Engineering, University of Toronto, 5 King's College Road, Toronto, Ontario, Canada M5S 3G8*

*corresponding author: (xyliu@mie.utoronto.ca)

in *IEEE Transactions on NanoBioScience,* in press.

## 4.1 Abstract

This paper reports a vision-based automated microfluidic system for morphological measurement and size-based sorting of the nematode worm *C. elegans*. Exceeding the capabilities of conventional worm sorting microfluidic devices purely relying on passive sorting mechanisms, our system is capable of accurate measurement of the worm length and width and active sorting of worms with the desired sizes from a mixture of worms with different body sizes. This function is realized based on the combination of real-time, vision-based worm detection and sizing algorithms and automated on-chip worm manipulation. A double-layer microfluidic device with computer-controlled pneumatic valves is developed for sequential loading, trapping, vision-based sizing, and sorting of single worms. To keep the system operation robust, vision-based algorithms on detecting multi-worm loading and worm sizing failure have also been developed. We conducted sorting experiments on 319 worms and achieved an average sorting speed of 10.3 worms per minute (5.8 s/worm) with an operation success rate of 90.3%. This system will facilitate the worm biology studies where body size measurement and size-based sorting of many worms are needed.

## 4.2 Introduction

The nematode worm *C. elegans* (or simply the worm) is a tiny model organism widely used in many areas of biology, including ageing, development, neuroscience, and behavior [1-4]. A *C. elegans* has four distinct larval stages and one adult stage, which are experimentally characterized by its body size. The body size of *C. elegans*, usually measured in its length, is a basic

physiological parameter, and its regulation mechanisms have been extensively studied in terms of genetic variations, signaling pathways, feedingconditions, among others [5-11]

In many experiments, the worm body size is typically used as a straightforward physiological marker to identify size-related phenotypes, which can then be analyzed for the potential biophysical and biochemical mechanisms regulating the worm body size. Conventionally, the body size measurement of *C. elegans* is performed either by an operator via visual inspection under an optical microscope or through off-line measurement using commercial image processing software (e.g., ImageJ and Wormlab), which is time-consuming and labor-intensive. These methods are especially inconvenient to use if a large number of *C. elegans* worms need to be sorted based on their size differences for further studies.

Recently, microfluidic devices have emerged as useful tools for *C. elegans* research, and have advanced various kinds of worm biology studies [12-30]. Many microfluidic devices have been reported for facilitating sorting of the *C. elegans* worms at different larval stages from their mixtures based on age-dependent properties (e.g., length, locomotion, and electrotaxis behavior) of *C. elegans* [15-19, 28-30]. Among these devices, several designs integrated novel microfluidic architectures, such as `smart maze' [17] engineered pillar arrays [18], and size adjustable microfluidic channels [30] for passive size-based sorting of *C. elegans* worms at different developmental stages. These passive worm sorting methods demonstrate high-throughput sorting capabilities; however, they are all based on pure microfluidic passive sorting mechanisms and cannot accurately measure the body sizes of individual worms. Therefore, they are unsuitable for use in experiments that directly employ worm size regulation as phenotypic trait and require size quantification and size-based sorting of many worms [31, 32].

For instance, the worm length naturally varies within a range of $\sim 10 \mu m$ during swimming in its culture medium. The existing microfluidic devices, although capable of conducting size-based worm sorting based on certain passive fluidic mechanisms, can never detect such size variance with an accuracy of $< 10\ \mu m$. A commercial worm sorting instrument so called the BioSorter (Union Biometrica) is also available and are capable of sorting *C. elegans* based on the worm body size measured through fluorescence imaging, but it is fairly expensive and thus not easily accessible to every worm biology laboratories. In addition, its algorithms for measuring the worm body morphology cannot be customized for specific experimental needs. Therefore, affordable and

customizable platforms for automated body size measurement and size-based sorting of *C. elegans* are still highly demanded.

This paper reports an automated microfluidic system, which combines automated microfluidic control and computer vision techniques, for high-accuracy body size measurement and size-based sorting of *C. elegans* worms. A microfluidic device with computer-controlled, on-chip pneumatic valves is developed to sequentially load single worms into a worm observation chamber, and a host computer, which integrates customized image-processing algorithms and a multi-channel pressure control unit, is used to accurately measure the length and width of the worm body and coordinate the pneumatic-valve operations accordingly for automated size-based worm sorting. The system's accuracy of worm size measurement is comparable to that of commercial worm analysis software (WormLab). Proof-of-concept experiments are performed to sort young adult worms (900-1000 $\mu m$ length) from a swarm of L4, young adult, and adult worms, demonstrating an average sorting speed of 10.4 worms per minute (5.8 s per worm) with a success rate of 90.3%. We also conduct typical viability tests on the sorted worms and confirm that the device does not impose adverse effects on their physiological conditions. This microfluidic system hold great potential to significantly facilitate *C. elegans* studies that use worm body size parameters as experimental readouts and need high-speed size-based worm sorting.

## 4.3 System setup and operation

### 4.3.1 System setup

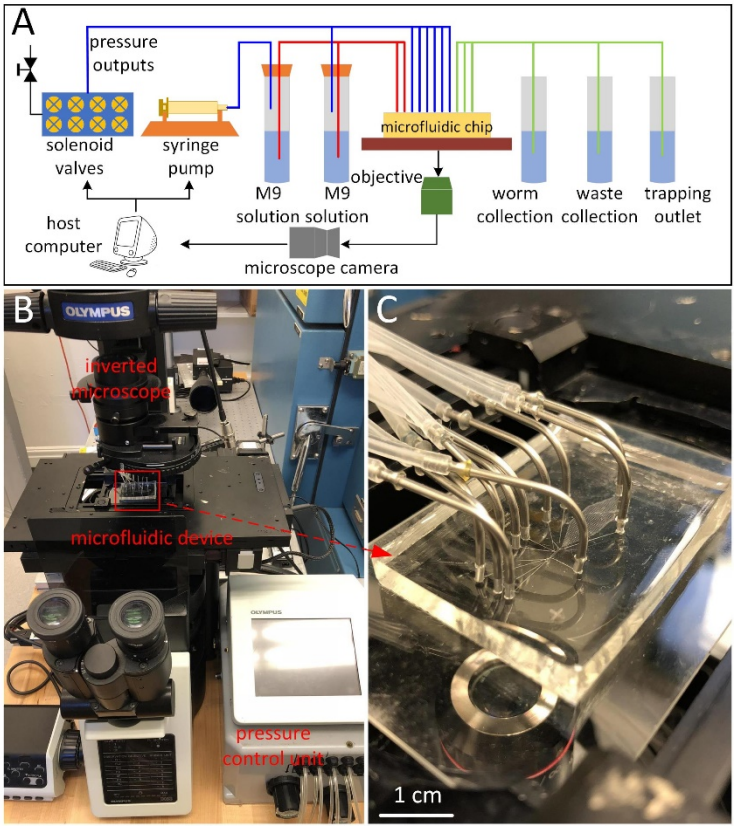


Figure 4-1 Experimental setup of the worm sorting system. (A) Schematic system setup. (B)(C) Photographs of (B) the system and (C) the microfluidic device.

The worm sorting system, as shown in Figure 4-1 was established based on an inverted microscope (IX83, Olympus) with a 4x objective, and a CMOS camera (acA2000-340km, Basler; 2040x1080 pixels) was used for real-time imaging (50 fps) of single worms inside the worm observation chamber of the microfluidic device. To control the pneumatic valves through regulated pressures, we developed a 16-channel pressure control unit. The pressure unit consists of a microcontroller (mega2560, Arduino), three manually-adjustable pressure regulators (ARG20-N01G1-Z, SMC Pneumatics), 16 solenoid valves (S10MM-30-24-2/A, Pneumadyne Inc.), and a circuit board with 16 transistors (2N3094) to turn on/off the valves. The camera and the pressure unit were controlled by a host computer (3.1GHz CPU, 16G RAM). Customized computer vision and hardware control algorithms were implemented using C++ in Microsoft Visual Studio 2016, and the computer vision algorithms were composed using OpenCV functions (version 3.4). This system can be readily

established based on an optical microscope existing in any worm biology laboratory with three additional items added (i.e., the microfluidic device, the pressure control unit, and the syringe pump). Thus, our method provides a more cost-effective solution for size-based worm sorting than the commercial BioSorter.

### 4.3.2 Microfluidic device design and fabrication

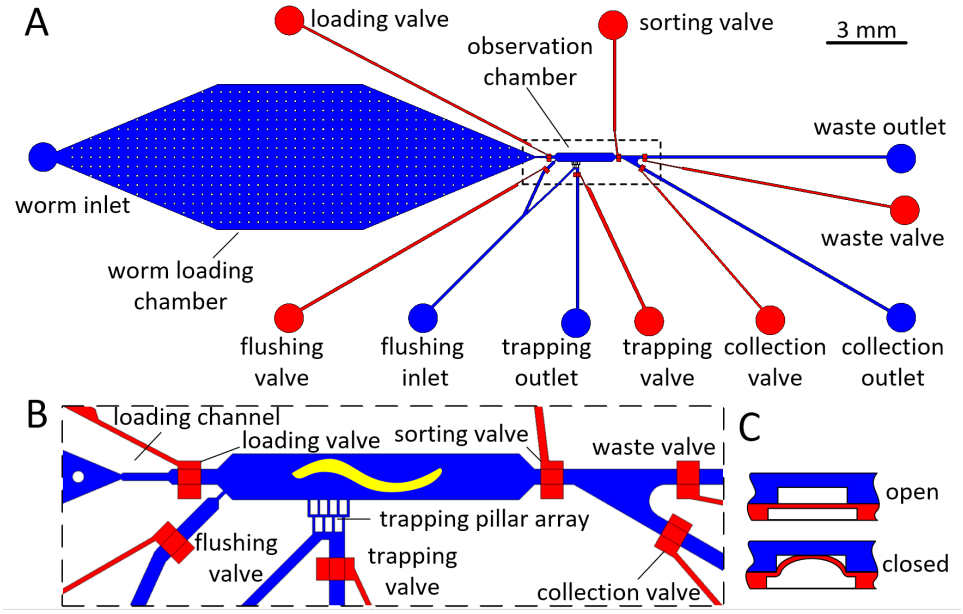


Figure 4-2 Schematic of the double-layer microfluidic device. (A) Microfluidic channel design. (B) Details of the observation chamber. (C) On/off mechanism of the two-layer microfluidic system.

The microfluidic device consists of two microchannel layers, as shown in the blue and red in Figure 4-2.The fluidic channels were arranged in the top flow layer to manipulate single worms, and the pneumatic valves were integrated in the bottom control layer. The cross-section view of a pneumatic valve is shown in Figure 4-2C to illustrate its operation principle. The channel height of the top flow layer was designed to be 45 $\mu m$ (approximately the average diameter of young adult worms), which confines the vertical movement of a worm during worm imaging and thus improve the accuracy of body size measurement. The microchannels in the top flow layer can be separated into three regions based on functionality: (i) the loading chamber, (ii) the observation chamber, and (iii) the downstream sorting channels.

The worm loading chamber is a large worm storage area supported by micro-pillar arrays, as shown in Figure 4-2A. For worm loading, unsynchronized *C. elegans* worms (at different developmental stages) on a culture plate are manually picked using a pipette and loaded into the worm loading inlet of the microfluidic device. During worm picking, the picked worms were sequentially transferred into multiple droplets of pure M9 solution on a clean agar plate, and this process removed large impurities from the picked worm bodies and avoided clogging of the microfluidic device with loaded worms. As a preparation step, a positive pressure of 5 psi will be applied to the device inlet to flush small impurities and worms at L1 and L2 stages out of the worm loading chamber and only leave larger worms (L4, young adult, and adult stages) that are stopped by the pillars for subsequent sorting. The spacing between adjacent pillars was set to be 240 $\mu m$ to reduce the loading speed of single worms and avoid device clogging and double loading (two worms enter the observation chamber together) [18].

The observation chamber, with a width of 300 $\mu m$ and a length of 2100 $\mu m$, was designed to contain a single worm with enough space for swimming, and the field of view (FOV) of the microscope (with a 4x objective) always covers the entire observation chamber for worm size measurement. Specifically, the entrance of the observation chamber is a 60 $\mu m$ wide loading channel with a 30 $\mu m$ nip at its front (Figure 4-2B). The 30 $\mu m$ nip of the loading channel was designed to be slightly narrower than the average diameter (~35 $\mu m$) of L3 worms (the smallest among the mixture of L3, young adult and adult worms we will sort) to reduce the chance of multi-worm loading into the chamber and improve the operation success rate. In our experiments, we did not observe clogging of the nip by a single worm even for the young adult and adult worms with body widths larger than the nip width, which is mainly because of the highly deformable worm body allowing it squeeze through the nip.

As the width of the observation chamber (300 $\mu m$) is much larger than that of the loading channel (60 $\mu m$), there is a flow rate drop of the incoming fluid when it enters the observation chamber [20], which reduces the entering speed of the worm and leaves longer response time for the pneumatic micro-valves to close the observation chamber and trap the loaded worm. Note that the down stream sorting valves (waste and collection valves) are closed during worm loading, and the fluid from the loading channel will flow to the trapping outlet (Figure 4-2B). Thus, the worm flushed with the fluid through the loading channel will be trapped by the trapping pillar array (pitch:

15 $\mu m$) at the junction of the trapping channel and the observation chamber. This trapping effect further lowers the speed of the worm and completely avoids any worm escape out of the observation chamber due to its high entering speed. The trapping channel and the flush channel are connected together just outside the trapping pillar array.

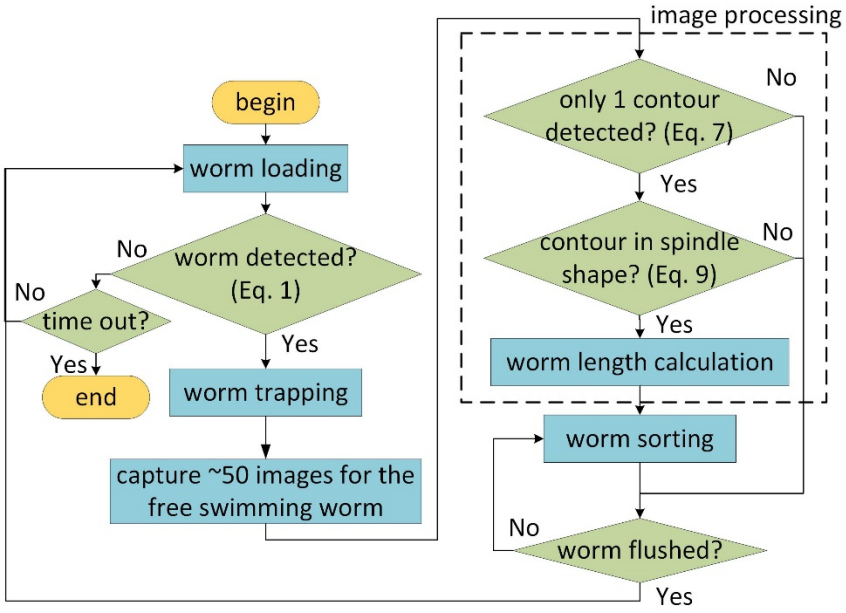


Figure 4-3 Flowchart of the system operation procedure.

When the size measurement of the current worm is completed, a 20 psi pressure will be applied to the flush inlet to flush the worm out of the observation chamber for downstream sized-based sorting. The straight flow channel at the outlet side of the observation chamber is to collect the waste worms of no interest (e.g., worms with undesired sizes, multiple worms simultaneously loaded into the observation chamber, or worms with failed size measurements), for which the waste valve is opened and the collection valve is closed. If a worm is measured to have the desired size, it will be sorted to the collection channel (waste valve off and collection valve on). The microfluidic device was fabricated from polydimethylsiloxane (PDMS) via standard multi-layer soft lithography. The mould masters of the two device layers were fabricated through photopatterning SU-8 2025 on silicon wafers. Pre-cured PDMS was prepared with base-curing agent w/w mixing ratios of 5:1 and 20:1 for moulding the top flow layer and the bottom control layer, respectively. The thickness of the bottom control layer was controlled to be 40 $\mu m$ by spin-coating the uncured PDMS on its mould master at 1500 rpm.

### 4.3.3 Operation procedure for automated worm sorting

By visually detecting individual loaded worms and regulating the valves (through the pressure unit), the system is capable of repetitively loading a single worm into the observation channel, analyze its body size parameters (length and width), and sort it based on its measured length. The sorting process consists of three operation steps: (i) the loading step, (ii) the trapping/sizing step, and (iii) the sorting step. The corresponding on/off states of the valves and supplied pressures are shown in *Table 4.3-1*.

At the loading step, a constant loading flow of 5 $\mu l/s$ is applied to the worm loading inlet by a syringe pump (Figure 4-1A) to load single worms sequentially into the observation chamber. In the meanwhile, the sorting valve and the flushing valve are closed so that the main fluidic flow through the observation chamber could travel from the loading channel, through the trapping pillar array, to the the trapping channel. As a result, once a worm is loaded into the observation chamber, it will be trapped at the trapping pillar array because of the fluidic pressure. A worm detection algorithm (see *Section 4.4.1*) running continuously on the host computer detects whether the worm body has completely entered the observation chamber (which is called a `complete loading'). When a complete loading is detected, the loading valve is closed and the loading flow is shut off, and the trapping valve is opened to move the entering worm to the trapping pillar array. In addition, the syringe pump quickly withdraws 10 $\mu l$ fluid to prevent the loading of a second worm. The back flow caused by the syringe pump releases the loaded worm from the trapping pillar array and makes the worm ready for body size measurement. The body size parameters of the worm are repeatedly measured from 50 consequent image frames by a customized image processing algorithm, and the 50 measurements were averaged to provide the final data. If the measured worm body length is within a user-specified range, the downstream waste valve is closed the collection valve opened, and the flushing pressure is turned on to flush the worm into the collection outlet. Otherwise, the worm will be flushed into the waste outlet. Then, the whole process will start again to sort the next worm. Typically, the entire sorting process takes 5.8 s.

Table 4.3-1 States of the valves and supplied pressures at three operation steps

| System states | worm inlet | flushing pressure | loading pressure | flushing valve | trapping valve | sorting valve | waste valve | collection valve |
|---|---|---|---|---|---|---|---|---|
| loading | on | off | open | closed | open | closed | open | closed |
| trapping | off | off | closed | closed | closed | closed | open | closed |
| sorting | off | on | closed | open | closed | open | depending on the worm length | depending on the worm length |

## 4.4 Techniques for automated worm sorting

### 4.4.1 Worm detection inside the observation chamber

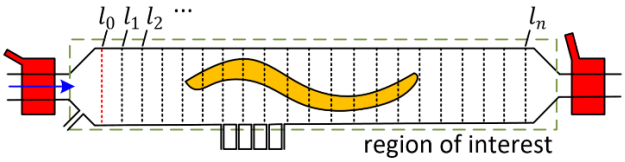


Figure 4-4 Worm detection graph within the observation chamber.

In the sorting experiments, a complete worm loading needs to be first detected to trigger the worm trapping process (by the trapping chamber) and prevent the loading of a second worm. For a worm being carried by the 5 $\mu l/s$ flow through the 60 $\mu m$ wide loading channel, its captured image sequence appears to be only a blurred shadow. Thus, the detection algorithm needs to be not only fast but also effective to pick up the blurred worm image.

In the worm detection algorithm, the average pixel intensity of a specific area in the observation chamber is used as a reliable indicator for the presence of a worm, since the worm body is darker than the channel background and the occupancy of an area by the worm body will cause significant drop in the average pixel intensity of that area. To improve the image processing speed, we continuously measured the average intensity drops of a series of parallel lines along the chamber width (Figure 4-4). The lines $l_0, l_1, \dots, l_n$ evenly spread throughout the observation chamber with a pitch of $d$. A background thread repetitively calculated the average intensity drops of the lines during real-time imaging. The worm was considered to be detected if either one of the following two criteria was satisfied.

$$\begin{cases} \exists i \in \{0, \dots n\} s.t. \Delta I(\bar{l}_i) > \delta, \Delta I(\bar{l}_{i+1}) > \delta, \Delta I(\bar{l}_0) < \delta \\ argmax_i\{\Delta I(\bar{l}_i) > \delta, \Delta I(\bar{l}_{i+1}) > \delta\} > \dfrac{L}{d}, \Delta I(\bar{l}_0) \geq \delta \end{cases} \quad (4.4\text{-}1)$$

where $\Delta I(\bar{l}_i)$ is the average intensity drop of the pixels on the line $l_i$, $\delta$ is an experimentally determined threshold, and $L$ is the length of a young adult worm. The first criterion indicates that a worm larger than $d$ has been completely loaded, while the second one indicates that the body portion longer than the threshold $L$ has been loaded. In our experiments, $d$ = 120 $\mu m$, $L$ = 1000 $\mu m$. Through our testing, the worm detection algorithm took less than 2 $ms$ to process one image frame and provided a detection success rate of 100%.

### 4.4.2 Vision-based worm size measurement

In the trapping step, the microscope camera takes the image of the observation chamber at a frame rate of 50 fps, and the worm body size parameters are repeatedly measured for 1 s (50 consequent frames). We developed custom-made image processing algorithms for worm body size measurement so that our system could readily integrate and customize the algorithms for automated operation. To ensure system operation reliability, we adopted mature algorithms here for rapid recognition of worm body boundaries and accurate measurement of the worm size.

#### a) Worm length measurement

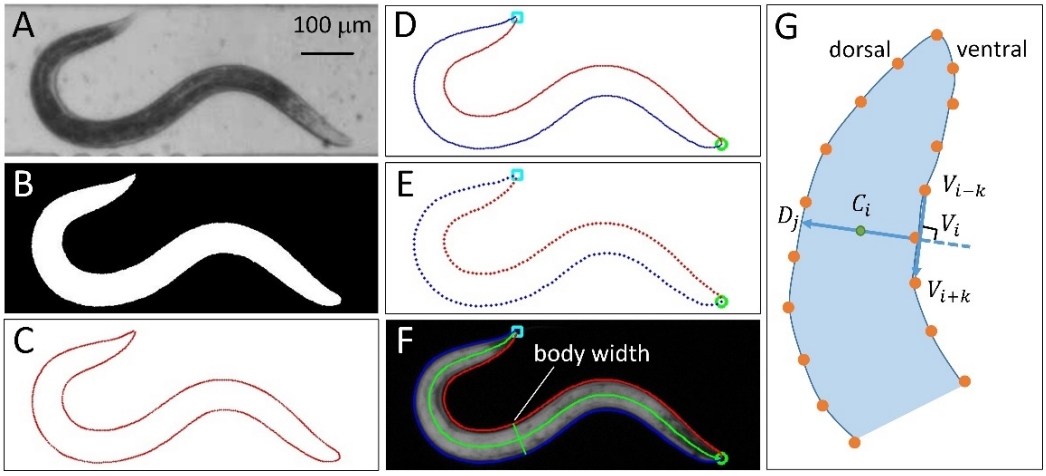


Figure 4-5 Image processing algorithm for calculation of worm morphology features. (A) Original image of a worm confined within the observation chamber. (B) Binarized image. (C) Extracted worm boundary. (D) Dorsal and ventral sides of the worm on its boundary. (E) Resample of the dorsal and ventral sides. (F) Calculation of the centerline and the width on the worm body. (G) Schematic view of the algorithm.

Before an experiment begins, a region of interest (ROI) will be selected on the live video displayed by the system control software, which covers the observation chamber. One frame of the ROI grabbed initially before worm loading is used as a background image. Once a worm image is grabbed, as illustrated in Figure 4-5A, it is first subtracted by the background image to remove unnecessary features of the chamber edges and the background texture. Then, the ROI is averaged by a 3x3 *Gaussian* mask to reduce image noise and binarized using the *Otsu* method [33]. A 3x3 *erode* and *dilate* operator is applied to the resultant image, to eliminate the small debris in the

image (Figure 4-5B). After that, all the contours within the image are identified, and only the largest one is detected as the boundaries of the worm body (Figure 4-5C).

The obtained worm contour points are evenly re-sampled by a fixed distance with a linear interpolation method. Denoting the re-sampled points as $P_i, i = \{1,2 \dots n\}$, the acuity of a specific boundary point with respect to its adjacent points can be evaluated as

$$\begin{aligned} M_{k,i} &= (P_{i+k} - P_i)(P_{i-k} - P_i) \\ &\cong l_k^2 \cos \alpha_i \end{aligned} \tag{4.4-2}$$

where $k$ is the vector size, $l_k$ is the vector length, $\alpha_i$ is the acute angle between two intersection vectors. A larger $M_{k,i}$indicates a smaller $\alpha_i$ and a sharper boundary point. Thus, the worm tail can be identified by evaluating $M_{k,i}$, since it is the sharpest point on the worm body contour. However, this process is dependent on $k$, as a small $k$ leads to a local optimal point while a large $k$ leads to a biased result. To avoid this disadvantage, the large and small vector lengths are combined and the worm tail point $P_t$is defined by

$$t = argmax_i \left\{ M_{l_1,i} + \frac{l_1^2}{l_2^2} M_{l_2,i} \right\}, i \in \{1,2 \dots n\} \tag{4.4-3}$$

The head $P_h$ of the worm is defined as

$$t = argmax_i \left\{ M_{l_1,i} + \frac{l_1^2}{l_2^2} M_{l_2,i} \right\}, i \in \{1,2 \dots n\} - \{t - a, \dots t + a\} \tag{4.4-4}$$

where $a$ is the region width to exclude the tail area. In experiments, we set $a = n/4$, $l_1 = \mathrm{n}/40$, and $l_1 = \mathrm{n}/100$.

After identifying the head and tail points, the contour points of the worm body can be separated to the ventral and dorsal sides, as shown in Figure 4-5D. These two point sets are further re-sampled by distance through linear interpolation with a sample size of $s$. We get the ventral points $V_i$ and dorsal points $D_i$ ($i = \{1,2 \dots s\}$), as illustrated in Figure 4-5E. Figure 4-5G shows the calculation of centerline points $C_i$, which is defined by

$$C_i = \frac{1}{2}\left(V_i + D_j\right), i = \{1,2 \dots s\} \tag{4.4-5}$$

where

$$j = argmin_m\{(V_{i+k} - V_{i-k})(D_m - V_i)\}, m = 1 - a, \dots i + a \quad (4.4\text{-}6)$$

and $a$ is a parameter to limit the searching area and $a = 10$ in our experiments. With the centerline points defined, the worm length is calculated as

$$L = \sum_{i=1}^{s-1} |C_{i+1} - C_i| \quad (4.4\text{-}7)$$

In our experiments, we found $s = 100$ provided accurate measurement of the worm body length comparable to that of the commercial software WormLab. The accuracy of the length calculation can be further improved by increasing $s$.

**b) Worm width measurement**

Besides the worm length measurement, we also developed an algorithm for quantifying the worm body widths at different locations along its length. With the body widths measured, one can calculate the worm body volume by assuming circular cross-sections of different segments of the worm body. This worm body volume parameter could serve as an additional physiological parameter of the worm, and cannot be measured by the existing commercial software.

The width is the distance between the corresponding points on the dorsal and ventral sides, and it is distributed along the body as

$$w_i = |D_j - V_i| \quad (4.4\text{-}8)$$

where $D_j$ and $V_i$have been defined in *Section 4.4.2*. We define the width of a worm as the width in the middle point of the recognized worm body centerline ($w_{s/2}$; see Figure 4-5F). The worm width data were also used for detecting calculation failures of the body size measurement algorithm (see *Section 4.4.3*).

With the camera frame rate of 50 fps, between two adjacent frames the worm is not able to swim out of a distance of 20 pixels when it is confined within the observation chamber. Once the worm body in the first frame is recognized, the ROI of the next frame is reduced to the region extended from the rectangle enclosing the worm body by 20 pixels from its edges. With this much smaller ROI, the image processing time for the subsequent frames is greatly reduced. Based on our experiments, the average time required for body size analysis in each frame was 5 ms, 7 ms, 10 ms, 12 ms, 15 ms, and 17 ms for L1, L2, L3, L4, young adult, and adult worms, respectively.

To verify the accuracy of the proposed algorithm for worm length measurement, we continuously grabbed 20 images of worms at various developmental stages, and compare the worm length data calculated by our algorithm with those from the commercial software WormLab. As shown in Figure 4-6，there is no significant difference among all the 5 comparison groups for worm length measurement (average difference: 1.8%). The data measured by both our algorithm and WormLab show that the length of the same worm during locomotion vary in a range of $\sim 10mm$ during its natural undulation movement. The largest standard deviation (10.8 $\mu m$) of the worm length measured by our algorithm (Figure 4-6) was determined to be the measurement accuracy of our algorithm.

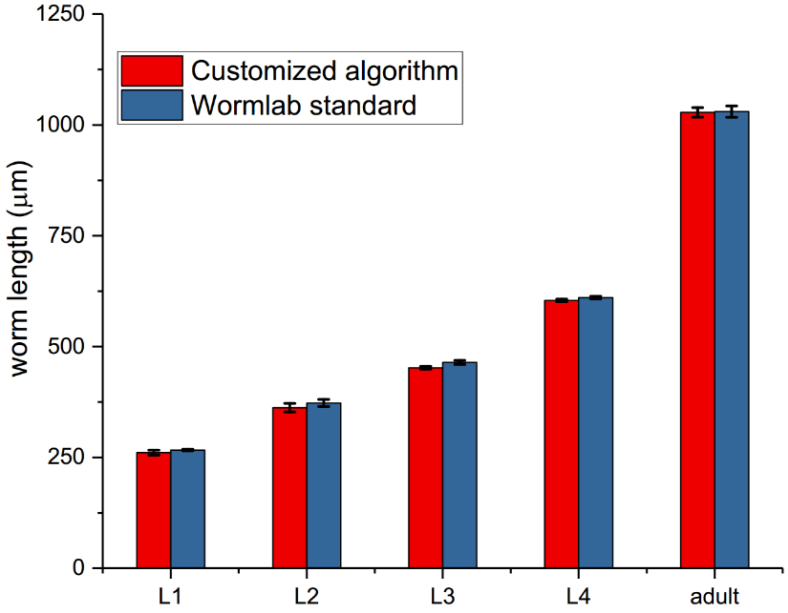


Figure 4-6 Comparison of the worm sizing results from our algorithm and the WormLab software (n=10).

### 4.4.3 Automatic detection of multi-worm loading

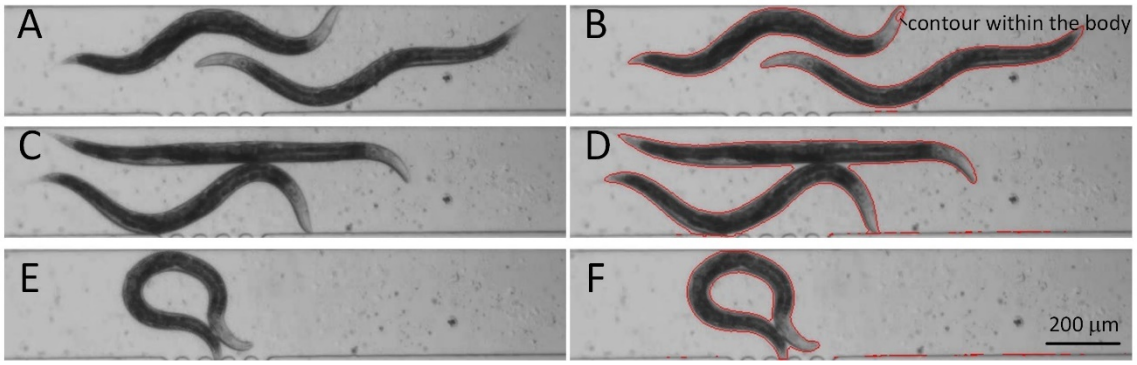


Figure 4-7 Detection of multi-worm loading and calculation failure. (A)(C)(E) Raw images illustrating cases of multi-worm loading, worm body contact, and self-coiling, respectively. (B)(D)(F) Contour detection results that cannot be further processed by the proposed worm length measurement algorithm.

If more than one worm is loaded into the observation chamber (Figure 4-7A), the measurement algorithm will not work properly. Also, the microfluidic device cannot separate the simultaneously loaded worms for downstream sorting. Although the nip design of the loading channel can reduce the chance of multi-worm loading, simultaneous loading of more than one worm into the observation chamber may still happen occasionally. To this end, we designed an image processing algorithm to automatically detect the multi-worm loading. Before the worm length calculation, all the identified contours within the ROI are extracted. The largest contour and the second largest contour are denoted as $\{P\}_1$ and $\{P\}_2$, respectively. If

$$\{P\}_1 \notin \{P\}_2 \; and \; card\{P\}_2 > \lambda \, card\{P\}_1 \qquad (4.4\text{-}9)$$

multi-worm loading is considered to be occurring, where $card\{P\}$ denotes the number of members in the set $P$. Due to non-uniform transparency of the worm body, some inner organs within the worm body may be occasionally detected as some connected regions (the small region in Figure 4-7B). The first condition, $\{P\}_1 \notin \{P\}_2$ is to avoid detecting the inner organs as a separate worm. The second condition is to ensure that the size of the connected domains the algorithm detects are large enough to be a second worm contour. $\lambda$ was set to be 0.25, which is the approximate size ratio between an adult worm and an L1 worm. Figure 4-7B shows two simultaneously loaded

worms detected by the algorithm. Upon being detected, all the simultaneously loaded worms contained in the observation chamber are directly flushed to the waste outlet without sorting.

There are also chances that two or more worms are loaded into the chamber, and their bodies contact each other in the image. This leads to the visual recognition of a connected contour of the two worm bodies. In this case, the multi-worm loading is detected by another algorithm for calculation failure, as discussed in *Section 4.4.4*.

### 4.4.4 Automatic detection of calculation failure

During the trapping procedure, multiple worms may be loaded into the observation chamber together and the worm sizing algorithm detects their bodies to be a single connected contour (Figure 4-7C and Figure 4-7D). The algorithm described in *Section 4.4.3* cannot detect this case. In addition, a single freely swimming worm may also display coiling behavior in some of the image frames (Figure 4-7E). One region of the body contacts with other regions, causing failure of the worm body sizing algorithm (Figure 4-7F). We designed another algorithm to detect both events of multi-worm loading with a connected body contour and single-worm coiling.

As discussed in [34], the width distribution along the worm body is characterized by

$$w_i = w_{\frac{s}{2}}(1 - e^{-0.1(s-|2i-s|)}) \tag{4.4-10}$$

To eliminate the failure calculations, the worm width is evaluated at several points along the worm centerline. Only the frames satisfying the following criteria are considered to contain a single worm feature without coiling:

$$\begin{cases} L_1 < L < L_a \\ a < \dfrac{L}{w_{\frac{s}{2}}} < b \\ w_i = w_{\frac{s}{2}}\left(1 - e^{-0.1(s-|2i-s|)}\right) + \eta w_i, i = \{\dfrac{s}{8}, \dfrac{s}{4}, \ldots \dfrac{7s}{8}\} \end{cases} \tag{4.4-11}$$

$L_1$and $L_a$ are the lengths of L1 and adult worms, respectively. $L_1 = 250\mu m$ and $L_a = 1000\mu m$ were used in our experiments. The boundaries of the length-to-width ratio $a$ and $b$ were set to be 8 and 17. $\eta$ is a false tolerance coefficient, and was set to be $-0.3 < \eta < 0.3$ in our experiments. The first and second criteria limit the length and length-to-width ratio of the calculation result, while the third criteria defines the qualified worm contour as a spindle shape as illustrated in *Equation* (4.4-10). Together with the restrictions of *Equation* (4.4-9), the target contour is bounded

to be a signal worm within the observation channel without self-coiling, which can be further processed by our algorithm. The above criteria are applied to analyzing each image frame during the worm trapping period (~50 frames in total), The frames violating these criteria will be neglected without worm size measurement, and the final length and width of the current worm body are calculated as the average values from all the qualified image frames.

## 4.5 Experimental results and discussions

### 4.5.1 Worm culture and microfluidic device preparation

We used wild type worm strain in the sorting experiments. Three batches of worms fed with OP50 *E. coli* are separately cultured in an incubator at 20$^{o}$ C for 45, 50 and 55 hours, allowing them to reach L4, young adult and adult stages, respectively. They were then picked out of their culture plates, mixed together, and washed by M9 solution for sorting. Before each experiment, the bottom flow channels were filled with M9 solution without any air bubble. The washed mixture of worms at L4, young adult and adult stages were loaded into the worm loading chamber for sorting experiments. We demonstrated sorting of worms at three consecutive developmental states (L4, young adult and adult), because in real biological experiments the size-based phenotypes of *C. elegans* usually have size difference of approximately 1-2 developmental stages.

### 4.5.2 Automatic sorting of young adult worms

The mixture of L4, young adult, and adult worms ranges in size from $600\ \mu m$ to $1300\ \mu m$. We aimed to sort out young adult worms and chose a typical size range of $900 - 1000\ \mu m$ for them. Figure 4-8 shows the screen shots of the observation chamber and the worm at the three operation steps, and Video S1 illustrates the real-time sorting operations without human intervention. We performed experiments on sorting five batches of worms with a total number of 319 worms, and statistics of the sorting results are summarized in *Table 4.5-1*.In total, 279 times of sorting were conducted, among which 252 times of sorting was successful (meaning that the body size measurement and sorting were both successful on a single worm), 23 times of sorting were detected to be multi-worm loading, and 4 times of sorting were detected to be calculation failures. The total time spent on the 252 successful sorts was 1460 s, corresponding to an average sorting speed of 10.4 worms per minutes (5.8 s per worm). The sorting success rate, which is defined as the ratio of the number of the successfully sorted worms to the total sorting times, was calculated to be 90.3%. The calculation failures occurred when a single worm had coiling behavior, or when

multiple worms were loaded simultaneously with their bodies contacted each other throughout entire worm trapping period (1 s) for body size measurement. One can see that the number of multi-worm loading cases is significantly higher than that of calculation failures.

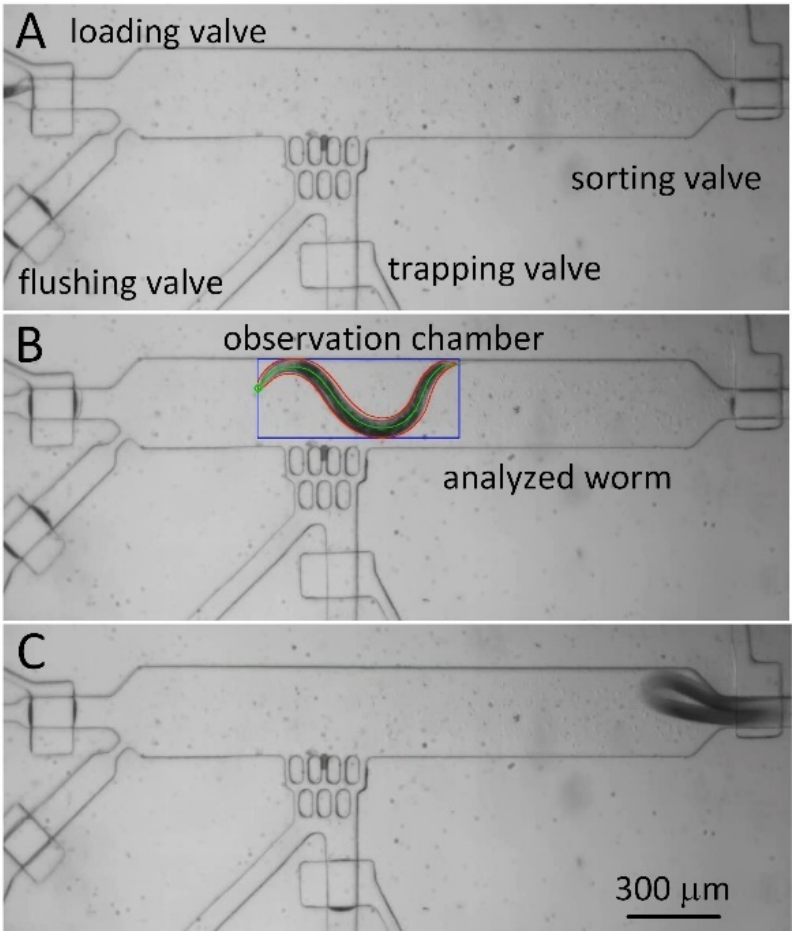


Figure 4-8 Screen shots of the observation chamber and the target worm at (A) the loading step, (B) the body size measurement step, and (C) the sorting step.

Table 4.5-1 Worm Sorting Experimental Results.

| | Time cost (second) | Sorting (times) | Multi-loading (times/worms) | Calculation failure (times/worms) |
|---|---|---|---|---|
| Batch 1 | 691 | 139 | 11/23 | 1/3 |
| Batch 2 | 196 | 47 | 7/17 | 1/3 |
| Batch 3 | 263 | 41 | 3/10 | 1/2 |
| Batch 4 | 168 | 29 | 1/2 | 1/4 |
| Batch 5 | 142 | 23 | 1/3 | 0 |
| Total | 1460 | 279 | 23/55 | 4/12 |

Table 4.5-2 The Comparison of Microfluidic *C. elegans* Sorting Devices Based on The Worm Size and/or Developmental Stage.

| References | Sorting mechanism | Reported speed | Sorting conducted | Size measurement |
|---|---|---|---|---|
| [22] | electrotactic response | 78 worms/min;>79% | 383 | No |
| [18] | electrotaxis response | 4.3±1.0 worms/min;95±8% | | No |
| [19] | electrotaxis response | 56 worms/min;82.62%–89.31% | ~200 | No |
| [24] | pillar arrays | 200 worms/min; >90% | | No |
| [25] | pillar arrays | >100 worms/min; >85% | >2000 | No |
| [26] | microchannels with tunable cross-section areas | 3.5 worms/sec;100% | | No |
| our system | vision-based size measurement | 5.8 sec/worm;90.3% | 319 | Yes |

*Table 4.5-2* compares our design with previously reported microfluidic worm sorting methods based on the worm size or developmental stage. One can see that, although our method does not provide the highest sorting speed and the highest success rate, it is the only method capable of simultaneous size measurement and size-based sorting of single worms. The function of worm size measurement ``on the fly" could benefit studies requiring accurate size-based sorting with size statistics of the sorted population.

### 4.5.3 Size validation of the sorted worms

To further evaluate the effectiveness of the worm sorting system, we collected the sorted young adult worms and the `waste' worms from the device's collection and waste outlets, respectively, and measured their lengths on two separate agar plates using the commercial software Wormlab. Figure 4-9A shows the body length distributions of the two groups. Figure 4-9B and C are the

photographs of sorted worms and `waste' worms. Note only portions of the sorted and 'waste' worms are shown here. From Figure 4-9A, one can observe that most of the sorted worms as young adults have body lengths within the range of $900 - 1000\ \mu m$, and nine worms have body lengths (measured by WormLab) slightly smaller than $900\mu m$ or slightly larger than $1000\mu m$ were also collected as young adults. This is due to the measurement inaccuracy ($10.8\ \mu m$) of the worm length measurement algorithm. Also, 20 worms collected from the waste outlet also has the body lengths falling into the range of $900 - 1000\ \mu m$. These worms the system missed were from the detected cases of multi-worm loading and calculation failure (67 worms in total).

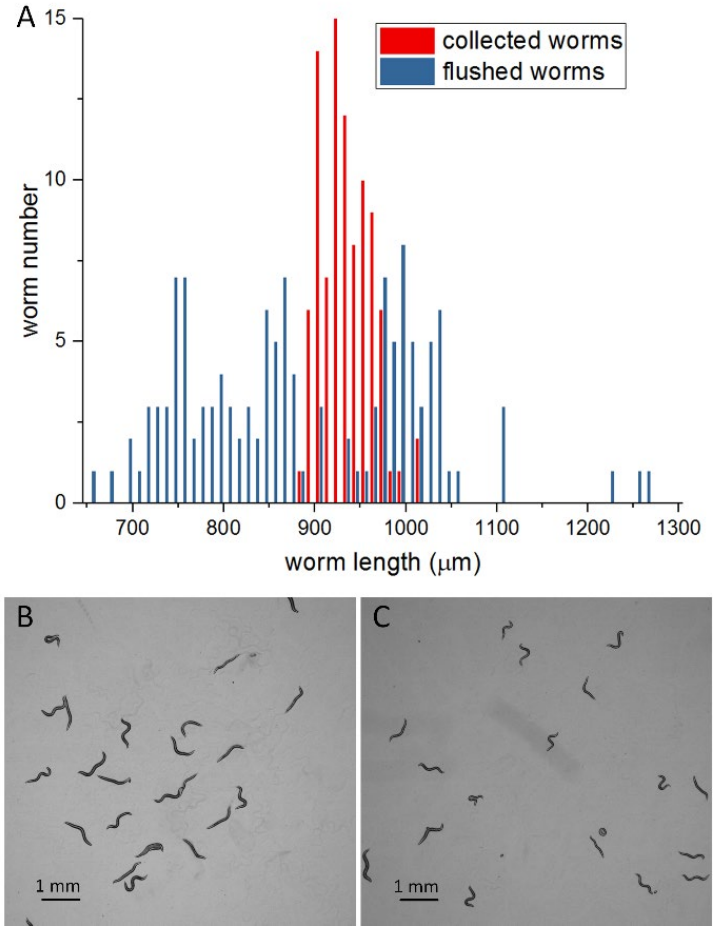


Figure 4-9 Post-sorting measurement. (A) Body length measurement data of the sorted worms using Wormlab. (B)(C) Photographs of (B) the sorted worms and (C) the `waste' worms.

Table 4.5-3 Post-Sorting Size Measurement Results

| Size range | Collected worms (93) | Flushed worms (130) |
|---|---|---|
| 900-1000 $\mu$m | 90.3% (84) | 23.1% (30) |
| Others | 9.7% (9) | 76.9% (100) |

### 4.5.4 Viability tests

To examine the possible impact on the physiology of the sorted worms, we measured two major developmental parameters (pharyngeal pumping rate and fecundity) of the sorted worms and the corresponding control group. The control group was cultured under the same condition as that of the sorted group. One hour after the sorting experiment, we transferred 20 hermaphrodite individuals from the sorted worms and 20 from the control group onto new agar plates, the pumping rates of which are measured for comparison (data shown in Figure 4-10A). After that, these hermaphrodite worms are further cultured on 40 new NGM plates with one worm in each plate for 24 hours. These hermaphrodite worms lay eggs during this period of time, and the number of eggs on each plate are counted as the fecundity (data shown in Figure 4-10B). From Figure 4-10 one can see that no significant difference was found on the pharyngeal pumping rate and fecundity of the sorted worms and the control ones, confirming that there was no evidence that our system caused any adverse effect on the development of the sorted worms.

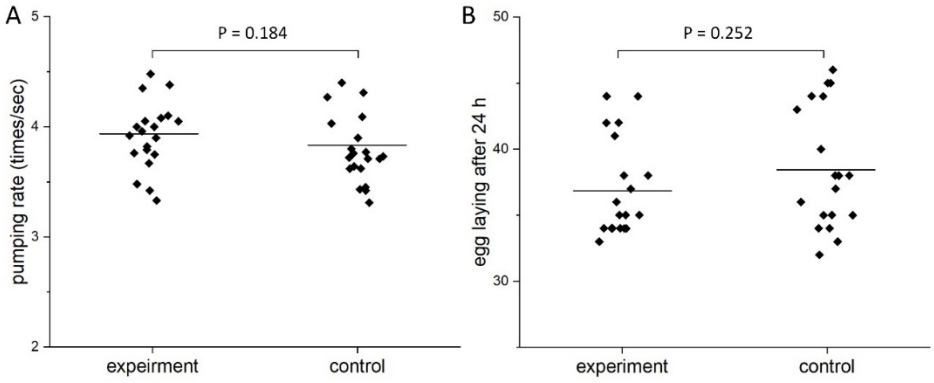


Figure 4-10 Survival testing results of the sorted worms. (A) and (B) are values (n=20) of the worm pumping rate and the progeny number, respectively.

## 4.6 Conclusions

We presented a vision-based microfluidic system, consisting of a microfludic device and image processing algorithms, for automated, size-based sorting of *C. elegans*. The microfluidic device is responsible for on-chip loading, trapping, imaging, and sorting of single worms. Customizable image processing algorithms were developed for accurate measurement of the worm body size parameters. Based on the sorting experiments of 319 worms, the system provided an average sorting speed of 10.4 worms per minute (5.8 s/worm) with an operation success rate of 90.3%. Post-sorting size measurements on the sorted worms demonstrated the effectiveness of the system.

## 4.7 Reference


[1] H. M. Ellis and H. R. Horvitz, "Genetic control of programmed cell death in the nematode C. elegans," *Cell,* vol. 44, no. 6, pp. 817-829, 1986.

[2] M. De Bono and C. I. Bargmann, "Natural variation in a neuropeptide Y receptor homolog modifies social behavior and food response in C. elegans," *Cell,* vol. 94, no. 5, pp. 679-689, 1998.

[3] A. Fire, S. Xu, M. K. Montgomery, S. A. Kostas, S. E. Driver, and C. C. Mello, "Potent and specific genetic interference by double-stranded RNA in Caenorhabditis elegans," *nature,* vol. 391, no. 6669, p. 806, 1998.

[4] C. A. Wolkow, K. D. Kimura, M.-S. Lee, and G. Ruvkun, "Regulation of C. elegans life-span by insulinlike signaling in the nervous system," *Science,* vol. 290, no. 5489, pp. 147-150, 2000.

[5] G. Soete, M. C. Betist, and H. C. Korswagen, "Regulation of Caenorhabditis elegans body size and male tail development by the novel gene lon-8," *BMC developmental biology,* vol. 7, no. 1, p. 20, 2007.

[6] R. B. Azevedo, P. D. Keightley, C. Laurén-Määttä, L. L. Vassilieva, M. Lynch, and A. M. Leroi, "Spontaneous mutational variation for body size in Caenorhabditis elegans," *Genetics,* vol. 162, no. 2, pp. 755-765, 2002.

[7] M. Fujiwara, P. Sengupta, and S. L. McIntire, "Regulation of body size and behavioral state of C. elegans by sensory perception and the EGL-4 cGMP-dependent protein kinase," *Neuron,* vol. 36, no. 6, pp. 1091-1102, 2002.

[8] T. Hirose, Y. Nakano, Y. Nagamatsu, T. Misumi, H. Ohta, and Y. Ohshima, "Cyclic GMP-dependent protein kinase EGL-4 controls body size and lifespan in C. elegans," *Development,* vol. 130, no. 6, pp. 1089-1099, 2003.

[9] J. E. Kammenga *et al.*, "A Caenorhabditis elegans wild type defies the temperature–size rule owing to a single nucleotide polymorphism in tra-3," *PLoS genetics,* vol. 3, no. 3, p. e34, 2007.

[10] C. Savage-Dunn, L. Yu, K. Gill, M. Awan, and T. Fernando, "Non-stringent tissue-source requirements for BMP ligand expression in regulation of body size in Caenorhabditis elegans," *Genetics research,* vol. 93, no. 6, pp. 427-432, 2011.

[11] W. Y. Fung, K. F. C. Fat, C. K. S. Eng, and C. K. Lau, "crm-1 facilitates BMP signaling to control body size in Caenorhabditis elegans," *Developmental biology,* vol. 311, no. 1, pp. 95-105, 2007.

[12] K. Chung, M. M. Crane, and H. Lu, "Automated on-chip rapid microscopy, phenotyping and sorting of C. elegans," *Nature methods,* vol. 5, no. 7, p. 637, 2008.
[13] M. M. Crane, K. Chung, and H. Lu, "Computer-enhanced high-throughput genetic screens of C. elegans in a microfluidic system," *Lab on a Chip,* vol. 9, no. 1, pp. 38-40, 2009.
[14] Y. Yan *et al.*, "A continuous-flow C. elegans sorting system with integrated optical fiber detection and laminar flow switching," *Lab on a Chip,* vol. 14, no. 20, pp. 4000-4006, 2014.
[15] P. Rezai, S. Salam, P. R. Selvaganapathy, and B. P. Gupta, "Electrical sorting of Caenorhabditis elegans," *Lab on a Chip,* vol. 12, no. 10, pp. 1831-1840, 2012.
[16] X. Wang *et al.*, "Highly efficient microfluidic sorting device for synchronizing developmental stages of C. elegans based on deflecting electrotaxis," *Lab on a Chip,* vol. 15, no. 11, pp. 2513-2521, 2015.
[17] F. Geier, A. Leroi, J. Bundy, J. Edel, and A. DeMello, "High-throughput age synchronisation of Caenorhabditis elegans," *Chemical communications (Cambridge, England),* vol. 47, no. 35, pp. 9801-9803, 2011.
[18] X. Ai, W. Zhuo, Q. Liang, P. T. McGrath, and H. Lu, "A high-throughput device for size based separation of C. elegans developmental stages," *Lab on a Chip,* vol. 14, no. 10, pp. 1746-1752, 2014.
[19] J. Yuan, J. Zhou, D. M. Raizen, and H. H. Bau, "High-throughput, motility-based sorter for microswimmers such as C. elegans," *Lab on a Chip,* vol. 15, no. 13, pp. 2790-2798, 2015.
[20] P. Song, X. Dong, and X. Liu, "A microfluidic device for automated, high-speed microinjection of Caenorhabditis elegans," *Biomicrofluidics,* vol. 10, no. 1, p. 011912, 2016.
[21] P. Song, W. Zhang, A. Sobolevski, K. Bernard, S. Hekimi, and X. Liu, "A microfluidic device for efficient chemical testing using Caenorhabditis elegans," *Biomedical microdevices,* vol. 17, no. 2, p. 38, 2015.
[22] R. C. Lagoy and D. R. Albrecht, "Microfluidic devices for behavioral analysis, microscopy, and neuronal imaging in Caenorhabditis elegans," in *C. elegans*: Springer, 2015, pp. 159-179.
[23] N. A. Bakhtina and J. G. Korvink, "Microfluidic laboratories for C. elegans enhance fundamental studies in biology," *Rsc Advances,* vol. 4, no. 9, pp. 4691-4709, 2014.
[24] C. B. Rohde, F. Zeng, R. Gonzalez-Rubio, M. Angel, and M. F. Yanik, "Microfluidic system for on-chip high-throughput whole-animal sorting and screening at subcellular resolution," *Proceedings of the National Academy of Sciences,* vol. 104, no. 35, pp. 13891-13895, 2007.
[25] A. San-Miguel and H. Lu, "Microfluidics as a tool for C. elegans research," in *WormBook: The Online Review of C. elegans Biology [Internet]*: WormBook, 2005.
[26] A. Ben-Yakar, N. Chronis, and H. Lu, "Microfluidics for the analysis of behavior, nerve regeneration, and neural cell biology in C. elegans," *Current opinion in neurobiology,* vol. 19, no. 5, pp. 561-567, 2009.
[27] Q. Wen *et al.*, "Proprioceptive coupling within motor neurons drives C. elegans forward locomotion," *Neuron,* vol. 76, no. 4, pp. 750-761, 2012.
[28] X. Manière, F. Lebois, I. Matic, B. Ladoux, J.-M. Di Meglio, and P. Hersen, "Running worms: C. elegans self-sorting by electrotaxis," *PloS one,* vol. 6, no. 2, p. e16637, 2011.

[29] B. Han, D. Kim, U. H. Ko, and J. H. Shin, "A sorting strategy for C. elegans based on size-dependent motility and electrotaxis in a micro-structured channel," *Lab on a Chip,* vol. 12, no. 20, pp. 4128-4134, 2012.
[30] L. Dong, M. Cornaglia, T. Lehnert, and M. A. Gijs, "Versatile size-dependent sorting of C. elegans nematodes and embryos using a tunable microfluidic filter structure," *Lab on a Chip,* vol. 16, no. 3, pp. 574-585, 2016.
[31] S. So, K. Miyahara, and Y. Ohshima, "Control of body size in C. elegans dependent on food and insulin/IGF-1 signal," *Genes to Cells,* vol. 16, no. 6, pp. 639-651, 2011.
[32] J. Jung, M. Nakajima, M. Kojima, K. Ooe, and T. Fukuda, "Microchip device for measurement of body volume of C. elegans as bioindicator application," *Journal of Micro-Nano Mechatronics,* vol. 7, no. 1-3, pp. 3-11, 2012.
[33] N. Otsu, "A threshold selection method from gray-level histograms," *IEEE transactions on systems, man, and cybernetics,* vol. 9, no. 1, pp. 62-66, 1979.
[34] N. Roussel, C. A. Morton, F. P. Finger, and B. Roysam, "A computational model for C. elegans locomotory behavior: application to multiworm tracking," *IEEE transactions on biomedical engineering,* vol. 54, no. 10, pp. 1786-1797, 2007.

# Link between chapter 4 and chapter 5

In the previous chapter, the development of computer controlled microfluidic system for the automatic morphologic measurement and screening of individual *C. elegans* is discussed, which brought fast sorting speed, high throughput, and superior accuracy compared over manual operations. In this schematic, a new microfluidic mechanism for worm preservation and separation is designed with a chamber filled up of micro pillar arrays to slow down the flushing speed of worm individuals. Inspired by this microfluidic design, a new double-layer microfluidic device is proposed for the automated microinjection of *C. elegans*. The worm loading structure remains to be the microfluidic chamber with micro pillar arrays, while the downstream observations part is revised to be a narrow microchannel with the diameter slightly smaller than that of the adult worm. The worm will be it will be automatically squeezed and immobilized, upon flushing into this narrow microchannel. One side of this narrow channel is constructed by an array of micro pillars and sealed by a microvalve. Before microinjection, the microvalve is closed to provide enough fluidic pressure for worm loading. When loading is completed, the microvalve will be opened to connect the microchip to the macro world. A microneedle attached on a XYZ 3-DOF micromanipulator will be controlled to insert into the microfluidic chip for the injection of *C. elegans*. The next chapter discusses the detailed device design and operation, and the robotic system construction for the microinjection of *C. elegans*. Novel techniques of contact detection and coordinate frame mapping are proposed to enable the automated injection process.

# Chapter 5

# Automated robotic microinjection of the nematode worm *Caenorhabditis elegans*

# Chapter 5: Automated robotic microinjection of the nematode worm *Caenorhabditis elegans*

**X. Dong[1,2], P. Song[1], X. Liu[2]***

[1]*Department of Mechanical Engineering, McGill University, 817 Sherbrooke Street West, Montreal, Quebec, Canada H3A 2K6*

[2]*Department of Mechanical and Industrial Engineering, University of Toronto, 5 King's College Road, Toronto, Ontario, Canada M5S 3G8*

*corresponding author: (xyliu@mie.utoronto.ca)

in *IEEE Transactions on Automation Science and Engineering,* under review

## 5.1 Abstract

The nematode worm *Caenorhabditis elegans* is a model organism widely used in biological research on genetics, development, neuroscience, and ageing. Microinjection is an effective and widely adopted method to create transgenetic worms, perform ribonucleic acid (RNA) interference of certain genes, and introduce different types of molecules into specific locations inside a worm body. Based on microfluidics and robotic micromanipulation techniques, we develop a robotic system for automated microinjection of *C. elegans* with greatly improved injection speed and success rate over traditional manual microinjection. A double-layer microfluidic device with computer-controlled pneumatic valves is developed for automated on-chip loading, immobilization, injection, and downstream sorting of single worms. A new autofocusing-based contact detection algorithm is proposed to find the optimal injection position along the depth direction of the microscope field of view. The direction and location of the needle tip are reliably identified using an image processing algorithm. Through experiments on 240 worms, the system demonstrates automated injection at a speed of 6 worms per minute (9.97 s/worm) with a pre-sorting success rate of 78.8% (post-sorting success rate: 100%), which are more than 25 times faster and 1.5 times higher than the speed (0.25 worm/min) and success rate (30%) of a proficient human operator, respectively. With the superior performance, this system will enable new large-scale gene and molecule screening studies on *C. elegans* that cannot be fulfilled by the conventional microinjection technique.

## 5.2 Note to pactitioners

In the worm biology community, there are thousands of research laboratories worldwide that routinely cope with worm microinjection experiments. This paper aims to present the functionality and performance of our automated robotic system for high-speed worm injection. Using the robotic system, a large number of *C. elegans* can be loaded into the microfluidic device for continuous worm immobilization and injection. A user-friendly graphic user interface (GUI) is developed to allow an operator to monitor the injection process on a computer screen, select the injection location inside the worm body (through computer mouse clicking), and direct the system (through keyboard input) for down-stream sorting of the successfully injected worms for further culture. Given its unique features such as high injection speed, high level of automation, and high success/survival rates, this system holds great potential to liberate worm researchers from the tedious manual injection process and provide unparalleled injection throughput and consistency.

## 5.3 Introduction

The nematode worm *C. elegans* has been widely used as a model organism for investigating how various gene products function at specific tissue, cellular, and synaptic foci and how foreign molecules/chemicals affect the worm's biological pathways [1]. These studies are usually realized by injecting genetic materials or chemicals into the worm body to either suppress the expression of certain genes or perturb specific biological pathways [2]. To guarantee that the required phenotype demonstrated in the child generation, usually a large number of adult worms are injected at the father generation. In worm biology laboratories, the required worm injection task is conducted manually. It takes a few hours for a proficient operator to prepare the facilities and perform injection for only a limited number of *C. elegans*, and the low throughput limits many biological studies that require large-volume worm injection. Furthermore, the inconsistent human operation leads to low success and survival rates of worm injection. All of these limitations call for the development of automated worm injection systems.

To reduce the human intervention level and improve the operation consistency of bio-microinjection, in the past two decades numerous robotic systems have been proposed for the injection of either suspended cells (e.g., embryo and oocyte) or adherent cells (e.g., Hela cell, fibroblast, and endothelial cell) [3-13]. For instance, based on vision-based membrane tension estimation, a force-controlled robotic system has been developed for microinjection of zebrafish

embryos. Automated microinjection systems have also been reported for high-speed injection of zebrafish and mouse embryos [11], in which a vacuum-based immobilization mechanism was proposed for immobilization many cells into a regular pattern [4, 7]. Different from single cells, alive *C. elegans* worms swim in solution or crawl on an agar plate, and the existing cell immobilization mechanisms cannot be directly applied to worm immobilization. Thus, effective worm immobilization mechanisms suitable for continuous robotic worm injection must be developed to overcome the bottleneck of automated worm injection.

Targeting automated worm injection, a few worm immobilization devices and injection systems have been reported to facilitate *C. elegans* microinjection [14-17]. An open channel microfluidic device was developed [17], which immobilize single worms using a vacuum-channel array. The operation of the device is relatively complex and was conducted manually; this makes the device incapable of conducting continuous loading and immobilization of many worms with high reliability. Furthermore, the cell injection procedure used in this work was not automated; that is, the regulation of the flow rate within the microchannel and the adjustment of the needle tip position were both conducted manually. In addition, because of the complex procedure designed for worm immobilization, this system has limited potential for large-scale, robust injection. Another nanomanipulation system was reported by M. Nakajima *et al* [15, 16]. to deliver nano-beads into the worm body within an environmental scanning electron microscope (E-SEM). However, E-SEM still cannot provide a completely biocompatible environment for fluid injection of live *C. elegans* due to its radiation and vacuum environment. Recently, a new worm immobilization method has been proposed for *C. elegans* microinjection, which employs temperature-sensitive hydrogel to immobilize the worm inside it. The problem of this method is that the immobilized worms are randomly scattered inside the hydrogel with random orientations. The search of the worms takes additional time, and the injection has to be performed along different injection angles (the angle between the injection needle and the worm body); these factors, to some extent, limit the system's operation efficiency and consistency[14].

Combining microfluidics and robotic micromanipulation techniques, we propose a new robotic system for automated, high-throughput injection of *C. elegans*. A microfluidic device, with six computer-controlled pneumatic valves, is developed for automatic loading, immobilization, and post-injection collection of single worms at a high speed. On this chip, a cribriform wall open

channel with the width slightly smaller than the diameter of adult worms is designed. Once an individual worm is flushed in, the fluid pressure is automatically closed to trap the worm inside the immobilization channel. Meanwhile, a glass needle tip controlled by a 3 DOF micromanipulator is moved into the open channel to perform automatic microinjection of the target worm via the gaps on the cribriform channel wall. Before each injection experiment, the system performs rapid and automatic preparation, including: (i) determination of the vertical position of the injection needle (along the depth direction of the microscope view) for worm injection, through an autofocusing-based contact detection algorithm; (ii) detection of the in-plane position (in the image frame) of the needle tip using a reliable image processing algorithm; and (iii) calibration of the coordinate transformation between the image frame and the robot frame. During an experiment, the system visually monitors the operation of the microfluidic device and correspondingly controls the on-chip valves and the injection robot to realize automatic worm injection. Injection experiments on 240 *C. elegans* worms are performed to fully test the system performance. This paper is an extension of a previous conference paper [18]. In this journal version, we include a new and more robust contact detection algorithm, more technical details of the system setup and operation, a detailed description of the needle tip recognition algorithm, and more experimental results (i.e., a much larger sample size of robotic worm injection and additional survival testing results of the injected worms).

## 5.4 Robotic worm injection system

### 5.4.1 System setup

The robotic worm injection system, as shown in Figure 5-1(a), consists of an inverted microscope (IX83, Olympus) with a 4x objective (NA: 0.13) for sample imaging, a microfluidic device with on-chip valves for worm immobilization and sorting, a three-degree-of-freedom (3-DOF) micromanipulator (MP285, Sutter) mounted with an injection needle for worm injection, a pressure-driven microinjector (IM-300, Narishige) connected with the injection needle for delivering a foreign material into the worm body, a motorized XY stage (ProScan III, Prior) for carrying the microfluidic chip under the field of view (FOV) of the microscope, a custom-made, computer-controlled pressure unit to regulate the operation of valves on the microfluidic device, and a host computer (3.1 GHz CPU) for system control. A COMS camera (Basler, A601f) mounted on the microscope is used to provide the visual feedback for the system.

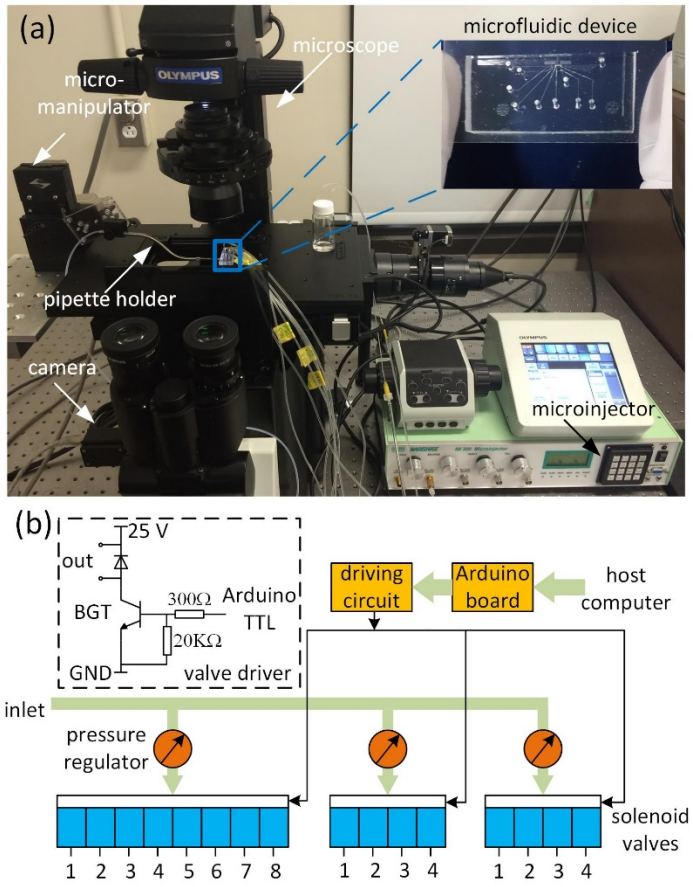


Figure 5-1 Setup of the robotic injection system. (a) Photograph of the system. (b) Schematic of the pressure unit for actuating the valves of the microfluidic device.

The custom-made pressure unit, as schematically shown in Figure 5-1(b), consists of 16 solenoid valves (S10MM-30-24-2/A, Pneumadyne Inc.), three manually adjustable pressure regulators (ARG20-N01G1-Z, SMC Pneumatics), a pressure inlet connected to a compressed nitrogen gas tank (output pressure: 85 psi), a driver circuit board for the 16 solenoid valves, and a microcontroller unit (Arduino UNO) connected with the host computer. The pressure unit could provide pressure sources in the range of 0-80 psi and at three different levels, to actuate on-chip pneumatic valves whose operations require different pressure levels. The driver circuit for a single valve is also shown in Figure 5-1(b).

### 5.4.2 Microfluidic device design

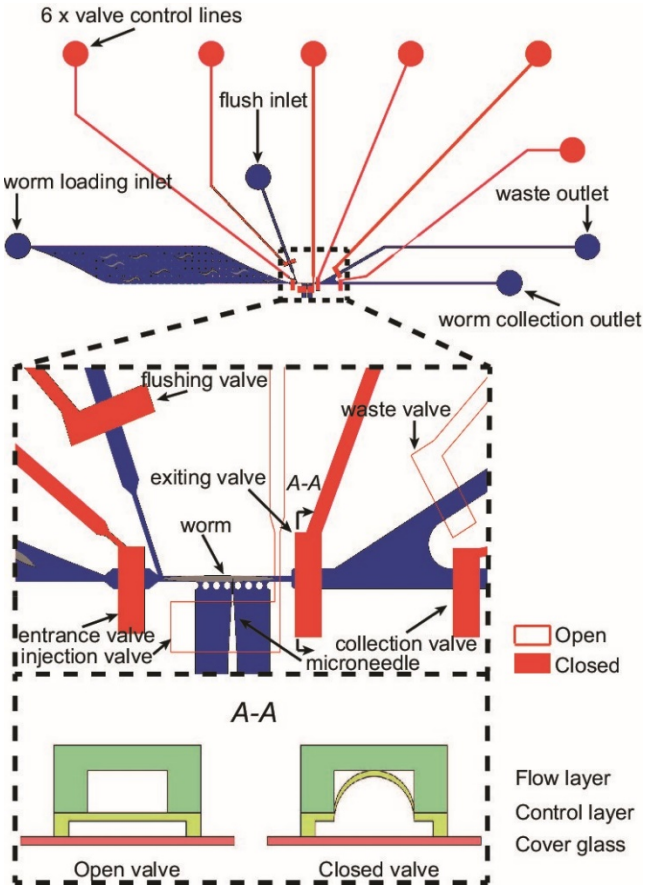


Figure 5-2 Schematic of the microfluidic device for worm immobilization.

The double-layer microfluidic device was designed for rapid single-worm loading, immobilization, and post-injection sorting. The device design, fabrication, and operation have been reported previously [19]. To make this paper self-contained, we briefly introduce its design here.

The device has 30 $\mu m$ rectangular control channels (red in Figure 5-2) on the bottom layer and 45 $\mu m$ tall flow channels (blue in Figure 5-2) on the top layer, and was fabricated from polydimethylsiloxane (PDMS) using standard multi-layer soft lithography [20]. Based on their functions, the device channels can be mainly divided into three regions: (i) a loading chamber, (ii) immobilization/injection channels, and (iii) downstream sorting channels. The loading chamber includes a micro-pillar array, and the spacing between adjacent micro-pillars is 300 $\mu m$, which is effective to filter out debris in the worm culture medium and allow young adult worm to swim through. This design avoids clogging of the immobilization channel and thus improves the reliability of device operation. The immobilization channel is 800 $\mu m$ long and 30 $\mu m$ wide,

which is slightly narrower than the diameter of a young adult worm (30-40 $\mu m$). The plug of a worm in the immobilization channel will significantly increase the channel's flow resistance, keeping another worm from entering.

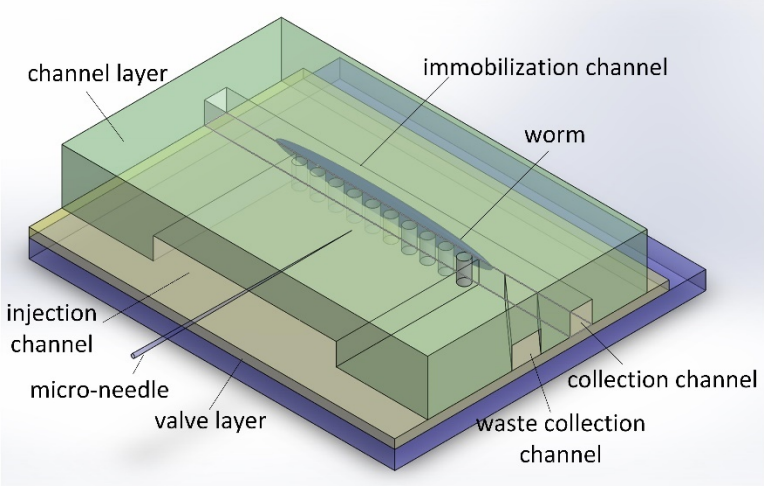


Figure 5-3 Detailed structure of the injection and immobilization channels.

An open-ended injection channel is perpendicularly connected to the immobilization channel, allowing an injection needle to be inserted through the open end of the injection channel and reach the immobilization channel (Figure 5-3). A row of micro-pillars (diameter: 40 $\mu m$, and pitch: 115 $\mu m$) is arranged at the junction of the immobilization and injection channels, which restrictan immobilized worm from swimming into the injection channel and in the meanwhile allow the needle to reach the worm body for injection. The width of the injection channel is set to be 420 $\mu m$, which covers the majority of the worm body for injection. A bifurcated channel is connected to the downstream of the immobilization channel, and regulated by two valves for post-injection worm sorting.

## 5.5 Experimental procedure

### 5.5.1 System preparation

Before each injection experiment, a microfluidic device, loaded with a batch of 40 worms, is firstly mounted onto the XY stage of the microscope. An injection needle loaded with injection material is then mounted on the micromanipulator horizontally (at $0^0$ tilting angle), with its tip in the microscope FOV and above the PDMS substrate outside the injection channel of the microfluidic device (‘contact detection area’ in Figure 5-5). Figure 5-4 shows the overall flow of the system

preparation and automated robotic injection. The system initiates the automatic preparation process by controlling the needle to contact the PDMS substrate, during which the vertical position (along the depth direction of the microscope FOV) of the needle-substrate contact point is detected using an autofocusing-based contact detection algorithm (see *Section 5.6.1*). After that, the needle tip is automatically lifted to the vertical level of 22.5 $\mu m$ (half of the injection channel height) above the PDMS surface, and the microfluidic device is moved towards the needle to insert the needle tip into the injection channel and place the injection and immobilization channels into the FOV. During the subsequent injection process, the vertical position of the needle tip remains the same, and its in-plane position is controlled inside the injection channel for worm injection.

Once the needle tip is moved into the injection channel, the tip position in the image coordinate frame is accurately detected using a tip recognition algorithm (see *Section 5.6.2*). To control the needle movement in the image coordinate frame, the mapping between the image coordinate frame (in pixels) and the micromanipulator coordinate frame (in $\mu m$) is calibrated automatically (see *Section 5.6.3*). Note that this automatic coordinate mapping process needs to be conducted every time a new injection needle is mounted onto the micromanipulator to compensate for the subtle difference in the needle length and alignment. Supplementary Video 1 shows the entire system preparation process.

### 5.5.2 Overall injection procedure

The control flow of the automatic injection process (Figure 5-4) was designed to maximize the parallelization level of different steps and thus increase the system efficiency. Table I summarizes the operation states of all the microfluidic valves and supplied pressures during the entire worm injection process.

To start the automatic injection, on-chip valves of the microfluidic device are set to the "worm loading state" (*Table 5.5-1*), and a constant pressure of 10 psi is applied to the worm loading inlet to sequentially drive individual worms into the immobilization channel. At this stage, the entrance and waste valves are fully opened while the exiting valve is partially closed, and other valves are kept closed. With a pressure-driven flow from the device inlet, a worm can be loaded into the immobilization channel. Once an immobilized worm is detected through image processing (see *Section 5.6.4*}), the entrance valve and the inlet driving pressure are automatically switched off to

minimize flow-induced worm movements during injection, and the injection valve is opened ("worm injection state" in *Table 5.5-1*) to allow the needle to reach the immobilized worm.

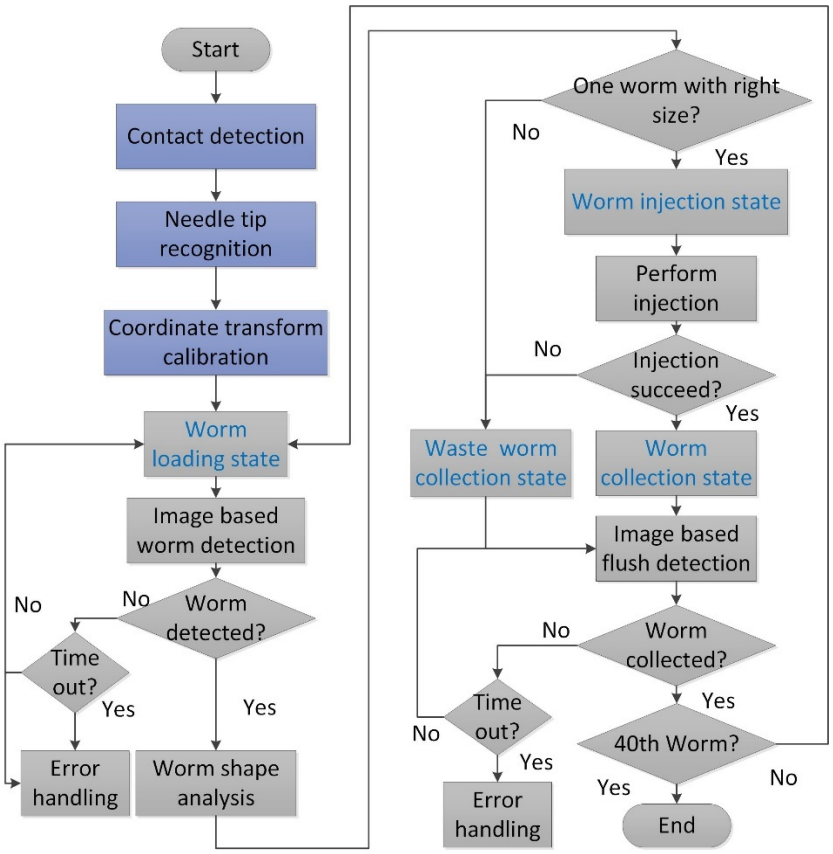


Figure 5-4 Flowchart of the robotic worm injection procedure.

Depending on the type of study requiring *C. elegans* injection, the location to deliver the injection materials inside the worm body could be different. The robotic system allows the user to identify the in-plane image coordinates of the target location on the computer screen through computer mouse clicking, and then controls the injection needle to penetrate the worm body and deliver a controlled amount of injection material to the desired location. If the material delivery is successful, the worm body will slightly expand along its longitudinal direction (see Supplementary Video 2). We have experimentally verified that this is a reliable indicator for a successful injection (see data in *Section* ***Error! Reference source not found.***). During injection, the user readily monitors the elongation of the worm body upon material delivery on the computer screen, and indicates to the system, through keyboard input, whether the current injection is successful. After injection, the injection valve is closed and the existing valve is opened. The pressure source connected to the

flush inlet is turned on, and the flush valve is opened so that the worm could be flushed out of the immobilization channel. For a successful injection, the worm collecting valve is opened to guide the injected worm to the collection outlet; otherwise, the waste valve is opened to let the worm reach the waste outlet ("worm collection/discard state" in *Table 5.5-1*). When the worm is visually detected to be flushed out of the immobilization channel, the system is switched back to the "worm loading state", and the next worm is loaded. This process is repeated until all the worms loaded to the device are injected. Supplementary Video 2 shows the automatic injection process.

Table 5.5-1 Operation states of the microfluidic device.

| System states | loading inlet | flushing inlet | entrance valve | injection valve | collection valve | exiting valve | flushing valve | waste valve |
|---|---|---|---|---|---|---|---|---|
| Worm loading state | on | off | on | off | off | partially off | off | on |
| Worm injection state | off | off | off | on | off | off | off | on |
| Worm collection/discard state | off | on | off | off | on | on | off/on | on/off |

## 5.6 System automation techniques

### 5.6.1 Autofocusing-based contact detection

In this system, the injection needle is required to be operated in the injection channel in the top layer of the microfluidic device, as shown in Figure 5-5. As a result, the vertical position of the needle is a critical factor that significantly influences the injection success rate, since injecting either the upper or lower portion of the worm body will increase the risk of needle tip slipping on the worm body (Figure 5-5). Thus, the optimal vertical level of the needle tip for injection is the middle position of the channel height (Figure 5-5).

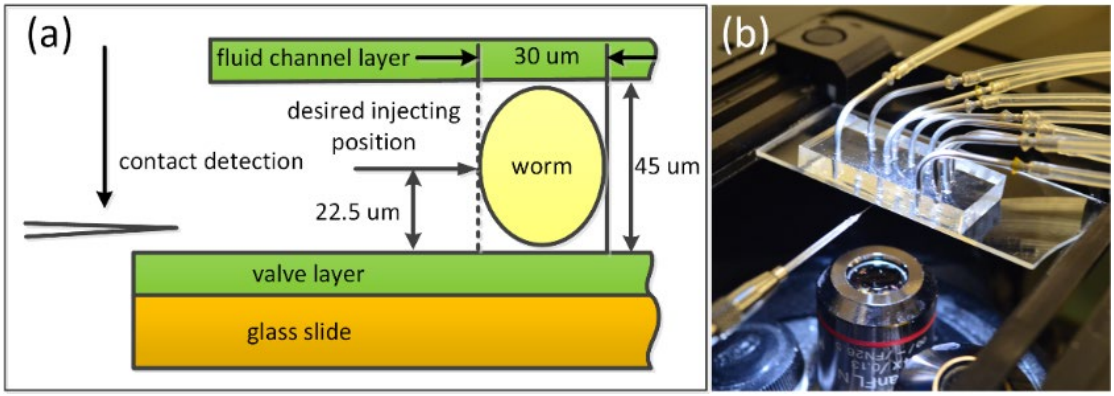


Figure 5-5 Autofocusing-based contact detection. (A) Schematic of determining the vertical injection position through contact detection. (B) Photograph of configuration of the injection needle and the photograph during contact detection.

A contact detection mechanism was developed based on Tenenbaum's autofocusing algorithm [21, 22], to detect the vertical position at which the needle tip contacts with the PDMS substrate. To improve the contact detection accuracy, a 40x objective was automatically switched into the optical path for imaging, providing a shallow depth of field of 2.2 $\mu m$. The image is first focused, through the microscope $z$-motor, on the PDMS substrate where the contact will take place. The injection needle tip, initially a few hundreds of micrometers above the PDMS substrate, is then lowered toward the PDMS substrate at a constant speed of 10 $\mu m$/s, during which its in-focus level is evaluated by calculating the following focus objective function:

$$F = \sum_{ROI_x} \sum_{ROI_y} (S_x(x,y)^2 + S_y(x,y)^2) \qquad (5.6\text{-}1)$$

where $S_x(x,y)$ and $S_y(x,y)$ are the convoluted images by the *Sobel* operators. As the injection needle tip is mounted horizontally, its in-focus image reveals sharp and clear edges, leading to the maximum focus objective function. The contact detection algorithm records the vertical position of the needle tip from which the needle tip image becomes in-focus, which corresponds to the vertical contact point of the tip and the substrate.

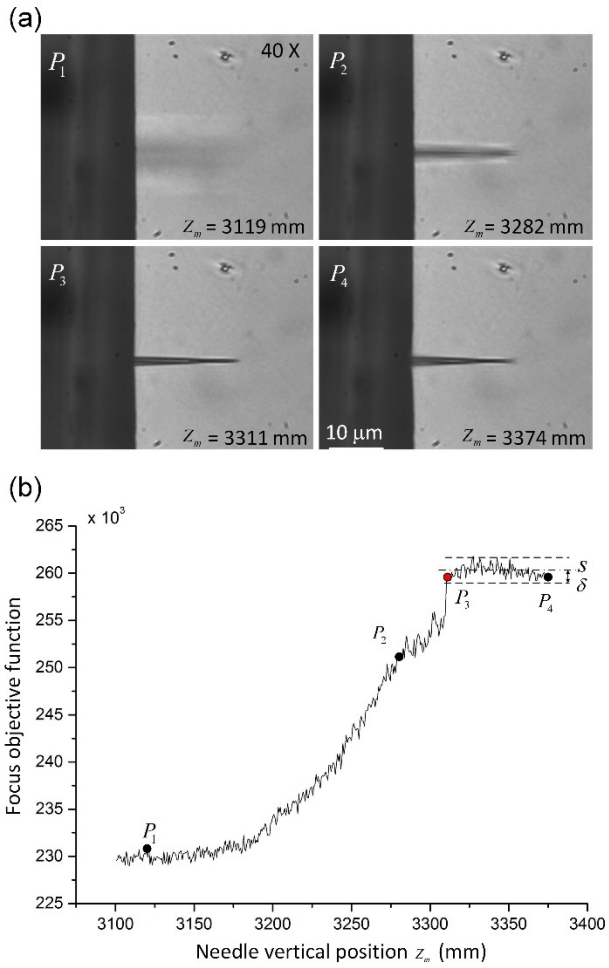


Figure 5-6 Experimental results of autofocusing-based contact detection. (a) Image frames of the needle tip at 40x at four different vertical positions. (b) Focus objective function vs. needle vertical position.

Figure 5-6 shows an image sequence (Figure 5-6(a)) of the needle tip captured during contact detection, and the corresponding values (Figure 5-6(b)) of the focus objective function as a function of the needle vertical position $Z_m$ (in the micromanipulator frame). When the needle tip is out of focus, only its blurred shadow can be observed ($P_1$ and $P_2$ in Figure 5-6(a)). The objective function $F$ gradually increases as the tip moves towards the focal plane (Figure 5-6(b)). Once the contact occurs, $F$ remains at a relatively stable level ($P_3$ and $P_4$ in Figure 5-6(a)) since the PDMS surface constrains the needle tip from lowering further. Our algorithm automatically detects the starting point of the stable level ($P_3$ in Figure 5-6(a)], and records the corresponding vertical contact position $Z_{mc}$.

$$Z_{mc} = argmin_{Z_m}\{F(Z_m) \geq \bar{s} - \delta\} \quad (5.6\text{-}2)$$

where $\bar{s}$ and $\delta$ are the average and standard deviation of the focus objective function in its stable level ($P_3$ and $P_4$ in Figure 5-6(a)), respectively. With the same microscope illumination condition, the threshold of $\bar{s} - \delta$ was found to remain at a stable value, and thus is effectively for determining the vertical contact position $Z_{mc}$. Compared with the contact detection algorithm proposed in our previous system in [18], this algorithm has been tested to be more reliable and also robust to illumination changes.

Ignoring the small contact-induced deformation of the PDMS substrate, the optimal vertical position for worm injection is defined as 22.5 $\mu m$ (half of the injection channel height) above the vertical contact position (Figure 5-5). The needle tip is then lifted to the optimal injection position, and the microfluidic device is moved towards the needle tip to insert it into the injection channel. In the meanwhile, the immobilization channel is moved into the FOV.

### 5.6.2 Visual detection of the needle tip

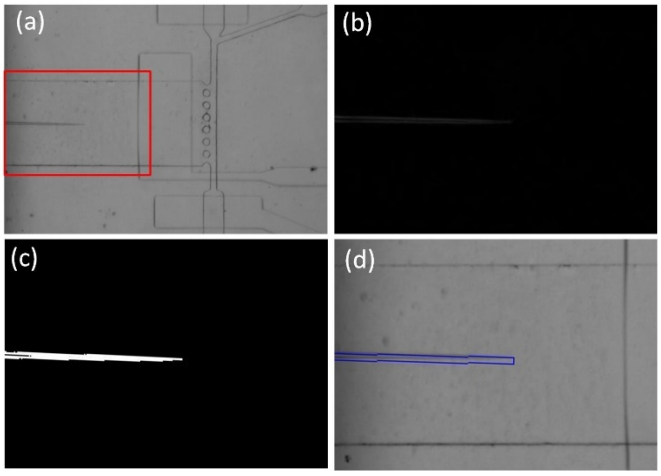


Figure 5-7 Image processing frames for needle tip recognition.

After contact detection, image coordinates of the needle tip need to be visually recognized for coordinate mapping between the micromanipulator frame and the image frame. To acquire a background image of the injection channel, the needle tip is temperately moved out of the channel, the system grabs a background image from the camera, and the needle tip is moved back to its initial position inside the injection channel (Supplementary Video 1). Then, a region of interest (ROI) including the needle tip (the red rectangle in Figure 5-7(a)) is selected by the user on the

computer screen, and tip recognition algorithm is applied to the selected ROI. The current ROI is subtracted by the corresponding portion of the previously grabbed background image to eliminate the background features, and the resultant image is shown in Figure 5-7(b). A Gaussian blur operator is applied to the resultant image to reduce the image noises. The dimension of the blur operator is selected to be 3 to avoid eroding the edge of the needle.

The denoised ROI is binarized through *Ostu* adaptive thresholding to identify the needle tip region (Figure 5-7(c)). *Canny* edge detection followed by rotated rectangle pattern fitting are then applied to the obtained binary ROI, and the fitted rectangle with the largest connected domain area is recognized as the needle area (Figure 5-7(d)). The rightmost pixel of the recognized needle area is identified as the needle tip.

### 5.6.3 Coordinate transformation calibration

In order to control the in-plane motion of the needle tip based on the visual feedback, the coordinate transformation between the image frame and the micromanipulator frame needs to be routinely performed. Considering the existence of small misalignments between the micromanipulator frame and the camera frame, we proposed a linear-regression-based calibration method to accurately determine the mapping relationship between the two frames.

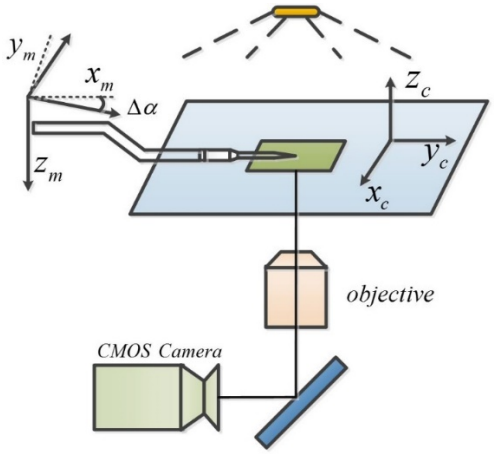


Figure 5-8 Coordinate frames of the robotic system.

As illustrated in Figure 5-8, the micromanipulator frame $x_m, y_m, z_m$ and the image frame $x_i, y_i$ have a small misalignment. Considering only in-plane motions of the needle tip during worm injection, it is easy to obtain that

$$P_m = kA^{2\times2}P_i + B^{2\times1} \tag{5.6-3}$$

where $k$ is a magnification scalar, and $A$ an orthogonal matrix subject to $A^TA = I$. $P_m = [x_m, y_m]^T$ and $P_i = [x_i, y_i]^T$ are the projected coordinates of a point in the micromanipulator frame and the camera frame, respectively. Here, we denote $kA$ as $\bar{A}$for simplicity.

To calibrate the coordinate mapping, the needle tip is moved by small displacements to multiple positions within the injection channel, and the system records in-plane coordinates of the tip's positions in: (i) the micromanipulator frame (from the position feedback of the micromanipulator): $(x_{m1}, y_{m1})$ ... $(x_{mn}, y_{mn})$;and (ii) the image frame (through visual recognition of the needle tip): $(x_{i1}, y_{i1})$ ... $(x_{in}, y_{in})$.The parameter $n$ is the number of tip positions. Then, the coefficient matrices of coordinate transformation $B$ and $\bar{A}$ can be determined by

$$[B \quad \bar{A}]^T = (X^TX)^{-1}X^T[P_x \quad P_y] \tag{5.6-4}$$

where

$$P_x = [x_{m1} \quad \cdots \quad x_{mn}]^T \tag{5.6-5}$$

$$P_y = [y_{m1} \quad \cdots \quad y_{mn}]^T \tag{5.6-6}$$

$$X = \begin{bmatrix} 1 & x_{i1} & y_{i1} \\ \vdots & \vdots & \vdots \\ 1 & x_{in} & y_{in} \end{bmatrix} \tag{5.6-7}$$

Note that all the recorded positions: $(x_{i1}, y_{i1})$ ... $(x_{in}, y_{in})$. should not be in a straight line, which ensures that $rank(X) = 3$ and $X^TX$ is invertible. In our experiments, we moved the needle tip to a grid of 3x3 positions with a pitch of 115$\mu m$, and carried out the coordinate mapping calibration in real time. Once the calibration is completed, the system is ready for worm injection.

### 5.6.4 Visual detection of worm loading and unloading in the immobilization channel

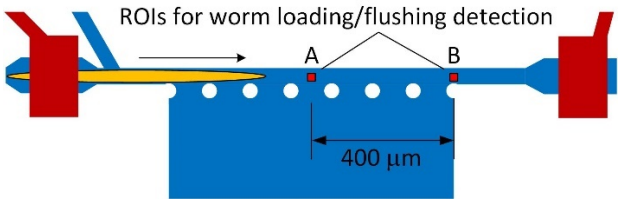


Figure 5-9 Schematic of the regions of interest (ROIs) inside the immobilization channel for visual detection of worm loading and unloading in the injection channel.

During automated worm injection, the loading and unloading of a worm in the immobilization channel will be monitored by an image processing algorithm so that the on-chip valves can be activated accordingly to switch between different operation states (*Table 5.5-1*). The algorithm constantly monitors the average pixel intensities of tow ROIs (10x10 pixels) in the immobilization channel (Figure 5-9). When a worm is loaded into the injection channel, its body will fill the two ROIs and makes their average intensities significantly decrease (because of the darker worm body than channel background). By comparing the current average intensities of the two ROIs with that of the channel background, the loading and unloading of the worm can be detected.

The worm loading and unloading events are defined by the following two inequalities, respectively:

$$\frac{1}{4s^2}\sum_{P_x-s}^{P_x+s}\sum_{P_y-s}^{P_y+s}(I_0(x,y)-I(x,y)) \geq \delta_1 \qquad (5.6\text{-}8)$$

$$\frac{1}{4s^2}\sum_{P_x-s}^{P_x+s}\sum_{P_y-s}^{P_y+s}(I_0(x,y)-I(x,y)) < \delta_2 \qquad (5.6\text{-}9)$$

where $I_0(x,y)$ and $I(x,y)$are background image and current image correspondingly. $\delta_1$and $\delta_2$ are experimentally determined thresholds. $s = 5$ in the experiment.

We selected the two ROIs in the middle (ROI-A) and right-end (ROI-B) positions of the immobilization channel (Figure 5-9). When the average intensities of both ROIs decrease by a value larger than a threshold, it indicates a worm has been completely loaded into the immobilization channel. The recovery of the ROI average intensities back to its original background value means the worm have been flushed out of the immobilization channel. Monitoring the average intensities of the ROIs avoids any false worm detection caused by small particles passing through the ROIs. Under the illumination we used in our experiments, the average intensity of each ROI drops by 120—150 for most worms. Leaving some quantity margins, $\delta_1 = 80$ and $\delta_1 = 30$ were used in our experiments.

### 5.6.5 Injection volume control

The delivered volume of injection material is determined by the injection pressure level, the pressure pulse duration, and the diameter of the needle tip. The injection volume control is critical to achieve consistent biological results from the injected worms, and can also enable the

quantitative study of dose effect on specific biological processes of the injection worm. Using a needle tip with typical outer and inner diameters of 5 $\mu m$ and 3.5 $\mu m$ respectively, we calibrated the injection volume as a function of the pressure level and the pressure pulse duration. Deionised water was used as the injection sample for volume calibration. By supplying a short pressure pulse to the injection needle, a small spherical water drop was delivered into mineral oil, and the shape of the water drop was immediately measured at 10x using *Hough* circle pattern fitting. Figure 5-10 shows the experimental results of injection volume calibration (n = 5).

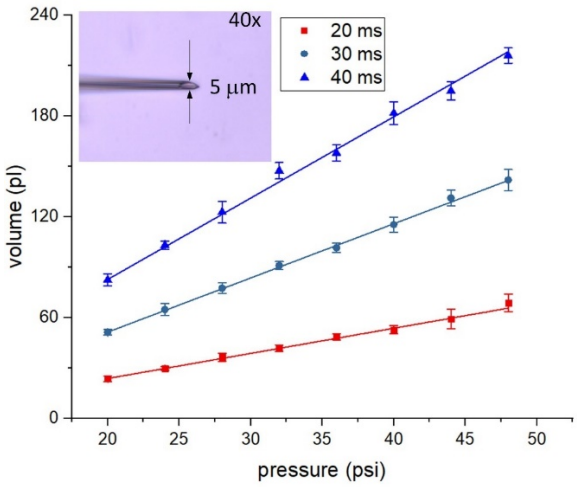


Figure 5-10 Calibration results of the injection volume as functions of injection pressure and pressure pulse width.

### 5.6.6 Worm culture and preparation

The *C. elegans* used in our experiments was wild type N2 strain cultured using on a standard procedure [23]. Microinjection is usually performed on young adult worms, and we synchronized young adult worms by culturing worm embryos for 54 hours at $20^0$C on agar plates seeded with OP50 *E. coli* [19]. Before injection, the young adult worms with diameters of 35--40 $\mu m$were selected and sequentially transferred into three droplets of M9 medium to wash off the *E. coli* and other small impurities from their bodies, and finally loaded into the inlet of the microfluidic device using a pipette. All the young adult worms were injected within 30 min after they were transferred from the culture plate.

## 5.7 Experimental results and discussions

### 5.7.1 Experimental results

In the experiments, FITC fluorescent dye was first injected to visualize the material delivery into the worm body through fluorescence imaging. The injection/retraction speeds were both 5000 $\mu m$. By applying a 30 $ms$ pulse of 31 psi pressure to the injection needle (inner diameter: 3.5 $\mu m$), 85 pl of FITC dye was injected into the worm body. As shown in Figure 5-11(a), the fluorescence intensity of the proximity of the injection location inside the worm body is much higher than that of the channel background, indicating successful delivery of the FITC dye. Note that the injection channel also shows a low green fluorescence because of the diffusion of FITC dye from the needle tip into the injection channel. Upon the material delivery, it was also observed that the worm body expanded along its longitudinal direction (see Supplementary Video 2). To verify if the worm body expansion could be used as a reliable indicator for material delivery, another 20 worms were injected with the FITC dye, and the correlation of the worm body expansion and the successful material delivery was found in all the 20 injections. Thus, the worm body expansion upon injection was used in the following experiments to count the injection success rate.

To evaluate the system performance, deionized water was automatically injected into 240 worms (6 batches and 40 worms/batch). The automated worm injection process was shown in Supplementary Video 2. Two performance parameters were quantified based on the experiment data: injection speed and success rate. The success of an injection was evaluated by visually observing the worm body expansion upon injection, and the success rate is defined as the ratio of the number of successfully injected worms (with body expansion) to the total number of injected worms.

The system demonstrated an average injection speed of 6 worm/min (average processing time: 9.97 s/worm) with a success rate of 78.8%, and these parameters are both superior over the performance of manual injection (speed: 0.25 worms/min, success rate: ~30%; data provided by a proficient worm injection operator [24]). During injection, the user monitored the injection of each worm and instruct the system (through keyboard input) whether or not the current injection was successful, and the system then sorted the successfully injected worms into the sample collection outlet of the microfluidic device. Therefore, the post-sorting success rate is 100%, meaning that all the worms in the sample collection outlet were successfully injected. Among the average worm

processing time of 9.97 s, the average worm loading, injection, and flushing time is 2.7 s, 5.51 s, 1.76 s respectively.

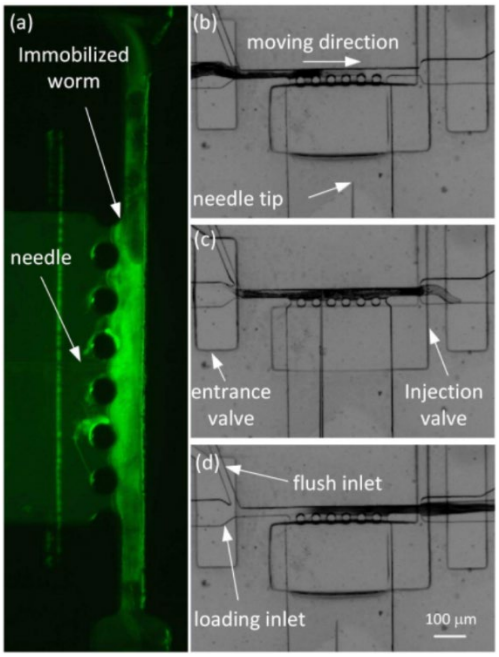


Figure 5-11 Photographs of the worm injection process. (a) Fluorescent image of the worm body right after fluorescent dye is delivered. (b) Worm loading. (c) Worm immobilization and injection. (e) Worm flushing after injection.

The failure modes of the system causing the 21.2% failed injections include: (i) no material delivery upon injection (no worm body expansion; 18.2%); and (ii) simultaneous loading of two worms into the immobilization channel (3%). The unsuccessful material delivery could be possibly due to temporary clogging of the needle and/or non-penetration of the worm body. The loading of two worms can be further alleviated by better size synchronization of the worms loaded into the microfluidic device.

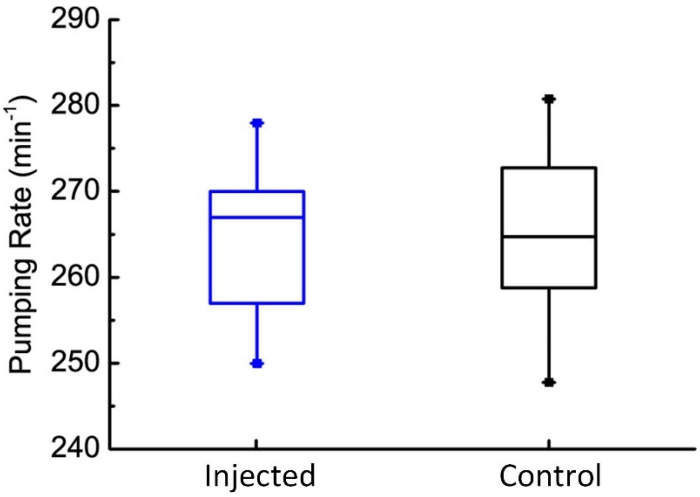


Figure 5-12 Experimental results of the pharynx pumping rates of the injected worm group and the control group.

From Supplementary Video 2, one can observe that there is a small amount of lysis from the worm body upon retracting injection needle. Accordingly, we also examined the potential physiological impact imposed on the injected worms through measurement of the worm's pharynx pumping rate. The pumping rate of the worm pharynx corresponding its food intake, and is an important measure of the worm's physiological condition. As shown in Figure 5-12, the pumping rates measured from the injected worms are 240-280 pumps/min, which is in the common range of that of the wild type N2 worms [25]. In addition, the pumping rate data from the injected and control group do not reveal significant difference ($p>0.3$).

## 5.8 Discussion

In conventional worm injection, a young adult worm is transferred from the petri-dish to a glass slide under the microscope, on which a drop of oil is placed for worm immobilization. Then, a micromanipulator is controlled manually to inject the worm. The worm preparation and injection are both time-consuming and tedious, and requires significant training of the operator. Our experiment on robotic injection of 240 *C. elegans* worms demonstrated that the developed system is capable of automatically injecting worms at a speed of 9.97 s per worm with a pre-sorting success rate of 78.8%. The high operation efficiency mainly results from the continuous and efficient worm loading and immobilization (2.7 s/worm). The time required for worm injection (5.5 s/worm) and sorting (1.76 s/worm) is longer than the worm loading time since the injection

and sorting speeds are limited by several parameters such as the maximum speed of the micromanipulator, the response time of the microfluidic valves, and the time required for the user to indicate a successful injection.

Note that human involvement is still needed to identify the injection location in the immobilized worm body and indicate a successful injection during conscious operation of the system. Because of the round section shape, the worm orientation along the dorsal-ventral axis cannot be controlled during immobilization. As a result, it remains difficult to detect the worm gonad via computer vision, since the morphology within the worm body varies for every individual worm. It is possible to integrate worm orientation control mechanisms into the microfluidic device [26], which could make the visual recognition of the worm gonad feasible.

## 5.9 Conclusions

We presented an automated robotic system for high-throughput injection of *C. elegans*. A vision-based contact detection algorithm was adopted to determine the optimal injection position along the $z$-axis. Based on effective image processing algorithm, the needle tip was efficiently identified online from the microscope camera image for accurate position control. In addition, a multi-layer PDMS device was designed to rapidly load, immobilize, flush, sort, and collect the worms. Experiments based on the injection of 240 worms showed that the system can perform *C. elegans* injection at a speed of 9.97s per worm with a success rate of 78.8%.

## 5.10 Reference


[1] M. Rieckher, N. Kourtis, A. Pasparaki, and N. Tavernarakis, "Transgenesis in Caenorhabditis elegans," in *Transgenesis techniques*: Springer, 2009, pp. 21-39.

[2] L. A. Berkowitz, A. L. Knight, G. A. Caldwell, and K. A. Caldwell, "Generation of stable transgenic C. elegans using microinjection," *Journal of visualized experiments: JoVE,* no. 18, 2008.

[3] Z. Ni, A. Bolopion, J. Agnus, R. Benosman, and S. Régnier, "Asynchronous event-based visual shape tracking for stable haptic feedback in microrobotics," *IEEE Transactions on Robotics,* vol. 28, no. 5, pp. 1081-1089, 2012.

[4] X. Liu *et al.*, "Automated microinjection of recombinant BCL-X into mouse zygotes enhances embryo development," *PloS one,* vol. 6, no. 7, p. e21687, 2011.

[5] Y. Sun and B. J. Nelson, "Biological cell injection using an autonomous microrobotic system," *The International Journal of Robotics Research,* vol. 21, no. 10-11, pp. 861-868, 2002.

[6] A. Ghanbari, W. Wang, C. E. Hann, J. G. Chase, and X. Chen, "Cell image recognition and visual servo control for automated cell injection," in *2009 4th International Conference on Autonomous Robots and Agents*, 2009, pp. 92-96: IEEE.

[7] W. Wang, X. Liu, D. Gelinas, B. Ciruna, and Y. Sun, "A fully automated robotic system for microinjection of zebrafish embryos," *PloS one,* vol. 2, no. 9, p. e862, 2007.
[8] W. H. Wang, X. Y. Liu, and Y. Sun, "High-throughput automated injection of individual biological cells," *IEEE Transactions on automation science and engineering,* vol. 6, no. 2, pp. 209-219, 2009.
[9] Z. Lu, P. C. Chen, J. Nam, R. Ge, and W. Lin, "A micromanipulation system with dynamic force-feedback for automatic batch microinjection," *Journal of micromechanics and microengineering,* vol. 17, no. 2, p. 314, 2007.
[10] X. Liu, Z. Lu, and Y. Sun, "Orientation control of biological cells under inverted microscopy," *IEEE/ASME Transactions on Mechatronics,* vol. 16, no. 5, pp. 918-924, 2011.
[11] H. B. Huang, D. Sun, J. K. Mills, and S. H. Cheng, "Robotic cell injection system with position and force control: Toward automatic batch biomanipulation," *IEEE transactions on robotics,* vol. 25, no. 3, pp. 727-737, 2009.
[12] Y. Zhang, K. K. Tan, and S. Huang, "Vision-servo system for automated cell injection," *IEEE transactions on industrial electronics,* vol. 56, no. 1, pp. 231-238, 2009.
[13] H. Maruyama, N. Inoue, T. Masuda, and F. Arai, "Selective injection and laser manipulation of nanotool inside a specific cell using optical ph regulation and optical tweezers," in *2011 IEEE International Conference on Robotics and Automation*, 2011, pp. 2674-2679: IEEE.
[14] C. L. Gilleland, A. T. Falls, J. Noraky, M. G. Heiman, and M. F. Yanik, "Computer-assisted transgenesis of Caenorhabditis elegans for deep phenotyping," *Genetics,* vol. 201, no. 1, pp. 39-46, 2015.
[15] M. Nakajima, T. Hirano, M. Kojima, N. Hisamoto, M. Homma, and T. Fukuda, "Direct nano-injection method by nanoprobe insertion based on E-SEM nanorobotic manipulation under hybrid microscope," in *2011 IEEE International Conference on Robotics and Automation*, 2011, pp. 4139-4144: IEEE.
[16] M. Nakajima *et al.*, "Local Nano-injection of Fluorescent Nano-beads inside C. elegans based on Nanomanipulation," in *2012 IEEE/RSJ International Conference on Intelligent Robots and Systems*, 2012, pp. 3241-3246: IEEE.
[17] X. Zhao, F. Xu, L. Tang, W. Du, X. Feng, and B.-F. Liu, "Microfluidic chip-based C. elegans microinjection system for investigating cell–cell communication in vivo," *Biosensors and Bioelectronics,* vol. 50, pp. 28-34, 2013.
[18] X. Dong, P. Song, and X. Liu, "An automated robotic system for high-speed microinjection of Caenorhabditis elegans," in *2015 IEEE International Conference on Robotics and Automation (ICRA)*, 2015, pp. 996-1001: IEEE.
[19] P. Song, X. Dong, and X. Liu, "A microfluidic device for automated, high-speed microinjection of Caenorhabditis elegans," *Biomicrofluidics,* vol. 10, no. 1, p. 011912, 2016.
[20] M. A. Unger, H.-P. Chou, T. Thorsen, A. Scherer, and S. R. Quake, "Monolithic microfabricated valves and pumps by multilayer soft lithography," *Science,* vol. 288, no. 5463, pp. 113-116, 2000.
[21] X. Liu, W. Wang, and Y. Sun, "Dynamic evaluation of autofocusing for automated microscopic analysis of blood smear and pap smear," *Journal of microscopy,* vol. 227, no. 1, pp. 15-23, 2007.

[22] Y. Sun, S. Duthaler, and B. J. Nelson, "Autofocusing in computer microscopy: selecting the optimal focus algorithm," *Microscopy research and technique,* vol. 65, no. 3, pp. 139-149, 2004.
[23] L. R. Girard *et al.*, "WormBook: the online review of Caenorhabditis elegans biology," *Nucleic acids research,* vol. 35, no. suppl_1, pp. D472-D475, 2006.
[24] C. Juan, *private communication,* 2014.
[25] X. Ai, W. Zhuo, Q. Liang, P. T. McGrath, and H. Lu, "A high-throughput device for size based separation of C. elegans developmental stages," *Lab on a Chip,* vol. 14, no. 10, pp. 1746-1752, 2014.
[26] I. de Carlos Cáceres, N. Valmas, M. A. Hilliard, and H. Lu, "Laterally orienting C. elegans using geometry at microscale for high-throughput visual screens in neurodegeneration and neuronal development studies," *PloS one,* vol. 7, no. 4, p. e35037, 2012.

# Link between chapter 5 and chapter 6

In the previous two chapters, the system structures, microfluidic device designs, the image processing algorithms, and the robotic micromanipulation techniques for the automated *C. elegans* screening and automated *C. elegans* microinjection systems are discussed respectively. Both these two systems are microfluidic-based micromanipulation systems designed to replace the labor-intensive and time-consuming experiments in worm biology laboratories with standard operations automated by machines.

In this chapter, another activation method for the manipulation of *C. elegans* — light stimulated robotic micromanipulation is introduced. Based on a 1024x768 digital micromirror device (DMD), a pattern light illumination system on an inverted microscope is constructed with the capability of generate spatial and temporal laser beams with a fully programmable manner. This system is built with the resolution of 17 μm/3 μm under 4x /20x objectives, which can target desired single cell or tissues while the rest of the body remain unexcited. With this system, a live worm is converted into an artificially controllable microrobot-animal through muscle optogenetic method. Important bio-mechanics result for the generation of thrust force for serpentine locomotion is derived and verified by dynamic simulation and optogenetic experiments. The detailed system structures, muscle activation methods, and close-loop control approach are discussed in the next chapter.

# Chapter 6

# Towards a Live Soft Microrobot: Light-Driven Locomotion Control of *Caenorhabditis Elegans*

# Chapter 6: Towards a live soft microrobot: light-driven locomotion control of *Caenorhabditis elegans*

**X. Dong[1,2], S. Kheiri[2], Y. Lu[3,4], Z. Mei[3,4], X. Liu[2,5]***

*[1]Department of Mechanical Engineering, McGill University, 817 Sherbrooke Street West, Montreal, Quebec, Canada H3A 2K6*

*[2]Department of Mechanical and Industrial Engineering, University of Toronto, 5 King's College Road, Toronto, Ontario, Canada MS 3G8*

*[3]Lunenfeld-Tanenbaum Research Institute, 600 University Avenue, Room 870*

*Toronto, Ontario, Canada M5G 1X5*

*[4]Department of Physiology, University of Toronto, 1 King's College Circle, Toronto, Ontario, Canada M5S 1A8*

*[5]Institute of Biomaterials and Biomedical Engineering, University of Toronto, 164 College Street, Toronto, Ontario, Canada, M5S 3G9*

*corresponding author: (xyliu@mie.utoronto.ca)

*To be submitted.*

## 6.1 Summary

Learning from the locomotion of existing natural microscale organisms is the most effective strategy for creating small-scale robots, as the common macro actuation methods are usually not functioning in the micro-world due to the small Reynolds number and the scaling of physical effects [1-4]. Recently, bio-inspired small-scale robots have demonstrated amazing locomotion capabilities, and examples include the flagella-propelled micro-swimmer [5], the light-actuated micro-earthworm [6], the magneto-aerotactic bacteria micro-carrier [7], and many others [8-10]. These bio-inspired microrobots, however, are either developed to mimic biological locomotion patterns with artificial materials or by harnessing the organism locomotion with artificial structures. Here we introduce a new approach for creating an untethered, highly-controllable soft micro robo-worm directly from a live nematode worm *Caenorhabditis elegans*. The worm is paralyzed to shut down the neuronal systems, while its muscular cells remain excitable and can be stimulated optogenetically to reproduce its locomotion. Through dynamic modelling and experimental

verification of worm crawling, we found that the phase difference between the worm body curvature and the muscular activation pattern generates the thrust force for crawling locomotion. By reproducing the phase difference on the muscular groups via optogenetic excitations with patterned lights, we successfully emulated the worm crawling behaviors such as straight forward crawling, shallow turnings and omega turning, in a programmable manner. Furthermore, with real-time visual feedback of the controlled worm crawling, we realized closed-loop regulation of the movement direction and destination on a paralyzed worm. Our integrated approach for muscular excitation and locomotion control enlightens a new route for microrobot development—the micro robo-worm, which converts a natural live worm into a controllable microrobot.

## 6.2 Main text

Using a *C. elegans* strain that specifically expresses channelrhodopsin in muscle cells, we can optogenetically excited specific groups of muscle cells by blue light in the presence of trans-retinol [11] (Supplementary Information S1; Figure 6-4), with only the illuminated body muscles act as soft actuators for locomotion. To override muscle cell's endogenous inputs from the nervous system, we treated the worm by ivermectin, an agonist of glutamate-gated chloride channel so that neurons were hyperpolarized while muscles remained excitable (Supplementary Information S1). Thus, instead of commanding the motion of muscles with motor neuron input from the worm itself, our approach is to program the micropattern of a blue laser beam to induce artificially muscular contraction (Figure 6-1a & 1b) and reproduce the serpentine motion on a paralyzed *C. elegans*.

The understanding of the biomechanical interaction between the worm body and the environment is necessary to identify the muscular patterns that effectively drive the crawling of *C. elegans*. To start with, we examined the muscular activity for the moving of normal worms through muscle calcium imaging (Figure 6-1c), and found that there always existed a mis-alignment between the muscular activity and the worm body shape during forward movement (Figure 6-1c) [12]. Moreover, this mis-alignment reversed its direction when the worm crawled backward (Figure 6-1c). Since both the muscular activity and the body curvature are close to a sinusoidal shape, we define this mis-alignment as the phase difference $\Delta\varphi$ for the *C. elegans* crawling locomotion. Inspired by the phase difference, we built a mathematical model for the release of muscular energy (Supplementary Information S2; Figure 6-5 to Figure 6-9)), and derived the explicit expression of the *C. elegans* crawling thrust force $F_m$ as

$$F_m = -\frac{2\pi^2}{L}\rho M_0 \mathrm{Sin}(\Delta\varphi) \quad (6.2\text{-}1)$$

where $L$ is the undulation body wavelength, $\rho$ is the attack angle of the movement trajectory, $M_0$ is the amplitude of muscle torque. This relationship was further verified by dynamics simulation of the worm serpentine locomotion and characterization experiments of the worm crawling speed (Supplementary Information S3-S6; Figure 6-8 to Figure 6-13). Consequently, as illustrated by *Equation* (6.2-1), to generate artificial serpentine locomotion on a robo-worm, the phase difference must be reproduced through programmed optogenetic stimulation of its muscle cells.

To accurately stimulate selected muscular groups and reproduce the phase difference on the robo-worm, we developed a patterned-light illustration system integrated with two closed control loops: the laser micropattern formation loop and the worm locomotion tracking loop (Figure 6-1; Figure 6-14; Supplementary Information S7). The laser beam, initiated from a 473 blue laser source, was enlarged via a 10× beam expander and reflected by a 1024×768 pixel digital micromirror device (DMD) to form a computer-controlled laser micropattern. The micropatterned laser beam was processed by a 4f optical system and a tube lens-objective couplet to shrink its size and focus it on the worm body. A near infrared (NIR) lamp house (transmission wavelength > 700 nm) was used for worm shape imaging, which avoids activation of ChR2 unintentional during experiments. The worm position and morphologic features were analysed real-time from the microscopic vision and feed back to the system controller for automatically keeping the worm body in the microscope field of view (by driving the X-Y stage) and conducting spatial and temporal stimulation of the worm muscles to control its locomotion (Figure 6-1d; Figure 6-15). This design provides a high projection resolution of 12.3 μm and 3 μm with 4× and 20× objectives respectively, as well as a large working space of 114 mm × 75 mm motorized by the X-Y stage (Figure 6-16). In addition, enabled by multi-thread programming, this system achieved a closed-loop illumination updating rate of 40 fps with 8-bit adjustable beam intensity, which surpasses the previously reported optogenetic worm stimulation systems [13, 14] (Supplementary Information S8-S9; Figure 6-16; Figure 6-17; Supplementary Video 1).

With this system, we quantitatively tested the curvature of the activated worm body segments as a function of the laser intensity for muscle stimulation. Upon illumination, the targeted worm body muscle segment contracted rapidly within 1.5 s and held at its maximum contraction curvature (Figure 6-1e; Supplementary Video 2). Once the laser was off, the body bending curvature reduced

gradually, and finally remained at a non-zero stable value. Without ivermectin, muscle relaxation is actively potentiated by inhibitory neurotransmitter GABA, released by the D-type motor neurons. For the robo-worm, muscle relaxation depends on a much slower process of dissipation of intracellular $Ca^{2+}$ [15], until the muscular force is balanced with the external friction on agar substrate (Figure 6-1e). To further investigate the muscle bending properties, we stimulated different body segments with various laser intensity. Higher laser intensity induced a stronger muscular contraction (Figure 6-1h, Supplementary Video 2), with the ventral and dorsal body side exhibited difference in sensitivity (Figure 6-1f). Chloride channels affected by ivermectin may be expressed not only in neurons, but also unevenly in body wall muscles [16], which may account for the difference in response between the ventral and dorsal sides (Figure 6-1f). The characterized muscular contraction properties serve as the actuator response characteristic for our design of the worm locomotion controller.

To simplify the laser micropattern control, the sinusoidal muscular activation curve was binarized as stripe patterns existing alternatively on the dorsal and ventral side of the worm body (Figure 6-1g; Figure 6-2a; Figure 6-12; Supplementary Information S5). By scanning the patterned laser beams continuously from the head to tail, we emulated the phase difference $\Delta\varphi$ on the robo-worm, and successfully generated continuous serpentine locomotion of the robo-worms on an agar substrate (Figure 6-1i; Supplementary Video 3). Since a stimulated muscle segment remained partially bent after the laser stimulation was off, the crawling speed of a robo-worm (0~50 μm/s; Figure 6-13a) was slower than a natural worm. The effective stimulation of one robo-worm lasted for no more than 10~15 minutes, which may be resulted from muscle fatigue, ion concentration equilibrium across the membrane, or exhaustion of ATR. Post-experiment robo-worms were able to recover to their normal state after being cultured on non-ivermectin plates overnight (Supplementary Information S1).

Based on the experiments for optogenetically generating serpentine locomotion of a *C. elegans*, we calculated the phase difference and the resultant crawling speed under various laser scanning speeds. In the experiment, the measured worm moving speed reduced monotonically as the calculated phase difference $\Delta\varphi$ amplitude decreased within $(-\frac{\pi}{2}, 0)$ (Equation (6.2-1)). The experimental results for the stimulated crawling locomotion, in turn, support our proposed theory for thrust force generation (Figure 6-13; Supplementary Information S6).

Similar to the locomotion of a natural worm, the stimulated undulation pattern of a robo-worm swings alternately to the ventral and dorsal sides repetitively (Figure 6-1h). When the laser beam was initiated at the tip of the head, the head bends towards stimulated side (Supplementary Video S3). The bending deepens continuously as the beam spot scans along the head-to-tail direction until the next laser beam starts to stimulate the opposite side at the head tip. The general moving direction, therefore, is determined by the angle bias of the head region (L/2 length portion from the head tip), while the body segments follow its adjacent anterior region to provide thrust during forward movement [17, 18] (Figure 6-2a; Figure 6-12).

From a robotic perspective, the crawling of natural *C. elegans* consists of 5 basic behavioural motifs: forward crawl, backward crawl, shallow turn (slight turnings on the crawling path [19]), gradual turn, and omega turn. Since the body contractions are adjustable with the stimulation laser intensity (Figure 6-1f), we attempted to mimic the natural crawling pattern by manipulating the intensity amplitude of the laser beam illuminated in the head region, with fixed beam intensities at the body to provide stable thrust force (Figure 6-2a). Through open-loop locomotion trigger, we first identified a balance couplet of stimulation intensities that induce equal bending curvatures and waving angles on the dorsal and ventral side (dorsal intensity = 1, ventral intensity = 0.18; Figure 6-2b3). Applying the balance intensity couplet repetitively to the head region, the robo-worm was able to move in a straight line (Figure 6-2b2; Supplementary Video 5). The curvature heatmap[20], which quantifies the bending curvature of along the body centreline, shows that both the natural (Figure 6-2b1; Figure 6-2b5) and artificial (Figure 6-2b2; Figure 6-2b4) forward crawling exhibited uniformed patterns. Shallow turns were achieved by increasing or decreasing the intensity of a single laser pattern on the straight moving route, respectively (Figure 6-2c and Figure 6-2d; Supplementary Video 5), as shown in the curvature map of both natural and induced shallow turns (labelled in Figure 6-2c4, Figure 6-2c5; Figure 6-2d4, Figure 6-2d5). Corresponding to the curvature map, decreased (Figure 6-2c3) and increased (Figure 6-2d3) bending angles are measured respectively, at the manipulated laser patterns. Further, gradual turns were reproduced by repetitively stimulating the worm head with biased intensity couplet (Figure 6-2e; Supplementary Video 5). Omega turn was achieved by increasing the intensity and width of a single laser pattern throughout its illumination from the head to tail (Figure 6-2f; Supplementary Video 5), shown as a dark and wide stripe in the curvature map for both natural and controlled movement (Figure 6-2f4, Figure 6-2f5), with a decrease bending angle observed in the control

measurement (Figure 6-2f3). Thus, artificially controlled locomotion patterns resembled the normal locomotion in both the movement path and bending curvature map (Figure 6-2). We reasonably extrapolate that the laser patterns we used could serve as the replacement of a normal worm's neuronal inputs during crawling, thus enabling the programming and control of a paralyzed worm as a live soft microrobot.

Based on the locomotion control scheme, backward crawling could be similarly emulated by reversing direction of the moving laser pattern, as shown in the fluorescent image of the muscular activity (Figure 6-1c). However, the tail of robo-worms in our experiments could not be stimulated to swing as the head. This could be caused by the relative low expression of ChR2 or smaller amount of myosin in the tail muscles.

Besides mimicking the natural nematode crawling locomotion, we attempted to enable the robo-worm with the ability of automatically seeking its destination, using vision-based closed-loop control technique. The worm locomotion status and morphologic features were calculated in real time from the images grabbed by the microscope camera (Figure 6-1d; Figure 6-19; Supplementary Information S10). Based on the visual feedback, we modelled the kinematics of the serpentine scrawling mathematically as a zig-zag curve characterized by the dorsal and ventral bending angles $\alpha_i, \beta_i$ (Figure 6-18), where $\alpha_i, \beta_i$ are regulated by the intensity of the laser intensity $P_D(i)$ and $P_V(i)$. The moving direction of the worm is defined as the vector direction of two adjacent points with the same phase on the zig-zag route ($d_i$ in Figure 6-18a). We consequently conclude the control objective as a two-input-one-output system with the input $u(i) = [P_D(i)\ P_V(i)]^T$ and the output $y(i) = d(i)$. Within one zig-zag period, we were able to control the moving direction by manipulating the intensity of each laser beam, which is simply formulated as

$$d(i+1) = d(i) + \big(\beta(i) - \alpha(i)\big) = d(i) + \Big(f_V\big(P_V(i)\big) - f_D\big(P_D(i)\big)\Big) \qquad (6.2\text{-}2)$$

where $f_D$ and $f_V$ are the muscle sensitivities to lasers on the dorsal and ventral sides, respectively. A predictive-P control scheme was proposed for regulating the moving direction $d(i)$ and the moving destination (Figure 6-18b, Figure 6-19, Supplementary Information S11). Specifically, as shown in Figure 6-18b, for the vertical reference direction $r_{ref}$, higher intensity $P_D$ were adopted for the current control cycle to reduce the bending angle $\alpha$, so that the moving direction $d$ was aligned closer to the reference $r_{ref}$.

Using the closed-loop control scheme, we regulated the moving direction (Figure 6-3a) and the destination (Figure 6-3b) of the robo-worm. For moving direction control, our experiments demonstrated that optogenetically-controlled worms with random initial crawling directions (Figure 6-3a) were regulated to eventually crawl horizontally after small overshots (Figure 6-3a1; Supplementary Video 6). For destination regulation, the robo-worms were also able to move to pre-designed destinations under the predictive-P controller, as shown by the three bathes of controlled crawling from a fixed origin A to the same destination B (Figure 6-3b; Supplementary Video 7). On an agar substrate, we defined a virtual wall with a small opening of virtual gate and defined a destination on the other side of the wall. By specifying an intermediate destination at the virtual gate (point O in Figure 6-3c), the worms showed the capability of passing through the obstacle to reach pre-defined destinations (Figure 6-3c; Supplementary Video 8).

Furthermore, we also demonstrated the controlled navigation of a worm passing through a maze. A PMMA thin film was laser-cut into a maze shape and placed on an agar substrate (Figure 6-3d2). To achieve the controlled maze navigation, we specified a series of intermediate destinations along the desired navigation path as the guiding points for worm locomotion control (P1 to P5 in Figure 6-3d1). Through point-to-point position control, we guided the worm to crawl through the maze (Figure 6-2d; Figure 6-20; Supplementary Video 9). The vision-based close-loop control scheme enables the robo-worm with the 'sense of space' to navigate through obstacles to reach pre-defined destinations. With this technology, we converted a paralyzed worm into a live, programmable robo-worm with control of its crawling direction and destination.

Animals are the best robots, especially in the micro-world [1, 2]. In this paper, we managed to interrupt the sensorimotor program in a live worm and replaced it with engineered visual sensing, feedback control, and optogenetic excitation loop to create a live microrobot. Besides it prospers in robotics, we believe that with this technology, more bio-mechanics phenomena and the underlying neuronal basis for the nematode serpentine crawling could be further investigated.

## 6.3 Figures

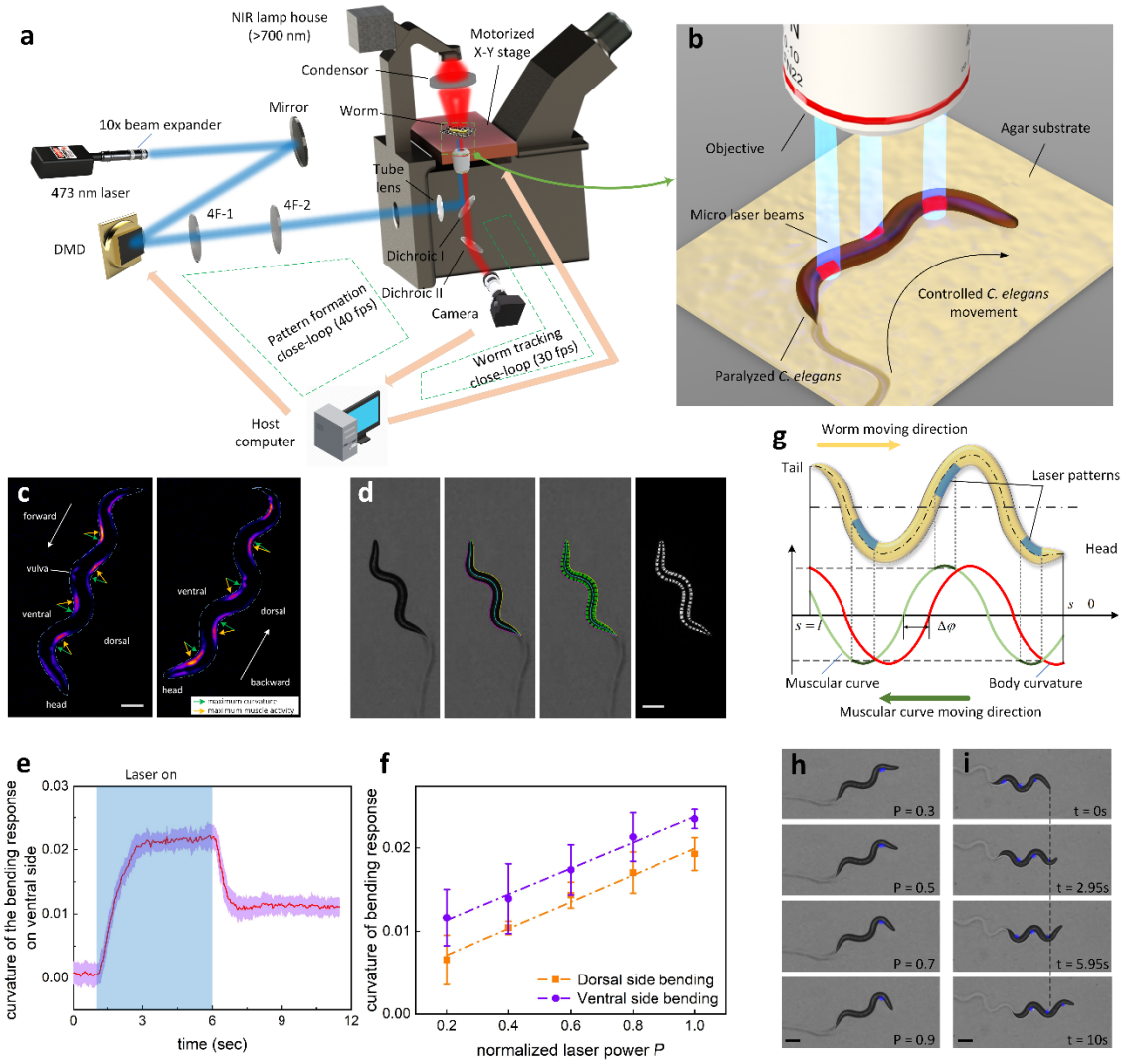


Figure 6-1 The patterned-light illumination system to selectively excite the muscular cells on worm body.

**a.** The system hardware structures and automation components for the construction of the pattern light illumination system on an inverted microscope. **b.** The illustration of light-driven muscle group activation on a C. elegans for controlled locomotion. **c.** Muscular calcium fluorescent images for the AQ2953 transgenic animal during **1)** forward crawling and **2)** backward crawling, respectively (scale bar = 50 μm). **d.** The image processing sequence and performance of the pattern light projection system: **1)** the original image captured by the microscope camera, **2)** the detection of worm boundaries and centreline, **3)** worm body segmentation to analyse the muscle group position, **4)** laser projection on the microscope sample plane of the analyzed muscle pattern (scale

bar = 100 μm). **e.** The temporal response of the worm body curvature under laser beam stimulation (n=5). **f.** The contraction of the dorsal and ventral worm body muscles under increased laser power (n=5). **g.** The binarized moving sinusoidal laser pattern used to drive the crawling locomotion of the robo-worm on agar plate. **h.** The photos for worm muscular bending response under various laser power. **i.** Artificially stimulated serpentine crawling of the robo-worm with binarized moving sinusoidal laser patterns (scale bar = 100 μm).

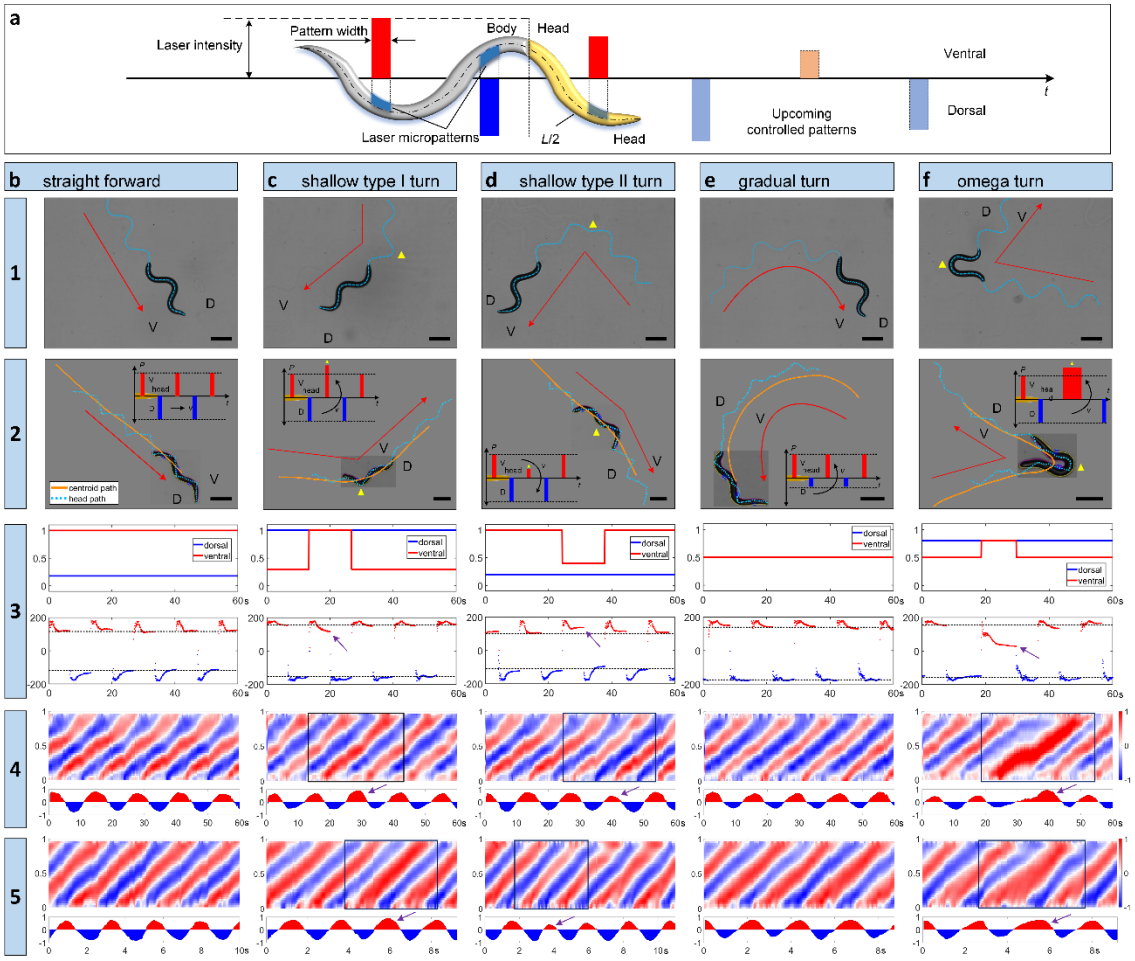


Figure 6-2 The open-loop control of paralyzed C. elegans to reproduce the natural locomotion behaviors on agar plate.

**a.** The open-loop control schematic figure for the regulation of robo-worm locomotion pattern. The head region is defined as the body portion equal to half of the undulation wavelength. The controlled crawling of 5 different behavioural motifs of **b.** straight forward crawl, **c.** shallow type I turn, **d.** shallow type II turn, **e.** gradual turn, and **f.** omega turn were reproduced. For each of the behavioural motif, **1)** the illustration crawling path of a natural worm, **2)** artificially controlled movement route, **3)** the experimental data for input laser intensity *P* on the dorsal and ventral sides, and the corresponding measured bending angles on the dorsal and ventral sides, **4)** the normalized curvature maps for controlled movement, and the curvature of the middle body section along the time line. (x axis indicates the timeline, y axis of 0 to 1 indicates body sections from head to tail), and **5)** the normalized curvature maps for natural movement were tested (scale bar = 100 μm).

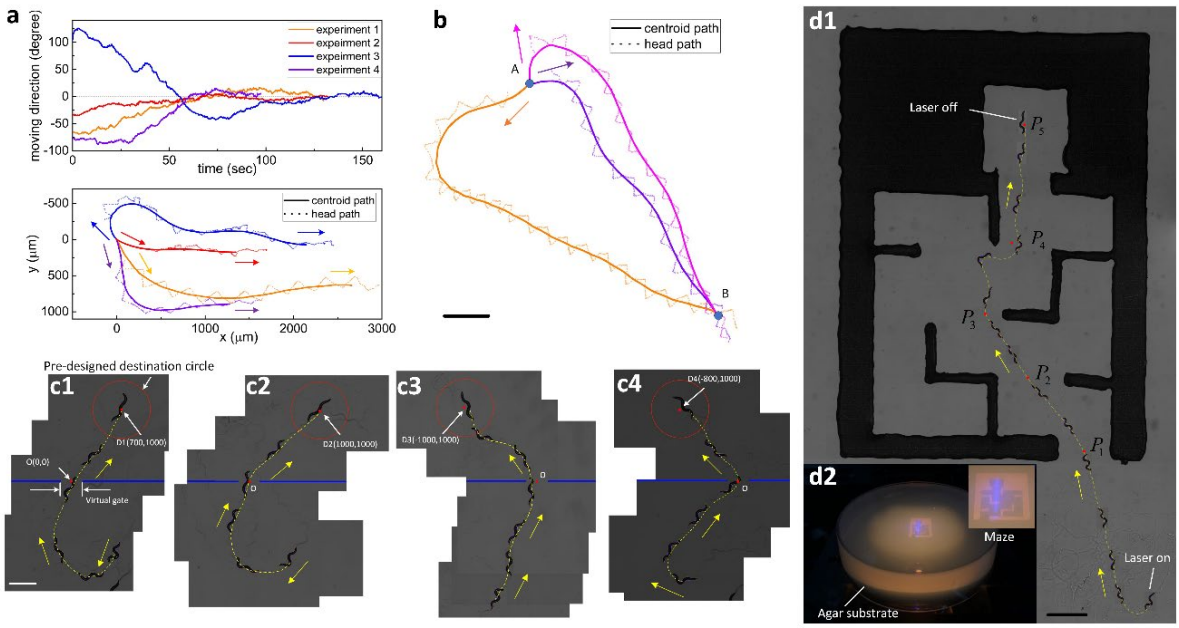


Figure 6-3 Close-loop control results of the paralyzed transgenic C. elegans Pmyo-3-ChR2 for the regulation of the moving direction and destination.

**a.** Four batches of experiments for the regulation of the worm moving direction to horizontal from random starting direction with close-loop regulation scheme. **a1)** The controlled movement direction and **a2)** The movement path. **b.** Control the movement of worm from the start point A to a pre-defined destination B (scale bar = 500 μm). **c.** Four batches of experiments for the close-loop controlling of the worm to move pass through a gate to reach the pre-defined destinations on the other side of the gate (scale bar = 500 μm). **d.** The demonstration experiment to navigate the worm automatically move through a maze. **d1)** The stitched movement path, **d2)** The experiment setup on the microscope sample plane (scale bar = 1000 μm).

## 6.4 Reference


[1] S. Palagi and P. Fischer, "Bioinspired microrobots," *Nature Reviews Materials,* p. 1, 2018.

[2] D. Rus and M. T. Tolley, "Design, fabrication and control of origami robots," *Nature Reviews Materials,* p. 1, 2018.

[3] M. Sitti, "Miniature soft robots—road to the clinic," *Nature Reviews Materials,* vol. 3, no. 6, p. 74, 2018.

[4] J. J. Abbott, Z. Nagy, F. Beyeler, and B. J. Nelson, "Robotics in the small, part I: microbotics," *IEEE Robotics & Automation Magazine,* vol. 14, no. 2, pp. 92-103, 2007.

[5] R. Dreyfus, J. Baudry, M. L. Roper, M. Fermigier, H. A. Stone, and J. Bibette, "Microscopic artificial swimmers," *Nature,* vol. 437, no. 7060, p. 862, 2005.

[6] S. Palagi *et al.*, "Structured light enables biomimetic swimming and versatile locomotion of photoresponsive soft microrobots," *Nature materials,* vol. 15, no. 6, p. 647, 2016.

[7] O. Felfoul *et al.*, "Magneto-aerotactic bacteria deliver drug-containing nanoliposomes to tumour hypoxic regions," *Nature nanotechnology,* vol. 11, no. 11, pp. 941-947, 2016.

[8] V. Magdanz, S. Sanchez, and O. G. Schmidt, "Development of a Sperm-Flagella Driven Micro-Bio-Robot," *Advanced Materials,* vol. 25, no. 45, pp. 6581-6588, 2013.

[9] W. Hu, G. Z. Lum, M. Mastrangeli, and M. Sitti, "Small-scale soft-bodied robot with multimodal locomotion," *Nature,* vol. 554, no. 7690, p. 81, 2018.

[10] S. Tottori, L. Zhang, F. Qiu, K. K. Krawczyk, A. Franco-Obregón, and B. J. Nelson, "Magnetic helical micromachines: fabrication, controlled swimming, and cargo transport," *Advanced materials,* vol. 24, no. 6, pp. 811-816, 2012.

[11] T. Bruegmann *et al.*, "Optogenetic control of heart muscle in vitro and in vivo," *Nature methods,* vol. 7, no. 11, p. 897, 2010.

[12] V. J. Butler *et al.*, "A consistent muscle activation strategy underlies crawling and swimming in Caenorhabditis elegans," *Journal of the Royal Society Interface,* vol. 12, no. 102, p. 20140963, 2015.

[13] J. N. Stirman *et al.*, "Real-time multimodal optical control of neurons and muscles in freely behaving Caenorhabditis elegans," *Nature methods,* vol. 8, no. 2, p. 153, 2011.

[14] A. M. Leifer, C. Fang-Yen, M. Gershow, M. J. Alkema, and A. D. Samuel, "Optogenetic manipulation of neural activity in freely moving Caenorhabditis elegans," *Nature methods,* vol. 8, no. 2, p. 147, 2011.

[15] Q. Wen *et al.*, "Proprioceptive coupling within motor neurons drives C. elegans forward locomotion," *Neuron,* vol. 76, no. 4, pp. 750-761, 2012.

[16] R. Ghosh, E. C. Andersen, J. A. Shapiro, J. P. Gerke, and L. Kruglyak, "Natural variation in a chloride channel subunit confers avermectin resistance in C. elegans," *Science,* vol. 335, no. 6068, pp. 574-578, 2012.

[17] C. Fang-Yen *et al.*, "Biomechanical analysis of gait adaptation in the nematode Caenorhabditis elegans," *Proceedings of the National Academy of Sciences,* vol. 107, no. 47, pp. 20323-20328, 2010.

[18] Z. Guo and L. Mahadevan, "Limbless undulatory propulsion on land," *Proceedings of the National Academy of Sciences,* vol. 105, no. 9, pp. 3179-3184, 2008.

[19] J. M. Gray, J. J. Hill, and C. I. Bargmann, "A circuit for navigation in Caenorhabditis elegans," *Proceedings of the National Academy of Sciences,* vol. 102, no. 9, pp. 3184-3191, 2005.

[20] T. Kawano, M. D. Po, S. Gao, G. Leung, W. S. Ryu, and M. J. N. Zhen, "An imbalancing act: gap junctions reduce the backward motor circuit activity to bias C. elegans for forward locomotion," vol. 72, no. 4, pp. 572-586, 2011.

## 6.5 Supplementary S1 - Muscle optogenetic basis, worm strain and preparations

### 6.5.1 Worm strains

The transgenic worms ZM5398 *hpls199* [*pJH2086 Pmyo-3::ChR2::EGFP*] and AQ2953 *ljIs 131* [*Pmyo-3-GCaMP3::RFP*] used in this paper for the optogenetics muscle excitation and muscle activity imaging are from Prof. Mei Zhen's lab in Lunenfeld-Tanenbaum Research Institute.

### 6.5.2 Muscle optogenetic basis

The paralyzed transgenic worm ZM5398 expressing ChR2 in the body muscle cells was used in this worm robot experiment under patterned 473nm blue laser stimulation. Naturally, *C. elegans* body wall muscle cells are activated by the acetylcholine released from motor neurons. In our experiments, the worms were pre-treated with ivermectin, which primarily hyperpolarizes neurons, and slightly hyperpolarizes muscle cells as well [1]. After ivermectin treatment, the worms were paralyzed. For the paralyzed worms, as shown in Figure 6-4, upon the illumination of blue laser beams and in the presence of ATR, ChR2 on the muscle membrane opens to allow the influx of $Ca^{2+}$ ions [2]. The entry of $Ca^{2+}$ initiates membrane depolarization that propagates along the sarcolemma and activates the voltage-gated calcium channels [2]. This finally triggers the release of $Ca^{2+}$ stored in sarcoplasmic reticulum into the cytosol. These $Ca^{2+}$ bind to troponin, change its shape, and lead to the displacement of actin and myosin with the energy supplied by ATP [2].

In general, the illuminated body muscular cells of ZM5398 worms will contract and shrink their lengths, in the meanwhile, they drag the movement of the adjacent body parts to create the bending torque along the worm centerline. Thus, a live worm was converted into an engineered micro bio-robot body that can be manipulated with laser beams.

### 6.5.3 Worm culture and age synchronization

Firstly, about 20 adult hermaphrodite ZM5398 transgenic worms were picked onto a new ATR NGM plate for each batch of worm culture. The ATR NGM plate was prepared through standard seeding process, and we used high concentration of ATR to increase the worm's response to laser stimulations (7.11 mg ATR powder was dissolved into 500 ul ethanol to prepare the 1 mol/ml ATR

solution, then 300 ul of the ATR ethanol solution was added into 10 ml OP50 media for the seeding of the NGM plate).

After 6 hours, the hermaphrodites were removed from the plate and the eggs were left on the agar, which resulted in the next generation of synchronized developmental stages. When the worms grew to the young adult stage, they were picked from the plate for paralyzation and the following worm robot experiments. The young adult worms were used in the experiments, because their sizes are big enough to be accurately stimulated by the patterned-light illumination system under 4× objective (12.3 μm laser resolution). Adult worms, however, were usually found with relatively smaller laser response, probably due to higher mass of muscle cells.

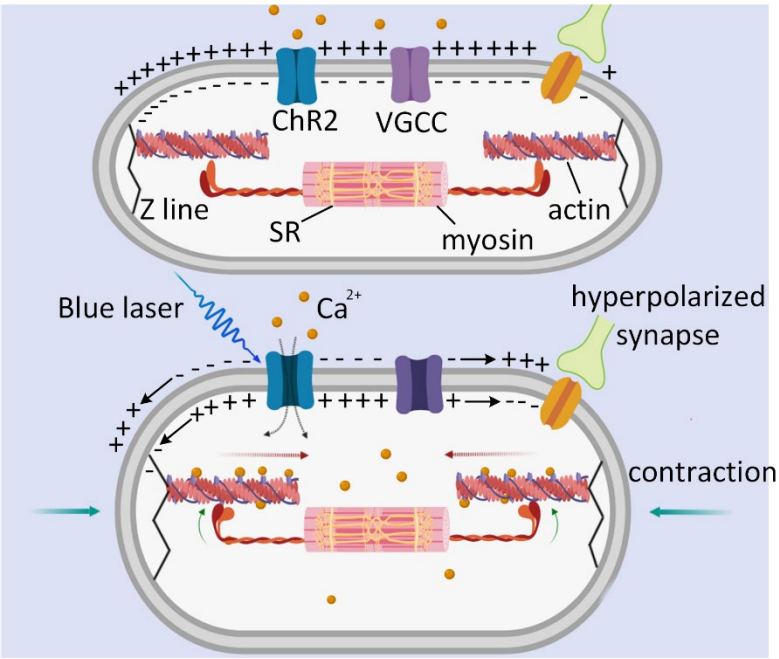


Figure 6-4 The molecular process illumination for optogenetic stimulation on muscular cells.

### 6.5.4 Worm paralysation

Ivermectin, a nematocidal agonist of glutamate-gated $Cl^-$ channels, was used to paralyze the worm before laser stimulation. One can refer to [3] for detailed description on the ivermectin treatment of *C. elegans*. Usually, low ivermectin concentration leads to longer paralysation treatment time, and the worm will recover to normal state after culture on agar plate for several hours until ivermectin is degraded [4]. High ivermectin concentration (> 0.1 mg/ml), however, will easily cause irreversible damage or even death of the worm individuals. The ivermectin plates we used in the experiments were prepared by spreading 100 μl 0.02 mg/ml ivermectin solution on the

surface of 5 ml agar NGM plate 24 hours before experiments (the ivermectin spreads through the agar and the resultant concentration is 0.0004 mg/ml in agar). The treatment of ivermectin was conducted by transferring the young adult individuals onto the ivermectin agar surface for 20~25 minutes until the worm were completely paralyzed and stops crawling on agar. After that, the paralyzed worms were transferred to new agar plates for robotic experiments.

For a successful locomotion control experiment, the entire paralyzed worm body of both the ventral and dorsal sides from head to tail must be sensitive to laser excitations. Continuous waves of muscular contraction can be, therefore, generated at desired body regions to drive the worm for serpentine crawling. In addition, the sensitivity of the dorsal and ventral sides has to be comparable, otherwise, the control capability could be greatly degraded as the one side of the worm is always bending more than the other side.

However, as the glutamate-gated $Cl^-$ channels are also expressed unevenly in the body wall muscles [1], the muscular cells are partially hyperpolarized as well. Unlike the paralysation of neurons, the muscular cells are paralyzed unevenly depends on the expression rate of the glutamate-gated $Cl^-$ channels. This is probably the reason for inconsistent laser responses on the dorsal and ventral sides, and along anterior-posterior axis, as we found in the muscle optogenetic experiments (Figure 6-1f). As a result, the current protocol leads to a success rate of the worm robot experiments of 5-10% of the total population (30 batches, ~30 worms in each batch, 7.1% success rate in total, a worm that can be stimulated to crawl continuously on the substrate is defined as a successful trial).

A possible improvement is to express histamine-gated chloride channel HisCl panneuronally in ZM5398 worms [5]. With HisCl, worms will be paralyzed with histamine. This method should eliminate the side effect of ivermectin treatment on *C. elegans* muscles.

### 6.6 Supplementary S2 - Thrust force derivation

The serpentine locomotion proposed based on the investigation of snake movement in 1980s quantitively defines a general type of stable snake-like locomotion in which the curvature of the organism's body shape and the bending torque generated by muscular groups are sinusoidal [6]. The locomotion of *C. elegans* on the agar substrate can also be considered as a serpentine locomotion pattern with unshearable body during crawling on agar. We have found, through theoretical analysis, that the thrust force for worm crawling locomotion is generated by the phase

difference between the worm body curvature and the muscle bending torque. The phase difference of *C. elegans* muscle calcium signal with respect to body curvature during stable crawling on agar is around $-40^0 \sim -50^0$ [7].

To further investigate the basic mechanism of serpentine locomotion, we built a theoretical model based on the release of muscular energy and derived the theoretical relationship between the phase difference and the generation of crawling thrust force, as discussed in this supplementary material.

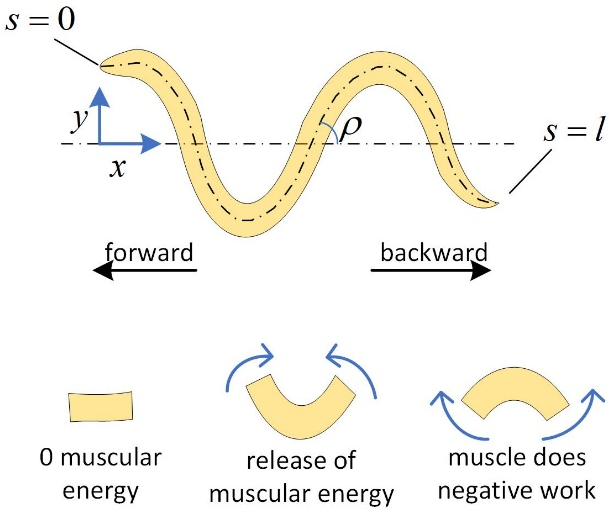


Figure 6-5 The serpentine definitions of the worm crawling locomotion. The worm curvature is defined along the worm body coordinate from $s = 0$ to $s = l$. The body section that bends according to the direction of muscular torque is regarded as the release of muscular energy, while the body section bending against the muscular torque is regard as the negative work conducted by muscles.

In the serpentine locomotion frame, the sinusoidal curvature along the worm body centerline coordinate during stable straight forward crawling locomotion is defined as

$$\kappa(s) = -\frac{2\pi\rho}{L}\cos\left(\frac{2\pi}{L}(s - vt)\right), s \in [0, l] \tag{6.6-1}$$

where $L$ is the undulating wavelength, $l$ is the worm length, $\rho$ is the attack angle of the body curve, $v$ is the speed of the worm, and $s$ refers to a unique cross-section on the worm body from head to tail. As time $t$ goes on, the worm moves along the serpenoid curve defined by $\kappa$, as shown in Figure 6-5. Please note that the curvature $\kappa$ we defined here can be negative.

Specifically, to analyze the activity of muscles during sable crawling locomotion, the muscular torque along the body centerline curvature is defined by

$$M(s) = M_0 \cos\left(\frac{2\pi}{L}(s - ut) + \Delta\varphi\right), s \in [0, l], \Delta\varphi \in [-\pi, \pi] \tag{6.6-2}$$

where $\Delta\varphi$ is the phase difference between $\kappa$ and $M$, $M_0$ is the torque amplitude. As shown in Figure 6-5, the release of muscular energy is defined by the bending of the worm body along the direction of muscle torque, while the bending along the inverse direction of muscle torque indicates that the kinetic energy of inertia is doing work to muscles. The zero phase difference $\Delta\varphi = 0$ occurs when the contraction of muscles correspond to the maximum bending sections, as indicated by the dark orange parts labeled on the worm body and the blue dash lines in Figure 6-7. Positive and negative phase difference indicate the misalignments between $M$ and $\kappa$.

We assume that the initial state of the worm is along a straight line, as shown by the 0 muscular energy released in Figure 6-5. Thus, for the given muscular torque $M$ and body shape $\kappa$, the energy released from the worm body is defined by

$$dE_M = -M(s)d\theta = -M(s)\kappa ds \tag{6.6-3}$$

The total muscular energy released by the body is

$$E_M = \int dE_M = -\int_{s=0}^{l} M(s)\kappa ds \tag{6.6-4}$$

Please note that the negative sign is derived here because of the direction definition of $M$ and $\kappa$ for the conduction of positive work.

Substituting curvature $\kappa$ and muscular torque $M$ into the above equation, we can explicitly derive the released muscular energy, at time instant $t = 0$, as

$$\begin{aligned} E_M &= -\int_{s=0}^{l} M_0 \cos\left(\frac{2\pi s}{L} + \Delta\varphi\right) \cdot \frac{2\pi\rho}{L}\cos\left(\frac{2\pi s}{L}\right) ds \\ &= \frac{\rho M_0}{4L}\left(4l\pi\cos(\Delta\varphi) + L\left(-\sin(\Delta\varphi) + \sin\left(\frac{4l\pi}{L} + \Delta\varphi\right)\right)\right) \end{aligned} \tag{6.6-5}$$

For simplicity, here we assume the original muscular energy before release within one body wavelength $L$ as $E_0$. Then, the muscular energy remained in one body wavelength $L$ is

$$E = E_0 - E_M|_{l=L} \tag{6.6-6}$$

$$= E_0 - \pi\rho M_0 \cos(\Delta\varphi)$$

The graphic of $E$ is plotted in Figure 6-6, which indicates that the remained muscular energy reaches its minimum (or the released muscular energy reaches its maximum) when $\Delta\varphi = 0$. For the given $M$ and $\kappa$, muscular energy cannot be further released if $\Delta\varphi = 0$.

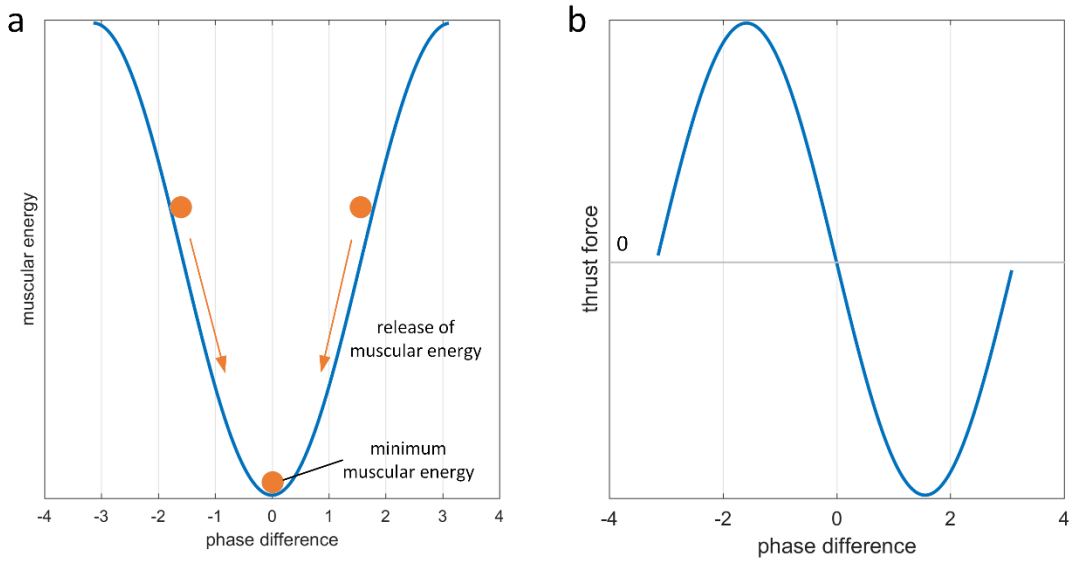


Figure 6-6 The theoretical figure from mathematical derivations. **a.** Theoretical muscular energy remains in the body of a single undulation wavelength $L$ with respect to the phase difference $\Delta\varphi$. **b.** Theoretical thrust force generated within a single undulation wavelength $L$ with respect to the phase difference $\Delta\varphi$.

The muscles must do positive work to make the worm move, and consequently, the worm crawling movement can be regarded as the process for the release of muscular energy. Thus, $\Delta\varphi$ must remain at a non-zero level to drive the forward or backward crawling.

In addition, the release of muscular energy indicates the tendency for $\Delta\varphi$ approaching 0. As shown in Figure 6-7, the dash blue line shows the corresponding muscular torque for the worm when $\Delta\varphi = 0$. Positive and negative phase misalignment $\Delta\varphi_2$and $\Delta\varphi_1$, shown by the yellow and green solid lines respectively, will force the body to move backward and forward respectively. During this process, the phase difference $|\Delta\varphi|$ will be reduced to release the muscular energy.

The phase difference during the serpentine locomotion is

$$\Delta\varphi = \Delta\varphi_0 + \frac{2\pi}{L}(v-u)t \tag{6.6-7}$$

For any initial phase difference $\Delta\varphi_0$, the worm must move to release its muscular energy. To quantitively investigate the crawling process, a general movement thrust force $F_m$ generated in one body wavelength $L$ can be defined to represent the strength of the movement tendency.

$$F_m = -\frac{dE}{ds} = -\frac{2\pi}{L}\frac{dE}{d(\Delta\varphi)} = -\frac{2\pi^2}{L}\rho M_0 \mathrm{Sin}(\Delta\varphi) \tag{6.6-8}$$

The graphic of $F_m$ is shown in Figure 6-6. No thrust force is generated when $\Delta\varphi = 0$.

In our theory, the movement thrust force $F_m$ is induced by the phase difference $\Delta\varphi$ between $M$ and $\kappa$. For stable crawling locomotion of *C. elegans* on an agar substrate, muscle torque $M$ also moves along the body as the worm crawls on agar, and the worm moving speed $u$ equals to the muscular speed $v$ to achieve stable $F_m$, as indicated by *Equation* (6.6-8). The resultant thrust force $F_m$ are balanced by the passive resistance of friction and viscosity from the substrate to maintain a stable moving speed.

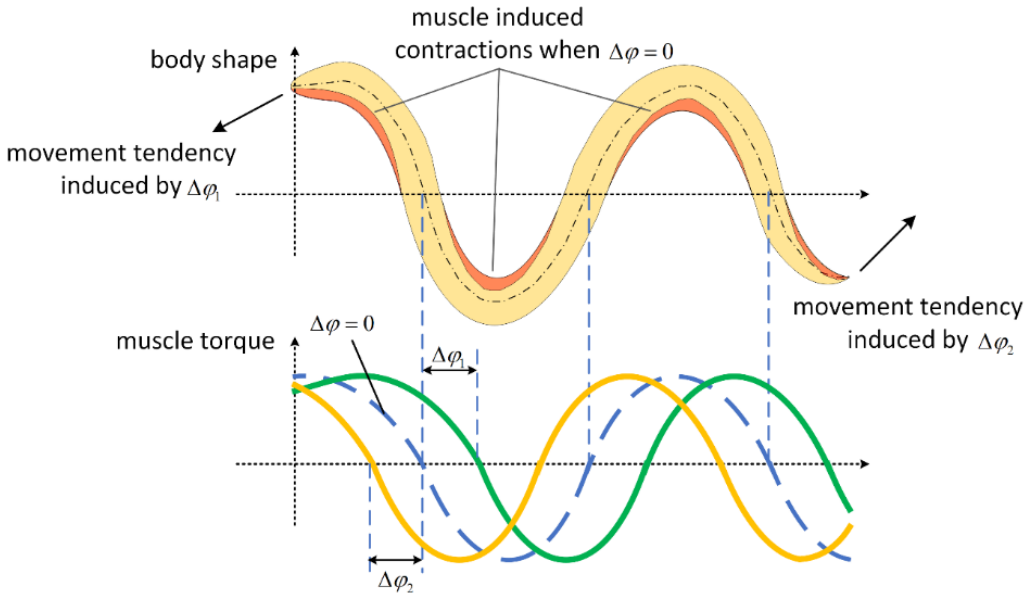


Figure 6-7 Phase difference induced movement tendency. The blue dash line indicates the sinusoidal phase of the body curvature. The muscular torque with phase difference $\Delta\varphi_1$ and $\Delta\varphi_2$ is driving the body move forward and backward respectively to make the curvature phase align with the muscular phase.

To further verify this proposed theory, we analyzed the dynamic model of the worm crawling locomotion and calculated $F_m$ based on the dynamic model in the next sections.

## 6.7 Supplementary S3 - Dynamic model of worm crawling

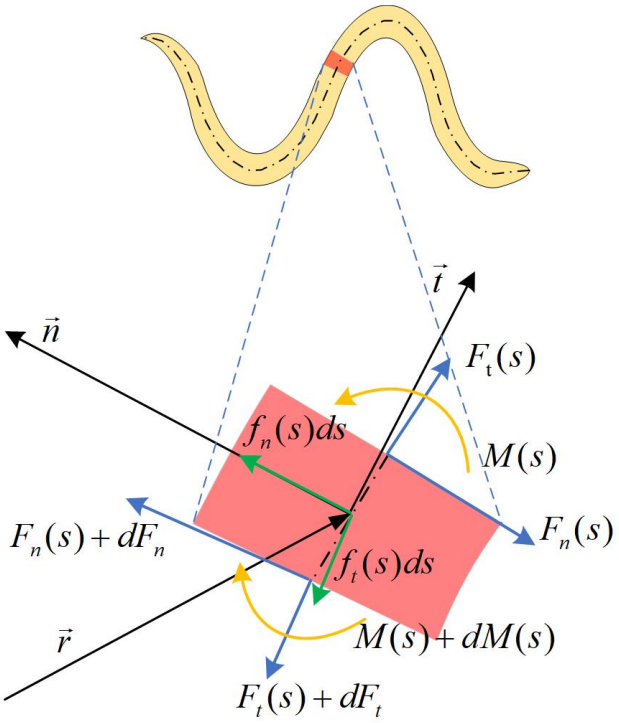


Figure 6-8 Schematic for the dynamical analysis for the serpentine crawling locomotion of *C. elegans* on agar substrate**.** The internal forces exerted by the adjacent body sections are denoted by capital $F$, while the external forces exerted by the environment are denoted by low-case $f$.

We take a thin film section during crawling for example, referred by $\vec{r}(s,t)$ in Figure 6-8, to analyze the forces acting on it. According to the *Newton-Euler equation*, the movement of the tiny body section with the length of $ds$ can be described by

$$\begin{cases} d\boldsymbol{F} + \boldsymbol{f}ds = m_0\boldsymbol{a}ds \\ d\boldsymbol{M} + \vec{t} \times \boldsymbol{F}ds = I_0\beta\vec{z}ds \end{cases} \tag{6.7-1}$$

where $\vec{n}, \vec{t}, \vec{z}$ refer to the normal, tangential and vertical unit vector respectively. $\boldsymbol{F} = \boldsymbol{F}(s,t) = F_t\vec{t} + F_n\vec{n}$ is the internal force resultant for tensile force and shear force applied by the adjacent body sections, and $\boldsymbol{M} = M(s,t)\vec{z}$ is the internal resultant moment through $s \in [0, l]$ on the worm body, while $\boldsymbol{f} = \boldsymbol{f}(s,t) = -f_t\vec{t} + f_n\vec{n}$ is external force resultant for the resistance force and supportive force applied by the agar substrate. $m_0$ is the mass density along the body centerline.

$I_0$ is the rotational inertia around the mass center of this small section. Further, it is easy to know that the acceleration $\boldsymbol{a}$ and angular acceleration $\beta$ can be derived as

$$\begin{cases} \boldsymbol{a} = \dfrac{d}{dt}\left(\dfrac{d}{dt}\vec{r}\right) = \dfrac{d}{dt}\left(v\vec{t}\right) = \dfrac{dv}{dt}\vec{t} + v\dfrac{d\vec{t}}{dt} = \dfrac{dv}{dt}\vec{t} + \kappa v^2\vec{n} \\ \beta = \dfrac{d}{dt}\left(\dfrac{d}{dt}\theta\right) = \dfrac{d}{dt}\left(\dfrac{d\theta}{ds}\dfrac{ds}{dt}\right) = \dfrac{d}{dt}(\kappa v) = \dfrac{d\kappa}{ds}v^2 + \kappa\dfrac{dv}{dt} \end{cases} \tag{6.7-2}$$

where $\kappa$ is the curvature of the worm body prosed in the previous section, and $v$ is the tangential speed of this body section proposed in the previous section. Please note that the derivations of the unit vectors along the body coordinate are formulated as

$$\begin{cases} \dfrac{d}{ds}\vec{n} = -\kappa\vec{t} \\ \dfrac{d}{ds}\vec{t} = \kappa\vec{n} \\ \dfrac{d}{ds}\vec{z} = 0 \end{cases} \tag{6.7-3}$$

By integrating the above equations we have the dynamics description of worm crawling locomotion on agar as follows, which is similar to the description in[8].

$$\begin{cases} \dfrac{d}{ds}F_t - \kappa F_N - f_t = m_0\dfrac{dv}{dt} \\ \dfrac{d}{ds}F_N + \kappa F_t + f_n = m_0\kappa v^2 \\ \dfrac{d}{ds}M + F_N = I_0\left(\dfrac{d\kappa}{ds}v^2 + \kappa\dfrac{dv}{dt}\right) \end{cases} \tag{6.7-4}$$

For stable crawling movement, the boundary condition of $F_t(L) = F_t(0)$ will be adopted to guarantee that the locomotion is periodic and stable.

For a given serpentine locomotion of muscular torque $M$, curvature $\kappa$, external friction $f_t$, and moving speed $v$, the internal force distribution of $F_t$, $F_N$, and the external passive supportive force $f_n$ can be solved. The difference between serpentine crawling and swimming depends on the property of external environment. When the worm is on the agar surface with sufficient lateral frictions $f_n$, the environment should be able to provide enough $f_n$ to maintain the serpentine shape ($\max(f_n) < f_{nM}$; $f_{nM}$ is the maximum support force the environment can provide to the worm). Otherwise, if the substrate cannot provide enough frictions ($\max(f_n) > f_{nM}$), the body segments

will perform lateral movement other than sliding along a serpentine path, which results in swimming rather than serpentine crawling.

## 6.8 Supplementary S4 - Numerical calculation of thrust force

In this section, we attempted to verify the proposed thrust force theory (*Equation* (6.6-8)) by calculating the numerical values of the thrust force under various activation muscular torques (*Equation* (6.6-2)), based on the dynamic model (*Equation* (6.7-4)).

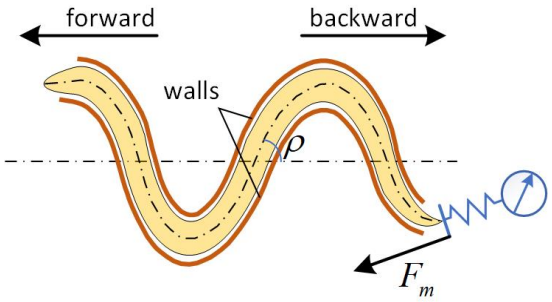


Figure 6-9 The worm confined within a serpentine path for the dynamic simulations. The walls can exert sufficient support force $f_n$ to maintain the serpentine shape of the worm, no matter what the activation muscular torque is. No friction is designed, and the thrust force $F_m$ generated by the muscular activation can be measured at the tail.

In most cases for the analysis of serpentine locomotion, the dynamic model contains more variables than equations; consequently, to further study the crawling locomotion, assumptions have to be made to solve the equations (e.g. $f_n$ is assumed to be sinusoidal in [8]), which inevitably leads to unreliable results. To avoid making any artificial assumptions and investigate the muscle excitation patterns that drive the worm move forward, we built the following experimental situation that can be accurately quantified by the dynamic movement model.

As shown in Figure 6-9, a worm with its normal crawling shape is confined between rigid walls, and the tensile force at the tail $F_m$ is measured by a force sensor. From definition, it is obvious that $F_t(0) = 0$ and the thrust force $F_m = F_t(l)$. Since the worm is confined within a rigid path without movement, the above dynamic description is simplified to the static version as

$$\begin{cases} \frac{d}{ds}F_t - \kappa F_N - f_t = 0 \\ \frac{d}{ds}F_n + \kappa F_t + f_n = 0 \\ \frac{d}{ds}M + F_n = 0 \end{cases} \tag{6.8-1}$$

which is similar to what is proposed in [9].

The curvature of the wall is defined as

$$\kappa = -\frac{2\pi\rho}{L}\cos\left(\frac{2\pi s}{L}\right), s \in [0, l] \tag{6.8-2}$$

which is the curvature we proposed in *Equation* (6.6-1) at $t = 0$. The serpenoid shaped walls are closely contacting the body, so arbitrary large supporting force $f_{nM}$ can be provided to the worm body from the environment, and lateral sliding will be completely avoided. The environmental resistance force $f_t$ consists of the friction $f_c$ and the viscosity $f_v$ when the worm is crawling on the agar substrate. To better analyse the locomotion tendency and the movement thrust force, we assume that the friction is insignificant. Since the worm is not moving, the viscosity is also negligible at this moment. We can therefore simulate the thrust force $F_m$ of the worm by applying muscle active torque

$$M(s) = M_0\cos(\frac{2\pi}{L}s + \Delta\varphi), s \in [0, l] \tag{6.8-3}$$

which is the muscle torque we proposed in the first section at $t = 0$. The parameters we chose for the simulation: $L = 500\ \mu m, l = 1000\ \mu m, M_0 = 1000\frac{\mu N}{\mu m}, \rho = \frac{\pi}{4}, f_c = 0$.

The simulated distribution for the inner shear force $F_n$, inner tensile force $F_t$, and the external support force $f_n$along the body coordinate is shown in Figure 6-10. In this simulation schematic, the force measured at the anchor point (the tail) $F_m = F_t(l)$ is corresponding to the movement thrust force generated by the muscle torque defined in *Equation* (6.6-8). One can see that for phase difference $\Delta\varphi = 0$ and $\pi$, the inner tensile force $F_t$ is period and $F_m = 0$, which means that the worm is stable, and no thrust force is generated. If $\Delta\varphi = 0$, the worm will not move even when the worm is release at the tail, since $F_t(l) = 0$ at this moment.

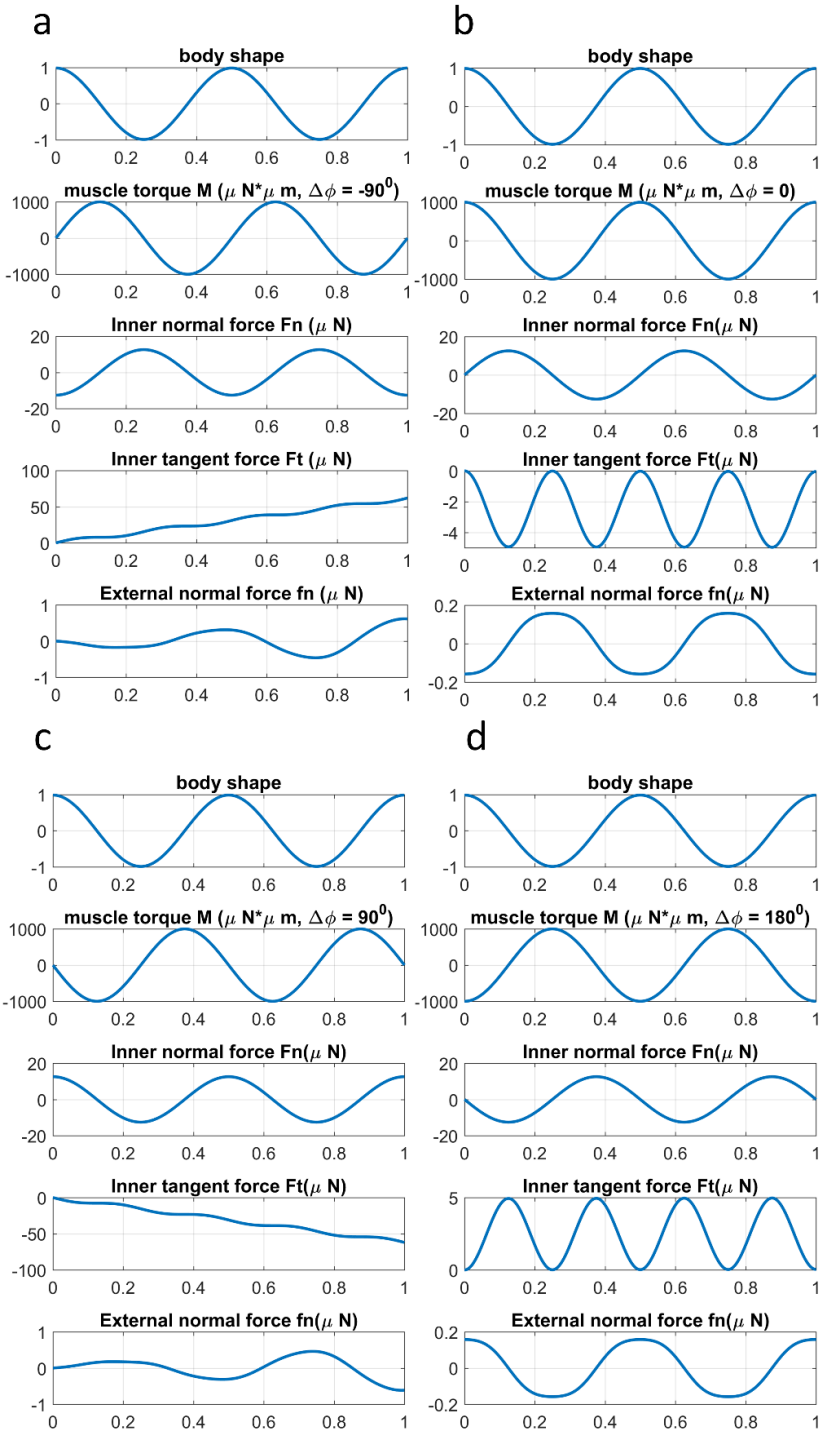


Figure 6-10 The simulation results for the phase difference of **a.** $\Delta\varphi = -\pi/2$ **b.** $\Delta\varphi = 0$ **c**. $\Delta\varphi = -\pi/2$ **d.** $\Delta\varphi = -\pi$, respectively.

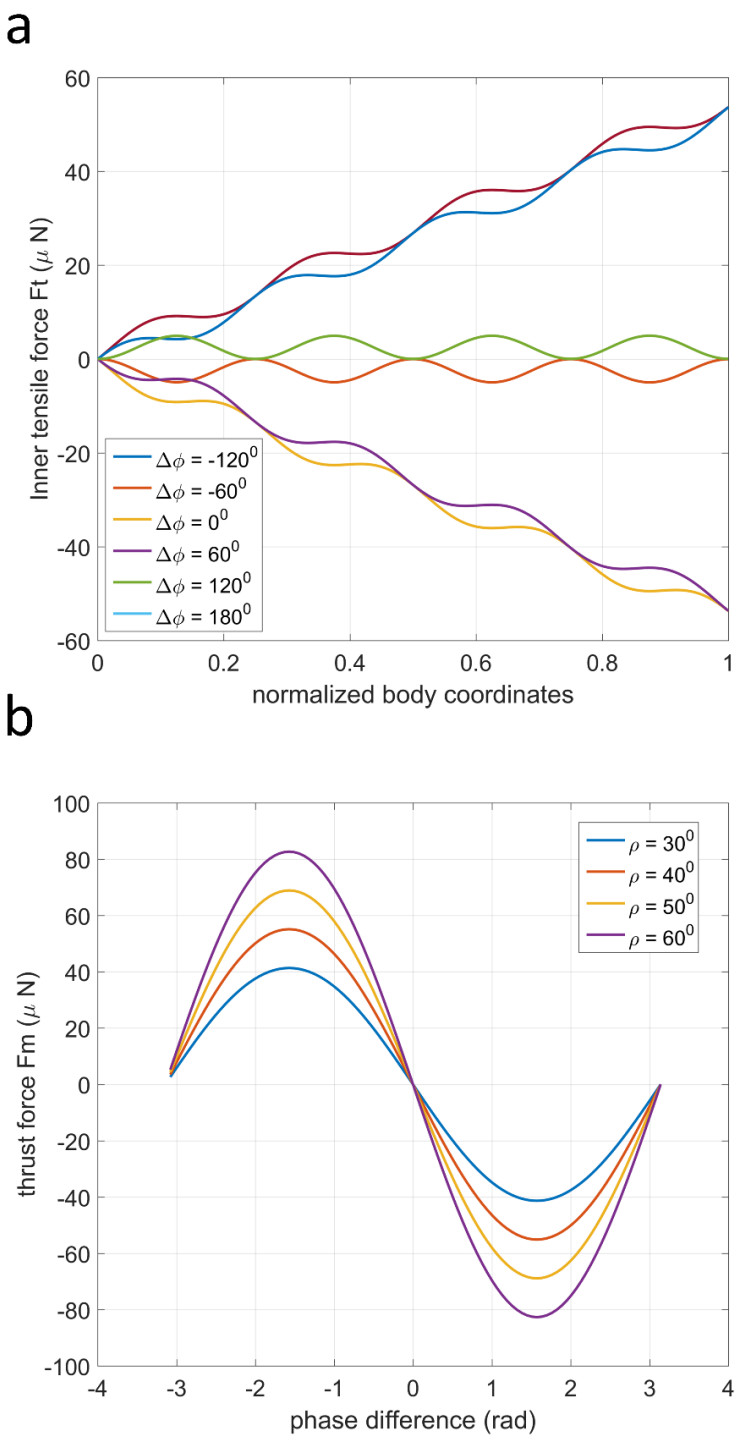


Figure 6-11 The simulation results for inner tensile force $F_t$. **a.** The distribution of $F_t(s)$ along the body coordinates under different phase difference $\Delta\varphi$. **b.** The thrust force $F_m = F_t(l)$ with regards to the variance of phase difference $\Delta\varphi$.

Furthermore, the variation of $F_t$ along the worm body coordinates was simulated under difference phase difference (Figure 6-11**a**) and difference attack angle $\rho$ (Figure 6-11**b**). Since phase difference $\Delta\varphi$ has the period of $2\pi$, only the situation within $[-\pi, \pi]$ was taken in to consideration. From Figure 6-11, it is obvious that negative $\Delta\varphi$ induces positive thrust $F_m$ for forward locomotion, while positive $\Delta\varphi$ induces negative thrust $F_m$ for backward locomotion. Meanwhile, the thrust force $F_m$ reaches it maximum when $\varphi = -\frac{\pi}{2}$ or $\frac{\pi}{2}$, and the amplitude of $F_m$ calculated from the theoretical model *Equation* (6.6-8) ($F_m = 41.3\ \mu N$ for $\rho = 30^0$; $F_m = 55.1\ \mu N$ for $\rho = 40^0$; $F_m = 68.9\ \mu N$ for $\rho = 50^0$; $F_m = 82.7\ \mu N$ for $\rho = 60^0$) matches the simulation results in Figure 6-11**b**.

Thus, from the above analysis, we can see that the generation of thrust force is supported by the dynamic simulation of the serpentine locomotion.

### 6.9 Supplementary S5 - Binarized sinusoidal pattern to reproduce phase difference

As indicated by *Equation* (6.6-8), the thrust force for serpentine locomotion is generated by the phase difference $\Delta\varphi$. Therefore, to trigger the worm locomotion on agar, we designed a moving sinusoidal laser patterns along the worm body axis to artificially generate the phase difference by optogenetic laser stimulation.

The paralyzed worm body illuminated by the binarized sinusoidal blue laser patterns bends into a S shape, as shown in Figure 6-12a and Figure 6-12b. When the pattern moves backward along the body axis, negative phase difference is generated to induce the forward sliding of the worm body on agar, as shown in Figure 6-12c.

In our experiments, we are moving the muscular torque curve $M$ with a constant speed $u = kl$ ($k$ is a speed ratio with respect to the length of the body; we are using $k = 0.04$ in our experiments).

$$M(s) = M_0 \cos\left(\frac{2\pi}{L}(s - ut)\right), s \in [0, l] \tag{6.9-1}$$

At the starting phase of stimulation, phase difference $|\Delta\varphi|$ increases within $[0, \pi/2]$ as the laser pattern keeps moving backward. The increase of $\Delta\varphi$ leads to the accumulation of thrust force $F_m$. Once $F_m$ is large enough to overcome the friction $f_c$ the worm body will slide forward, and the exceeding part will be balanced by the viscosity of agar $f_v$. In addition, the sinusoidal muscular

torque $M$ continuously keeps the body as the serpenoid "S" shape during movement. The initiation of stimulated crawling by optogenetics are shown in Supplementary Video S3.

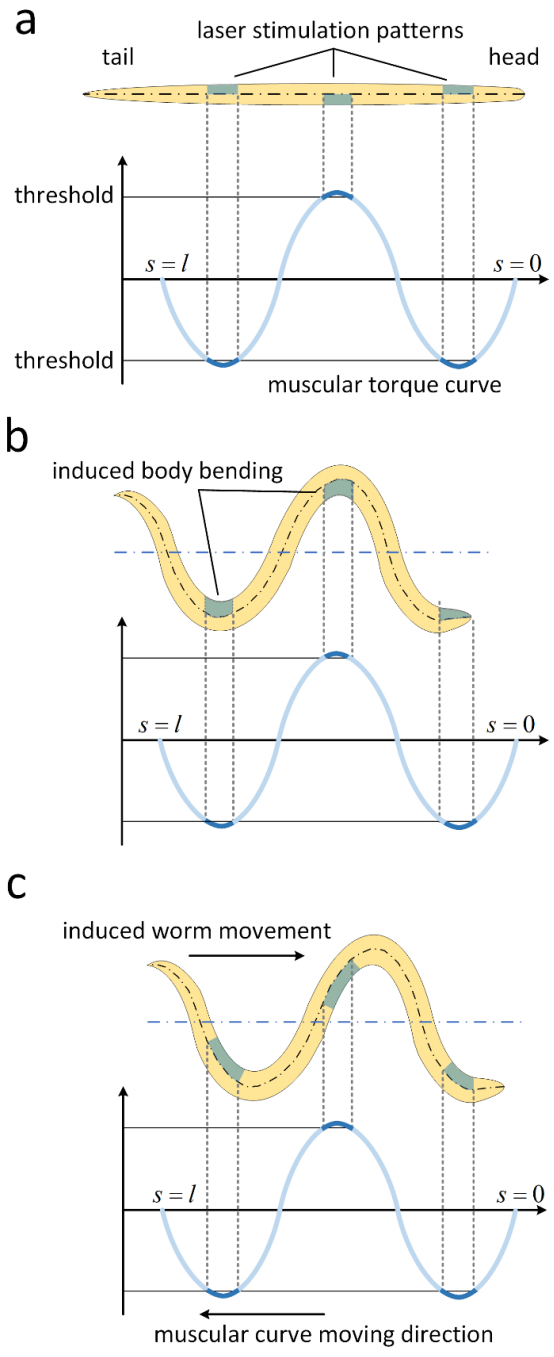


Figure 6-12 The binarized sinusoidal laser pattern designed to trigger the worm locomotion. **a.** The initiate position for laser stimulation. **b.** The laser induced bending on the paralyzed worm body.

**c.** The movement of the paralyzed worm as the response of phase difference reproduced on the worm body.

If the worm crawling speed $v$ is smaller than muscular speed $u$, phase difference $\Delta\varphi$ increases to further improve $v$ until $v = u$, and a constant phase difference is maintained to achieve stable crawling locomotion. Thus, the worm moving speed $v$ is regulated by the muscular driving speed $u$. If $v$ is always smaller than $u$ even when the phase difference $\Delta\varphi$ has accumulated to $-\frac{\pi}{2}$ (the maximum point of $F_m$), the worm will not be able to crawl normally (Supplementary Video S4). In this case, the bended body will move laterally on agar instead of moving forward along a serpenoid "S" path. This situation happens when muscular speed $u$ is set too large or the magnitude of $M_0$ is too small to drive the worm body.

### 6.10 Supplementary S6 - Experimental verification of the proposed theory

The proposed thrust force theory has been verified by the calculation of crawling dynamics as discussed in Section 6.8. As we successfully induced the crawling of paralyzed worm by reproducing phase difference on the paralyzed worm with patterned light stimulation (Section 6.9), we proposed experiments to verify the derived thrust force theory experimentally.

Direct measurement of the micronewton level thrust force as shown in Figure 6-9 would be extremely difficult. Instead, there are two necessary conditions we can check experimentally from the proposed theory.

The first one is the induced crawling speed of the worm. In our theory, the stimulated speed $v$ must equal to the speed of the scanning laser beams $u$, so a stable phase difference $\Delta\varphi$ and a stable thrust force $F_t$ can be consequently achieved to maintain the serpentine locomotion (*Equation* (6.6-7)). Through muscular optogenetic excitation with the binarized sinusoidal patterns, we measured the worm moving speed (head speed and centroid speed) with image processing algorithms under various laser activation speed $u = kl$, as shown in Figure 6-13**a**. The speed was qualified by the time derivative of the head and centroid position on the image plane. Both $v$ and $u$ were quantified as the portion of body length moved per second. Figure 6-13**a** shows that the induced centroid movement speed of the worm $v$ closely resembles the laser scanning speed $u$, which validates the proposed theory in speed regulation (Section 6.9).

The second one is the relationship between the worm moving speed $v$ and the phase difference $\Delta\varphi$. Instead of measuring $F_t$ directly, we transferred the $F_t$ to the worm moving speed that we can measure by images in our experiments.

Generally, the thrust force generated by muscle contraction will be balanced by the substrate resists of friction and viscosity during crawling.

$$F_t = \int_0^l f_t ds \tag{6.10-1}$$

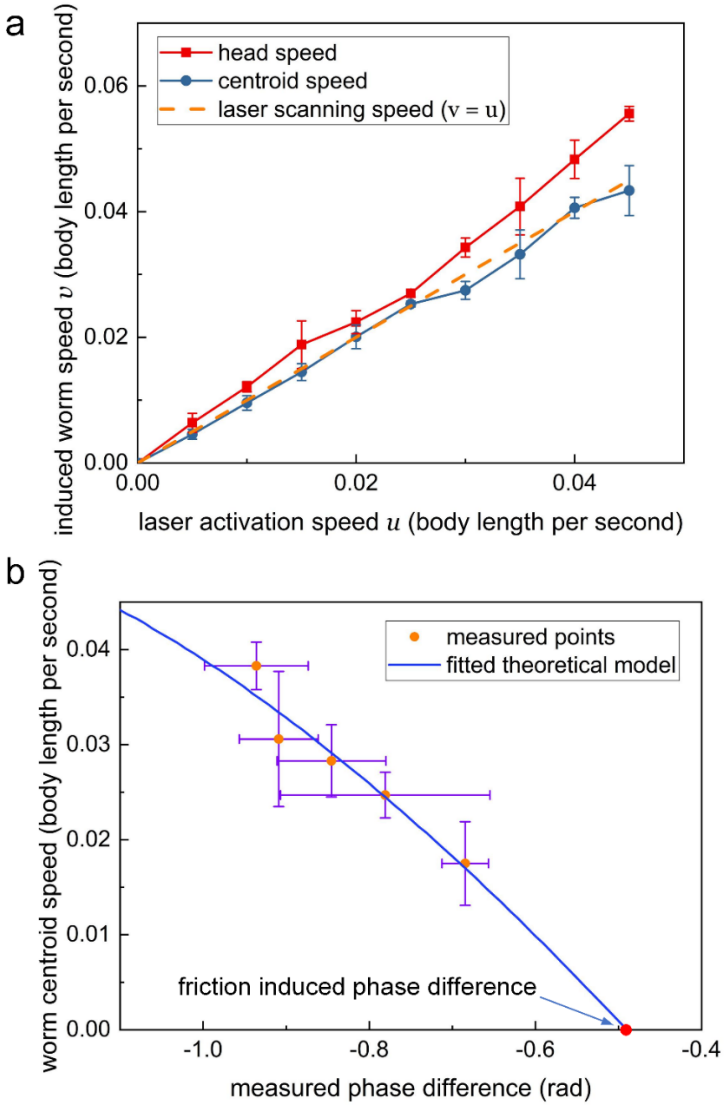


Figure 6-13 The experimental data for the speed regulation of optogenetic stimulated serpentine locomotion. **a.** The stimulated movement speed of the paralyzed worm with respect to different

laser activation speed (n=5). **b.** Measured worm centroid speed with respect to measured phase difference (n=5).

By substituting $F_t$ and $f_t$, the above equation can be written as

$$-\frac{2\pi^2}{L}\rho M_0 \mathrm{Sin}(\Delta\varphi) = \int_0^l (f_c + f_v)ds \tag{6.10-2}$$

where $\int_0^l f_c ds = cl$ is the general friction, $\int_0^l f_v ds = A\mu v$ is the general viscosity along the body. $c$ is the friction coefficient, $A$ is the cross section area of the worm, $\mu$ is the viscosity coefficient of the agar, $v$ is worm moving speed. Therefore, *Equation* (6.10-2) can be further written as

$$-\frac{2\pi^2}{L}\rho M_0 \mathrm{Sin}(\Delta\varphi) = cl + A\mu v \tag{6.10-3}$$

By developing image processing algorithms to analyze the resultant phase differences between the applied laser patterns and the induced worm body curvature, we quantitatively measured the speed $v$ as a function of $\Delta\varphi$, as shown in Figure 6-13**b**. Each of the data point was collected by stimulating the movement of a single worm (so that $\alpha$, $M_0$, $l$ would be constant) with constant stimulation wavelength $L$ ($L$ is used as $0.55l$ in our experiments), on the agar substrate ($c$ is constant) under various scanning speed $u$. The phase difference was qualified by calculating the distance between the local maximum bending segments and the corresponding stimulation laser pattern on the body coordinate (in our case, $L = 0.55l$ means $2\pi$ phase on the body coordinates).

Since the laser stimulation of a single worm only lasts for 10~15 minutes, the number of the collected data within such short period of time is too small to verify the sinusoidal structure of *Equation* (6.6-8). However, an obvious trend for the reducing of worm moving speed $v$ can be observed as the phase difference $\Delta\varphi$ decreases (Figure 6-13**b**). In addition, the intercept on the x axis is not zero, which indicates the portion of thrust force used to overcome the friction. Thus, the experimental results for thrust for generation agree with the proposed theory.

## 6.11 Supplementary S7 - System hardware constructions

From activation level, the system consists of two hardware close-loops: i) the pattern formation loop to project laser beams onto the worm body; ii) the worm tracking loop to keep the worm in the center of FOV when it crawls on agar, as discussed in the main text. The hardware components of these two close-loops are shown in Figure 6-14**a** and Figure 6-14**b** respectively. The miniature

patterned-light projection system was integrated on an inverted microscope (Olympus, IX83) with a high-speed microscope camera (Basler, ace2000-340kmNIR). The worm paralyzed on the agar plate was placed upside down on a motorized X-Y stage (Prior, Precision III) on the microscope sample plane. The 473 nm blue laser beam generated by a laser source (Dragonlaser, 473FN200) is magnified by a beam expander (Dragonlaser, LBE-10X), and reflected by a mirror (Thorlabs, PF20-03-P01) to project onto the DMD chip (ViALUX, V-7001). The laser beam patterned by the micromirrors arrays illuminates through a 4F lens sequence (Thorlabs, AC300-050-A, AC508-100-A-ML). Then, a customized dichroic (Semrock, FF670-SDi01-18x26) reflects the beam and change its direction. The laser beam passes through the microscope tube lens (Edmund Optics, LENS ACH 25 X 175 VIS-NIR INK), and finally gets shrunken by the microscope objective (Olympus, UPlanFL 4× / UPlanFL 10×) to form the micrometer-sized image pattern on the worm body.

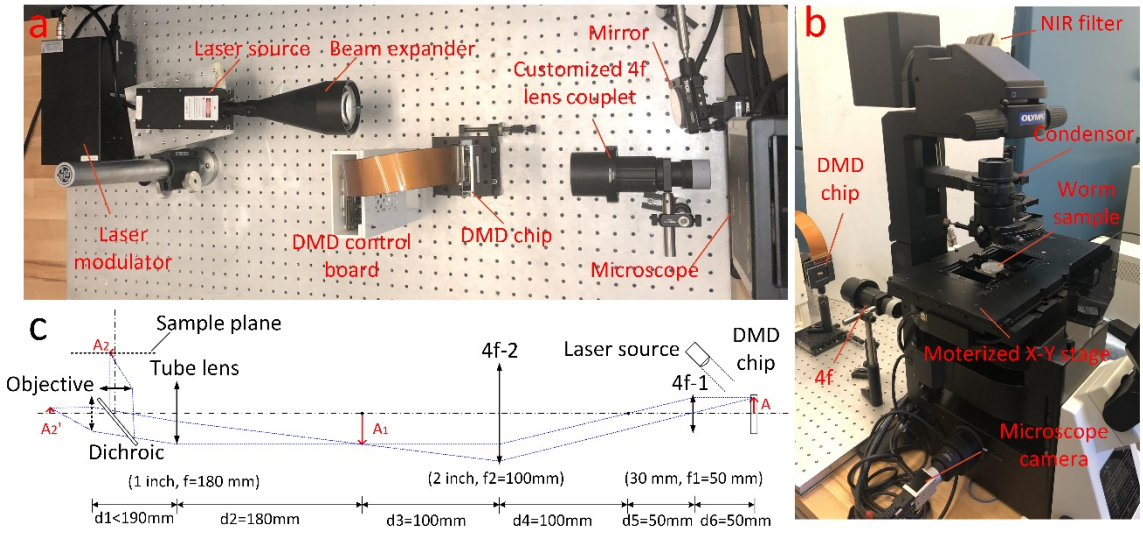


Figure 6-14 The system hardware structure for the illumination system. **a.** The photograph for the optical setup. **b.** The photograph for the customized microscope setup. **c.** Optical configuration for the pattern-light illumination system.

### 6.11.1 Overall imaging configuration

The imaging system was designed to project the real image of the pattern formed by the DMD micromirror arrays onto the microscope sample plane with condensed size, as shown by the imaging path from pattern $A$ to pattern $A_2$ in Figure 6-14**c**. To better illustrate the light path, the virtual image of $A_2$ is plot as $A_2'$, so all the optics can be represented on a single straight centerline.

Most of the inverted microscopes are designed as infinity-corrected systems, which allows for flexible alignment between the tube lens and the objective, as shown in Figure 6-14**c**. However, since the light incident angle of the DMD chip is usually 12 degrees, the space is limited for the layout of light source due to the restriction of d1 (d1 < 190 mm for Olympus microscopes). Therefore, we elongated the light path coaxially with a 4f system. As shown in Figure 6-14**c**, the laser pattern $A$ digitally programed on the DMD chip (diagonal 0.7 inch) is the original image in the optical system. The patterned light passes through the 4f system and forms a real image at $A_1$, and further condenses in size via the tube lens-objective couplet to form the virtual image at $A_2'$ (or the corresponding real image at $A_2$). By programming the 1024×768 original digital images patterned by the DMD chip, the shrunken patterns on the microscope sample plane can be manipulated to illuminate the micrometer scale target regions.

### 6.11.2 Microscope customization

The pattern-light projection system was built on the Olympus IX83 inverted microscope. Several original subsystems on the microscope need to be customized for the imaging and locomotion control of the worm.

*Pattern projection*: The fluorescent light source and illuminator on the back side of the microscope were completely removed and replaced by an achromatic doublet (Edmund Optics, LENS ACH 25 X 175 VIS-NIR INK). This achromatic doublet was placed inside the fluorescent port by a 3D printed holder and used as the objective tube lens for the laser pattern formation. In addition, the original dichroic in the filter cube turret (dichroic I in Figure 6-1) was replaced by a high-pass customized one (Semrock, FF670-SDi01-18x26) which reflects the blue patterned light onto the sample plane, and in the meanwhile, allows the bright field NIR lights to be imaged by the microscope camera.

*Brightfield illumination*: The sensitive wavelength for the ZM5398 worm is around 400 to 500 nm. To minimize the disturbance stimulations initiated by the bright field illumination lights, a NIR filter with the transmission wavelength longer than 700 nm was used at the top filter cube. In addition, a NIR enhanced camera (Basler, ace2000-340kmNIR) was employed to capture the worm body shape.

### 6.11.3 Worm tracking loop

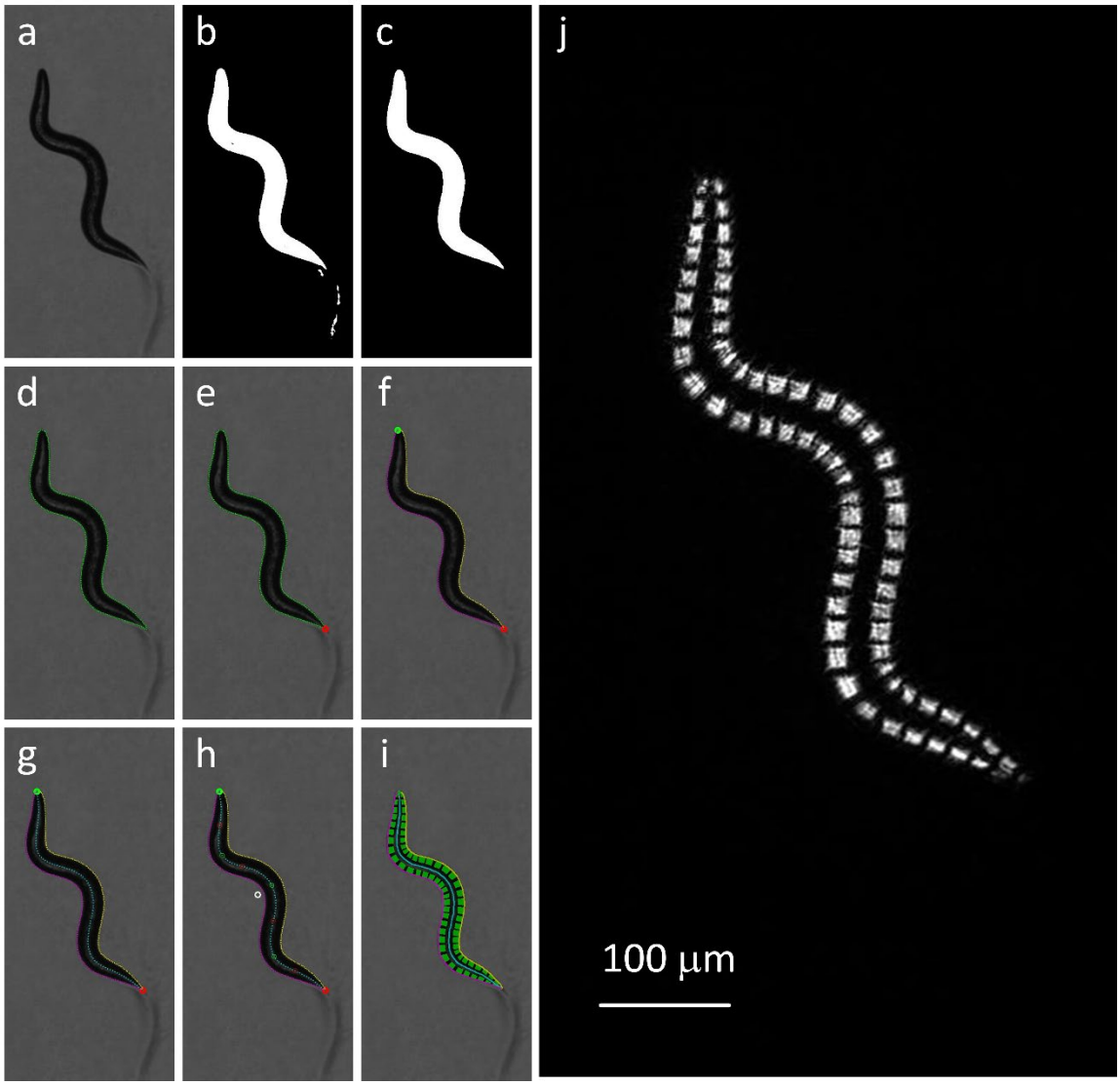


Figure 6-15 The image processing algorithms for the real-time tracking of C. elegans. a. The original image grabbed by the microscope camera. b. The binarized image. c. The purified binarized image. d. The contour of the worm. e. The tail detection on the worm image. f. The head detection on the image. g. The centerline calculation on the image. h. The mass center and the curvature calculation. i. The segmentation of the worm body. j. The projected worm pattern on the microscope sample plane with 4× objective

Since the FOV of the microscope camera covers the range of only 3.5 mm under 4× objective, the worm could easily crawl out of observation after a few minutes of movement. The worm tracking system is designed to control the positioning of the X-Y motorized stage to keep the worm within

FOV. In the feedback channel of the worm tracking loop, a high-speed image processing algorithm is designed to analyze the worm centroid position based on the worm boundary images grabbed by the microscope camera (Section 6.12). The analysis result is then subtracted by the center coordinates of FOV to calculate the control error, which provides feedback to a PD controller and regulates the displacement of the motorized X-Y stage. In our experiments, the camera was operating at the frame rate of 340 fps, and the X-Y stage speed is set as 6.5 mm/s. The overall operating speed of the worm tracking loop was regulated as 40 fps. Considering the average movement speed (~0.15 mm/s) of N2 worms, the worm centroid was always kept in the center of FOV throughout the experiments.

### 6.11.4 Pattern formation loop

Besides the worm centroid coordinates, the image processing algorithms also analyzes the worm boundaries and curvatures during the experiments simultaneously (Figure 6-2c). In our experiments, both the ventral and dorsal side of the worm were segmented into 100 sections for the stimulation of each body muscle groups selectively. Based on the analyzed worm morphologic features, the algorithm automatically constructs the laser pattern on the DMD chip to reflect the laser beams onto the microscope sample plane. Throughout the experiments, the worm morphologic features of positions and shapes were updated automatically with the frame rate of around 40 fps. Each time for the pattern update, the corresponding laser beam position, shape and intensity were re-calculated according to the input of the worm direction control.

## 6.12 Supplementary S8 - Image processing for the real-time worm movement tracking

To perform closed-loop control of the proposed robo-worm, effective feedback method has to be developed to detect the real-time status of the controlled locomotion. In the experiments, we were analyzing the worm position, curvature and moving direction from the images grabbed by the high-speed microscope camera.

Before the image processing, the ROI (region of interest) that containing the entire worm is automatically determined based on the worm boundary analysis result of the last image frame. Firstly, the original image of the worm (Figure 6-16a) is filtered by a 3x3 *Gaussian* mask to reduce image noises, and binarized with *Otsu* method to separate the worm body from the background features (Figure 6-16b). A 3x3 erode and dilate operator is applied to the resultant image, to eliminate the small debris in the image. Then, contour detection is conducted on the binarized

image, and the largest contour (Figure 6-16c) within ROI is recognized as the worm boundaries (Figure 6-16d).

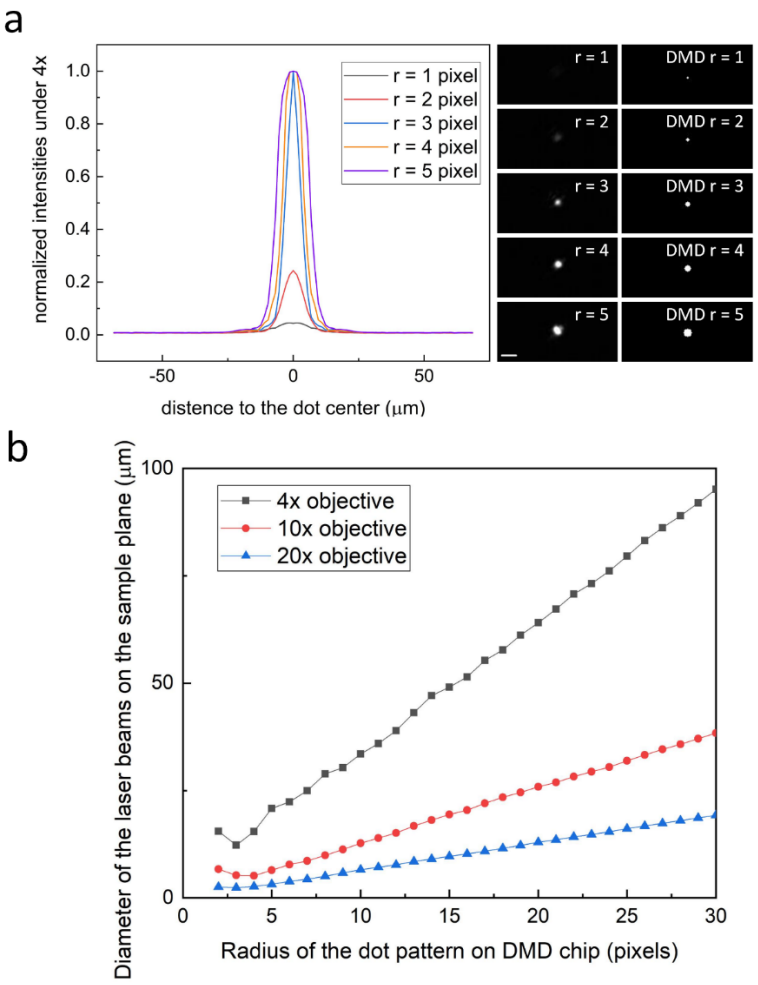


Figure 6-16 The spatial resolution of the pattern light illumination system. **a**. The power distribution of the dot pattern on the image sample plane (scale bar = 30 μm). **b**. The size of the laser beam with respect to different original pattern size on the DMD chip, measured by the area above 20% of the maximum power.

The obtained worm contour are discrete points distributed on the worm boundaries, and a linear interpolation method is applied to resample the points with a fixed distance before further process. Denote the resampled contour points as $p_i, i = 1, \dots n$, the acuity of a specific point with respect to its adjacent points can be evaluated as

$$G_{k,i} = (p_{i+k} - p_i) \cdot (p_{i-k} - p_i) \approx l_k^2 cos\omega_i \qquad (6.12\text{-}1)$$

where $k$ is the size of the vector used for acuity calculation, $l_k^2$ is the vector length, $\omega_i$ is the acute angle between two intersection vectors. Since the worm tail is usually the sharpest point on the boundary, the tail point $p_t$ is defined by

$$t = \arg max_i\{C_{k,i}\}, i \in \{1, \dots n\} \tag{6.12-2}$$

as shown in Figure 6-16e. In addition, since the head point $p_h$ is the second sharpest point on the boundary, it is detected by

$$h = \arg max_i\{C_{k,i}\}, i \in \{1, \dots n\} - \{t - a, \dots t + a\} \tag{6.12-3}$$

where $a$ is the region width to exclude the tail area.

The contour points can then be separated into two point sets of dorsal and ventral, after identifying the head and tail. These two point sets are further resampled with a fixed distance through linear interpolation into the sample size of $m$. As shown in Figure 6-16f, we get the ventral points $v_i$ and dorsal points $d_i$. For any point $v_i$ on the ventral side, we can find a point on the dorsal side $d_j$, such that $\overrightarrow{v_i d_j}$ is perpendicular to the boundary tangent vector at point $v_i$. Mathematically, $d_j$ can be defined as

$$j = \arg min_x\{(v_{i+k} - v_{i+k}) \cdot (d_j - v_i)\}, c \in \{i - a, \dots i + a\} \tag{6.12-4}$$

where $k$ is the length of tangent vector, $a$ is a parameter to limit the searching area. Then, the point $c_i$ on the worm centerline can be detected as the midpoint of $\overrightarrow{v_i d_j}$

$$c_i = \frac{1}{2}(v_i + d_i), i \in \{1, \dots m\} \tag{6.12-5}$$

as shown in Figure 6-16g. The detection for the worm centerline points is not accurate from mathematical definition, but it is fast and effective in practical use. Based on the worm centerline points $c_i$, the curvature of the worm can also be calculated. Figure 6-16h shows the maximum curvature and zero curvature points on the worm centerline.

In addition, by finding the corresponding perpendicular point of the centerline point $c_i$on both the dorsal and ventral sides, we can segment the worm body into several distinct sections, as shown in Figure 6-16i. Transferring the image coordinates into the DMD frame, the segmented worm pattern can be projected onto the microscope sample plane. As shown in Figure 6-16j, each of the small section is projected by a micrometer sized laser beam.

As the projection resolution is 12.3 μm under 4× objective, we have extended the small sections with a tiny distance away from the centerline, so as to avoid stimulating the muscular cells on the opposite side of the worm body.

### 6.13 Supplementary S9 - System performance tests

In this supplementary material, we tested the projection resolution of the developed patterned-light illumination system and discussed the features of the c++ software we developed with multi-thread coding techniques.

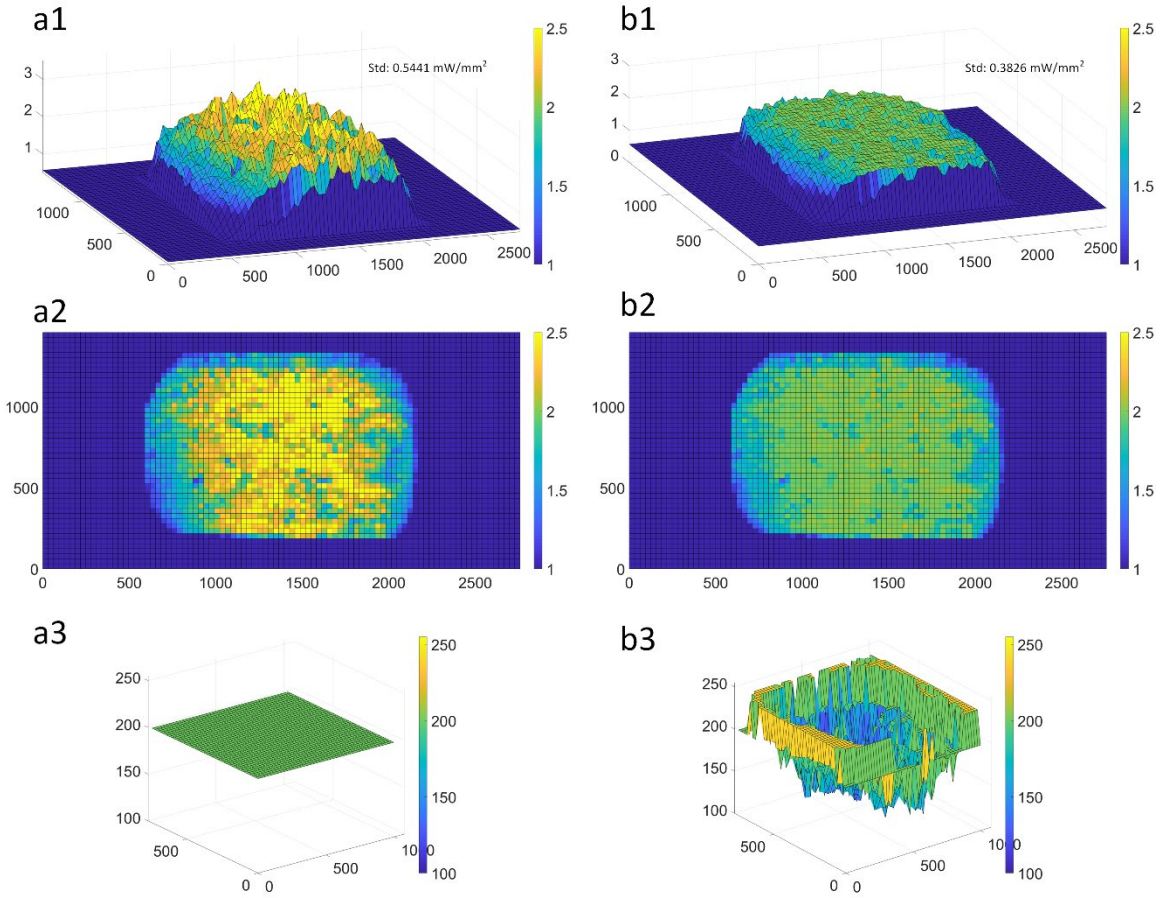


Figure 6-17 Software compensation for the laser power distribution. **a1 & a2.** The 3D view of the laser power distribution without compensation. **a3**. The DMD pixel intensity without compensation. **b1 & b2**. The 3D view of the laser power distribution after compensation. **b3**. The DMD pixel intensity after compensation.

### 6.13.1 Spatial performance tests

To test the spatial performance of the pattern light illumination system, we generated a series of circle patterns on the DMD chip with the size from 1 to 30 DMD pixels and measured the corresponding patterns on the camera image, as show in Figure 6-16. It can be seen in the laser power distribution figure (Figure 6-16**a**) that the size of the projected laser pattern reduces as the DMD pattern pixels decreases, and the laser pattern becomes rarely detectable as the DMD pattern size decreases to 2 (above 20% of the maximum laser power is considered as region illuminated on the sample plane). Thus, the laser pattern formed by r=3 DMD pixels is considered as the resolution of the developed system. As shown by the dot size figure in Figure 6-16**b**, the resolution was measured as 12.3 μm, 5.3 μm and 2.4 μm for 4×, 10× and 20× objectives respectively. Please note that the r=3 pattern is smaller than r=2 pattern as shown in Figure 6-16**b.** This is because that the illuminated region is considered as the camera pixels points with intensity above 20% of the global maximum intensity. As r=2 pattern is much dimmer than that of r=3, the threshold generated by the 20% power for the illuminated region of r=2 pattern is lower than that of r=3, and consequently, r=2 pattern is larger than r=3 pattern.

In addition, a series of single dot patterns with the size of 5 DMD pixels were created to scan from the left-top to the right-bot of the DMD chip, and the power of each pattern was measured (Thorlabs, PD100) and plotted in the power distribution within FOV. It can be observed in Figure 6-17 that the DMD chip is mapped to the region in the center of the camera FOV. Because of the Gaussian wavefront of the laser beam, the intensity is slightly higher in the center region and lower in the boundaries (Figure 6-17a). The imaging noise is also decreasing the uniformity of the beams (Figure 6-17a and Figure 6-17b). Based on the linear relationship between the duty ratio of each DMD pixels and the corresponding projected laser intensity, we developed a software compensate algorithm to increase the projection uniformity (Figure 6-17c and Figure 6-17d). As shown by Figure 6-17d, the compensated power distributes more evenly on the sample plane.

### 6.13.2 Software features

During the past decade, similar miniature projection systems built on microscope were proposed for the targeted stimulation of *C. elegans*, including the LCD projector-based illumination system [10, 11], the Colbert system [12], as well as the commercial MIGHTEX system. It worth mentioning that our miniature projection system has the superior performance among the previous

counter systems, not only for the hardware employed, but also for the multi-thread software and algorithms we developed to coordinate the operating of the hardware. In the following, several software performance features of the proposed system are listed.

*Pattern update rate:* In our system, the images are uploaded to the DMD chip (1024×768) sequentially to achieve the online update of the laser pattern. The update time cost of the worm pattern is tested as 6 ms for 1-bit images and 13 ms for 8-bit images, which leads to the 166 fps and 77 fps pattern update rate corresponding. It is much faster than the previous systems.

*Image processing time cost:* The image processing time cost for the 2040x1088 worm image is 8 ms, 12 ms, and 15 ms for L4, young adult, and adult worms, respectively. The time cost is further reduced during the experiments by re-assigning the FOV size according to the analysis result of the previous image frame.

*Laser power uniformity:* As we have developed software compensation for the laser power within the illumination region, the power distribution is much more uniform than the previous ones.

*Adjustable laser power:* The laser power of the pattern is tunable in the range of 0-15 mW/mm$^2$. Furthermore, the laser intensity of each projected regions within a single beam pattern are fully controllable by assigning the duty ratio of the corresponding DMD pixels. With the tunable micro laser beam power, we successfully controlled the moving direction and destination of the worms.

## 6.14 Supplementary S10 - Kinematic modelling for close-loop control

### 6.14.1 The zig-zag kinematic model

The worm is supposed to crawl forward along a serpentine path under sinusoidal laser pattern stimulation, in which the worm head waves to the left and right alternatively, as shown by the red lines in Figure 6-18**a**. The 2D points on the agar plate where the worm head waves to the dorsal crest are denoted as $D_i$, and ventral crest are denoted as $V_i$, where $i = 0,1,2 \ldots$ indicates the time sequence. It is obvious that $D_i$ and $V_i$ are also the positions that the laser beams start to stimulate the dorsal and ventral sides of the head muscles. Each laser beam projected on to the worm body corresponds to a specific crest point on the head path.

a

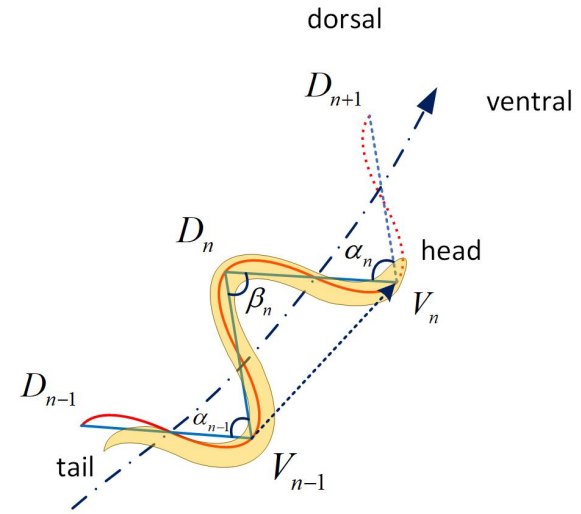


b

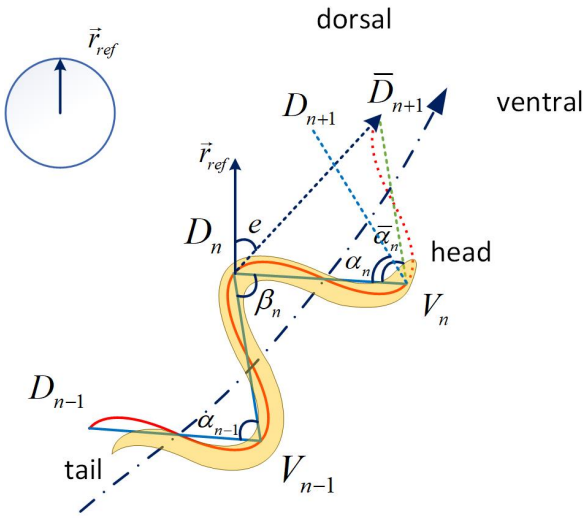


Figure 6-18 The schematic figures for close-loop modelling and controls. **a.** The schematic for the zig-zag modelling. **b.** The schematic for the close-loop direction regulation of the paralyzed worm.

As shown by the blue lines in Figure 6-18**a**, by connecting the points ... → $V_{n-1}$ → $D_{n-1}$ → $V_n$ → $D_n$ → ⋯ sequentially with straight lines, the serpentine locomotion path can be simplified as a zig-zag route. Each turning point on the zig-zag route has a waving angle $\alpha_i$ and $\beta_i$ , $i = 0,1,2$ ... Stronger laser power $P_V$ or $P_D$ of the beam on the dorsal or ventral side will induce larger bending curvature and smaller $\alpha_i$ or $\beta_i$, which can be denoted as

$$\alpha_i = f_V(P_V(i)) \text{ and } \beta_i = f_D(P_D(i)) \text{ , } i = 0,1,2 \ldots \quad (6.14\text{-}1)$$

where $P_V(i) \in [0,1], P_D(i) \in [0,1], \alpha_i \in [0,\pi], \beta_i \in [0,\pi]$.

We know from the basic muscle optogenetics that stronger stimulation light power leads to stronger muscle contraction:

$$\alpha_i \propto \frac{1}{P_V(i)} \text{ and } \beta_i \propto \frac{1}{P_D(i)}, i = 0,1,2 \ldots \quad (6.14\text{-}2)$$

It is reasonable to make the inference that $f_V$ and $f_D$ are with the same structure but different coefficients. However, we are not able to conclude a clear mathematical structure of $f_V$ and $f_D$ in our experiments, due to the large uncertainty of the muscle optogenetics process on the live worm (please refer to the large error bar of power-curvature response curve in Figure 6-2). In addition, the parameters for the response of worm muscles differs in every worm individual, rendering the mathematical conclusion of a single worm response insignificant for control purpose. This is the challenge for the locomotion regulation of the worm robot.

With fixed stimulation pattern wavelength $L$, the locomotion of *C. elegans* is simplified to be a sequence of bending angles:

$$\alpha_0\beta_0 \to \cdots \alpha_{n-1}\beta_{n-1} \to \alpha_n\beta_n \to \alpha_{n+1}\beta_{n+1} \to \cdots \quad (6.14\text{-}3)$$

In the zig-zag model frame, the open-loop locomotion mimic for the free moving N2 worms (Figure 6-3. In the main text) can be denoted as

*Straight forward movement*: $\tau = \alpha_i = \beta_i, i = 0,1,2 \ldots$

*Shallow I turn*: $\tau = \alpha_i = \beta_j, i = 0,1,2 \ldots n-1, n+1, \ldots, j = 0,1,2 \ldots$while $\alpha_n < \tau$.

*Shallow II turn:* $\tau = \alpha_i = \beta_j, i = 0,1,2 \ldots n-1, n+1, \ldots, j = 0,1,2 \ldots$while $\alpha_n > \tau$.

*Gradual turn*: $\alpha_i < \beta_i, i = 0,1,2 \ldots$

*Omega turn*: achieved by increasing the wavelength $L$ for the single duty laser pattern.

### 6.14.2 The definition for the moving direction

To regulate the direction, we first need an effective method to measure it. In this paper, we are evaluating the moving direction of serpentine locomotion by the **direction of phase (DOP)**. We define it as a vector that starts form the location on the head path with $2\pi$ phase before of the head and ends at the head. On the zig-zag kinematic model, DOP $\vec{d}$ is $\overrightarrow{d_V}(i) = \overrightarrow{V_{i-1}V_i}$ or $\overrightarrow{d_D}(i) =$

$\overrightarrow{D_{i-1}D_i}$ when it turns to the ventral or dorsal side respectively. As shown in Figure 6-18**a**, the current DOP is $\overrightarrow{V_{n-1}V_n}$.

Please note that the most straight forward method to evaluate the moving direction is to calculate the time derivative of the worm centroid. However, to control the worm moving direction, the worm cannot be treated as a moving point any longer, and more detailed information must be included. For the serpentine locomotion of the worm, the turning is usually achieved by the biased waving of the head, which is contributed by the forepart of the body. As a small variance of the head cannot be timely demonstrated in the change of the centroid, we proposed the definition of DOP here to clearly quantified the movement direction.

### 6.14.3 The control objective

In the frame of the zig-zag model, once the worm head reaches dorsal crest $D_i$, the laser beam $P_D(i)$ projected on the ventral side of the head muscle makes the worm head bend to the ventral crest $V_i$ with the angle $\beta_i$. After that, the laser beam $P_V(i)$ turns the head from $V_i$ to $D_{i+1}$ with the angle $\alpha_i$ to form the zig-zag path. Experimentally, $\alpha_i$ and $\beta_i$ can be jointly regulated by the laser intensity, illumination range and illumination time. For stable and continuously regulation of the bending angles, in our close-loop control of worm direction, the illumination range and time are fixed, and the intensities are chosen to manipulate each bending angles, and consequently, control the general moving path of the whole worm. In addition, only the beam intensities in the head region (L/2 from the tip; see Figure 6-2a in main text) are manipulated to change moving directions, while the body segments are illuminated with the maximum power to provide enough thrust force for the movement.

The control input of the direction regulation system is the laser power $\begin{bmatrix} P_V \\ P_D \end{bmatrix}$, and the output is the DOP on the head path $d(i)$. Once a laser beam projects on the worm head on either the dorsal or ventral side, the beam power $P_V$ or $P_D$ will be updated immediately in order to regulate the corresponding $\alpha_i$ and $\beta_i$. The beam power will remain constant during the process until the next beam starts stimulating the other side of the head muscles. The DOF of the controlled worm, as illustrated in Figure 6-18a, can be formulated as

$$d(i+1) = d(i) + \big(\beta(i) - \alpha(i)\big) = d(i) + \Big(f_V\big(P_V(i)\big) - f_D\big(P_D(i)\big)\Big) \qquad (6.14\text{-}4)$$

## 6.15 Supplementary S11 - Control synthesis for the soft robo-worm

### 6.15.1 System analysis

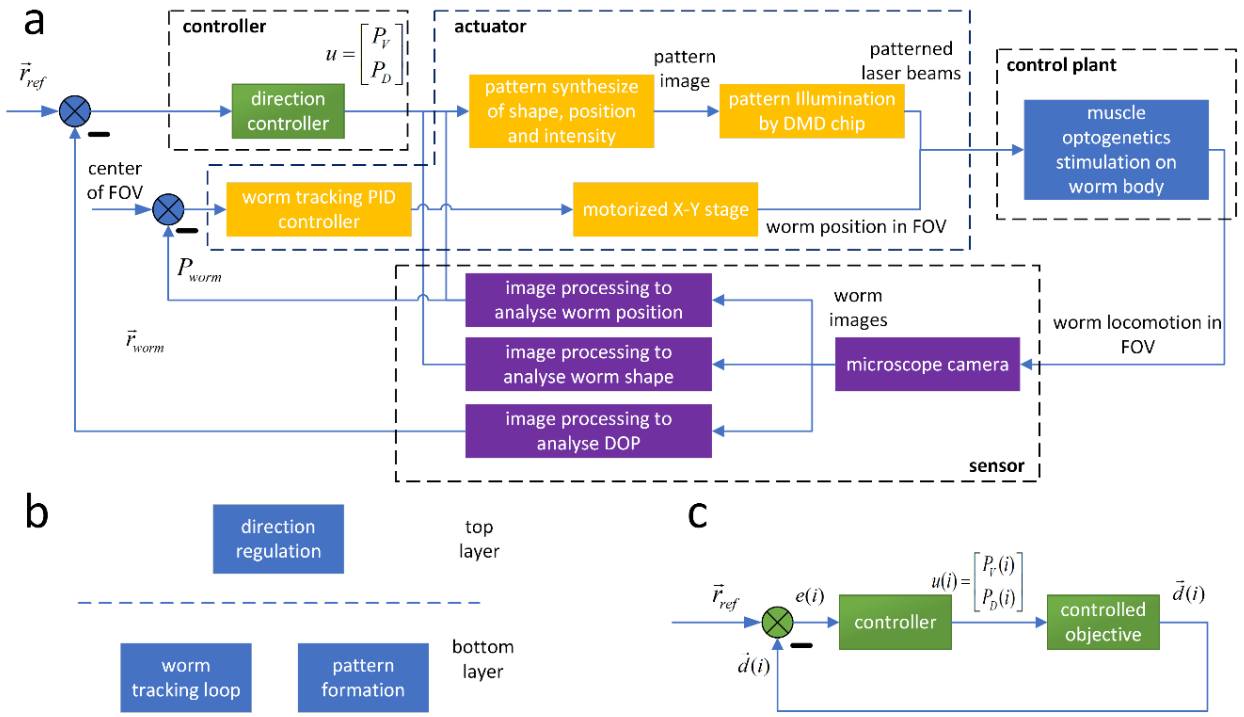


Figure 6-19 Block diagram for the worm locomotion control system. **a.** Detailed control structures of the whole locomotion control system, including worm tracking, pattern formation, and direction regulation. **b.** The two layers of the control structure. **c.** The simplified block diagram from the perspective of direction regulation in the top layer.

The general approach in this paper is to regulate the moving direction of the paralyzed worm via manipulating the intensities of the laser beams illuminated alternatively on the dorsal and ventral side of the worm body. The detailed system structure is plotted in the block diagram of Figure 6-19a.The two hardware close-loops (see Section 6.11) construct the activation basis for the system (see the actuator in Figure 6-19a). The worm tracking loop and the pattern formation loop work collaboratively to guarantee that the laser beams are projected accurately onto the desired positions of the worm body (Figure 6-19a). On top of the activation level, we added a control schematic for the regulation of the worm general moving direction (Figure 6-19b). Since the working speed of the bottom layer (40 fps for pattern formation loop and 30 fps for the worm tracking loop) is much faster than the top layer (updated when a new beam is scanning from the head; updating rate is about 0.17 Hz under 4% scanning speed), the whole bottom layer can be generally regarded as the

actuator part of the top layer. Therefore, the general system structure are simplified to a two-block layout from the perspective of direction control, as shown in Figure 6-19c. The controller calculates the laser power to be illuminated from the feedback direction error, while the controlled objective converts the input power to the moving direction of the worm as formulated by *Equation* (6.14-4).

### 6.15.2 Predictive-P feedback controller design for the direction track

To effectively regulate the movement direction of the worm robot without a clear structure of the response model *Equation* (6.14-4), we propose the **Predictive-P feedback control** for this specific controlled objective, a live worm.

DOP demonstrates the current locomotion state, however, it still cannot represent the biased tendency of the periodic head waving. Instead, we proposed an algorithm to predict the DOP of the next step and feed it back for the regulation of laser beam power. As shown in Figure 6-3, the head of the worm is at $V_n$ and a laser beam with the power of $P_V$ starts stimulating the ventral side head muscles to wave the head to dorsal side. If no adjustment is applied to the worm, the worm will probably repeat its previous behaviour in the last period and wave the head to $\overline{D}_{n+1}$. $\overline{D}_{n+1}$ is an estimation of $D_{n+1}$ with the bending angle of $\bar{\alpha}_n(\bar{\alpha}_n = \alpha_{n-1})$. With the DOP estimation, the system feedback error of the moving direction can be denoted as

$$e = r - \bar{d} \tag{6.15-1}$$

where $r$ is the direction of the reference vector $\vec{r}_{ref}$. $\bar{d}$ is the direction of the estimated DOP $\vec{d} = \overrightarrow{D_n\overline{D}_{n+1}}$.

Due to the time-varying properties and large peer-to-peer variance of the muscle optogenetic process across each worm individuals, we cannot identify any obvious dynamic structures for the response function $\alpha_i = f_V\big(P_V(i)\big)$ and and $\beta_i = f_D(P_D(i))$. Considering the low updating rate of this direction regulation (0.17 Hz) and the unexpecting properties of the control objective, we adopted the most basic control method P-control for the direction guidance of this live paralyzed worm in hope of achieving robust control performance. With the P-control schematic, the feedback regulation of the laser power $P$ is defined as

$$P_g(i+1) = P_g(i) + \Delta P_g(i) = P_g(i) + k_g(i)e_g(i) \tag{6.15-2}$$

where $g = V$ when the worm head is at the ventral side and about to wave to the dorsal side under $P_V(i+1)$, while $g = D$ when the worm head is at the dorsal side and about to wave to the ventral side under $P_D(i+1)$. $k_V$ and $k_D$ are nonlinear P-control coefficients to compensate for the sensitivity difference of the dorsal and ventral muscles.

$$\begin{cases} k_V(i) = k_P \dfrac{\sqrt{P_V(i)}}{\sqrt{P_V(i)} + \sqrt{P_D(i)}} \\ k_D(i) = k_P \dfrac{\sqrt{P_D(i)}}{\sqrt{P_V(i)} + \sqrt{P_D(i)}} \end{cases} \tag{6.15-3}$$

$k_P$ is used as 0.015 in our experiments. Specifically, as shown in Figure 6-18b, for the vertical reference direction $r_{ref}$, higher intensity $P_D$ are adopted for the current control cycle to reduce the bending angle $\alpha$, so that the moving direction $d$ will be aligned closer to the reference $r_{ref}$. In addition, to reduce the overshot for the regulation, the difference of the bending angle $\alpha_i$ and $\beta_i$ are restricted during the control process. Once $|\alpha_i - \beta_i|$ is larger than a predesigned threshold, the regulation will be applied in the opposite direction.

$$\begin{gathered} if\ \theta_i = |\alpha_i - \beta_i| > \theta_0 \\ \begin{cases} \Delta P_V(i) = -k_V(i)\theta_i \\ \Delta P_D(i) = -k_D(i)\theta_i \end{cases} \end{gathered} \tag{6.15-4}$$

where $\theta_0$ is a predesigned threshold (we defined $\theta_0 = 20^0$ in our experiments).

### 6.15.3 Point-to-point navigation for the *C. elegans* micro-bio-robot

Since the structure and parameters of $f_V$ and $f_D$ cannot be identified, it would be extreme difficult to accurately control the moving path of the worm robot. However, by slightly modifying the reference in the direction track controller as

$$r = \overrightarrow{M_c P} \tag{6.15-5}$$

where $M_c$ is the centroid of the worm, and $P$ is the predesigned destination, the direction track loop can be improved to a proportional navigation control scheme. Within this scheme, the worm can be artificially guided to a predesigned destination. We have to noted here that, the steering capability of the robo-worm is limited in order to reduce the overshot, as shown in *Equation* (6.15-4). The worm would not be able to reach the destination if the worm is already close to the destination but its moving direction has not been stabilized towards the destination. Because the

changing rate of $r$ (*Equation* (6.15-5)) is too fast to be tracked and the resulting direction error $e$ (*Equation* (6.15-1)) is too large be compensated in these cases. Therefore, in the point-to-point experiments, the destination must be defined far away from the origin (3 mm in our experiments).

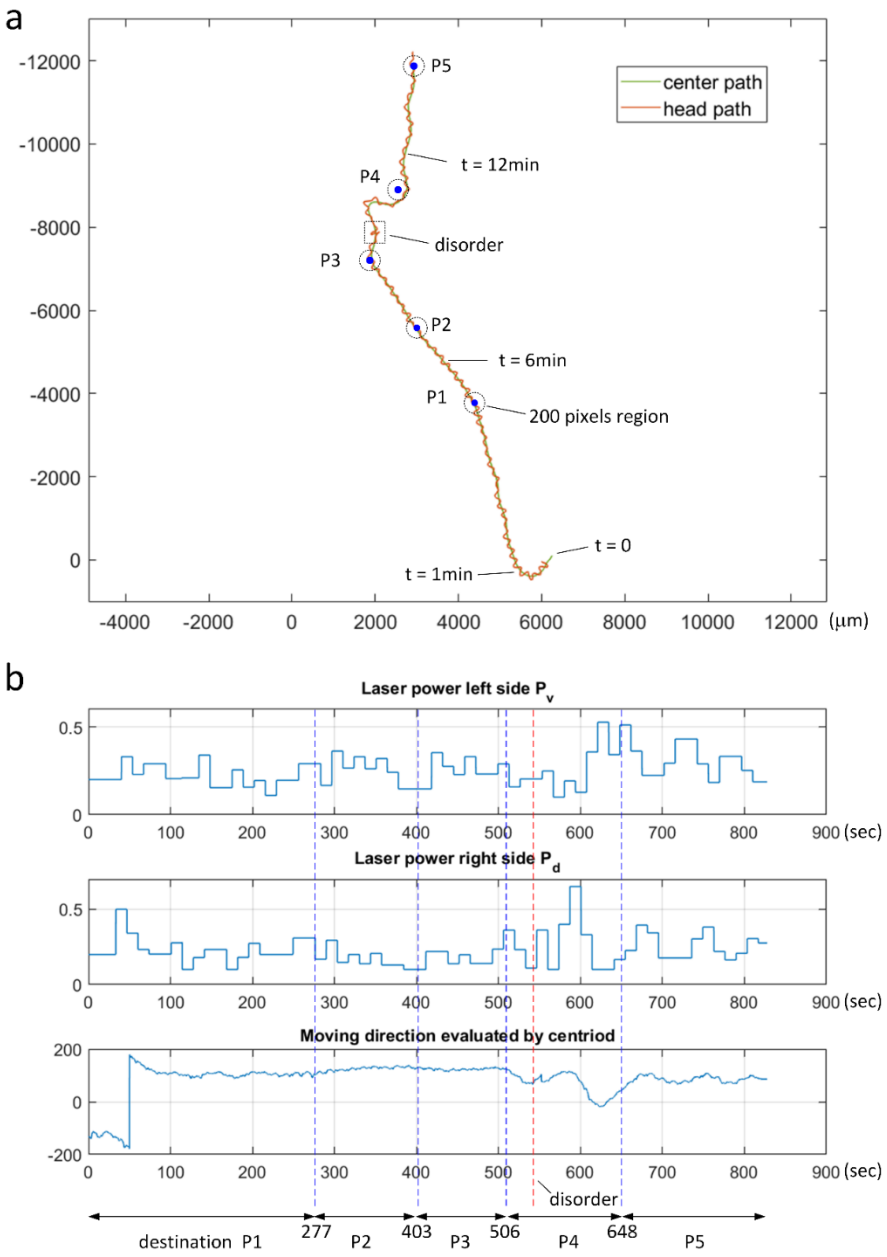


Figure 6-20 The data for the experiment of controlling the worm pass through a maze. **a.** The worm movement path on the agar. **b.** The laser power input and the measured moving direction.

By defining a series of intermediate destination points on the agar plate, we managed to control the paralyzed worm navigate through a maze, as illustrated in Figure 6-3 in the main text. In our

experiments, the worm will automatically navigate to the next destination when its centroid point is within 200 pixels to the current one, as labeled by the dash circle in Figure 6-20a. It can be seen in Figure 6-20a (also in the Supplementary Video S9) that the worm moves accurately to the pre-defined destinations of P1, P2, P3 and P5. During the experiment, a disorder of the worm happens at 541s when crawling towards P4, as the worm suddenly moved backward. The disorder induced false calculation for the DOP, and thus, the following control input of $P_v$ and $P_d$. As shown in Figure 6-20b, a suddenly increased laser power $P_d$ was provided to the worm body. However, the algorithm automatically adjusted the worm moving direction with a sharp turning and re-aligned the moving path towards P4. When the worm centroid moved into 200 pixels area of P4, the algorithm automatically switched its direction to the destination P5.

## 6.16 Supplementary references


[1] R. Ghosh, E. C. Andersen, J. A. Shapiro, J. P. Gerke, and L. Kruglyak, "Natural variation in a chloride channel subunit confers avermectin resistance in C. elegans," *Science,* vol. 335, no. 6068, pp. 574-578, 2012.

[2] T. Bruegmann *et al.*, "Optogenetic control of heart muscle in vitro and in vivo," vol. 7, no. 11, p. 897, 2010.

[3] J. A. Dent, M. M. Smith, D. K. Vassilatis, and L. Avery, "The genetics of ivermectin resistance in Caenorhabditis elegans," *Proceedings of the National Academy of Sciences,* vol. 97, no. 6, pp. 2674-2679, 2000.

[4] S. T. Laing *et al.*, "The transcriptional response of Caenorhabditis elegans to ivermectin exposure identifies novel genes involved in the response to reduced food intake," *PLoS One,* vol. 7, no. 2, p. e31367, 2012.

[5] N. Pokala, Q. Liu, A. Gordus, and C. I. J. P. o. t. N. A. o. S. Bargmann, "Inducible and titratable silencing of Caenorhabditis elegans neurons in vivo with histamine-gated chloride channels," vol. 111, no. 7, pp. 2770-2775, 2014.

[6] S. Hirose, *Biologically inspired robots: snake-like locomotors and manipulators*. Oxford University Press Oxford, 1993.

[7] V. J. Butler *et al.*, "A consistent muscle activation strategy underlies crawling and swimming in Caenorhabditis elegans," *Journal of the Royal Society Interface,* vol. 12, no. 102, p. 20140963, 2015.

[8] Z. Guo and L. Mahadevan, "Limbless undulatory propulsion on land," *Proceedings of the National Academy of Sciences,* vol. 105, no. 9, pp. 3179-3184, 2008.

[9] S. Hirose and H. Yamada, "Snake-like robots [tutorial]," *IEEE Robotics & Automation Magazine,* vol. 16, no. 1, pp. 88-98, 2009.

[10] J. N. Stirman *et al.*, "Real-time multimodal optical control of neurons and muscles in freely behaving Caenorhabditis elegans," *Nature methods,* vol. 8, no. 2, p. 153, 2011.

[11] J. N. Stirman, M. M. Crane, S. J. Husson, A. Gottschalk, and H. Lu, "A multispectral optical illumination system with precise spatiotemporal control for the manipulation of optogenetic reagents," *Nature protocols,* vol. 7, no. 2, p. 207, 2012.

[12] A. M. Leifer, C. Fang-Yen, M. Gershow, M. J. Alkema, and A. D. Samuel, "Optogenetic manipulation of neural activity in freely moving Caenorhabditis elegans," *Nature methods,* vol. 8, no. 2, p. 147, 2011.

# Chapter 7

# Conclusion

# Chapter 7: Conclusions and Future Work

## 7.1 Summary of the accomplishments

Routine experiments of *C. elegans* screening and transgenics are conducted manually in worm biology laboratories, which is especially time-consuming and labor-intensive even for skilled operators, but amenable for standard operations automated by machines. In this thesis, automated worm sorting and microinjection systems are developed, as well as their supporting microfluidic devices, image processing algorithms and robotic micromanipulation techniques, to reduce the manual works and increase operation success rate. The developed systems provide superior operation speed, throughput, accuracy and robustness compare over the manual operations. Besides the worm sorting and injection projects, a pattern-light illumination system for high-accuracy automated optogenetic experiments of *C. elegans* is developed. By investigating the serpentine dynamics of the worm, the crawling behavior of free-moving N2 worms are reproduced on a paralyzed worm. The integrated methodologies for muscular force stimulation and control approaches for this soft-body nematode worm enlightened a new route for robot development—a microrobo-nematode, which turns a live natural animal into an artificially controllable robot. In addition, the proposed optogenetic system could be used for further studies on serpentine locomotion biophysics and neuronal biology. In general, this thesis provides the following insights and techniques as organized below.

- *The development for the first of its kind soft robot – a C. elegans soft microrobot-animal is explored.*

  Muscle cell optogenetics allows to artificially activate the body muscles on a live worm expressing *ChR2* within muscular cells (*P-myo3-ChR2* in my project). By reproducing the phase difference between the muscle force and the paralyzed worm body shape with the developed pattern-light illumination system, The serpentine crawling is successfully induced on agar substrate with fully controllable manner, and thus, turned a live worm into a soft microrobot-animal. This is the first attempt, in the soft robotics field, to turn a live animal into a highly controllable robot that moves under human intentions.
- *The close-loop control method for a light-driven soft robot based on a kinematic model is designed.*

The soft robotics have been arising as an important research topic during the last decade, and most previous works are focusing on novel designs, new activation methods, and capability demonstrations. The robotic basis of modelling and control, however, is seldom investigated due to its intrinsic difficulty that the soft robots are usually with infinite DOFs. In my project for optogenetic controlling of worm locomotion, the serpentine locomotion of *C. elegans* with the zig-zag kinematic model is characterized, and further proposed a predictive-P control method to successfully regulate the moving direction and destination of the paralyzed worm based on the image feedback. The develop approaches for the soft robotic activation, sensation, modelling and control could be an important step and a successful example towards the engineering basis of soft robotics.

- *The generation of thrust force during serpentine locomotion for the first time is identified, and more importantly, the theoretical result is verified through both dynamic simulation and optogenetic experiments.*

  The thrust force can be considered as the released muscular energy per unit displacement during serpentine locomotion. Theoretically, for stable serpentine locomotion, the thrust force is generated by the phase difference between the muscular torque and worm body shape. With the serpentine dynamic model, the generation of thrust force is simulated, and the simulation results support the proposed theory. Further, the phase difference is reproduced on a paralyzed worm with muscle optogenetic method, and successfully achieved the continuous serpentine locomotion of the worm. By calculating the phase difference and the thrust force induced moving speed on the artificial stimulated movement, it is found that larger phase difference within $[0, \frac{\pi}{2}]$ leads to faster crawling speed. Thus, the proposed theory is also supported by the experimental results.

  Conventionally, the phase difference of serpentine locomotion is usually considered to be a constant value of $90^0$, however, in my experiments, the phase difference is identified to be a variable parameter for the crawling of *C. elegans* to regulate its moving thrust force. The proposed theory could be an important reference for the bio-mechanics of serpentine locomotion.

- *A precise pattern-light illumination system is constructed and a highly effective operation software with c++ multi-thread techniques is composed to fully tap its potential performance.*

I designed the optical configuration for a DMD based projection system, and constructed the system on an inverted microscope for the optogenetic stimulation of biosamples with the resolution of single cells (of 17 μm / 3 μm for 4x / 20x objectives respectively). The high-speed microscope camera, motorized X-Y stage, DMD chip and image processing algorithms are working cooperatively on the host computer to stimulate single cells on the free moving *C. elegans*. With the multi-thread programming techniques the operation software is composed in the MFC frame to conduct the movement tracking, body morphologic analysis, and optogenetic stimulation of the free moving worm simultaneously. This system could also be used for the neuronal biology and bio-mechanics studies.

- *A highly effective image processing algorithm for the continuous morphologic feature calculation of free-moving C. elegans is proposed.*

  The proposed algorithm is designed with the capability of analysing the worm boundaries, and the corresponding worm centerline, length, width, volume, body curvature, etc. with super fast calculation speed (5 ms, 7 ms, 10 ms, 12 ms, 15 ms, and 17 ms for L1, L2, L3, L4 and adult worms correspondingly for 2040x1088 images). By reducing the size of ROI, the algorithm speed can be further improved. This algorithm has been used for the online automated screening for *C. elegans*, and the optogenetic stimulation of the *C. elegans* worm.

- *The systematic methods of microfluidics design, pneumatic fluid flow rate control, and image feedback regulation for the high-throughput robotic micromanipulation of C. elegans are developed.*

  For both the worm screening and microinjection system, image-assisted double layer microfluidic mechanisms to manipulate individual *C. elegans* are proposed. The pressure regulation unit with 18 outputs is developed on an Arduino board to provide both positive and negative pressure for the regulation of the on-chip microvalves and fluid pressure. Image processing algorithms are integrated in the software system to provide state feedback for automatic operations. This technical frame can be easily extended for the micromanipulation of cells, microparticles and small organisms.

- *A series of novel techniques for the robotic micromanipulation of C. elegans are developed, including the automatic contact detection, and the automatic coordinate mapping.*

  The vertical relative position of the needle tip and microfluidic channel is critical to perform microinjection of *C. elegnas*. An autofocusing-based image processing algorithm is proposed

to detect the contact position of the needle tip and the microfluidic channel surface automatically. In addition, an image processing algorithm is designed to enable automatic coordinate mapping from the manipulator frame to the image frame. These techniques could be easily extended to the application scenarios that require the control of a second end effector in the main operation field.

- *An integrated software platform is composed in c++ for the coordinative control of the automation hardware, such as the microscope, camera, motorized stage, micromanipulator, microinjector, pneumatic components, to name just a few.*

  Besides the micromanipulation mechanisms and approaches, the supporting hardware and software platform to fulfill the tasks are also propsoed. The regulations of all the automation hardware are integrated on the host computer in a customized software program.

## 7.2 Thesis contribution

The following list summarizes the main findings and contributions achieved during the presented study:

1. The phase difference between the worm body shape and the activation muscle torque is the main contributing factor for the generation of thrust force during serpentine locomotion.
2. A pattern-light projection system was developed on the inverted microscope with the superior resolution, based on which a live *C. elegans* is turned into an artificially controllable soft microrobo-nematode.
3. An automated microfluidic system was developed for high-speed screening and morphologic measurement of *C. elegans*.
4. A computer vision-assisted robotic micromanipulation system was proposed for the high-throughput microinjection of *C. elegans*.

## 7.3 Future work

The proposed automation approaches and techniques could be an important step towards the universal automated operations of *C. elegans*. Nevertheless, it has to be noticed that a few experimental problems are not perfectly resolved with the developed techniques of automated worm sorting and worm microinjection, which are listed as follows.

For the automatic worm sorting system:

- The algorithm can recognise the worm morphologic features in a super fast manner, however, it can only provide accurate results when there is only one worm in the region of interests (ROI). If more than one worm is in the image, their body boundaries may connect or even overlap with each other, which will cause errors in the calculation results. Multi-worm loading still exist as the major factor that influences the success rate.
- The dimension parameters of the microfluidic device are designs for specific worm age ranges, and a single microfluidic device cannot suit for all worms. For example, a small nip with the opening size of 30 μm is designed at the entrance channel to achieve one-by-one worm loading. This small nip is capable of stopping the multi-loading of L3-adult worms (diameter larger than 35 μm), however, it is currently not functioning well for small sized worms of L1-L2 stages.

For the automatic worm microinjection system:

- I demonstrated the system performance by performing continuous injection of FITC fluorescent dye into the worm body for a batch of 60 individuals sequentially. Technically, to generate transgenic worms, a small amount of plasmid has to be injected into the worm gonad, so that a few oocytes will include the injected DNA into the cell body during development and further demonstrate the desired phenotypes in the F1 generation. In the microfluidic device, it is difficult to regulate the orientation of the worm body inside the microchannel and make the worm gonad face the injection side. This is the main factor that reduce the injection success rate in practical use.
- Since the worm is immobilized in the microchannel by squeezing it with a micro pillar array, extra inner liquid pressure is generated within the worm body. Thus, after the injection microneedle breaks the worm skin and deliver the injection materials into the worm body, a tendency for the leak of body liquid comes into being when the microneedle is retrieved. Although my following experiments of pharyngeal pumping rate and fecundity demonstrated that the leak make little harm to the worm health, the leaking liquid may contain some of the injected material and reduce the injection effectiveness.

Considering the above problems summarized through experiments, some topics are considered worth further investigation in the future, in order to put the automated worm sorting and injection systems into practical use.

- *In the worm microinjection system, the open channel microfluidic layout can be modified to regulate the axial orientation of the worm within the microfluidic channel.*

  Since the body stiffness of the worm ventral and dorsal sides are different, if bended, the worm body tends to use the dorsal part facing inside while the ventral part facing outside. Base on this phenomenon, a bended microfluidic channel can be adopted to adjust the axial orientation of the worms, and consequently, it would be easier to target the worm gonad during automated microinjection.
- *A more versatile algorithm could be proposed for the analysis of C. elegans morphologic features.*

  The current algorithm is designed to calculate the worm centerlines from its boundary. Thus, the algorithm cannot provide reliable results when the worm boundaries are connected or overlap with each other. More versatile image processing techniques of object structure modelling and deep learning worth further investigation for the worm feature analysis in complex conditions.

Besides the worm screening and worm microinjection projects, some interesting problems can be further pursued based on the patterned illumination system.

- *The bio-mechanics for serpentine locomotion can be further investigated on the developed pattern-light system.*

  Conventionally, the phase difference for the serpentine locomotion of snakes is considered as a constant of $90^0$, however, through both theoretical simulation and practical experiments, the phase difference for *C. elegans* is found to be smaller than $90^0$. In addition, the phase difference is a variable parameter depends on the external friction and viscosity. Further investigation can be conducted to discover the basic mechanism behind this difference between the serpentine locomotion of snakes and *C. elegans*.
- *The basic neuron biology investigations could be conducted on the developed pattern-light system.*

The optogenetic system can be used to investigate the basic biological topics of the generation of movement in the brain of the model organism *C. elegans*.

## 7.4 Publications

### 7.4.1 Refereed journals

- **Xianke Dong**, Pengfei Song, and Xinyu Liu, "Computer Vision-Based Microfluidic System for Real-Time Morphologic Measurement and Sorting of *C. elegans*," *IEEE Transactions on NanoBioScience*, accepted for publication.
- **Xianke Dong*,** Pengfei Song*, and Xinyu Liu. "A Microfluidic Device for Automated, High-Speed Microinjection of *C. elegans*," *Biomicrofluidics*, 10.1 (2016): 011912. (*contributed equally)
- **Xianke Dong**, Pengfei Song, and Xinyu Liu, " Robotic Prototyping for a New Type of Paper-Based Field-Effect Transistor," *IEEE Transactions on Industrial Electronics*. (under review)
- **Xianke Dong***, Pengfei Song*, and Xinyu Liu, "An Automated Robotic System for High-Speed Microinjection of *Caeborhabditis Elegans*," *IEEE Transactions on Automation Science and Engineering*. (*contributed equally, under review)
- **Xianke Dong**, Sina Kheiri, Yangning Lu, Zhen Mei, and Xinyu Liu, "Towards a Soft Microrobo-Nematode: Light-Driven Locomotion Control of *Caenorhabditis Elegans*", to be submitted to *Nature*.
- Fan Yang, Artiom Skripka, Antonio Benayas, **Xianke Dong**, Sung Hwa Hong, Fuqiang Ren, Jung Kwon Oh, Xinyu Liu, Fiorenzo Vetrone, and Dongling Ma. "An Integrated Multifunctional Nanoplatform for Deep-Tissue Dual-Mode Imaging." *Advanced Functional Materials*, 28.11 (2018): 1706235.
- Peng Pan, Juntian Qu, Weize Zhang, **Xianke Dong**, Wei Wei, Changhai Ru, and Xinyu Liu, "Robotic Stimulation of Freely Moving *Drosophila* Larvae Using a 3D-Printed Micro Force Sensor." *IEEE Sensors Journal* (2018).
- Weize Zhang, **Xianke Dong**, and Xinyu Liu. "Switched Fuzzy-PD Control of Contact Forces in Robotic Microbiomanipulation." *IEEE Transactions on Biomedical Engineering,* 64.5 (2017): 1169-1177.
- Lixian Zhang, **Xianke Dong**, Jianbin Qiu, Ahmed Alsaedi, and Tasawar Hayat, "H-infinity Filtering For a Flass of Discrete-Time Switched Fuzzy Systems," *Nonlinear Analysis: Hybrid Systems*, 14 (2014): 74-85.

### 7.4.2 Conference papers

- **Xianke Dong**, Pengfei Song, Xinyu Liu, “Vision-Based Automated Sorting of *C. elegans* on a Microfluidic Device” IEEE International Conference on Robotics and Automation (**ICRA**), May 20-24, 2019, Montreal, Canada.
- Peng Pan, Juntian Qu, Weize Zhang, **Xianke Dong**, Xinyu Liu, “Automated Robotic Stimulation of Freely Moving *Drosophila Larvae*” IEEE International Conference on Manipulation, Automation and Robotics at Small Scales (**MARSS**), July 4-7, 2018, Nagoya, Japan.
- **Xianke Dong**, Pengfei Song, Xinyu Liu, “Rapid Prototyping of Paper-Based Electronics by Robotic Printing and Micromanipulation,” IEEE International Conference on Automation Science and Engineering (**CASE**), August 20-23, 2017, Xi’an, China.
- Weize Zhang, **Xianke Dong**, Simon Silva-Da Cruz, Hossein Khadivi Heris, Luc G. Mongeau, Allen J. Ehrlicher, Xinyu Liu. "A Cost-Effective Microindentation System for Soft Material Characterization." IEEE International Conference on Mechatronics and Automation (**ICMA**), Aug 2-5, 2015, Beijing, China.
- **Xianke Dong***, Pengfei Song*, Xinyu Liu, “An Automated Robotic System for High-Speed Microinjection of *Caeborhabditis Elegans*,” IEEE International Conference on Robotics and Automation (**ICRA**), May 26-30, 2015, Seattle, U.S. (*contributed equally. **Best Conference Paper Finalist, Best Automation Paper Finalist**)
- **Xianke Dong***, Pengfei Song*, Xinyu Liu, “A Microfludic Device for High-Speed Age Synchronization of *Caenorhabditis Elegans*,” International Conference on Miniaturized Systems for Chemistry and Life Sciences (**MicroTAS**), October 25-29, 2015, Gyeongju, Korea. (*contributed equally.)
- Weize Zhang, **Xianke Dong**, Xinyu Liu, “Switched Fuzzy-PD Control of Contact Forces in Robotic Micromanipulation of *Drosophila* Larvae,” IEEE International Conference on Robotics and Automation (**ICRA**), May 26-30, 2015, Seattle, U.S.
- **Xianke Dong***, Pengfei Song*, Xinyu Liu, “A Microfluidic Device for Automated High-speed Microinjection of *Caeborhabditis Elegans*,” International Conference on Solid-State Sensors, Actuators and Microsystems (**Transducers**), June 21-25, 2015, Anchorage, U.S. (*contributed equally)

- **Xianke Dong***, Pengfei Song*, Xinyu Liu, "An Automated, High-speed Microdevice for *Caenorhabditis Elegans* Microinjection," ASME Global Conference on NanoEngineering for Medicine and Biology (**NBME**), April 19-22, 2015, Minneapolis, U.S. (*contributed equally.)

### 7.4.3 Book chapters

- **Xianke Dong**, Wes Johnson, Yu Sun, Xinyu Liu, “Robotic micromanipulation of cells and small organisms,” **Emerging Tools for Micro and Nano Manipulation**, eds. Yu Sun and Xinyu Liu. Wiley-VCH, 2015.